2014

DECELERATING OPEN CHANNEL FLOW OVER GRAVEL: TURBULENCE STRUCTURE & SENSOR DEVELOPMENT

Robert L. Stewart III
University of Kentucky, rlst223@gmail.com

STUDENT AGREEMENT:

I represent that my thesis or dissertation and abstract are my original work. Proper attribution has been given to all outside sources. I understand that I am solely responsible for obtaining any needed copyright permissions. I have obtained needed written permission statement(s) from the owner(s) of each third-party copyrighted matter to be included in my work, allowing electronic distribution (if such use is not permitted by the fair use doctrine) which will be submitted to UKnowledge as Additional File.

I hereby grant to The University of Kentucky and its agents the irrevocable, non-exclusive, and royalty-free license to archive and make accessible my work in whole or in part in all forms of media, now or hereafter known. I agree that the document mentioned above may be made available immediately for worldwide access unless an embargo applies.

I retain all other ownership rights to the copyright of my work. I also retain the right to use in future works (such as articles or books) all or part of my work. I understand that I am free to register the copyright to my work.

REVIEW, APPROVAL AND ACCEPTANCE

The document mentioned above has been reviewed and accepted by the student's advisor, on behalf of the advisory committee, and by the Director of Graduate Studies (DGS), on behalf of the program; we verify that this is the final, approved version of the student's thesis including all changes required by the advisory committee. The undersigned agree to abide by the statements above.

Robert L. Stewart III, Student

Dr. James F. Fox, Major Professor

Dr. Yi-Tin Wang, Director of Graduate Studies

DECELERATING OPEN CHANNEL FLOW OVER GRAVEL: TURBULENCE STRUCTURE & SENSOR DEVELOPMENT

DISSERTATION

A dissertation submitted in partial fulfillment of the
requirements for the degree of Doctor of Philosophy in the
College of Engineering
at the University of Kentucky

By

Robert Lynn Stewart III

Lexington, Kentucky

Director: Dr. James F. Fox, Professor of Civil Engineering

Lexington, Kentucky

2014

ABSTRACT OF DISSERTATION

DECELERATING OPEN CHANNEL FLOW OVER GRAVEL: TURBULENCE STRUCTURE & SENSOR DEVELOPMENT

This dissertation describes investigations of fully turbulent decelerating hydraulically roughbed flow over gravel and the development of technology to measure turbulence and associated sediment transport in streams. Theory is developed for predicting velocity distributions in simple uniform flow using the asymptotic invariance principle and tested using laboratory and field collected data. A mixed scale is developed that accounts for bed derived turbulent structures throughout the flows depth and is used to parameterize the external boundary's effect on the flow for the logarithmic and outer layers. The asymptotic invariance principle and similarity analysis is conducted for the equations of motion in the outer region of decelerating flow over gravel to define equilibrium conditions for this class of flows with the velocity scale is the freestream velocity. The combination of time series and time averaged statistical analysis of turbulent flow is used to elucidate the structure of flow under decelerating conditions. Time averaged statistical measures of turbulence confirm results of others for higher Froude number approaching transcritical and time series analysis shows the effects of decelerating flow on turbulence to be frequency dependent. Wireless velocity sensors were developed and found capable of measuring time averaged velocity and able to resolve macroturbulence from time series data. A semi-theoretical model of elastic deformation of cantilever beams under hydraulic forcing was coupled with circuit theory to develop a calibration procedure for the VBS that requires only three measurement points, one of which is at zero velocity. Light based sensors are developed to estimate light attenuation in water for ecological research or estimating sediment concentration in water. A semi-theoretical scaling of light attenuation and sediment properties was developed which predicts light attenuation from sediment properties. The combination of new theory on open channel velocity, turbulent structure and field sensors for measuring turbulence and sediment offers the possibility to extend our laboratory knowledge to realistic flow situations.

Key words: Nonuniform flow, Channel, Macrtoturbulence, Sensors, Light Attenuation

Robert Lynn Stewart III

8-27-2014

NONUNIFORM OPEN CHANNEL FLOW OVER GRAVEL: TURBULENCE STRUCTURE & SENSOR DEVELOPMENT

By

Robert Lynn Stewart III

Dr. James F Fox
Director of Dissertation

Dr. Yi-Tin Wang
Director of Graduate Studies

08-27-2014
Date

ACKNOWLEDGEMENTS

This work benefited greatly from contributions of my Dissertation committee, fellow graduate students, faculty, and technical staff from departments and laboratories. First and foremost, I'd like to thank my dissertation advisor, Dr. Jimmy Fox for everything. Specifically for enabling me to be better able to understand, test, and communicate nonuniform open channel hydraulics and associated processes. The opportunity to study under your guidance has truly been a blessing. I'd like to thank members of my dissertation committee: Dr. Yi-Tin Wang, Dr. Scott Yost, Dr. Johnathon Phillips and my outside examiner Dr. Donald Colliver, for encouraging me along the way, providing me with opportunities, stimulating my interest for science, testing my abilities, and for your time and interest in my education and future endeavors. Further, I'd like to thank the numerous graduate and undergraduate researchers that aided with sample collection and processing, Dr. Harnett for her hard work and assistance with sensor fabrication and design as well as technical support. I want to thank Drs. Sean Bailey and Carmen Agouridis for use of laboratory equipment. I have a special appreciation for the numerous graduate and undergraduate students for help with experimental design and data collection, there are too many to name them all but I would specifically like to think Dr. Bill Ford. Additionally I would like to thank Sheila, Suzy, and Mrs. Betty for helping me navigate the collegiate network.

I would like to thank by family friends and neighbors for their support, especially my parents and Micki and Chuck who were always there for me through the rollercoaster ride known as graduate school. A special thanks to my parents for supporting me in any venture that made me happy, including graduate school.

Finally, I'd like to thank the College of Engineering, U.S. Geological Society, the National Science Foundation, and the Kentucky Science and Engineering Foundation for providing financial support for my graduate studies and data collection.

TABLE OF CONTENTS

LIST OF TABLES

LIST OF FIGURES

Chapter 1: Introduction

1.1 SUMMARY

Open channel flow processes, including turbulence and the associated transport of suspended sediments, have important implications to river hydraulics and ecological functioning. My primary motivation to study these flows is an intellectual desire, I find water fascinating. The practical reason for studying open channel turbulence and sediment transport is to fulfill the need of society to understand these processes. This topic of study is interesting to me and benefits society by contributing to the body of knowledge. While numerous studies of turbulence and suspended sediment transport for uniform flows are reported, few studies exist for non-uniform flows, typical of open channels, where fluid energy is dissipated through turbulent mechanisms. There exists a lack of applicable theory, laboratory data, and data acquisition systems which collectively impede the understanding of sediment transport in non-uniform open channel flow over a rough bed. My interest to understand open channel flow has driven investigations of the equations of motion, an extensive data collection campaign, and the development of new sensor systems to collect much needed field measurements.

The study of open channel velocity distributions has been primarily focused on the using the boundary shear stress to scale the equations of motion (Wosnik et al. 2000). The difficulty in estimating bed shear stress has led to the development of many methods that produce inconsistent estimates of this quantity and empirical parameterization of equations is necessary to account for discrepancies between theoretical equations and observations. The structure of open channel flow over hydraulically roughbeds dictates the equations of motion be parameterized to account for near bed shear produced shedding eddies with diminishing effect on the flow as the free surface is approached.

The asymptotic invariance principal (AIP) is applied to the equations of motion in the outer region of uniform open channel flows over a rough bed from which the freestream speed is determined as the appropriate velocity scale. A mixed scale is developed that accounts for bed derived turbulent structures felt throughout the flow depth and is used to parameterize the external boundary's effect on the flow for the logarithmic and outer layers. This velocity scale parameterized for gravel beds collapsed velocity profiles in uniform flow collected in both laboratory and field studies. This

theoretical analysis circumvents the difficulties associated with estimating bed shear stress by providing a theoretical basis for predicting velocity distributions using the easily obtained freestream velocity.

Boundary layer studies define equilibrium conditions using AIP to account for the continually developing boundary layer by maintaining that the terms in the equations of motion maintain the same streamwise dependence (Castillo & George 2001). Nonuniform open channel flow continually develops in the streamwise direction and it is hypothesized that the AIP provides a definition of equilibrium to account for streamwise dependence of the equations of motion. The AIP was applied to turbulent fully rough non-uniform open channel flow over gravel to investigate this hypothesis and develop a new equilibrium definition applicable to this class of flows. The new outer scaling derived from the AIP and found to collapse measurements from rivers and laboratory environments when equilibrium conditions were satisfied.

The structure of turbulence in decelerating open channel flows has been described with time average metrics (Song & Graf 1994; Kironto & Graf 1995), however time series analysis of turbulence is lacking. The structure of turbulence in large part dictates behavior of time averaged velocity characteristics and research is needed to connect turbulent processes with time averaged observations. Time series analysis of open channel flows over gravel is necessary to elucidate the scale dependent effect flow deceleration has on turbulent structure and time averaged statistics. Experiments are developed to investigate the effects of flow deceleration on the structure of turbulence and to extend the existing datasets to higher Froude numbers approaching transcritical conditions.

Experimental examinations of decelerating flow over gravel are largely limited to laboratory conditions as velocity sensing technology applicable to field studies are scarce (Roy et al. 2004). In recent years technological advancements have brought about a revolution in environmental sensing technology (Rundel et al. 2009). Inexpensive sensor technology capable of measuring velocity at temporal and spatial scales necessary for verifying computation fluid dynamic models was satisfied with the development of the velocity bend sensor (VBS). Collaborations with electrical engineers from the University of Louisville are convalesced in order to develop velocity sensors capable of measuring

large scale turbulent motions responsible the transport of sediment.

Sediment is a major cause of pollution and habitat degradation in freshwater streams (Davies-Colley & Smith 2001). The need for inexpensive suspended sediment concentration measurements at temporal and spatial scales necessary to identify hot spots of high sediment flux and for calibrating numerical models was satisfied with the development of the light attenuation sensor system (LASS). Development of LASS in conjunction with VBS should enable observations necessary to understand the interactions between suspended sediment transport and turbulence.

Understanding the effects of turbulence and associated suspended sediment transport requires investigating the impacts of suspended sediment on the aquatic ecosystem. Suspended sediments reduce the light available for photosynthesis and may limit primary production in some of the world's most productive aquatic ecosystems (Kirk 1994). There exists a need to relate sediment properties to light attenuation.

The results of this research includes advancements in the theory of open channel turbulence and light attenuation by sediment, unique data sets by which to validate theories, and technological advancements to aid in the measurement of open channel flow, turbulence, and suspended sediment concentration. These contributions may prove useful for the efficient design of river hydraulic projects, ecological assessment and modeling of aquatic ecosystems. Each of these topics is essential to link ecology and hydraulics to support modern research efforts.

The format of this dissertation is independent chapters each contributing significantly to the body of literature. Each chapter is complete with its own symbols, references, and tables & figures. Each chapter is currently published, accepted for publication, or in preparation of publication.

1.2 REFERENCES

Castillo, L., & George, W. K. (2001). Similarity analysis for turbulent boundary layer with pressure gradient: outer flow. *AIAA journal*, *39*(1), 41-47.

Davies-Colley, R.J., & Smith, D. G. (2001) "Turbidity, suspended sediment, and water clarity: a review." *JAWRA Journal of the American Water Resources Association*, 37(5), 1085-1101. DOI: 10.1111/j.1752-1688.2001.tb03624.

Kirk, J. T. O. (1994) *Light and photosynthesis in aquatic ecosystems*, Cambridge

University Press, Cambridge, U.K.

Kironoto, B. A., & Graf, W. H. (1995). Turbulence characteristics in rough non-uniform open-channel flow. *Proceedings of the ICE-Water Maritime and Energy*, *112*(4), 336-348.

Roy, A. G., Buffin-Bélanger, T., Lamarre, H., and Kirkbride, A. D. 2004. Size, shape and dynamics of large-scale turbulent flow structures in a gravel-bed river. Journal of Fluid Mechanics, 500: 1–27.

Rundel, P.W., Graham, E.A., Allen, M.F., Fisher, J.C., and Harmon, T.C. 2009. Environmental sensor networks in ecological research. New Phytologist 182(3): 589-607.

Song, T., and Graf, W.H. 1994, Non-uniform open-channel flow over a rough bed. *Journal of Hydroscience and Hydraulic Engineering*, 12(1): 1-25.

Wosnik, M., Castillo, L., & George, W. K. (2000). A theory for turbulent pipe and channel flows. *Journal of Fluid Mechanics*, 421, 115-145.

Chapter 2: Mixed Scaling for Open-Channel Flow over Gravel and Cobbles

Adapted with permission from Fox, J. F. and Stewart, R. L. (2014) Mixed Scaling for Open Channel Flow Over Gravel and Cobbles, *Journal of Engineering Mechanics* DOI: 10.1061/(ASCE)EM.1943-7889.0000793, 06014010.

2.1 SUMMARY

Mixed scaling that includes inner and outer variables is developed for open channel flow over gravel and cobbles. Similarity analysis is performed following classification of the flow as an equilibrium turbulent boundary-layer using the asymptotic invariance principle. A mixed scale that accounts for the variation of turbulent length in the vertical is used to parameterize the external boundary impact on the flow for the logarithmic and outer layers. The resultant scale uses freestream velocity, hydraulic radius, and characteristic bed particle size D_{84}. The results are consistent with empirical gravel-bed river research and applications, and nicely include the variation of the turbulent flow structure into the scaling. We verify the results using data from gravel- and cobble-bed flumes and rivers and comparison with earlier methods. A single coefficient, semi-theoretical model collapses laboratory and field data well. An integral approach is applied to allow the asymptotic invariance principle equilibrium to be more applicable in future practice.

2.2 INTRODUCTION

The focus of this technical note is mixed scaling for turbulent open channel flow over gravel- and cobble-beds. This class of flows is typical of streams and rivers in high gradient topography, e.g., upland first order streams and rivers in mountainous regions. This class of flows is a subset of turbulent boundary-layers with two notable characteristics, namely: (1) the flow can be defined as an equilibrium turbulent boundary-layer using the asymptotic invariance principle; and (2) this class of flows has been

reported to deviate from the wall similarity hypothesis whereby turbulent motions above the near-wall layers are independent of surface conditions.

An equilibrium turbulent boundary-layer is one in which the solutions exhibit self-similarity and the boundary-layer equation does not show dependence on the streamwise (x) coordinate. By defining the equilibrium solution based on the asymptotic invariance principle (AIP), it is assumed that all velocity, turbulent length scale and pressure gradients maintain the same x dependence in order for the conditions to be equilibrium (George and Castillo, 1997). The AIP equilibrium definition results in outer scaling of the velocity deficit (U_∞-U) (where U_∞ is the free-stream velocity and U is the streamwise mean velocity) by U_∞. AIP equilibrium contrasts the more traditional equilibrium derivation by Clauser (1956) which maintains that no explicit dependence of velocity exists on the x coordinate and as a result the velocity deficit is dependent upon the local friction velocity (U_*). AIP equilibrium was introduced by George and Castillo (1997) after realizing that equilibrium boundary layers as defined by Clauser are very difficult to generate and maintain. Belcher and Fox (2011) provided similarity analysis and results of the AIP equilibrium definition extended to turbulent open-channel flow over a gravel-bed that includes external forcing due to gravity. Belcher and Fox (2011) show that U_∞ is an appropriate outer scale for gravel-bed flume and river flows and the scaling collapses lab and field data well, especially in comparison with normalization of the more traditional U_*.

For fully turbulent open channel flow over gravel- and cobble-beds it is recognized that the roughness particles at the bed can impact turbulence throughout the entire flow depth (Roy et al., 2004; Fox and Belcher, 2011). This concept disagrees with the wall similarity hypothesis first suggested by Townsend (1976). Townsend's wall similarity hypothesis states that at high Reynolds numbers, the turbulent motions in the outer layer are independent of surface conditions except for indirect influence by roughness through its role in determining the friction velocity and boundary-layer thickness. Townsend's wall similarity hypothesis has been the subject of much turbulent boundary-layer scaling research with many rough-walled studies observing that the mean velocity deficit behaves similarly outside the roughness sublayer (Wu and Christensen, 2007). However, gravel- and cobble-bed open channel flow is characterized by low to

moderate relative submergence of bed particles. Amir and Castro (2011) recently showed that for fully rough turbulent boundary-layers with $h/\delta>0.15$ (where h is the roughness height and δ is the boundary-layer thickness) the entire flow is affected by the turbulence in the near-wall region. The universality results, or lack thereof, by Amir and Castro (2011) are consistent with recent turbulence measurements and visualization in laboratory and field tests of turbulent open channel flow over gravel- and cobble-beds (Roy et al. 2004; Hurther et al. 2007; Fox and Belcher, 2011). Near the gravel and cobble particles at the bed, hairpin-like vortices are generated that scale with the particles from which they are shed (Hurther et al., 2007; Belcher, 2009). When moving away from the roughness layer, the turbulent flow structure consists of connected hairpin-like packets that eject away from the bed to form alternating high momentum/low momentum cells termed macroturbulence that scale with the flow depth (Hurther et al., 2007). In this manner, turbulence away from the near-wall region is shown to be impacted by an inner variable associated with particles at the bed with decreasing importance when moving towards the free-surface where the outer variable reflective of the macroturbulence dimensions dominates.

We sought to combine the AIP equilibrium definition together with the recent findings by Amir and Castro (2011) and experimental visualization results to provide mixed scaling of the logarithmic and outer layers for turbulent open channel flow over gravel- and cobble-beds. After formulating our result in the similarity analysis section, we compare our approach using experimental and field data from gravel- and cobble-bed flumes and rivers. We then perform statistical analysis to show the advancement of our method over George and Castillo (1997) and Belcher and Fox (2011) for the case of open channel flow with large roughness elements. Finally, integral analysis is used to produce a roughness relationship and provide a relationship between U_∞ and the friction slope for a simplified condition in order that our method can be more easily applied in the field.

2.3 SIMILARITY ANALYSIS

Our similarity analysis first applies the AIP definition of George and Castillo (1997) to the gravity driven, open channel flow (Belcher and Fox, 2011). We then use a mixed scale to complete the derivation for the problem of large roughness elements. Figure 1 provides a definition sketch for open channel flow over gravel and cobbles. U_∞

is shown in Figure 1 and is the maximum velocity of the velocity profile and physically associated with inviscid external flow. δ is the vertical distance from the lower troughs between roughness elements to the location of U_∞. In Figure 1, flow over the rough bed is divided vertically into the roughness, logarithmic and outer layers (Nikora et al., 2001). The roughness layer is characterized by flow separation from large roughness elements and the turbulent structure and shear stresses reflect the shedding mechanism. The AIP definition and resultant derivation can be applied to flow above the roughness layer in the logarithmic and outer layers where viscous effects can be neglected. The streamwise momentum and continuity equations for the logarithmic and outer layers of a turbulent open channel at high Reynolds are

$$U\frac{\partial U}{\partial x}+V\frac{\partial U}{\partial y}=gS-\frac{1}{\rho}\frac{\partial P_\infty}{\partial x}+\frac{\partial}{\partial y}(uv) \tag{1}$$

and

$$\frac{\partial U}{\partial x}+\frac{\partial V}{\partial y}=0, \tag{2}$$

where x and y are streamwise and vertical coordinates, U and V denote streamwise and vertical mean velocity that can vary in the x and y directions, g is gravitational acceleration, S is the friction slope, ρ is fluid density, P_∞ is the freestream pressure, and uv is the streamwise-vertical Reynolds stress. In Equation (1), the normal stresses and viscous terms are neglected for the logarithmic and outer layers because they are small away from the roughness layer. Similarity solutions for the deficit form of the mean velocity and fluid stress are

$$U-U_\infty=U_{SO}(x)f(\eta,\delta^+,\Lambda,\Theta) \tag{3}$$

and

$$uv=R_{SO}(x)r(\eta,\delta^+,\Lambda,\Theta). \tag{4}$$

U_{SO} and R_{SO} are the velocity and fluid stress scales, and f and r denote functions for the velocity and Reynolds stress profiles, respectively, in the logarithmic and outer layers for which a solution is sought. $\eta=\frac{y}{\delta}$ is the similarity variable. δ^+ is the local Reynolds number ($\delta^+=\delta U_* \nu^{-1}$, where ν is kinematic viscosity). Λ is the energy gradient parameter

that accounts for the impact of external conditions including gravitational acceleration and the freestream pressure gradient (George and Castillo, 1997; Belcher and Fox, 2011). Θ is a parameter representing a dependence on any external condition that may affect the downstream flow (George and Castillo, 1997). Based on the AIP equilibrium definition, f and r become independent of δ^+ as the Reynolds number goes to infinity. With δ^+ removed, the similarity functions are substituted for U and uv into the momentum equation (Equation 1), the momentum equation is manipulated, and the external flow condition for the energy gradient and an expression for V based on continuity are included. The similarity analysis yields

$$\left[\frac{U_\infty \delta}{U_{SO}^{\,2}}\frac{\partial U_{SO}}{\partial x}+\frac{\delta}{U_{SO}}\frac{\partial U_\infty}{\partial x}\right]f+\left[\frac{\delta}{U_{SO}}\frac{\partial U_{SO}}{\partial x}\right]f^2-\left[\frac{\delta}{U_{SO}}\frac{\partial U_{SO}}{\partial x}+\frac{\partial \delta}{\partial x}\right]f'\int_0^\eta f d\eta$$
$$-\left[\frac{U_\infty}{U_{SO}}\frac{\partial \delta}{\partial x}-\frac{\delta}{U_{SO}}\frac{\partial U_\infty}{\partial x}\right]f'\eta=\frac{R_{SO}}{U_{SO}^{\,2}}r' \tag{5}$$

The bracketed terms in Equation (5) maintain the same x dependence based on the AIP equilibrium definition (George and Castillo, 1997). U_{SO} and U_∞ maintain the same x dependence, and by including the external flow condition it is required that

$$\frac{\partial \delta}{\partial x},\quad \frac{\delta}{U_\infty}\left(\frac{\partial U_\infty}{\partial x}\right),\text{ and }\quad \frac{\delta}{U_\infty^{\,2}}\left(g\Im-\frac{1}{\rho}\frac{\partial P_\infty}{\partial x}\right) \tag{6}$$

maintain the same x dependence.

In terms of scaling, results from the similarity analysis using the AIP definition are that U_∞ can be used as an appropriate velocity scale, the solution is independent of δ^+, and Λ is constant (George and Castillo, 1997; Castillo and George, 2001; Belcher and Fox, 2011). The functional dependence of the deficit reduces to

$$\frac{U-U_\infty}{U_\infty}=f\left(\frac{y}{\delta},\Theta\right) \tag{7}$$

As mentioned, Θ is a parameter for the dependence on external upstream conditions. For the class of boundary-layers with low h/δ, turbulence far from the near-wall region is only indirectly influenced by roughness and the external impact on the logarithmic and outer layers will be dominated by an upstream effect. Θ for this class of flows can be corrected for external conditions using the displacement thickness divided by the

boundary-layer thickness (Zagarola and Smits, 1998). For our case of open channel flow over gravel and cobbles, Belcher and Fox (2011) suggested the use of R/aD_{84} for Θ, where R is the hydraulic radius, D_{84} is the particle diameter for which 84% of particles are finer, and a is a variable that accounts for the scale of vortices shed from bed particles. In this case, the roughness height (h) is specified as D_{84} based on experimental results and field measurement, which show that the larger particles control the shed turbulent length scale (Manhart, 1998; Lacey and Roy, 2007; Belcher, 2009), and empirical results that the velocity distribution correlates better with D_{84} than with other particle sizes in the bed (Limerinos, 1970).

We can improve parameterization of Θ and use a mixed scale for Equation (7) based on the recent universality study by Amir and Castro (2011) combined with our understanding of the turbulent processes through experimental and field visualization results (Roy et al., 2004; Fox and Belcher, 2011). Flow over roughness elements with low to moderate relative submergence will gradually modify turbulence throughout the entire flow depth (Amir and Castro, 2011). Physically, shed vortices scale with D_{84} near the bed and throughout the roughness layer (Belcher, 2009). Moving away from the roughness layer, scaling with D_{84} remains important but gradually diminishes. The turbulent structure consists of connected vortices, i.e., hairpin-like packets, that eject away from the roughness layer and increase streamwise length scale (Hurther et al. 2007; Belcher, 2009). Closer to the free-surface, the structure is dominated by macroturbulence that scales with outer variables (Roy et al., 2004; Fox and Belcher, 2011). Based on these results, Θ should be scaled for the external condition of D_{84}/R close to the bed, and the external bed condition diminishes when moving farther from the bed. Equation (7) is thus bounded as

$$\frac{U-U_\infty}{U_\infty} = f\left(\frac{y}{\delta}, \frac{D_{84}}{R}\right) \qquad \text{and} \qquad \frac{U-U_\infty}{U_\infty} = f\left(\frac{y}{\delta}\right) \tag{8a,b}$$

close to the bed and at R, respectively. The decreased importance of the external bed condition can be parameterized as linear and summarized as

$$\frac{U-U_\infty}{U_\infty} = \Theta\, f\left(\frac{y}{\delta}\right), \quad \text{where} \quad \Theta = \frac{1}{R}\left[\left(1-\frac{D_{84}}{R}\right)y + D_{84}\right] \quad . \tag{9}$$

The results enable the logarithmic and outer layers of gravel- and cobble-bed

rivers and flumes to be scaled with the freestream velocity, hydraulic radius, and D_{84}. These results are consistent with traditional river research and applications, as R/D_{84} has been used as an empirical parameter to understand flow roughness and velocity distributions in gravel- and cobble-bed rivers.

2.4 DATA COMPARISON AND STATISTICAL ANALYSIS

We performed data comparison and statistical analyses to verify the results in Equation (9) with field and laboratory tests from gravel- and cobble-bed rivers and flumes and provide comparison with earlier methods. Table 1 provides hydraulic conditions, sediment characteristics, study type and location, and velocity instrumentation for the datasets included in our analyses. Data from five published studies were used including the laboratory studies by Belcher and Fox (2009) abbreviated as BF and Nikora et al. (2001) abbreviated as N, and the field studies by MacVicar and Roy (2007) abbreviated as MR, Afzalimehr and Rennie (2009) abbreviated as AR, and Tritico and Hotchkiss (2005) abbreviated as TH. In addition, two new laboratory velocity profile data collected with an acoustic Doppler velocimeter for the same arrangement as Belcher and Fox (2009) in a gravel-bed flume, which are abbreviated as PS. For all tests, the roughness elements were nonporous, rigid gravel, spherical or cobble particles (see Tab 1) covering the channel bed. For most studies the particles were also immobile, although bedload motion is possible during the MacVicar and Roy (2007) study. Figure 2 shows the mixed outer scaling of the field and laboratory data. Visually, the mixed outer scaling from Equation (9) collapses the data well. Data collapse is less pronounced for $0.2 < y/\delta < 0.4$ because a number of the data points from the field studies fall within the roughness layer at this level. For example, transition from the roughness layer to the logarithmic layers occurs at approximately $y/\delta = 0.36$ for MR-3 and $y/\delta = 0.33$ for TH-8-16, and the theoretical similarity collapse in Equation (9) is applicable only to the logarithmic and outer layers. We highlight the range of conditions represented in Figure 2. Reynolds numbers range from 10^4 to 10^6 supporting the hypothesis that the turbulent structure of the flow is similar in laboratory and field environments. All tests were subcritical but the Froude number ranges across this classification from 0.24 to 0.85 supporting a range of gravel- and cobble-bed river conditions from moderate to high flows.

We also performed statistical analyses to produce a single coefficient, semi-

theoretical model that collapses laboratory and field data for the mixed scaled velocity distribution in gravel- and cobble-bedded open channels. Our semi-theoretical model is compared with models that use the earlier similarity methods of George and Castillo (1997) and Belcher and Fox (2011). A balanced field and laboratory dataset was selected from the range of data in Figure 2 in order to avoid biasing of results since laboratory velocity profiles tended to include many more velocity measurements in the vertical than field velocity profiles. In the analyses, five velocity profiles were used from the laboratory datasets that covered the range of moderate and higher flows for the flumes (BT-1, BT-3, N-1, PS-1 and PS-2). Velocity points were randomly selected from the datasets to produce a total of 30 laboratory data points used in the statistical analysis. Similarly, six field velocity profiles were selected that included the range of moderate and higher flows (i.e., bankfull conditions) for the river sites (TH-8-1, TH-8-7, TH-8-16, MR-2, MR-3, and MR-4), and velocity measurements were randomly selected to produce a total of 30 field data points used in the statistical analysis. We restricted the data points chosen for analyses to the logarithmic and outer layer velocity measurements (see Fig 1). Points at $y=\delta$ were omitted due to the fact that by definition the ordinate calculates to zero for the method of George and Castillo (1997) and Belcher and Fox (2011).

Figure 3 provides single coefficient equations for laboratory and field data for the outer region velocity distribution in gravel- and cobble-bedded open channels using our similarity method and that of George and Castillo (1997) and Belcher and Fox (2011). Visually and quantitatively using the coefficient of determination as a measure of goodness-of-fit, our similarity method provides better agreement with the data as compared to the earlier published methods. We point out that this is the case for all data within the statistical analysis as well as separately for the laboratory data and the field data. Collapse was very good for the laboratory data (R^2=0.95). Scatter remained in the field measurements around the logarithmic fit (R^2=0.55) although our best fit line in Fig 3a did not appear to bias the field measurements.

The remaining scatter in the field data was difficult to constrain. We performed statistical regression analyses to assess additional dependence of c_1 for individual velocity profiles upon flow and sediment variables including D_{84}, U_∞, δ, R, $Re\#$, $Fr\#$ and k^+, and no significant statistical dependence was found. Rather, remaining variability of

field data is attributed to a number of realities of field measurements in gravel- and cobble-bed rivers during moderate and high flows. For example, the highest flow measurements were collected by MacVicar and Roy (2007) during a bankfull river event where stream velocities exceeded $2ms^{-1}$. During these conditions, appropriate selection of the velocity profile origin, y_0, may be difficult, although choice of y_0 can substantially impact the velocity distribution (Smart, 1999). The actual roughness height might also vary from D_{84} during moderate and high flow events if the bed is dynamic and bedload motion is prevalent, which would impact the velocity distribution. Finally, the location of the velocity profile measurements with respect to individual gravel and cobble particles would impact the logarithmic and outer layer velocity profiles since the large roughness elements can impact the flow structure throughout its depth. This latter reason for scatter has prompted the use of double-averaging (i.e., time- and space-averaging) of velocity measurements for open channel flow with gravel- and cobbles (Nikora et al., 2001). While the Nikora et al. (2001) and Belcher and Fox (2009) laboratory datasets were double averaged, the field velocity measurements compared in our analysis were not double-averaged. We point out that no such datasets currently exist in the literature to our knowledge for moderate and high flow (i.e., bankfull) open channels with gravel- and cobble-beds. Franca et al. (2008) provides a comprehensive double-averaged velocity dataset for two cobble-bed streams in France. However, these data were collected during summer, low water conditions when almost the entire velocity profile was within the roughness region. Future studies will be welcomed, albeit arduous, that collect double-averaged velocity data for moderate and high flow conditions.

2.5 INTEGRAL ANALYSIS

The AIP equilibrium definition produces a velocity distribution for open channels with gravel- and cobble-beds that is dependent upon U_∞. The AIP derived relationship (see Fig 3a) can be applied for gravel- and cobble-bed rivers and flumes by measuring U_∞ near the free-surface using mean velocity measurements or a neutrally buoyant tracer and coupling the measurements with D_{84}, R and δ. However, we recognize that measuring U_∞ might not always be practical and researchers and practitioners might desire a formulation of $U(y)$ based on the friction slope. We address this need by examining the dependence of the depth-average velocity, V, and freestream velocity, U_∞, upon the

friction slope. We emphasize a subclass of boundary layers with assumptions that are typical for bulk parameterization of velocity, shear and roughness relationships in rivers and include flow uniformity and fully developed conditions. While these conditions may never truly exist in gravel- and cobble-bed mountain rivers, their assumption is typical of the traditionally applied open channel flow momentum equation for roughness calculations. Our added assumptions relax gradients in Equation (5) because the free-stream velocity, pressure and boundary layer height lose dependence on the streamwise direction, and the gravity force in the flow direction is balanced by the friction force. This concept is quantified using analysis of the integral momentum equation in steady uniform flow which reduces to a balance between shear and gravitational acceleration as

$$\tau_0 = \rho g R S \tag{10}$$

In this manner, the frictional force encompasses both skin friction and that associated with drag, e.g., fluid bending over large gravel/cobbles. From dimensional analysis, it is well recognized that τ_0 can be balanced with the depth-average velocity, V, by including the influence of roughness and deriving the classical Chézy formula as

$$V = C\sqrt{RS_e}, \tag{11}$$

where C is the Chézy coefficient.

Following from our theoretical derivation in Equation (9) and empirical fit in Fig 3a, we evaluated the behavior of V and U_∞ to estimate a Chézy-type roughness relationship. Figure 4 shows the results for both V and U_∞ as a function of $\sqrt{RS_e}$ for the studies included in Table 1. The dependence of C upon $\sqrt{\frac{R}{D_{84}}}$ is shown in the coefficient of determination's goodness-of-fit and the equations provided in Figure 4. These roughness results in Fig 4a agree well with other reported roughness relationships for gravel- and cobble-bed rivers where the Chézy coefficient is proportional to the logarithm of the relative submergence or a power equation where the exponent placed on the relative submergence is less than one (Bray, 1979; Bathurst, 1985; Rice et al., 1998). The results in Fig 4b allows the AIP-derived velocity distribution with dependence on U_∞ to be more easily calculated by practitioners.

2.6 DISCUSSION

Equation (9), the data verification, and the single parameter fit in Fig 3a reinforce

the validity of a non-constant parameter for the external conditions due to the fact that gravel- and cobble-bed channels deviate from Townsend's wall similarity hypothesis. This class of boundary-layer with large roughness elements appears to feel the impact of the roughness elements upon the flow structure throughout the depth. The physics of this phenomena is yet to be fully resolved and it is quite plausible that the flow detachment mechanism extends away from the bed into the outer region when roughness elements are large while at the same time the macroturbulent feature of the flow exhibits universality. This idea would support the results of Amir and Castro (2011) and our mixed-scale collapse presented in this study but also support macroturbulence universality results presented by Hommema and Adrian (2002) and Smits et al. (2011). Qualitative evidence of visual flow patterns in gravel- and cobble-bed rivers also supports this concept as large form induced vortices shed from large roughness elements at the bed have been described as funnel-like structures that travel to the free surface where they are manifested as boils (Roy et al., 2004).

2.7 CONCLUSIONS

The notable analyses and findings in the present technical note are the following:

1. A mixed-scale similarity analysis results in Equation (9) for the logarithmic and outer layers of open channels with gravel and cobble beds. Our analysis builds off of earlier work by George and Castillo (1997) and Belcher and Fox (2011).
2. Statistical analyses is performed to compare the present results with that of George and Castillo (1997) and Belcher and Fox (2011), and we show that the goodness-of-fit is better for our new method when considering all laboratory and field data together, laboratory data alone, or field data alone.
3. A single coefficient, semi-theoretical model that collapses both laboratory and field data is presented in Fig 3a for the outer region velocity distribution in gravel- and cobble-bedded open channels.
4. An integral approach is applied in Fig 4 that addresses the impact of the friction slope and roughness upon the depth-average and freestream velocity. Our integral analysis allows the AIP equilibrium to be more applicable to future practice.

We make a final point about the hydraulic conditions and limitations of the results

in Equation (9). Similarity analysis is based on the assumption of unidirectional flow and positive friction slope. The data used for verification in Figure 2 were from straight hydraulic flumes with gravel sized particles or relatively straight, unidirectional sections in gravel- and cobble-bed rivers. Further, Equation (9) is limited to positive gradients such as riffles, the thalweg, and rivers at moderate to high flows. Castillo and George (2001) show that three unique values exist for zero, adverse and favorable pressure gradients, and similarly the mixed outer scaling should be revisited for example to better scale the velocity deficit in backwater pools. Finally, the work is applicable to relatively low values for the relative submergence and thus may not be directly applicable to plane sand beds. That being said, the mixed outer scaling is potentially applicable to sand bed streams with pronounced bedform height; however further research will be needed in this area. Broader implications of this research are that relaxing the need for Clauser-like equilibrium opens possibilities for river flow modeling in future research and application.

2.8 ACKNOWLEDGEMENTS

We will like to thank three anonymous reviewers for their input that helped greatly improve the quality of this paper. We will like to thank Cheree Bailey for her assistance with graphics. We acknowledge National Science Foundation project #0918856 and the University of Kentucky, Department of Civil Engineering for partial support of Robert Stewart's salary.

2.9 LIST OF SYMBOLS:

a = turbulent length scale interacting with particles at the bed

D_{84} = particle diameter for which 84% of the bed material bed is finer, mm

f = similarity function for U-U_∞

$Fr\#$ = Froude number, = $U_{ave}(gH)^{-1/2}$

g = acceleration of gravity, ms^{-2}

h = roughness height, m

H = flow depth, m

k^+ = roughness Reynolds number, = $U_* D_{84} v^{-1}$

P_∞ = freestream pressure, Pa

r = similarity function for uv

R = hydraulic radius, m

$Re\#$ = Reynolds number, = $U_{ave}Hv^{-1}$

R_{SO} = fluid stress scale for the logarithmic and outer layers, Pa

S = friction slope, m/m

U = mean streamwise velocity, ms^{-1}

U_{ave} = depth average velocity, ms^{-1}

U_{SO} = streamwise velocity of the logarithmic and outer layers, ms^{-1}

U_{∞} = freestream velocity, ms^{-1}

U_{*} = friction velocity, ms^{-1}

uv = streamwise-vertical Reynolds stress, m^2s^{-2}

V = mean vertical velocity, ms^{-1}

x = streamwise coordinate, m

y = vertical coordinate, m

δ = boundary layer thickness, m

δ^{+} = local Reynolds number, = $\delta U_{*}v^{-1}$

η = similarity variable

Θ = parameter representing external conditions

Λ = energy gradient parameter

ρ = fluid density, kgm^{-3}

v = fluid viscosity, m^2s^{-1}

2.10 REFERENCES

Afzalimehr, H. and Rennie, C.D. (2009). Determination of bed shear stress in gravel-bed rivers using boundarly layer parameters. *Hydrological Sciences*, 54(1): 147-159.

Amir, M. and Castro, I.P. (2011). Turbulence in rough-wall boundary layers: universality issues. *Experiments in Fluids*, 51(2): 313-326.

Bathurst, J.C. (1985). "Flow resistance estimation in mountain rivers." *Journal of Hydraulic Engineering*, ASCE, 111(4), 625-643.

Belcher, B. (2009). Vortex model of open channel flows with gravel beds. PhD Thesis, University of Kentucky, Lexington, Kentucky.

Belcher, B., and Fox, J. (2009). Discussion of Rodriguez, J. F., and Garcia, M. H. 2008. Laboratory measurements of 3-D flow patterns and turbulence in straight open channel with rough bed. *Journal of Hydraulic Research*, 46(4), 454-465.

Belcher, B.J. and Fox, J.F. (2011). Outer scaling for open channel flow over a gravel bed. *Journal of Engineering Mechanics*, ASCE, 137(1): 40-46.

Bray, D.I. (1979). "Estimating average velocity in gravel-bed rivers." *J. Hydraul. Div*. ASCE, 105(HY9), Proc. Paper 14810, pp.1103-1122.

Castillo, L., and George, W. K. (2001). Similarity analysis for turbulent boundary layer with pressure gradient: outer flow. *AIAA*, 39, 41-47.

Clauser, F. H. (1956). The turbulent boundary layer. *Adv Appl Mech*, 4, 1-51.

Franca, M.J., Ferreira, R.M.L. and Lemmin, U. (2008) "Parameterization of the logarithmic layer of double-averaged streamwise velocity profiles in gravel-bed river flows." *Advances in Water Resources*, 31:915–925.

George, W.K. and Castillo, L. (1997). Zero-pressure-gradient turbulent boundary layer. *Appl Mech Rev*, 50(11), 689-729.

Hommema, S. E., and Adrian, R. J. (2002). "Similarity of apparently random structures in the outer region of wall turbulence." *Experiments in Fluids*, 33, 5-12.

Hurther, D., Lemmin, U. and Terray, E.A. (2007). Turbulent transport in the outer region of rough-wall open-channel flows: the contribution of large coherent shear stress structures (LC3S). *Journal of Fluid Mechanics*, 574: 465-493.

Lacey, R. W. J., and Roy, A. G. (2007). "A comparative study of the turbulent flow field with and without a pebble cluster in a gravel bed river." *Water Resources Research*, 43(W05502).

Limerinos, J. T. (1970). "Determination of manning coefficient from measured bed roughness in natural channels." United States Geological Survey.

MacVicar, B. J., and Roy, A. G. (2007). Hydrodynamics of a forced riffle pool in a gravel bed river: 1. Mean velocity and turbulence intensity. *Water Resources Research*, 43(124).

Manhart, M. (1998). "Vortex shedding from a hemisphere in a turbulent boundary layer." *Theoretical and Computational Fluid Dynamics*, 12(1), 1-28.

Nikora, V., Goring, D., McEwan, I. and Griffiths, G. (2001) Spatially averaged open-channel flow over a rough bed. *Journal of Hydraulic Engineering*, ASCE, 127(2): 123-133.

Rice, C.E., Kadavy, K.C. and Robinson, K.M. (1998) "Roughness of loose rock riprap on

steep slopes." *Journal of Hydraulic Engineering*, ASCE, 124(2):179-185.

Roy, A. G., Buffin-Belanger, T., Lamarre, H., and Kirkbride, A. D. (2004). Size, shape and dynamics of large-scale turbulent flow structures in a gravel-bed river. *Journal of Fluid Mechanics*, 500, 1-27.

Smart, G.M. (1999) "Turbulent velocity profiles and boundary shear in gravel bed rivers." *Journal of Hydraulic Engineering*, ASCE, 125(2):106-116.

Smits, A.J., McKeon, B.J., Marusic, I. (2011). "High-Reynolds number wall turbulence." *Annu. Rev. Fluid Mech*. 43:353-75.

Townsend, A.A. (1976). The structure of turbulent shear flow, 2nd ed. Cambridge University Press, Cambridge, UK.

Tritico,H.M. and Hotchkiss, R.H. (2005). Unobstructed and obstructed turbulent flow in gravel bed rivers. *Journal of Hydraulic Engineering*, 131(8): 635-645.

Wu, Y. and Christensen, K.T. (2007). Outer-layer similarity in the presence of a practical rough-wall topography. *Physics of Fluids*, 19: 085108.

Zagarola, M. V., and Smits, A. J. (1998). Mean-flow scaling of turbulent pipe flow. *Journal of Fluid Mechanics*, 373, 33-79.

2.11 TABLES AND FIGURES

Table 2.1. Attributes for velocity data scaled in Figure 2.

Test	Location	Velocimeter §	Averaging	D_{84} (mm)	σ_g (mm)	U_∞ (m s^{-1})	δ (m)	R (m)	$Re\#$	$Fr\#$	k^+
BF-1	Flume with angular stone	PIV	double	5.6	1.4	0.62	0.034	0.035	1.9×10^4	0.78	206
BF-2		PIV	double	5.6	1.4	0.76	0.051	0.048	3.5×10^4	0.83	245
BF-3		PIV	double	5.6	1.4	0.83	0.06	0.056	4.6×10^4	0.83	262
BF-4		PIV	double	5.6	1.4	0.83	0.066	0.061	5.2×10^4	0.8	273
PS-1		ADV	time	5.6	1.4	0.9	0.07	0.061	7.2×10^4	0.82	357
PS-2		ADV	time	5.6	1.4	0.94	0.091	0.07	9.2×10^4	0.85	379
MR-2	Gravel bed river in Eastern Quebec, Canada	ECM	time	190	3.4	2.25	0.64	0.64	1.2×10^6	0.53	34030
MR-3		ECM	time	190	3.4	1.8	0.74	0.7	1.1×10^6	0.38	56716
MR-4		ECM	time	190	3.4	1.7	1.05	0.85	1.5×10^6	0.36	71841
N-1	Flume with uniform spheres	ADV	double	21	1	0.8	0.081	0.12	1.2×10^5	0.5	1609
AR-1	Salmon River, Canada	ADV	time	90	1.3	0.88	0.46	0.64	4.7×10^5	0.26	9851

Table 2.1 (continued)

TH-7-27	Mountainous gravel bed rivers in Pacific Northwest, United States	ADV	time	106	2.2	0.51	0.22	0.28	1.1×10^5	0.26	3586
TH-8-1		ADV	time	106	2.2	0.66	0.35	0.39	2.1×10^5	0.24	5485
TH-8-7		ADV	time	48	2.2	0.54	0.2	0.26	1.2×10^5	0.27	2340
TH-8-16		ADV	time	55	2.2	0.77	0.33	0.44	3.3×10^5	0.29	3393
TH-8-22		ADV	time	190	3.1	0.63	0.31	0.46	2.6×10^5	0.35	10209

§ PIV is particle image velocimetry; ADV is acoustic Doppler velocimetry; ECM is electromagnetic current meter.

Figure 2.1. Definition sketch.

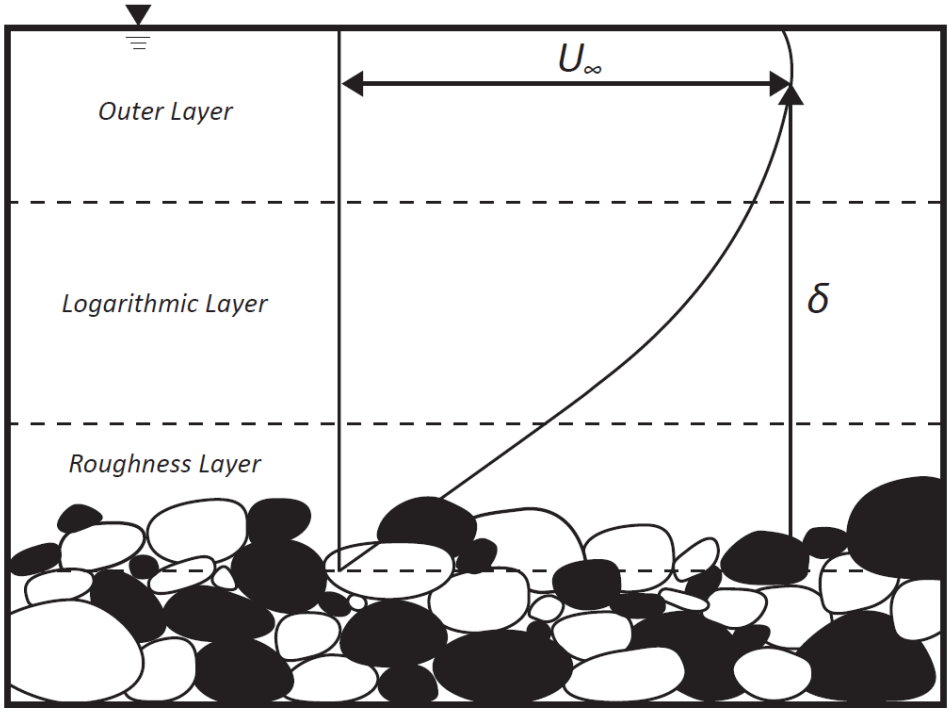

Figure 2.2. Mixed scaling of field and laboratory data from gravel- and cobble-bed streams and flumes using Equation (9).

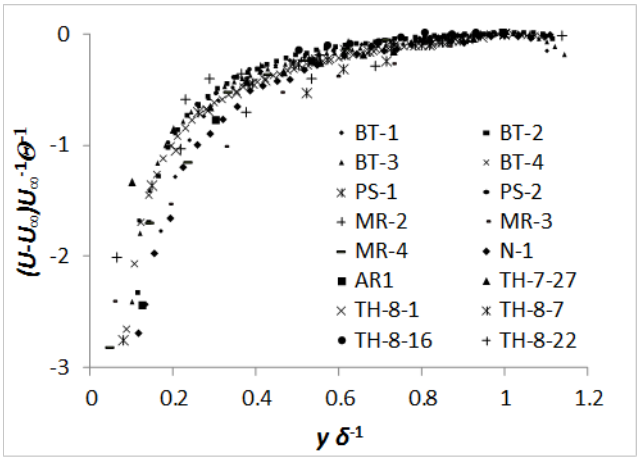

Figure 2.3. Statistical analyses of scaling methods using laboratory and field data.

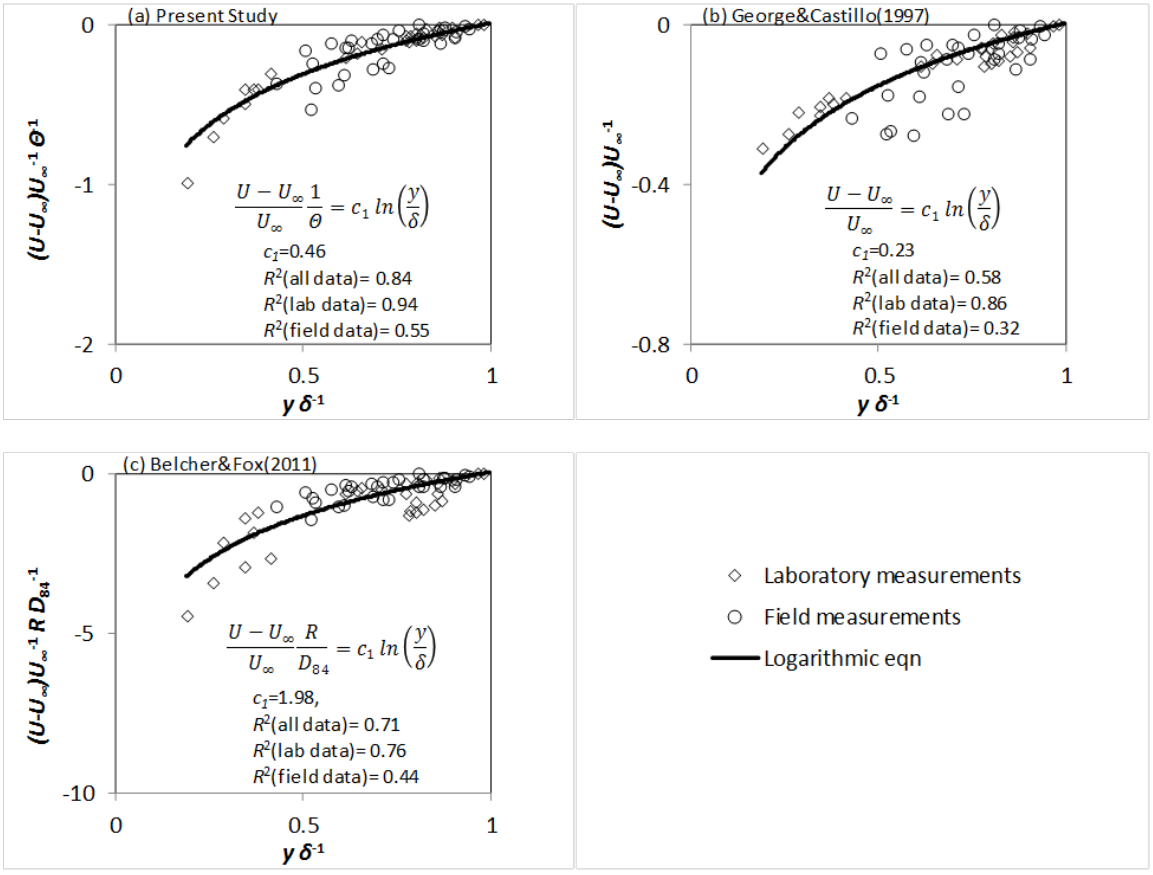

Figure 2.4. Roughness relationships for the data in Table 1.

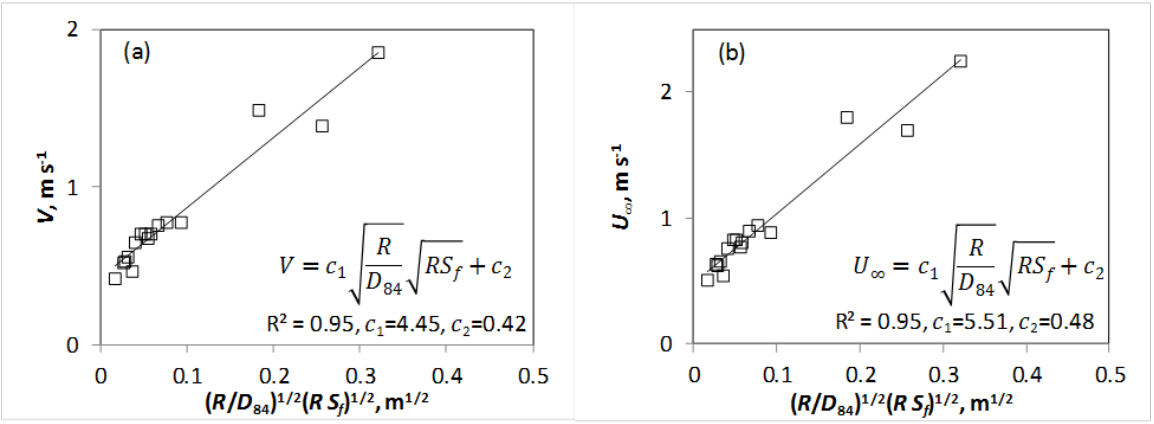

Chapter 3: Outer Region Scaling Using the Freestream Velocity for Nonuniform Open Channel Flow Over Gravel

3.1 SUMMARY

The theoretical basis for outer region scaling using the freestream velocity for nonuniform open channel flows over gravel is presented and tested. Owing to the gradual expansion of the flow within the nonuniform case presented, it is hypothesized that the flow can be defined as an equilibrium turbulent boundary layer using the asymptotic invariance principle. We support the hypothesis using similarity analysis to achieve a solution followed by further testing with experimental datasets. For the latter, we use 38 new experimental velocity profiles across three nonuniform flows over gravel in a hydraulic flume and 51 published velocity profiles collected over gravel in a hydraulic flumes and rivers. Our results support the nonuniform flow as AIP equilibrium, which is reflective of the consistency of the turbulent structure's form and function within the expanding flow. However, roughness impacts when comparing across the different published experimental datasets. As a secondary objective, we show how previously published mixed scales can be used to assist with scaling the velocity deficit and thus empirically accounting for the roughness effects that extend into the outer region of the flow. One practical implication of this study is providing the theoretical context to relax the use of the elusive friction velocity when scaling nonuniform flows in gravel bed rivers; and instead to apply the freestream velocity. A second point that is highlighted by our results is that scaling of nonuniform flow in gravel bed rivers is not fully resolved in a theoretical sense and we still are relying to some degree on empiricism; as we resolve the form and function of macroturbulence in the outer region, we hope to work towards closing this research gap.

3.2 INTRODUCTION

The motivation of this paper is to present, test and provide application of the theoretical basis for outer region scaling using the freestream velocity (U_∞) for nonuniform open channel flows over gravel. The open channel flows over gravel are classified as fully hydraulically rough turbulent flow with relatively large roughness elements that can be felt throughout much of, if not the entire, flow depth. We focus on a nonuniform case for these turbulent flows in which the fluid is gradually varied and

expanding in the vertical due to an adverse pressure gradient. In application, the nonuniform flow case is typical of mountainous gravel and cobble bed rivers in decelerating pools that are constrained by streambank sidewalls.

Nonuniform open channel flows over gravel is classified as a subset of turbulent boundary layer flows with a number of notable characteristics. First, the flow is hydraulically rough and the Reynolds number is high producing appreciable separation of inner and outer scales such that a clear overlap region develops, i.e., seen classically when profiles display an appreciable length of logarithmic behavior (Smits et al. 2011). The high Reynolds number of the flow suggests that we can expect unique scaling for the inner roughness region and the outer region, the latter of which is our focus herein.

Second, due to the adverse pressure gradient impacting the open channel, the flow is nonuniform, decelerating and the outer region of the turbulent boundary layer is gradually expanding in the vertical direction as the boundary layer height, δ, increases while the freestream velocity, U_∞, at δ decreases as a function of x. The high Reynolds number and gradual nature of the expansion dictate that the turbulent structure of the flow maintains its general function in transferring potential and kinetic energy to dissipated heat as well as its general double-layer form. However the enhancement of the vertical velocity explicit in the continuity equation and its influence on sustaining the Reynolds shear stresses throughout the profile (Song, 1994).

Third, the outer fluid structure does not fully lose memory of the shear structure initiated by the roughness elements at the bed. It has been argued in early literature using scaling and roughness laws and now recently using experimental results that bed initiated turbulence impacts the flow structure throughout its entire depth including the outer layer (Einstein and Barbarossa, 1952; Vanoni and Nomicos, 1960; Rouse, 1965; Hurther et al., 2007; Belcher, 2009; Amir and Castro, 2011). While the connectivity between the outer region turbulent structure and near bed shedding has not been fully resolved, a fairly consistent paradigm has emerged that includes near-bed generation of hairpin-like vortices that eject away from the bed in the form of connected hairpin-like packets that evolve to alternating high momentum/low momentum cells (Hurther et al., 2007; Belcher, 2009).

In terms of outer region scaling of the nonuniform flow, we consider the two

characteristics above including the high Reynolds number and consistency of the turbulent structure throughout the gradual expansion, which suggest the fluid be defined as an equilibrium turbulent boundary layer where the dynamical influences of the fluid develop together (Wosnik, 2000). The nonuniform flow can be defined using the equilibrium solution based on the asymptotic invariance principle (AIP), which assumes that all velocity, turbulent length scale and pressure gradients maintain the same x dependence (George and Castillo, 1997). AIP equilibrium implies that the transformation mechanisms between potential energy and kinetic energy throughout the boundary layer are consistent, and therefore the turbulence structure is not changing form in the streamwise direction; the streamwise velocity is self-similar when properly scaled; and the energy gradient parameter is constant.

The AIP equilibrium definition has been shown to result in outer scaling of the velocity deficit, U_∞-U, where U_∞ is the free-stream velocity and U is the streamwise mean velocity by U_∞. AIP equilibrium has been derived for flat plate boundary layers with zero, favorable and adverse pressure gradients and open channels with favorable gradients (George and Castillo, 1997; Castillo and George, 2001; Belcher and Fox, 2011), however, AIP equilibrium has not been derived or tested for the nonuniform open channel flow case. The gradual vertical expansion and consistent turbulent structure of nonuniform flow over gravel prompted us to hypothesize that the flow case can be defined by AIP equilibrium. One application of this scaling would be that nonuniform flow in gravel bed rivers could be predicted using the easily measurable U_∞ as compared to the often used, but elusive, friction velocity.

Our objective was to derive the AIP equilibrium solution for the nonuniform flow case with gradual expansion indicated by wall normal velocity and flow deceleration; and test the applicability of the U_∞ scaling that results from the similarity analysis. For the latter, we collect 38 new experimental velocity profiles across three nonuniform flows over gravel in a hydraulic flume. We also use 51 published velocity profiles collected over gravel in a hydraulic flumes and rivers for testing the AIP equilibrium solution. Our own data was needed, beyond the data already available in the literature, to: (i) account for Froude number conditions approaching transcritical flows that are typical of decelerating pools in steep mountainous gravel and cobble bed rivers, and (ii) provide

many velocity profiles for the same expanding boundary layer and thus allow further testing of AIP equilibrium by checking that the energy gradient parameter is constant.

As a secondary objective, we also considered and tested several empirical outer region scaling's that can be combined with U_∞ to provide a mixed scale. One characteristic of the AIP-equilibrium solution is that U_∞ alone may not collapse the velocity deficit due to variations in external flow conditions and boundary conditions, e.g., variations in the pressure gradient and roughness elements (Castillo and George, 2001). We test empirical scalings of Zagarola and Smits (1998) and Fox and Stewart (2014) using our newly collected experimental data and the previously mentioned literature data. Zagarola and Smits (1998) and Fox and Stewart (2014) were chosen due to the fact that they have been shown to perform well for boundary layers with large roughness elements.

3.3 SIMILARITY ANALYSIS

The theoretical basis for outer region using the freestream velocity (U_∞) for nonuniform open channel flows over gravel is presented by defining the equilibrium solution based on the asymptotic invariance principle (AIP) and performing similarity analysis of the streamwise momentum equation. By defining the equilibrium solution based on AIP, it is assumed that all velocity, turbulent length scale and pressure gradients maintain the same x dependence for the conditions to be equilibrium (George and Castillo, 1997). Similarity analysis that applies the AIP definition has been reported in a number of publications for flat plate boundary layers with zero, favorable and adverse pressure gradients and open channels with favorable gradients (George and Castillo, 1997; Castillo and George, 2001; Belcher and Fox, 2011; Fox and Stewart, 2014). Based on this earlier work coupled with considerations for nonuniform flow, we derive the AIP similarity analysis solution and thus extend the definition to the case of nonuniform open channel flow with an adverse pressure gradient manifested at the free surface. Thereafter, we consider several mixed scales reported in the literature that can potentially be combined with U_∞ and applied to nonuniform open channel flow over gravel to account for external conditions and roughness effects that AIP cannot collapse alone.

The AIP definition and resultant derivation can be applied to nonuniform open channel flow above the roughness layer in the logarithmic and outer layers where viscous

effects can be neglected. The streamwise momentum and continuity equations for the logarithmic and outer layers of a turbulent open channel at high Reynolds number are

$$U\frac{\partial U}{\partial x}+V\frac{\partial U}{\partial y}=gS-\frac{1}{\rho}\frac{\partial P_{\infty}}{\partial x}+\frac{\partial}{\partial y}\left(\overline{u'v'}\right)+\frac{\partial}{\partial x}\left(\overline{u'u'}\right) \quad \text{, and} \tag{1}$$

$$\frac{\partial U}{\partial x}+\frac{\partial V}{\partial y}=0, \tag{2}$$

where x and y are streamwise and vertical coordinates, U and V denote streamwise and vertical mean velocity that can vary in the x and y directions, g is gravitational acceleration, S is the bed slope, ρ is fluid density, P_{∞} is the freestream pressure, $\overline{u'v'}$ is the streamwise-vertical Reynolds stress, and $\overline{u'u'}$ is the streamwise normal stress. In Equation (1), the viscous terms are neglected for the logarithmic and outer layers because they are small away from the roughness layer. The normal stress term is also neglected from Equation (1) based on the consideration that it is small relative to the Reynold's shear term. To justify the omission, the normal stress term was evaluated upstream of a large obstruction to provide a conservative case for investigation. Experimental analysis suggested the normal stress term was an order of magnitude smaller than the vertical gradient of shear stress in the outer region. Thus, it is reasonable to neglect the streamwise gradient of the normal stress component even in non-uniform flow. The flow evaluated experimentally represents a large obstruction and pronounced adverse energy gradient causing deviation from uniform flow; at normal depth the gradient would be identically zero and thus for most cases of obstructed flow this assumption should remain valid.

Similarity solutions for the deficit form of the mean velocity and fluid stress are

$$U-U_{\infty}=U_{SO}(x)f\left(\eta,\delta^{+},\Lambda,\Theta\right) \tag{3}$$

and

$$\overline{u'v'}=R_{SO}(x)r\left(\eta,\delta^{+},\Lambda,\Theta\right). \tag{4}$$

U_{SO} and R_{SO} are the velocity and fluid stress outer scales, and f and r denote functions for the velocity and Reynolds stress profiles, respectively, in the logarithmic and outer layers

for which a solution is sought. $\eta = \frac{y}{\delta}$ is the similarity variable. δ^+ is the local Reynolds number ($\delta^+=\delta U_* \nu^{-1}$, where ν is kinematic viscosity). Based on the AIP equilibrium definition, f and r become independent of δ^+ as the Reynolds number goes to infinity. Therefore, f and r are removed from the brackets in Equations (3) and (4) and the similarity functions are no longer dependent on the friction velocity. Λ is the energy gradient parameter that accounts for the impact of external conditions including gravitational acceleration and the freestream pressure gradient; and we will show later that Λ is constant for a given nonuniform flow case where the velocity scale, length scale and pressure gradient exhibit the same x dependence (George and Castillo, 1997; Belcher and Fox, 2011). Θ is a parameter representing a dependence on any external condition that may affect the downstream flow. There is no argument for removing Θ as perturbations to the flow structure by upstream objects such as large roughness elements occur regardless of Reynolds number.

After removing δ^+ from the similarity solutions in Equations (3) and (4), the similarity functions are substituted for U and $\overline{u'v'}$ in the momentum equation of Equation (1) to yield

$$\left(U_{so}f + U_\infty\right)\frac{\partial\left(U_{so}f + U_\infty\right)}{\partial x} + V\frac{\partial U_{so}f}{dy} + V\frac{\partial U_\infty}{dy} = gS - \frac{1}{\rho}\frac{\partial P_\infty}{\partial x} + \frac{\partial R_{so}r}{\partial y} \tag{5}$$

We note that the vertical gradient of U_∞ is zero since U_∞ is constant for any location in the streamwise direction and the vertical gradient of f can be concisely written as $\frac{\partial f}{\partial y} = \frac{\partial f}{\partial \eta}\frac{\partial\left(y/\delta\right)}{\partial y} = \frac{f'}{\delta}$. Expanding and representing derivatives of f and r with respect to η as f' and r' allows Equation (5) to be rewritten as

$$U_{so}f\frac{\partial U_{so}f}{dx} + U_\infty\frac{\partial U_{so}f}{dx} + U_{so}f\frac{\partial U_\infty}{dx} + U_\infty\frac{\partial U_\infty}{dx} + \frac{VU_{so}}{\delta}f' = gS - \frac{1}{\rho}\frac{\partial P_\infty}{\partial x} + \frac{R_{so}}{\delta}r' \tag{6}$$

The number of parameters in Equation (6) can be reduced by relating the freestream pressure gradient to the freestream velocity (i.e. at the boundary layer edge) assuming that viscosity is negligible at δ using the Euler's equation applied to open channel flow as

$$\frac{\partial}{\partial x}\left(\frac{1}{2}U_\infty^2\right)+\frac{1}{\rho}\frac{\partial P_\infty}{\partial x}+gS=0$$

or .

$$\frac{1}{\rho}\frac{\partial P_\infty}{\partial x}=gS-U_\infty\frac{\partial U_\infty}{\partial x} \tag{7}$$

Assuming inviscid flow at the boundary location is commonly practiced as velocity gradients are theoretically non-existent and Euler's equation is a reasonable approximation to the equations of motion. The assumption does not restrict the limit of the solution space to the boundary; it simply allows us to make outer parameters comparable. By using Euler's equation to describe the freestream pressure gradient in terms of freestream velocity and canceling terms, we arrive at

$$U_{so}f\frac{\partial U_{so}f}{dx}+U_\infty\frac{\partial U_{so}f}{dx}+U_{so}f\frac{\partial U_\infty}{dx}+\frac{VU_{so}}{\delta}f'=\frac{R_{so}}{\delta}r' \quad . \tag{8}$$

Equation (8) is the momentum equation written in terms of similarity solutions for mean velocity and Reynolds shear stress. Next, the vertical velocity component, V, is written in terms of U using the continuity equation specified for the similarity solution as

$$\frac{\partial V}{\partial y}=-\frac{\partial U}{\partial x}=-\frac{\partial U_\infty}{\partial x}-f\frac{\partial U_{so}}{\partial x}-U_{so}\frac{\partial f}{\partial x} \quad . \tag{9}$$

Integrating Equation (9), allows the vertical velocity to be expressed as

$$\int\frac{\partial V}{\partial y}\partial y=\int_0^y\frac{\partial V}{\partial y}\partial y=V(y)=-\frac{\partial U}{\partial x}=-\left(\int\frac{\partial U_\infty}{\partial x}\partial y+\int f\frac{\partial U_{so}}{\partial x}\partial y+\int U_{so}\frac{\partial f}{\partial x}\partial y\right) \tag{10}$$

Note it is technically incorrect to evaluate an integral at the variable for which integration was perfomed to, however use of a dummy variable makes this technically correct. $V(y)$ in equation (10) requires we enforce the no slip boundary condition at the wall. We can observe that the freestream velocity and outer velocity scale do not depend on y and can be moved out of the integral. These integrals can be written in terms of the similarity variable η using the following relations

$$\eta=y/\delta, \quad \partial y=\delta\partial\eta, \quad \frac{\partial f}{\partial x}=\frac{\partial f}{d\eta}\frac{\partial\eta}{dx}=f'\frac{-y}{\delta^2}\frac{\partial\delta}{\partial x}=-\frac{\eta f'}{\delta}\frac{\partial\delta}{\partial x}, \tag{11}$$

and upon substitution

$$V(y) = -\frac{\partial U}{\partial x} = -\delta\eta\frac{\partial U_\infty}{\partial x} - \delta\frac{\partial U_{so}}{\partial x}\int_0^\eta f\,\partial\eta + U_{so}\frac{\partial\delta}{\partial x}\int_0^\eta \eta f'\,\partial\eta \quad . \tag{12}$$

Using integration by parts, we can integrate with respect to η and evaluate at η to arrive at the function for wall normal velocity component written in terms of similarity solutions and variable as

$$V(y) = -\frac{\partial U}{\partial x} = -\delta\eta\frac{\partial U_\infty}{\partial x} - \delta\frac{\partial U_{so}}{\partial x}\int_0^\eta f\,\partial\eta + U_{so}\frac{\partial\delta}{\partial x}\left(\eta f\big|_0^\eta - \int_0^\eta f'\,\partial\eta\right). \tag{13}$$

We substitute Equation (13) for the wall normal velocity component into Equation (8) as

$$\begin{aligned} &U_{so} f\frac{\partial U_{so} f}{dx} + U_\infty\frac{\partial U_{so} f}{dx} + U_{so} f\frac{\partial U_\infty}{dx} \\ &+\frac{U_{so}}{\delta} f'\left(-\delta\eta\frac{\partial U_\infty}{\partial x} - \delta\frac{\partial U_{so}}{\partial x}\int_0^\eta f\,\partial\eta + U_{so}\frac{\partial\delta}{\partial x}\left(\eta f\big|_0^\eta - \int_0^\eta f'\,\partial\eta\right)\right) = \frac{R_{so}}{\delta} r' \end{aligned} \quad . \tag{14}$$

The gradient of the similarity function in the streamwise direction goes to zero as per the definition of similarity solutions for equilibrium flows. Gathering like terms of f and multiplying Equation (14) by $\delta\, U_{so}^{-2}$ yields

$$\begin{aligned} &f^2\left[\frac{\delta}{U_{so}}\frac{\partial U_{so}}{dx}\right] + f\left[\frac{\delta U_\infty}{U_\infty^2}\frac{\partial U_{so}}{dx} + \frac{\delta}{U_{so}}\frac{\partial U_\infty}{dx}\right] \\ &+\eta f'\left[-\frac{\delta}{U_{so}}\frac{\partial U_\infty}{\partial x}\right] + \eta f' f\left[\frac{\partial\delta}{\partial x}\right] - f'\left[\frac{\delta}{U_{so}}\frac{\partial U_{so}}{\partial x} + \frac{\partial\delta}{\partial x}\right]\int_0^\eta f\,\partial\eta = \frac{R_{so}}{\delta} r' \end{aligned} \quad . \tag{15}$$

The result in Equation (15) is similar to the AIP similarity analysis by others (Castillo and George, 2001; Belcher and Fox, 2010) with one notable difference: the integral for vertical velocity at η was evaluated continuously in this analysis rather than at the boundary. The robustness of the result is it allows the limit as x goes to infinity of all bracketed terms to maintain the same x-dependence while allowing independence of the similarity variable η. For all terms in Equation (15) to maintain the same streamwise (x) dependence the following relationship must hold

$$\frac{\delta}{U_{so}}\frac{dU_{so}}{dx} \sim \left(\frac{U_\infty}{U_{so}}\right)\frac{\delta}{U_{so}}\frac{dU_{so}}{dx} \sim \frac{d\delta}{dx} \sim \left(\frac{U_\infty}{U_{so}}\right)\frac{d\delta}{dx} \sim \frac{R_{so}}{U_{so}^2} \tag{16}$$

where ~ indicates the idea of 'same x dependence'. Full similiarity is only possible if

$U_{so} \sim U_\infty$, and (17)

$$R_{so} \sim U_{so}^2 \frac{d\delta}{dx} \sim U_{\infty}^2 \frac{d\delta}{dx} \quad . \tag{18}$$

Similarity solutions exist when the U_∞ and δ scales produce deficit profiles that are asymptotically independent of the local Reynolds number and thus independent of x. In terms of scaling, results from the similarity analysis using the AIP definition are that U_∞ can be used as an appropriate velocity scale for the velocity deficit in Equation (3). In this manner, collapse of U-U_∞ profiles *via* U_∞ provides a first test for AIP defined equilibrium when applied to nonuniform flow where external conditions and boundary conditions are constant. In addition, independent constraints arise from Equations (16) through (18) if equilibrium conditions are satisfied as

$$\frac{d\delta}{dx} \sim \frac{\delta}{U_\infty}\frac{dU_\infty}{dx} \sim \frac{\delta g}{U_\infty^2}\left(S - \frac{d\delta}{dx}\right) . \tag{19}$$

Using Equation (19), equilibrium can only be satisfied when the energy gradient parameter is constant as

$$\Lambda \equiv \frac{\delta}{\left(d\delta/dx\right)}\frac{g}{U_\infty^2}\left(S - \frac{d\delta}{dx}\right) = \text{ constant, and equivalently} \tag{20}$$

$$\Lambda \equiv \frac{\delta}{\left(d\delta/dx\right)}\frac{1}{U_\infty}\frac{dU_\infty}{dx} = \text{constant} \tag{21}$$

Equation (21) can be integrated for non-zero values of Λ to yield

$$\delta \sim U_\infty^{-1/\Lambda} \tag{22}$$

Equation (22) provides a second test for AIP defined equilibrium when applied to nonuniform flow where external conditions and boundary conditions are constant and the condition is based on maintaining the constant energy gradient parameter for similarity.

Results in Equation (15) admits solution to the boundary layer equations for the outer region of nonuniform open channel flow *via* AIP and in turn scale U-U_∞ with U_∞. The solution encompasses Clauser-equilibrium but yet is more robust in that: theoretically AIP-equilibrium, unlike Clauser, provides a pressure gradient parameter that can remain constant for the nonuniform flow case (i.e., the energy gradient defined by Clauser is dependent upon the changing Froude number for nonuniform open channel flows); in practice, U_∞ provides an outer layer parameter that is measureable in comparison with the often elusive U_*; and within an experimental setting, AIP-

equilibrium provides an equilibrium that can be maintained (George and Castillo, 1997).

However, external flow conditions and boundary conditions of nonuniform flows limit the AIP-equilibrium solution in Equation (15) and thus limit universal scaling of the velocity deficit *via* U_∞ alone due to variations associated with Λ and Θ for different flow cases. Λ of a nonuniform adverse pressure gradient can vary due to U_∞ at the onset of the pressure gradient as well as the geometry of the hydraulic control inducing the adverse gradient. In the case of open channel flow over gravel, Θ will be indicative of the low to moderate relative submergence of roughness particles at the bed that can impact the turbulent flow structure throughout the entire flow depth including the outer layer (Einstein and Barbarossa, 1952; Vanoni and Nomicos, 1960; Rouse, 1965) as exemplified by recent visualization results from the field and laboratory (Roy et al., 2004; Fox and Belcher, 2011).

3.4 EMPIRICAL MIXED SCALING LAWS

To account for variation of Λ and Θ in the nonuniform case herein, we consider several empirical scalings that can be combined with U_∞ to provide a mixed scale for collapsing the outer region deficit. The empirical mixed scaling of Zagarola and Smits (1998) scales the velocity deficit with U_∞ and the ratio of the displacement thickness (δ^*) to the boundary layer height where δ^* is defined as

$$\delta^* = \int_0^\delta \left(\frac{U_\infty - U}{U_\infty} \right) \partial y \tag{23}$$

The displacement distance represents the velocity lost from the theoretical inviscid flow profile when the effects of viscosity, no slip boundary condition and roughness elements on the velocity distribution are considered (Zagarola and Smits, 1998). The AIP outer flow scaling derived in Equation (15) assumed the outer region was independent of viscosity, wall effects were only directly accounted for by enforcing the no slip at the wall boundary condition in the equation for the wall normal velocity, and there was no theoretical reasoning to advocate the removal of external conditions. The Zagarola and Smits (1998) scaling suggests that external conditions are accounted by multiplying f by the ratio $\delta^*:\delta$. The Zagarola and Smits (1998) result has produced one of the most effective empirical scalings to normalize the mean velocity deficit profiles in rough boundary layers subject to pressure gradients and has been shown to remove the effects

of roughness, freestream turbulence and Reynolds number (Brzek et al. 2010). However, estimation of δ^* requires detailed knowledge of the velocity distribution rendering it impractical for estimating velocity in a predictive sense for realistic flow scenarios.

A second empirical scaling that is tested for nonuniform open channel flow over gravel is that proposed by Fox and Stewart (2014) and uses a function of R/D_{84} for Θ, where R is the hydraulic radius, and D_{84} is the particle diameter for which 84% of particles are finer. The R/D_{84} scaling considers that flow over roughness elements with low to moderate relative submergence will gradually modify turbulence throughout the entire flow depth (Belcher and Fox, 2010; Amir and Castro, 2011). Physically, shed vortices scale with D_{84} near the bed and throughout the roughness layer (Belcher, 2009) and moving away from the roughness layer, scaling with D_{84} remains important but gradually diminishes. The D_{84} dependence results from the turbulent structure consisting of connected vortices that eject away from the roughness layer, increase in streamwise length scale, and give way to macroturbulence closer to the free-surface that scales with outer variables (Roy et al., 2004; Hurther et al. 2007; Belcher, 2009; Fox and Belcher, 2011). Based on this knowledge, Θ was parameterized as

$$\Theta = \frac{1}{R}\left[\left(1 - \frac{D_{84}}{R}\right)y + D_{84}\right] \quad , \tag{24}$$

which allows for scaling *via* the external condition of D_{84}/R close to the bed; and the external bed condition diminishes when moving farther from the bed to scale with R. The scaling result enables the logarithmic and outer layers of gravel flows to be scaled with U_∞, R, and D_{84}. The latter two parameters are consistent with traditional river research and applications, as R/D_{84} has been used as an empirical parameter to understand flow roughness and velocity distributions in gravel- and cobble-bed rivers. Unlike the Zagarola and Smits (1998) scaling, the R/D_{84} scaling provides parameters that are easily measureable in the field making it practical for prediction of the streamwise velocity distribution in realistic flow scenarios.

3.5 EXPERIMENTAL DATASETS

To test the results of the AIP equilibrium solution in Equation (15) as well as provide comparison with the empirical mixed scaling laws, newly collected as well as previously published datasets were applied. Published datasets for hydraulic rough

nonuniform flow over gravels vary widely in terms of relative submergence (R/D_{84}), where R is the hydraulic radius and D_{84} is the bed particle size for which 84% are finer), however, there was an absence of moderate Froude number ($\mathrm{Fr}=U_b\,(gH)^{-½}$ cases, where U_b is the bulk velocity, g is gravitational acceleration, and H is flow depth) flows that are more typical of decelerating pools in steep mountainous gravel and cobble bed rivers. This provided one reason for collecting new experimental data, and therefore 38 new experimental velocity profiles across three nonuniform flows over gravel in a hydraulic flume were collected with Froude number ranging from 0.45 to 0.81 and relative submergence ranging from 8 to 17. A second reason for collecting additional data was that few published datasets provided enough repetition profiles from nonuniform flows with the same external conditions (e.g., pressure gradient, roughness type) to test the uniqueness of the energy gradient parameter (Λ). For this reason, we collected at least 10 profiles at different depths with the same pressure gradient and roughness types in order that Λ could be tested *via* Equation (22).

After reviewing the literature, 51 published velocity profiles were also included to test the scaling. To our knowledge, the 51 profiles represent all published data of fully hydraulically rough, nonuniform, gradual decelerating open channel flow over gravels in both gravel bed rivers and flumes. Table 1 summarizes the 10 datasets collected in our hydraulic flume and from the literature. The datasets in Table 1 are detailed as follows: PS indicates datasets that were collected in a hydraulic flume in the present study; velocity measurements were collected from previous studies in laboratory flumes and reported by Afzalimehr et al. (2012) abbreviated as Af10, Afzalimehr & Anctil (1999) abbreviated as AA99, Ahmed et al. (1998) abbreviated as Ah98, Song & Chiew (2001) abbreviated as SC01, Song (1994) abbreviated as So94; and field datasets were collected in gravel-bed river field studies and reported by MacVicar & Roy (2007) abbreviated as MR07 and Afzalimehr & Rennie (2009) abbreviated as AR09. Table 2 lists the hydraulic conditions for the individual profiles in each dataset.

As shown in Table 1, the datasets collected in the present study as well as the literature datasets represent fully hydraulically rough, nonuniform open channel flow over gravel. All datasets are fully hydraulically rough as indicated by k^+ greater than 70. The data spans a wide range of relative submergence $R\ D^{-1}_{84}$ and three orders of

Reynolds numbers ($R=U_bHv^{-1}$, where v is kinematic viscosity) from 10^{-4} to 10^{-6}. In addition, the datasets span a wide range of subcritical flows as the Froude number varies from 0.19 to 0.81 across datasets. In the following, we briefly describe the newly collected data and its quality as well as the previously published literature data. A comprehensive database of all data used in this paper is published online as part of this publication.

We performed experiments using a tilting, recirculating flume 12 m long and 0.61 m wide. The upstream end of the flume was attached to a headbox connecting the water supply pipe to the flume. The head box was partially filled with 7cm cobble to dissipate turbulent energy from the supply line and 12.7 cm long by 6.4 mm diameter honeycomb was used to provide rectilinear flow at the flume inlet. The channel discharged into a settling tank prior to entering the reservoir to prevent aeration of the reservoir and excessive turbulence in the reservoir which may introduce pressure fluctuations at the intake of the supply line. The inlet of the supply line in reservoir was divided into multiple inlet ports which prevented the "bathtub" vortex from transporting air into the supply line. To provide hydraulic rough flow over gravel, the flume bed was surfaced with angular gravel sized aggregates embedded on fiberglass-resin panels and channel side walls were acrylic plates. Particle size distributions of the bed material were measured using a photogrammetric microscopy technique in which particles were identified and digitized using vector drawing software then characterized in terms of a single dimension using an equivalent circle diameter (Belcher 2009). Particle size analysis found the flume bed material to have D_{84} =5.7mm, standard deviation 1.4 mm and D_{50}= 4.4mm. The flume slope was determined by measuring bed elevations at 1m increments using the Wild Nak1 survey level vertical accuracy of $\pm 10^{-5}$ m m^{-1}and survey rod measurement precision of 3.1mm and accuracy of $\pm 2.5\ 10^{-4}$ m m^{-1}. The survey level was placed 3 m downstream of the flume outfall and rod was positioned along the center of the flume channel at 1m increments to determine elevation. Measurement accuracy of flume elevation was approximately ±0.3mm, less than half the smallest demarcation on survey rod therefore half measurement precision on survey rod was used to assess the accuracy of flume bed elevations to be ±1.5mm. Using standard propagation of error techniques and neglecting any covariance in measurements of length and elevation the

accuracy of flume slope is approximately ±0.00125 m m^{-1}. Flume slope was adjusted by elevating the flume entrance. When the slope was adjusted to 0.006 the surveyors traded jobs and the rod holder became the level operator which provided a check that flume elevations were correct.

The ADV measurement location was fixed to reduce any possible effects of varying upstream conditions due to slight discrepancies in bed roughness distribution. This further reduced the number of times the ADV was repositioned which provided consistency of ADV location and orientation for all test conditions. The ADV was mounted on a specially designed measurement carriage equipped with a mechanical screw mechanism for adjustment of ADV elevation. This ensured a high level of precision (±0.635mm) and accuracy in positing the probe over the bed. At the onset of equipment setup the ADV mounting rod was cranked 100 times and the resulting displacement was measured to be 2.5 in (or 0.635mm/crank). The ADV mounting rod extended into the flume bed through a hole cut to the precise size of the rod to minimize the gap between the rod and flume bed. A silicone gasket was placed into the hole cut for the ADV mounting rod to prevent any upwelling or down welling. The combination of using a rigid ADV mounting rod and stabilizing the rod with the flume bed reduced ADV vibrations which can interfere with turbulence measurements (Dancey 1990).

ADV sensors also have a serious disadvantage: velocity measurements near the water surface are not possible with an ADV oriented to obtain near bed measurements. Following the collection of measurements with the probe in the down looking position, the probe was reoriented side-looking to obtain near surface measurements. The downlooking probe collected measurements at 0.5mm above the bed elevation to 54mm above the bed when flow depths permitted. The down looking probe was unable to collect good data in the region from 1-2cm and 3.3-3.8cm above the bed as acoustic signals reflected from the bed resulted in poorly correlated velocity signals by the ADV. The sidelooking ADV was able to obtain measurements within 2cm of the free surface.

Extreme care was taken to ensure proper ADV alignment with flow coordinate system. *TKE* and V_{mag} distributions were inspected to ensure proper vertical placement of the measuring volumes for the downlooking and sidelooking. The coordinate systems of the sidelooking and down looking ADV were matched in the vertical by applying a

numerical vertical translation to one coordinate system such that discontinuities were removed from the *TKE* and V_{mag} profiles. After ensuring that the measuring volumes corresponding to each ADV orientation were properly aligned the vertical orientation of all measurements were adjusted such that at y=0 V_{mag}=0.

After the sidelooking and down looking ADV data was properly aligned in the vertical direction. The ADV coordinate system was rotated to correspond to the stream coordinate system. First the sidelooking ADV data was rotated to match the orientation of the downlooking ADV data. Proper orientation of was assumed to occur when discontinuities in velocity and Reynolds stress distributions where removed. Typically ADV data is aligned with the flow direction by providing a rotation that maximizes the streamwise velocity component. This was not done since these flows are known to have vertical components. Instead a rotation was provided to all data that minimized the transverse velocity component. Rotation matrices preserved the orthogonal coordinate system and are given as

$$R_x(\alpha)=\begin{bmatrix}1 & 0 & 0\\ 0 & \cos(\alpha) & -\sin(\alpha)\\ 0 & \sin(\alpha) & \cos(\alpha)\end{bmatrix}$$

$$R_y(\alpha)=\begin{bmatrix}\cos(\alpha) & 0 & \sin(\alpha)\\ 0 & 1 & 0\\ -\sin(\alpha) & 0 & \cos(\alpha)\end{bmatrix} \qquad (24)$$

$$R_z(\alpha)=\begin{bmatrix}\cos(\alpha) & -\sin(\alpha) & 0\\ \sin(\alpha) & \cos(\alpha) & 0\\ 0 & 0 & 1\end{bmatrix}$$

Where α is the rotation angle about the respective axis.

Stabilization of the flow prior to collecting velocity measurements was ensured by measuring flow depth in the channel and verified by the stabilization of velocity statistics. Stabilization time required following a variation in obstruction location varied depending on obstruction size and flow rate but where generally achieved within 5 minutes, however velocity measurements commenced no sooner than 10 minutes following the placement of flow obstruction in a new location. The blockage ratio used to create the APG increased the flow depth and significantly increased the volume of water stored in the

channel. The channel storage volume was obtained from the flume reservoir decreasing the reservoir elevation which affects flume flow rate by increasing the head difference between the head box and reservoir. The reservoir depth was measured frequently and maintained at a constant value for all obstruction sizes to maintain a constant flow rate. Further verification of constant flume flow rate was confirmed using acoustic Doppler transducers placed on the flume supply line. The stabilization time required following the change in obstruction size confirmed by stabilization of velocity statistical moments was typically less than 10 minutes. The pump used to circulate water dissipated heat energy into the system which increased water temperature, to prevent variations in fluid properties during experiments the flume was started a minimum of one hour prior to data collection and water temperature were periodically monitored throughout experimentation to verify a constant temperature was maintained. Velocimetry was performed using a 50 Hz *SonTek MicroADV*, where ADV denotes acoustic Doppler velocimeter. 4500 temporal data points were collected at each spatial location during testing to produce time series of three dimensional components of velocity recorded at 0.02 s. The ADV measures velocity in a small sampling volume (0.09 cm^3) with resolution of 0.01 cm s^{-1} and accuracy of 1% of measured velocity. Data collected with the ADV was processed with the Bureau of Reclamations software WinADV32 which was used filter data as suggested by the probe manufacturer. To ensure good quality data, filtering was performed to remove points with SNR<15 and correlation <70% as described by (Wahl 2000).The overall quality of our data is highlighted in Figure 1.

Figure 1 shows typical examples of spectra, timeseries, streamwise velocity distributions and Reynolds shear stress distributions. Fig 1a shows a typical example of streamwise velocity spectra plotted with Kolmogorov -5/3 law as dotted line indicating that the inertial subrange exists and sufficient scale separation likely exists to seek independent similarity solutions to the inner and outer boundary layer equations. Fig 1b shows a typical segment of streamwise velocity timeseries. The time series signal displays fast and slow fluctuating velocity variations indicating the passing small and large scale turbulent structures typical of fully turbulent gravel bed flows. Fig 1c shows typical velocity profiles collected at various streamwise directions for a single flow rate. The velocity distributions decrease as flow depth increases to satisfy continuity. Fig 1d is

typical Reynolds shear stress distributions collected at various distance from the flow obstruction for a single flow rate. The Reynolds stress distribution increases from the bed to the maximum value attained around y/H=0.2 then decreases as the free surface is approached. The Reynolds shear stress distribution is convex in the region from y/H=0.2 to the free surface, typical of APG open channel flows (Song & Graf 1994; Kironoto & Graf 1995).

The present study (PS) dataset consists of 38 velocity profiles obtained from three flowrates. For each flow rate three blockage ratios were used to create the APG. The highest flow rate contains 13 velocity profiles, the middle flow rate 14 profiles and lowest flow rate contains 11 profiles. Each velocity profile presented in this manuscript consists of 7 to 28 velocity points. The number of data points collected for each profile depended on flow depth while the number of data presented here was further reduced as some velocity data were not considered usable for estimating time average velocity if 30% (1200) of data remained after filtering time series based on SNR and signal correlation.

Song (1994) (So94) performed tests in a 16.9 m long and 0.6 m wide recirculating flume with glass sidewalls and fixed gravel bed. The size distribution of the gravel was analyzed by the method of Wolman, being D_{50}= 1.23 cm, D_{16}= 0.9 cm and D_{84}= 1.65 cm. The adverse pressure gradient was developed by changing the bed slope and by regulating the tailgate located downstream of the measuring section. Flow rate was measured using an electromagnetic flow meter installed in the conduit supplying the flume. The flume flow depth was measured using two ultrasonic limnimeters with an accuracy of 1 mm. 3D velocity measurements were made using and ADV profiler. Flow equilibrium was verified by plotting $UU^{-1}{}_{\infty}$ and $-\overline{u'v'}\ U_*^{-2}$ and observing a nearly self-similar distributions over the measuring reach.

Ahmed et al. (1998) (Ah98) conducted experiments in a 20-m-long and 1.22-m-wide recirculating flume with a fixed natural sand glued to a wooden board which formed the bed. The sand grains had a mean size of 1.84 mm and a geometric standard deviation of 1.2 mm. Velocity measurements were obtained using a Prandtl tube and data acquisition system sampling at 10 Hz to collect at least 2000 samples which were averaged to estimate mean velocity. Experimental uncertainties in estimated velocities

were 1% at the 95% confidence level. The APG was developed by placing a cylindrical obstruction downstream of the sampling locations.

Afzalimehr & Anctil (1999) (AA99) performed tests in 8.8 m long and 0.61 m wide recirculating flume with glass sidewalls and layer of immobile gravel which formed the bed. The APG was developed by adjusting slope, flow rate Q and opening of the tailgate downstream of the measuring location. Velocity measurements were recorded using an ADV and water depth measured using mobile point gage limnimeter.

Song & Chiew (2001) (SC01) performed tests in a 18 m long and 0.6 m wide recirculating flume with glass sidewalls and fixed sand sized bed material. 3D velocity measurements were made with SonTek ADV sampling at 25 Hz for a minimum of 120 seconds. The APG was developed by varying the flow rate Q, bed slope S, and the opening of the tailgate downstream of the measuring location. The upper half of the profile was measured using an uplooking probe. While the lower half was measured with a downlooking probe.

MacVicar & Roy (2007) (MR07) performed velocity measurements in Moras Creek, a gravel-bed river located in eastern Quebec, Canada. The test section had a riffle-pool geometry and was relatively straight and narrow section representative of riffle-pool dynamics. A Wolman pebble count was used to survey the bed and estimate a representative grain size distribution. Velocity measurements were collected from temporary bridges using electromagnetic current meters (ECMs). Velocities were measured during bankfull flow conditions where rainfall throughout the sampling maintained sufficiently long time periods of stable water levels and thus unsteadiness of the flow data with respect to a hydrograph was minimized for the field data (MacVicar & Roy 2007). Marsh-McBirney 523 ECMs were used to measure velocity in two-dimensions at a sampling rate of 20 Hz for 120 seconds.

Afzalimehr and Rennie (2009) (AR09) reported velocity measurements for the Ghamasiab River, a gravel-bed river located in western Iran. The selected reaches were straight and devoid of in-stream vegetation and bed forms. All measurements were made during periods of constant low-flow discharge. A Wolman pebble count was used to survey the bed and estimate a representative D_{50} and D_{84} within each cross section. The primary evidence of non-uniform flow was the longitudinal variation in width, depth,

grain size, and velocity. However the authors indicate flow non-uniformity was clear they were unable to quantify the pressure gradient responsible. Velocity measurements were made using a micro-current propeller meter (propeller diameter of 5 cm). Velocity measurements were collected using 3D SonTek MicroADV sampling at 50 Hz for 90 seconds. The instrument has a sampling volume of 0.09 cm^3 with resolution of 0.01 cm s^{-1} and accuracy of 1% of measured velocity. Data collected with the ADV was processed with the Bureau of Reclamations software WinADV32 which was used filter data as suggested by the probe manufacturer. To ensure good quality data, filtering was performed to remove points with SNR<15 and correlation <70% as described by (Wahl 2000). The probe was oriented down looking to obtain velocity measurements in the lower portion of the flow and oriented side-looking to obtain near surface measurements.

Afzalimehr (2010) (Af10) performed tests in a 8.8-m-long and 0.6 m wide recirculating flume with immobile cobble sized bed material. The cobble size distribution was evaluated using Wolman's method and a geometric standard deviation and D_{50} was estimated from the particle size distribution. During testing, the bed slopes were varied between 0.007-0.02 and APG was developed by adjusting the downstream tailgate. Three-dimensional velocity measurements were made using a down looking Acoustic Doppler Velocimeter (ADV) sampling at 25 Hz for about 300 seconds. The data were filtered at a minimum signal to noise ratio (SNR) of 15 and a minimum correlation value of 70% using WinADV (Wahl 2000) and used to calculate velocity statistics.

3.6 COMPARISON OF SCALING LAWS

In Figure 2, the velocity deficit is scaled using the three scaling approaches for each experimental study. In the left column, U-U_∞ is scaled with U_∞ according to the AIP similarity analysis. Velocity distributions within each dataset collapse reasonably well with U_∞ alone providing evidence that flows presented here generally satisfied AIP equilibrium conditions. Exceptions to collapse by U_∞ in column one of Figure 2 have a common theme that the velocity profiles not displaying self-similarity likely have the presence of an external factor which could perturb the turbulent flow structure.

The PS data scaled by U_∞ shows a few profiles (see hollow symbols) plotting slightly below the rest of this dataset. The profiles in PS dataset plotting below the remainder of the dataset where profiles measured just upstream of the flow obstruction

used to create the APG, it is possible that these velocity distributions were under the influence of localized perturbations as flow was directed around the obstruction. The variation of H at each flow rate changes the relative submergence of bed particles that may represent external conditions not accounted for by AIP similarity analysis. For each of the three flow rates represented by PS, velocity profiles display self-similarity regardless of distance upstream of the flow obstruction indicating that each flow satisfied AIP equilibrium conditions. AIP equilibrium is further supported for the PS datasets by using the second test identified via Equation (22). As shown in Figure 3, U_∞ plotted versus δ in logarithmic form for the three flow rates in the present study indicate a straight line for each condition. The parameters are related by the power function given in Equation (22) with the slope of the line indicating Λ. We find that Λ constant and the second test for AIP equilibrium conditions are satisfied for these conditions. We can see that each of these three equilibrium flows had separate constant energy gradient parameter in the stream wise direction and that self-similar velocity distributions developed confirming that AIP equilibrium conditions were satisfied.

The Song (1994, So94) dataset for which much recent research on the effects of AGP in open channel flows is based collapses well when scaled by U_∞. Flows in So94 where shown by the author to satisfy the more stringent Clauser equilibrium conditions and it appears that these flows also satisfy the AIP conditions for equilibrium as indicated by self-similarity of the velocity distributions. The Ahmed et al. (1998, Ah98) and Song & Chiew (2001, SC01) datasets collected in flumes with bed material at the sand and gravel threshold (i.e., about 2 mm) with high relative submergence showed an even tighter collapse than those of the present study and Song (1994). Comparison of the studies tends to support the idea that U_∞ alone may not account for the impact of relative submergence across the flow depth, which has been shown to impact the flow structure (Nikora et al, 2001).

The MacVicar & Roy (2007, MR07), Afzalimehr and Rennie (2009, AR09) and Afzalimehr (2010, Af10) datasets do not show the degree of self-similarity displayed by the previously mentioned datasets suggesting that at least a subset of these flows may not satisfy AIP equilibrium conditions, at least when comparing within the studies. The solid symbols are profiles that do not collapse with the remaining datasets while the open

symbols display self-similarity with the datasets collected by other researchers. The MacVicar & Roy (2007) and Afzalimehr and Rennie (2009) datasets were collected from natural gravel bed rivers, and the Afzalimehr (2010) data set was collected from flume flows with large low relative submergence particles. The MacVicar & Roy (2007) was collected by flow entering a pool in a natural gravel bed river where the presence of strong secondary currents was likely as was noted in the paper by the inflected profiles near the free surface. The spatial heterogeneity of bed roughness common to gravel bed rivers also suggests some of these velocity distributions may have been affected by individual roughness elements representing an external condition not accounted for in the AIP similarity analysis. The Afzalimehr (2010) dataset represents flow conditions where the entire flow depth is directly affected by the roughness elements (R/D_{84} was between 1 and 2), and the scaling derived from AIP similarity anlaysis requires an additional parameter to account for bed roughness.

By observing the center column of Figure 2, the velocity profiles from all datasets display self-similar distributions when scaled using the Zagarola and Smits (1998) scaling. The ratio $\delta^*:\delta$ represents an average distance of velocity lost from each profile by the effects of viscosity and bed roughness on the resistance and flow structure. The collapse of these datasets indicates that the ratio of $\delta^*:\delta$ accounts for changing external conditions in each of these datasets to eliminate the effects of perturbations to the turbulent flow structure. The present study's datasets scaled by Zagarola and Smits (1998) is compared with the scaling using U_∞ alone: it can be seen that deviations from the self-similar distribution is virtually removed suggesting that for those flume conditions the effects of APG and relative roughness is removed. The remaining datasets each show self-similar velocity distributions when the outer scaled velocity deficit is adjusted by the ratio $\delta^*:\delta$. These results indicate that AIP equilibrium is satisfied and that the ratio $\delta^*:\delta$ accounts for external conditions associated with bed roughness, which were not considered in the AIP similarity analysis alone.

The right column of Figure 2 shows the mixed scale of Fox and Stewart (2014) for U-U_∞ parameterized using inner variables to account for the decreasing effect of bed roughness further into the core of the flow. The scaling is an improvement over using free stream velocity alone which is an expected result since this parameterization of

external conditions was designed to account for change in turbulent structure as the bed normal distance increases. The comparison shows that parameterization that makes use of gravel bed flow parameters to account for lost velocity due to the impact of bed roughness on the velocity distributions improves the collapse over U_∞ alone.

Figure 4 shows all data plotted for each of the three scalings examined. Fig 4a shows that velocity deficit profiles scaled by the free stream velocity collapse reasonably well to a single curve. The collapse of profiles from individual datasets was better than the collapse for all data sets combined which is not surprising. It is more remarkable that profiles collapse as well as they do given the wide range of flow conditions from which profiles were obtained. This illustrates the robustness for the AIP equilibrium conditions to be satisfied over a wide range of flows. The deviation of velocity profiles from the self-similar distribution indicate the presence of external conditions affecting the flow structure which has not been accounted for by scaling with U_∞ alone. The deviation of laboratory collected datasets alone is such that profiles with large relative submergence tend to plot toward the top of the graph while profiles in flows with low relative submergence plot on the bottom. This finding is consistent with reports from boundary layer flows over smooth and rough surfaces (Castillo et al. 2004). This reflects the impact of roughness elements across the entire depth of open channel flow. In Fig4b the outer scaled velocity deficit is shown parameterized using the ratio δ^*:δ which had been shown in turbulent boundary layer flows to remove the effects of Reynolds number and upstream conditions from the velocity profiles. Fig4b clearly shows that the Zagarola and Smits (1998) scaling removes the effect of energy gradient and roughness from the velocity distributions that was not removed by free stream velocity alone. This scaling was able to account for a wide range of bulk flow parameters as described in Table1 and any additional unknown external perturbation applied on the flow. Fig4c shows outer scaled velocity deficit parameterized according to Fox and Stewart (2014). The collapse of velocity profiles when scaled in this manner is an improvement over freestream velocity alone. The velocity deficit no longer displays a dependence on relative roughness as was seen in Fig 4a. This indicates that parameterization of external perturbations to the flow structure is well described by the gravel bed parameters R and D_{84} and that flow structure becomes less dependent on bed conditions further away from

the bed.

3.7 CONCLUSIONS

The AIP similarity solution in Equation (15) for nonuniform open channel flow over gravel supports the hypotheses that the flow case can be defined by AIP equilibrium. The hypothesis is further supported by comparison with newly collected and previously published experimental data for nonuniform open channel flow over gravel from flumes and rivers as well as the condition in Equation (22) for the newly collected dataset. The ability to define the nonuniform flow case as AIP equilibrium is attributed to the consistent form and function of the double-layer turbulent structure through a gradual vertical expansion. While the wall normal velocity likely can increase interaction between the near wall roughness and outer regions, the expansion is gradual enough such that transformation mechanisms between potential energy and kinetic energy throughout the boundary layer are consistent, and therefore the turbulence structure is not changing form in the streamwise direction. The self-similarity of the streamwise velocity and the constant energy gradient parameter support this concept.

The empirical scalings of Zagarola and Smits (1998) and Fox and Stewart (2014) showed to better collapse all data when comparison with U_∞ alone. The result is attributed to ability of the empirical methods to account for variable pressure gradients and roughness types, which AIP similarity solution alone does not consider. The mixed scaling approach of Zagarola and Smits (1998) provides the best collapse to the data, however the practicality of measuring the displacement thickness negates the applicability of this approach outside of the research setting, which has also been highlighted by others. Nevertheless, the single ratio of δ^*:δ and lack of dependence on the vertical highlight potential for further extension of the Zagarola and Smits (1998) method, e.g., using empirical connectivity between δ^* and measureable quantities. The Fox and Stewart (2014) mixed scaling approach accounts for the variation of turbulent length in the vertical to parameterize the external boundary impact on the flow for the logarithmic and outer layers. These results suggest turbulence growth in APG open channels is similar to that of uniform flows; this hypothesis should be validated in future research. Using easily obtained parameters the Fox and Stewart (2014) scaling allows estimation of velocity profiles applicable to field research where detailed velocity

measurements is either not possible or difficult to obtain.

One significant application of this contribution is the relaxing the use of the friction velocity for scaling nonuniform flows in gravel bed rivers. In this sense, U_∞ provides an alternative to the traditional Clauser defined equilibrium based on scaling with the friction velocity. The AIP definition is expected to provide a more achievable definition of equilibrium and Clauser equilibrium is in fact a subset of AIP (Maciel et al. 2006). Further, friction velocity can be rather elusive in practice with numerous publications prescribing and comparing methods for its estimation, with different methods showing estimates varying by as much as 30% (Biron et al. 2004; Song & Graf 1995; Afzalimehr & Rennie 2009). For example, the Clauser method of estimating friction velocity by fitting a logarithmic velocity distribution to measurements near the bed is highly subject to errors in estimations of the location of zero velocity and requires numerous measurements which may be difficult to obtain in realistic flows. Extrapolation of Reynolds stresses to bed is the preferred method of estimating U_* in turbulence research (Nezu & Nakagawa 1993), however this requires numerous multi-component velocity measurements where large errors are introduced by improper probe orientation with the flow direction. Estimation of U_* with the St. Venant equation requires estimation of water surface slope using measurements of flow depth which display small changes over the rather large streamwise distances between them. On the other hand, estimation of U_∞ requires only a single velocity measurement at a location where velocity gradients are small and thus errors introduced by improperly estimating the location of maximum velocity is not likely to have significant impact on estimates or the accuracy of predicted velocity distributions. The ability to accurately estimate U_∞ compared to that of the friction velocity may provide for the improved collapse of the velocity distributions.

However, the scaling of nonuniform gravel bed rivers is not fully resolved in a theoretical sense. In open channel flows over intermediate to large roughness, the relative motions and energy containing components of turbulent motions throughout the flow are dependent on surface roughness which represents Θ for these flows in the AIP similarity analysis. For this reason, parameterization of Θ for surface roughness is necessary in open channel flows similar to that seen in boundary layers where roughness elements are relatively large (Fox and Stewart, 2014; Amir and Castro, 2011). This

results presents a bit of a theoretical conundrum in that inner and outer regions are clearly separated consistent with high Reynolds number flows, yet roughness impacts are retained to some degree in the outer region thus disagreeing with Townsend's wall similarity hypothesis (Townsend, 1976). Resolution to this problem should focus on elucidating the form and function of the relatively weak but persistent macroturbulence within the outer region of the flow and thereafter integrating its imprint within the boundary layer equations.

3.8 ACKNOWLEDGEMENTS

We would like to thank all of the people who worked on this project including the both the graduate and undergraduate students. We acknowledge National Science Foundation project #0918856 and the University of Kentucky, Department of Civil Engineering for financial support of students. We would also like to thank the Kentucky NSF EPSCoR Research Scholar's Program for partial support of the graduate stipend.

3.9 LIST OF SYMBOLS

D_{16} = particle diameter for which 16% of particles are finer

D_{50} = particle diameter for which 50% of particles are finer

D_{84} = particle diameter for which 84% of particles are finer

Fr = $U_m(gH)^{-1/2}$ is the Froude number

H = Flow depth

P_∞ = the freestream pressure

Q = flow rate

Re = $U_bH\nu^{-1}$ is the Reynolds number

R_{so} = outer region fluid stress scale

$R_x(\alpha)$ = rotation matrix about the x-axis

$R_y(\alpha)$ = rotation matrix about the y-axis

$R_z(\alpha)$ = rotation matrix about the z-axis

S = bed slope

S_u = streamwise velocity spectrum estimated using fast Fourier transform method

TKE = turbulent kinetic energy

U = Time averaged streamwise velocity

U_b = bulk velocity

U_{so} = outer region velocity scale

U_∞ = free stream velocity

U_* = Shear velocity

V = mean wall normal velocity

V_{mag} = magnitude of the time average velocity vector

W = channel width

W/H = Aspect ratio

f = function describing the velocity profile

g = gravitational acceleration

k_s = equivalent roughness height

k^+ = $k_s U_* \nu^{-1}$ is the shear Reynolds number

r = function describing the Reynolds stress profile

x = stream wise direction

y = wall normal distance above flume bed

$\overline{u'v'}$ = streamwise-vertical Reynolds shear stress

$\overline{u'u'}$ = streamwise Reynolds normal stress

Λ = energy gradient parameter

Θ = parameter representing a dependence on external conditions

δ = boundary layer height

δ^+ = $\delta U_* \nu^{-1}$ is the local Reynolds number

δ^* = displacement thickness

η = y/δ normalized wall normal distance

ν = Kinematic viscosity

ω = frequency

κ = von Karman constant

ρ = fluid density

3.10 REFERENCES

Afzalimehr, H., & Anctil, F. (1999). Velocity distribution and shear velocity behaviour of

decelerating flows over a gravel bed. *Canadian Journal of Civil Engineering*, *26*(4), 468-475.

Afzalimehr, H., & Rennie, C. D. (2009). Determination of bed shear stress in gravel-bed rivers using boundary-layer parameters. *Hydrological sciences journal*, *54*(1), 147-159.

Afzalimehr, H. (2010). Effect of non-uniformity of flow on velocity and turbulence intensities over a cobble-bed. *Hydrological processes*, *24*(3), 331-341.

Afzalimehr, H., Najafabadi, E. F., & Gallichand, J. (2012). Effects of accelerating and decelerating flows in a channel with vegetated banks and gravel bed. *International Journal of Sediment Research*, *27*(2), 188-200.

Ahmed, F., & Rajaratnam, N. (1998). Flow around bridge piers. *Journal of Hydraulic Engineering*, *124*(3), 288-300.

Amir, M., & Castro, I. P. (2011). Turbulence in rough-wall boundary layers: universality issues. *Experiments in fluids*, *51*(2), 313-326.

Belcher, B. (2009). "Vortex model of open channel flows with gravel beds." Electronic dissertation, Univ. of Kentucky, Lexington, KY.

Belcher, B.J., and Fox, J.F. 2011. Outer Scaling for Open Channel Flow over a Gravel Bed. Journal of Engineering Mechanics 137(1): 40-46

Belcher, B., and Fox, J. 2009 (Discussion). Rodriguez, J.F., and Garcia, M.H., 2008, Rodriguez, J. F., and Garcia, M. H. 2008. Laboratory measurements of 3-D flow patterns and turbulence in straight open channel with rough bed. J. Hydraul. Res., 46(4): 454–465, J.Hydraul. Res., 47(5):685-688.

Biron, P. M., Robson, C., Lapointe, M. F., & Gaskin, S. J. (2004). Comparing different methods of bed shear stress estimates in simple and complex flow fields. *Earth Surface Processes and Landforms*, *29*(11), 1403-1415.

Brzek, B., Chao, D., Turan, Ö., & Castillo, L. (2010). Characterizing developing adverse pressure gradient flows subject to surface roughness. *Experiments in fluids*, *48*(4), 663-677.

Castillo, L., & George, W. K. (2001). Similarity analysis for turbulent boundary layer with pressure gradient: outer flow. *AIAA journal*, *39*(1), 41-47.

Castillo, L., Seo, J., Hangan, H., & Johansson, T. G. (2004). Smooth and rough turbulent

boundary layers at high Reynolds number. *Experiments in fluids*, *36*(5), 759-774.

Dancey, C. L. 1990. Measurements of second order turbulence statistics in an axial flow compressor via 3-component LDA. AIAA J., 90: 2017.

Einstein, H. A., & Barbarossa, N. L. (1952). River channel roughness. *Transactions of the American Society of civil Engineers*, *117*(1), 1121-1132.

Fox, J.F. and Belcher, B.J. 2011. Comparison of macroturbulence measured using decomposition of PIV, ADV and LSPIV data. *Journal of Hydr. Res.*, 49(1): 122-126.

Fox, J.F., and Patrick, A. 2008. Large-scale eddies measured with large scale particle image velocimetry. Flow Measurement and Instrumentation 19: 283–291

Fox, J. F. and Stewart, R. L. (2014) Mixed Scaling for Open Channel Flow Over Gravel and Cobbles, *Journal of Engineering Mechanics* DOI: 10.1061/(ASCE)EM.1943-7889.0000793, 06014010.

George, W. K., & Castillo, L. (1997). Zero-pressure-gradient turbulent boundary layer. *Applied Mechanics Reviews*, *50*(12), 689-729.

Hurther, D., Lemmin, U., and Terray, E. A. 2007. Turbulent transport in the outer region of rough-wall open-channel flows: The contribution of large coherent shear stress structures (LC3S). J. Fluid Mech., 574: 465–493.

Kironoto, B. A., & Graf, W. H. (1995). Turbulence characteristics in rough non-uniform open-channel flow. *Proceedings of the ICE-Water Maritime and Energy*, *112*(4), 336-348.

Maciel, Y., Rossignol, K. S., & Lemay, J. (2006). Self-similarity in the outer region of adverse-pressure-gradient turbulent boundary layers. *AIAA journal*, *44*(11), 2450-2464.

MacVicar, B. J., & Roy, A. G. (2007). Hydrodynamics of a forced riffle pool in a gravel bed river: 1. Mean velocity and turbulence intensity. *Water Resources Research*, *43*(12).

Nezu, I., and Nakagawa, H. 1993. Turbulence in open channel flows, A. A. Balkema, Rotterdam, The Netherlands.

Nikora, V., Goring, D., McEwan, I., & Griffiths, G. (2001). Spatially averaged open-channel flow over rough bed. *Journal of Hydraulic Engineering*, *127*(2), 123-133.

Rouse, H. (1965). Critical analysis of open-channel resistance. *Journal of the Hydraulics*

Division, *91*(4), 1-25.

Roy, A. G., Buffin-Bélanger, T., Lamarre, H., and Kirkbride, A. D. 2004. Size, shape and dynamics of large-scale turbulent flow structures in a gravel-bed river. Journal of Fluid Mechanics, 500: 1–27.

Smits, A. J., McKeon, B. J., & Marusic, I. (2011). High-Reynolds number wall turbulence. *Annual Review of Fluid Mechanics*, *43*, 353-375.

Song, T. (1994). ‘‘Velocity and turbulence distribution in nonuniform and unsteady open-channel flow.’’ Doctoral dissertation, Ecole Polytechnique Federale de Lausanne, Lausanne, Switzerland.

Song, T., and Graf, W.H. 1994, Non-uniform open-channel flow over a rough bed. *Journal of Hydroscience and Hydraulic Engineering*, 12(1): 1-25

Graf, W. H., & Song, T. (1995). Bed-shear stress in non-uniform and unsteady open-channel flows. *Journal of Hydraulic Research*, *33*(5), 699-704.

Song, T., and Chiew, Y.M. 2001. Turbulence measurement in nonuniform open-channel flow using acoustic Doppler velocimeter (ADV). Journal of Engineering Mechanics, 127(3): 219-232

Townsend, A. (1976). The Structure of Turbulent Shear Flow (Cambridge Monographs on Mechanics and Applied Mathematics).

Vanoni, V. A., & Nomicos, G. N. (1960). Resistance properties of sediment-laden streams. *Transactions of the American Society of Civil Engineers*, *125*(1), 1140-1167.

Wahl TL. 2000. Analyzing ADV data using WinADV. *Proceedings Joint Conference on Water Resources Engineering and Water Resources Planning and Management, American Society of Civil Engineers*, Minneapolis, 30 July–2 August. www.usbr.gov/wrrl/twahl/winadv.

Wosnik, M., Castillo, L., & George, W. K. (2000). A theory for turbulent pipe and channel flows. *Journal of Fluid Mechanics,* 421, 115-145.

Zagarola, M. V., & Smits, A. J. (1998). Mean-flow scaling of turbulent pipe flow. *Journal of Fluid Mechanics*, *373*, 33-79.

3.11 TABLES AND FIGURES

Table 3.1. Range of hydraulic conditions for the 10 datasets of nonuniform flow.

Data Set	Q (l s^{-1})	H (cm)	U_∞ (cm s^{-1})	δ (cm)	D_{50} (mm)	D_{84} (mm)	WH^{-1}	Fr	Re x10^{-5}	$k^+ = k_s U_* / \nu$	$U_\infty U_*^{-1}$	$R D_{84}^{-1}$
PS-1	43	9.6-14.5	62-85	8-12	4.4	5.7	4-6	0.51-0.81	0.5-0.5	257-361	12-14	13-17
PS-2	23	5.8-9.8	50-70	5-8	4.4	5.7	6-11	0.47-0.81	0.3-0.3	225-354	11-15	9-13
PS-3	17	5.6-7.9	44-63	5-7	4.4	5.7	8-11	0.45-0.74	0.2-0.2	208-282	11-13	8-11
So94	55-90	14.5-20.5	78-116	15-21	12.3	16.5	3-4	0.46-0.6	3.8-6.2	810-1140	15-18	6-7
Ah98	65	18.0	26-33	17-18	1.82	2.2	9-9	0.22-0.22	0.2-0.2	144-144	12-16	52-52
AA99	52	27.3-27.3	42-42	21-21	25.4	0	2-2	0.2-0.2	2.9-2.9	838-838	13-13	6-6
SC01	42.00	13.1-16.2	50-51	13-16	2.6	0	4-5	0.34-0.47	3.5-3.5	78-97	13-16	35-40
MR07	4900	81-134	167-223	66-105	60	190	4-7	0.31-0.59	11.3-15	15960-60040	7-20	3-5
AR09	NA	18-63	62-161	13-70	14-23	27-40	16-49	0.46-0.77	1.1-7.3	2432-6031	7-12	5-18
Af 10	40-80	23-27	38-75	21-24	80	96	2-3	0.19-0.39	1.5-3.3	2880-6720	11-14	1-1

Table 3.2. Hydraulic conditions for the individual profiles in each dataset.

Data Set	S	H (cm)	U_∞ (cm s^{-1})	δ (cm)	D_{50} (mm)	D_{84} (mm)	W (m)	$W H^{-1}$	Fr	Re x10^{-5}	k^+	$H D_{84}^{-1}$
PS-1.1	0.60	13.3	69	11.1	4.4	5.7	0.61	4.6	0.58	0.5	301	23.3
PS-1.2	0.60	13.7	67	10.4	4.4	5.7	0.61	4.5	0.56	0.5	260	24.0
PS-1.3	0.60	13.9	69	11.7	4.4	5.7	0.61	4.4	0.57	0.5	286	24.4
PS-1.4	0.60	14.3	65	11.7	4.4	5.7	0.61	4.3	0.53	0.5	257	25.1
PS-1.5	0.60	14.5	62	11.2	4.4	5.7	0.61	4.2	0.51	0.5	270	25.4
PS-1.6	0.60	10.4	81	7.7	4.4	5.7	0.61	5.9	0.74	0.5	358	18.2
PS-1.7	0.60	10.9	78	9.5	4.4	5.7	0.61	5.6	0.71	0.5	361	19.1
PS-1.8	0.60	11.2	79	9.5	4.4	5.7	0.61	5.4	0.70	0.5	334	19.6
PS-1.9	0.60	11.6	79	9.5	4.4	5.7	0.61	5.3	0.70	0.5	312	20.4
PS-1.10	0.60	11.6	77	9.5	4.4	5.7	0.61	5.3	0.67	0.5	273	20.4
PS-1.11	0.60	9.6	85	8.1	4.4	5.7	0.61	6.4	0.81	0.5	352	16.8
PS-1.12	0.60	10.0	85	8.1	4.4	5.7	0.61	6.1	0.79	0.5	334	17.5
PS-1.13	0.60	10.1	84	7.8	4.4	5.7	0.61	6.0	0.78	0.5	340	17.7
PS-2.1	0.60	5.8	70	4.5	4.4	5.7	0.61	10.5	0.81	0.3	318	10.2
PS-2.2	0.60	8.6	56	7.0	4.4	5.7	0.61	7.1	0.55	0.3	250	15.1
PS-2.3	0.60	8.9	54	7.2	4.4	5.7	0.61	6.9	0.52	0.3	235	15.6
PS-2.4	0.60	9.2	54	6.8	4.4	5.7	0.61	6.6	0.52	0.3	233	16.1
PS-2.5	0.60	9.6	51	7.5	4.4	5.7	0.61	6.4	0.49	0.3	231	16.8
PS-2.6	0.60	9.8	50	7.8	4.4	5.7	0.61	6.2	0.47	0.3	225	17.2
PS-2.7	0.60	7.0	69	5.7	4.4	5.7	0.61	8.7	0.74	0.3	300	12.3
PS-2.8	0.60	7.4	66	5.9	4.4	5.7	0.61	8.2	0.69	0.3	298	13.0

Table 3.2 (continued)

PS-2.9	0.60	7.5	66	5.7	4.4	5.7	0.61	8.1	0.69	0.3	320	13.2
PS-2.10	0.60	7.9	62	6.3	4.4	5.7	0.61	7.7	0.63	0.3	276	13.9
PS-2.11	0.60	8.0	61	6.5	4.4	5.7	0.61	7.6	0.62	0.3	281	14.0
PS-2.12	0.60	6.5	70	5.3	4.4	5.7	0.61	9.4	0.78	0.3	272	11.4
PS-2.13	0.60	6.8	70	5.7	4.4	5.7	0.61	9.0	0.76	0.3	306	11.9
PS-2.14	0.60	6.9	70	4.5	4.4	5.7	0.61	8.8	0.75	0.3	354	12.1
PS-3.1	0.60	6.9	54	5.9	4.4	5.7	0.61	8.8	0.58	0.2	239	12.1
PS-3.2	0.60	7.3	50	6.2	4.4	5.7	0.61	8.4	0.53	0.2	229	12.8
PS-3.3	0.60	7.5	50	6.4	4.4	5.7	0.61	8.1	0.52	0.2	219	13.2
PS-3.4	0.60	7.8	47	6.6	4.4	5.7	0.61	7.8	0.48	0.2	213	13.7
PS-3.5	0.60	7.9	44	6.7	4.4	5.7	0.61	7.7	0.45	0.2	208	13.9
PS-3.6	0.60	6.0	56	5.1	4.4	5.7	0.61	10.2	0.64	0.2	282	10.5
PS-3.7	0.60	6.2	55	5.3	4.4	5.7	0.61	9.8	0.62	0.2	276	10.9
PS-3.8	0.60	6.5	53	5.5	4.4	5.7	0.61	9.4	0.59	0.2	244	11.4
PS-3.9	0.60	6.6	53	5.6	4.4	5.7	0.61	9.2	0.58	0.2	254	11.6
PS-3.10	0.60	5.6	63	4.8	4.4	5.7	0.61	10.9	0.74	0.2	273	9.8
PS-3.11	0.60	5.6	59	4.8	4.4	5.7	0.61	10.9	0.69	0.2	279	9.8
So94-1	0.25	20.0	89	20.0	12.3	16.5	0.6	3.0	0.54	6.2	845	12.1
So94-2	0.90	18.0	78	18.0	12.3	16.5	0.6	3.3	0.49	4.8	875	10.9
So94-3	0.50	14.5	78	14.5	12.3	16.5	0.6	4.1	0.53	3.8	858	8.8
So94-4	0.50	16.5	96	16.5	12.3	16.5	0.6	3.6	0.56	4.8	967	10.0
So94-5	0.50	18.5	111	18.5	12.3	16.5	0.6	3.2	0.6	6.2	1140	11.2

Table 3.2 (continued)

So94-6	0.75	17.0	84	17.0	12.3	16.5	0.6	3.5	0.46	4.1	810	10.3
So94-7	0.75	20.5	82	20.5	12.3	16.5	0.6	2.9	0.46	5.5	817	12.4
So94-8	0.90	18.0	116	18.0	12.3	16.5	0.6	3.3	0.6	6.2	1140	10.9
Ah98-1.1		18.0	33	17.4	1.82	2.2	1.22	8.7	0.22	0.2	144	81.8
Ah98-1.2		18.0	26	17.3	1.82	2.2	1.22	8.7	0.22	0.2	144	81.8
Ah98-1.3		18.0	28	18.0	1.82	2.2	1.22	8.7	0.22	0.2	144	81.8
Ah98-1.4		18.0	29	18.0	1.82	2.2	1.22	8.7	0.22	0.2	144	81.8
Ah98-1.5		18.0	30	18.0	1.82	2.2	1.22	8.7	0.22	0.2	144	81.8
Ah98-1.6		18.0	31	18.0	1.82	2.2	1.22	8.7	0.22	0.2	144	81.8
Ah98-1.7		18.0	32	18.0	1.82	2.2	1.22	8.7	0.22	0.2	144	81.8
Ah98-1.8		18.0	33	18.0	1.82	2.2	1.22	8.7	0.22	0.2	144	81.8
AA99-1	0.70	27.3	42	21.1	25.4		0.61	2.2	0.2	2.9	838	10.7
SC01-1.1	0.75	16.2	51	16.2	2.6		0.6	3.7	0.342	3.5	78	62.1
SC01-1.2	0.75	14.6	51	14.6	2.6		0.6	4.1	0.397	3.5	85	56.2
SC01-1.3	0.75	13.1	50	13.1	2.6		0.6	4.6	0.47	3.5	97	50.2
MR07-1.1		81	223	66	60	190	6	7.4	0.59	13.4	60040	4.3
MR07-1.2		92	187	75	60	190	6	6.5	0.41	11.3	32908	4.8
MR07-1.3		118	167	105	60	190	6	5.1	0.37	14.8	33991	6.2
MR07-1.4		134	171	84	60	190	6	4.5	0.31	15.0	15960	7.1
AR09-1.1		28	108	28	18	31	8.4	29.7	0.66	3.1	3038	9.1
AR09-1.2		32	113	31	18	36	8	24.8	0.64	3.7	3816	9.0
AR09-1.3		25	90	17	21	40	7	27.7	0.57	4.8	4160	6.3

Table 3.2 (continued)

AR09-1.4		37	86	70	22	35	6	16.1	0.66	4.7	4130	10.7
AR09-1.5		28	97	34	20	40	7.5	26.5	0.58	2.8	3280	7.1
AR09-1.6		45	161	44	20	37	8.5	18.8	0.77	7.3	6031	12.2
AR09-1.7		18	62	13	21	38	9	49.2	0.46	1.1	2432	4.8
AR09-1.8		26	88	25	17	33	11.3	43.0	0.55	2.3	2607	8.0
AR09-1.9		38	121	37	22	33	10	26.1	0.62	2.3	3498	11.6
AR09-1.10		37	128	36	18	37	11	29.5	0.67	4.8	4255	10.1
AR09-1.11		30	98	29	14	30	12	39.6	0.57	3.0	2520	10.1
AR09-1.12		40	137	39	19	37	11	27.3	0.69	5.5	4588	10.9
AR09-1.13		34	104	36	16	30	10	29.2	0.57	3.6	2670	11.4
AR09-1.14		63	87	25	20	31	10	15.9	0.55	5.5	2480	20.3
AR09-1.15		33	108	32	16	27	10.5	31.5	0.60	3.6	2565	12.3
AR09-1.16		30	102	29	19	32	8	26.4	0.60	1.9	2944	9.5
AR09-1.17		23	80	22	23	40	8.9	38.2	0.53	1.9	3000	5.8
AR09-1.18		22	89	22	17	34	8.9	39.9	0.59	2.0	2584	6.6
AR09-1.19		26	86	25	18	33	7.5	28.5	0.54	2.3	2607	8.0
Af10-1	0.70	27.0	64	24.3	80	96	0.6	2.2	0.3	2.8	6720	2.8
Af10-2	1.00	26.0	67	23.4	80	96	0.6	2.3	0.37	3.3	4800	2.7
Af10-3	1.50	24.0	72	21.6	80	96	0.6	2.5	0.36	2.9	5760	2.5
Af10-4	2.00	23.0	75	20.7	80	96	0.6	2.6	0.39	3.0	4800	2.4
Af10-5	2.00	23.0	38	20.7	80	96	0.6	2.6	0.19	1.5	2880	2.4

Table 3.2 (continued)

Af10-6	2.00	23.0	57	20.7	80	96	0.6	2.6	0.29	2.3	3840	2.4
Af10-7	2.00	23.0	66	20.7	80	96	0.6	2.6	0.34	2.6	3840	2.4
Af10-8	2.00	23.0	75	20.7	80	96	0.6	2.6	0.39	3.0	4800	2.4

Figure 3.1. Examples of time series, spectra, streamwise velocity and Reynolds stresses for subset of the newly collected data. PS-#.##=Present Study-Data Set.(flow depth (cm))

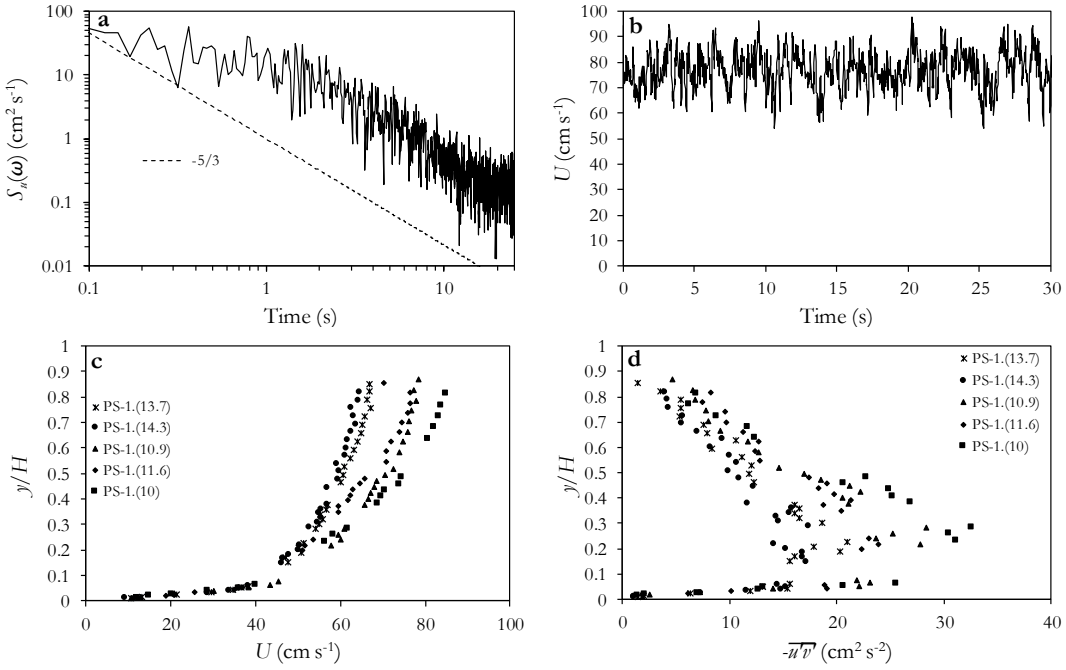

Figure 3.2. The velocity defect of nonuniform open channel flows over gravel for the present study (PS) and published datasets scaled with U_∞ (left column), Zagarola & Smits scaling (center column), and Fox and Stewart scaling (right column).

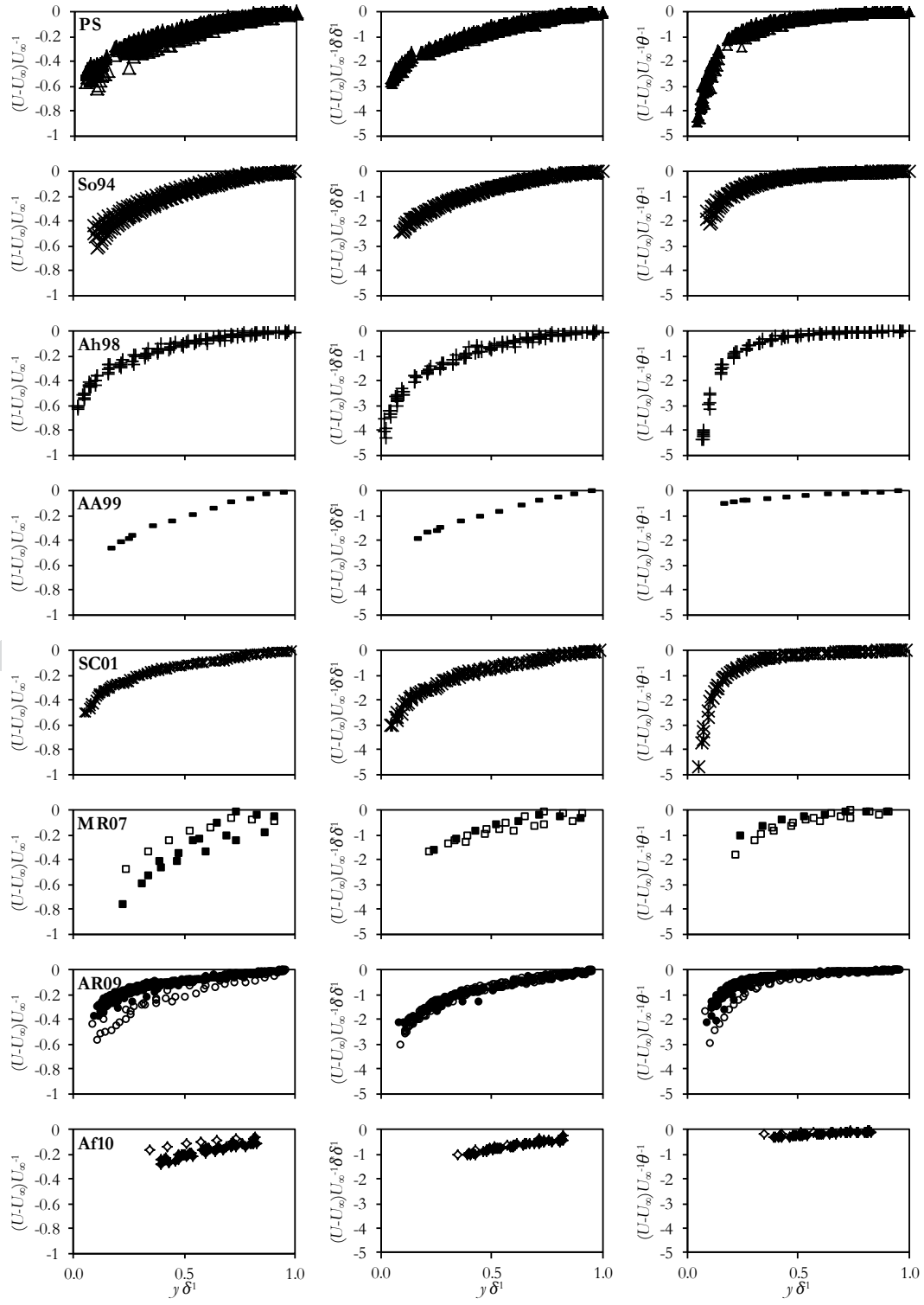

Figure 3.3. Estimation of A for the experimental datasets of the present study.

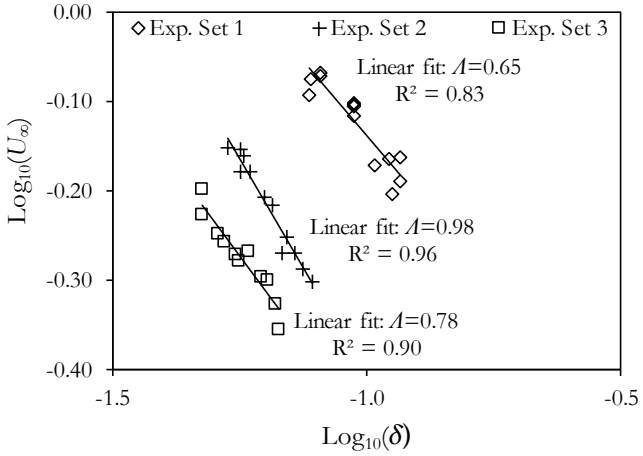

Figure 3.4. Scaling of the velocity defect for nonuniform open channel flows over a gravel bed using (a) U_∞, (b) the mixed scaling of Zagarola and Smits (1998) and (c) the mixed scaling of Fox and Stewart (2014).

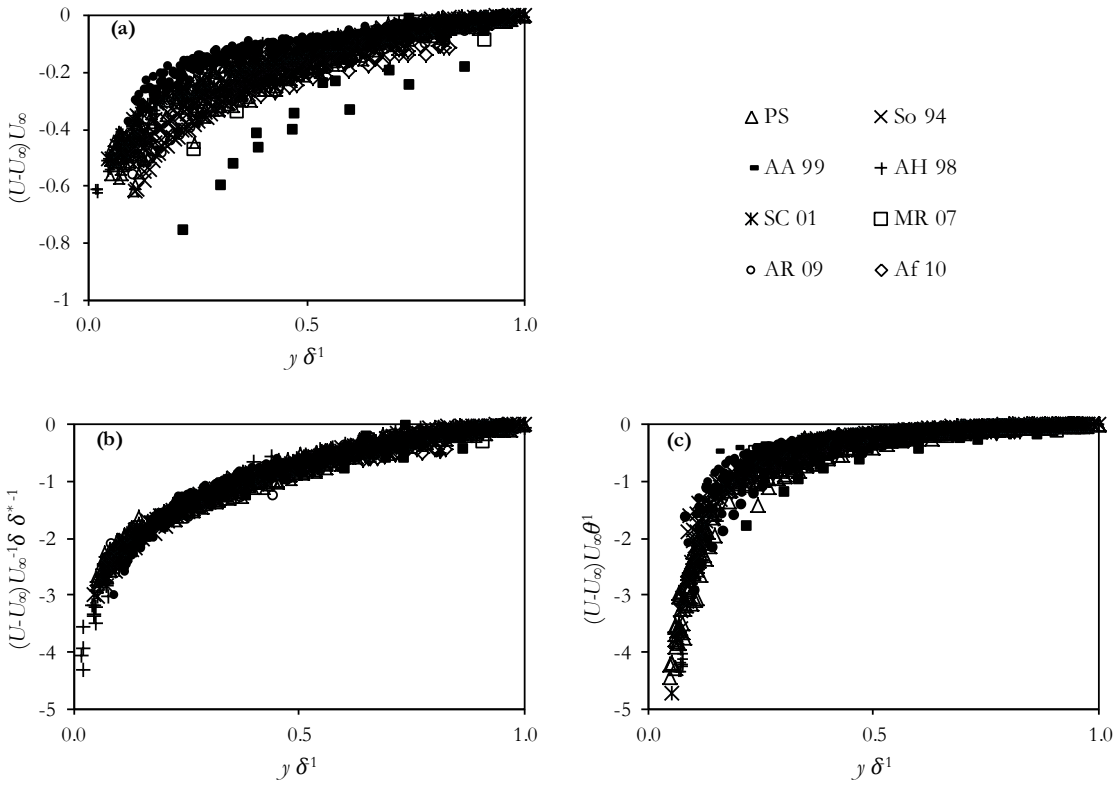

Chapter 4: Structure of Turbulence in a Gradually Decelerating Open Channel Flow Over a Gravel Bed

4.1 SUMMARY

New experimental dataset and turbulence analyses is presented for nonuniform, gradually decelerating, hydraulically rough, open channel flow over a gravel bed. The study overlaps previously reported nonuniform flow cases over gravel but extends the literature database to higher Froude numbers approaching transcritical. Results of the fluid structure including a dependence of the wake parameter upon the adverse pressure gradient and nonlinearity of the Reynolds stresses attributed to a non-zero vertical velocity corroborate previous findings reported in the literature for these higher Froude number conditions. Results show dependence of the streamwise components and primary shear stress on the friction velocity, which is attributed to a consistent bursting processes across the decelerating flow as shown using quadrant analysis. Analyses is also presented for secondary velocities, the three dimensional macroturbulence, and the secondary turbulent production and transport, which provides the major contribution of this paper. Results show (1) near uniformity of the vertical turbulence intensity profile as the flow decelerates; (2) amplification of transverse turbulence intensities towards the free surface;(3) and turbulence anisotropy throughout the flow depth; and (4) none of the secondary terms scale with friction velocity. Spectral analyses shows sustained, if not enhanced, turbulent energy throughout the decelerating flow for the macroturbulence wavenumbers in the streamwise, vertical and transverse; and results of applying the triple decomposition theorem shows the macroturbulence imprint on the velocity time series across the decelerating flow. Collectively the results suggest that the vertical expansion velocity within the decelerating flow interacts with the vertical velocity fluctuations to produce and transport turbulent energy that is redistributed to the streamwise and transverse velocity components by way of the macroturbulence. We support this idea by showing that the vertical turbulent energy production term calculated with the vertical expansion can be used to explain the excess energy production measured in the outer region.

4.2 INTRODUCTION

The behavior of turbulence in gradually varied decelerating open channel flows

over a rough bed can lead to improvements in predicting the transport and fate of sediments where rivers meet quiescent water bodies such as estuaries and lakes and aid in the design of conveyance networks and ecologic restoration efforts. The vast majority of turbulent research has focused on uniform flow conditions, however, many engineering situations of significance arise in which flow assumed to satisfy uniform conditions will yield unsatisfactory approximations to reality (Nezu 2005; Church et al. 2012). The structure of turbulence plays a significant role in determining the distribution of velocity and shear stress along the boundary (Coles 1956; Townsend 1976). It is necessary to understand how turbulence processes behave in decelerating open channel flows for the effective design of these conveyance systems in an ecologically sustainable (Hauer & Lamberti 2006 pg81, Sukhodolov et al. 2011; Venditti et al. 2013). It is interesting to us and valuable to practitioners of open channel mechanics to understand how slight deviations from uniform flow would impact the structure of macroturbulence and in turn impact environmental processes such as fine grained sediment transport.

The velocity distributions and turbulent processes in fully hydraulically rough turbulent uniform open channel flow over gravel have been well documented in the literature (Hurther et al. 2007; Rodriguez & Garcia 2008; Belcher 2009). These studies indicate vortex shedding from individual roughness elements induces a roughness region which extents approximately $2.5D_{84}$ (Belcher & Fox 2009). The amalgamation of multiple shed vortices produces hairpin packets which eject away from the bed, and in many instances reach the free surface and affect the entire flow structure (Shvidchenko & Pender 2001; Hurther et al. 2007; Belcher, 2009). The outer flow region is populated with quasi-streamwise roll cells and remnants of the near bed bursting process. We recognize that turbulence exists as a continuum from the viscous scale to at least the channel depth. However, we discretize all turbulent motions into two broad classes (Nezu and Nakagawa, 1993; Adrian et al., 2000; Hurther et al., 2007; Belcher, 2009) including: (i) the bursting process consisting of eddies shed from individual roughness elements with low momentum fluid packets moving away from the bed (ejections) and high momentum fluid moving toward the bed (sweeps); and (ii) macroscale structures or macroturbulence comprising the entire flow depth with a rolling motion and advecting in the streamwise direction (Shvidchenco & Pender 2001; Fox & Patrick 2008). These two prominent

turbulent processes are defined by a separation of scales but are intimately linked as bursting motions enhance large-scale flow structures and large scale motions are thought to initiate bursting by pumping high momentum fluid toward the bed (Roy et al. 2004; Adrian and Mersek, 2012). The bursting process and macroturbulence are used here to describe the manifestation of turbulent processes on velocity distributions.

Decelerating flow consists of a boundary layer continually developing in the streamwise direction, as flow gradually expands in the vertical direction streamwise velocity decreases to satisfy continuity. Satisfying the constraints of continuity induces a positive wall normal velocity component due to flow expansion called the expansion velocity. Theoretically derived expressions determine the expansion velocity as a function of local streamwise velocity, bed normal position and water surface slope (Song & Graf 1994; Kironoto & Graf 1995). The wall normal expansion velocity is a non-helical secondary flow of Prandtl's first kind (Church et al. 2012). The addition of the deceleration in the streamwise direction and vertical advection significantly alters the equations of turbulent momentum from the idealized uniform flow case. The decelerating streamwise velocity represents a decreased energy source to dampen production while the expansion vertical velocity potentially represents an increased secondary energy source for the production of turbulence. It is likely that turbulence provides a link for energy coupling between the expansion velocity and macroturbulent motions, however study of the uniform case is still an open topic in the scientific literature.

A number of studies have shown that the structure of turbulence in nonuniform gradually decelerating open channel flow over gravel differs from that of uniform open channel flow over gravel by a number of features including increased wake strength for the streamwise velocity distribution (Song & Graf 1994), nonlinearity of the primary Reynolds shear stress (Kironoto & Graf 1995), and an amplification of the streamwise and vertical turbulent intensities in the upper half of the flow depth (Song & Chiew 2001; Yang & Chow 2008). The stream wise velocity distribution in the inner region of decelerating flows is typically found to closely follow the log law however the outer region deviations from the log law are systematically accounted for by parameterizing the wake strength as a function of pressure gradient (Song & Graf 1994; Kironoto & Graf

1995; Song & Cheiw 2001; Afzalimehr 2010). The formation of the wake region develops due to the manifestation of large-scale mixing processes constrained primarily by inertia rather than by viscosity (Coles 1956). The vertical expansion velocity in the RANS equations for decelerating flows is shown responsible for non-linear Reynolds shear stress distributions (Yang et al. 2006). Enhanced Reynolds stress by the expansion velocity can explain the amplification of the streamwise and vertical turbulent intensities using mixing length theory (Yang & Chow 2008).

Implicit in the explanations of these past results for nonuniform gradually decelerating open channel flow over gravel has been an emphasis upon the primary bulk momentum changes of the nonuniform flow, including a dampened streamwise velocity and net positive wall normal velocity, and their impacts on turbulent energy production via the bursting mechanism in the near bed region. Reduction of turbulent fluctuations in decelerating flows occurs as the mean streamwise velocity gradient is reduced and turbulent energy production via the bursting process is reduced. Spectral analysis of decelerating flow displays the inertial subrange, characterized by -5/3 Kolmogorov slope, corresponding to the scale of individual bursts and remains consistent with uniform flows (Kironoto & Graf 1995). The ratio of ejections to sweeps in the bursting process determined using quadrant analysis has shown these processes are not significantly affected by decelerating flows (Afzalimehr et al. 2012). Thus, the bursting process in decelerating flows retains its form but is dampened as energy production from the mean velocity gradient is reduced. In the outer region of nonuniform flows, amplification of Reynolds stresses relative to the friction velocity implies the turbulence structure is more energetic relative to the bursting process and suggests an additional production mechanism potentially attributable to macroturbulence (Papanicolaou & Hilldale 2002).

However, we find that few studies have considered the mechanism of three dimensional macroturbulence in nonuniform gradually decelerating open channel flow over gravel, and the role of macroturbulence on sustaining and redistributing turbulent energy and in turn its potential to show imprint upon time-average quantities. The quasi-streamwise roll cell, vortical nature of the macroturbulence suggests the potential to assist with turbulent energy production due to interaction with primary and secondary energy gradients and redistribute energy in the vertical and transverse directions. Reasons that

macroturbulence has not been explicitly considered or studied previously for nonuniform gradually decelerating open channel flow over gravel may be attributed to: (i) the lack of decomposed turbulence visualization results from digital particle image velocity measurements and acoustic Doppler velocimetry profiles until recently for open channel flows with gravels (Hurther et al., 2007; Belcher, 2009); (ii) the loss of the imprint of macroturbulence on Reynolds averaged turbulence terms and thus the lack of knowledge of its presence in the flow (Church et al. 2012), and (iii) perhaps the lack of investigations where macroturbulence is highly prominent, for example, Shvidchenko and Pender (2001) suggest that a number of studies over gravel beds do not show pronounced macroturbulent features as identified in large scale fluctuations in velocity signals.

Our objective was to investigate the structure of turbulence for nonuniform gradually decelerating open channel flow over gravel with specific emphasis placed on elucidating the role of macroturbulence on sustaining and redistributing energy. We focus on a hydraulically rough nonuniform gradually decelerating open channel flow over gravel with a Froude number ranging from 0.5 to 0.8. By providing experimental results of time average quantities and statistical measures for this flow case, we overlap previously reported flow studies that have Froude number up to 0.6 for nonuniform open channel over gravel, but also we extend the nonuniform turbulent open channel flow literature database to the higher Froude numbers approaching transcritical flows. More importantly, we have performed in depth investigations of the uniform open channel flow over gravel for this Froude number range with similar relative submergence and have shown the pronounced presence of macroturbulence through the use of decomposed acoustic Doppler velocimeter data, decomposed digital particle image velocimetry data, and decomposed large scale particle image velocimetry data (Fox et al., 2005; Fox and Patrick, 2008; Belcher, 2009; Fox and Belcher, 2009). Our visualization and measurements of macroturbulence for the uniform flow case enabled us to hypothesize that the macroturbulence may play a substantial role in the structure of turbulence for the case when the flow was nonuniform and gradually decelerating. With our objective and hypothesis in mind, we use traditional Reynolds average turbulent quantities and instantaneous and statistical measures of the three dimensional instantaneous velocity signal in order to discern how the streamwise mean velocity deceleration coupled with

the increased vertical expansion wall normal velocity impacts the structure of turbulence including turbulence production, i.e., bursting near the bed and macroturbulence in the outer region.

4.3 METHODS

4.3.1 Facility Description

The experiments were conducted at the Hydraulics laboratory, University of Kenucky, Lexington Kentucky using a tilting recirculating flume 12 m long, 0.61 m wide. Turbulent fully rough gradually decelerating open channel flow over gravel was investigated. These flows are representative of many natural stream configurations, the experimental methods are consistent with previous research, and flow conditions overlap the existing literature database and extend it to transcritical flow conditions. Data collection methods and flow conditions were designed to enable comparison of flow description with previous literature results on gradually decelerating flows and turbulent structure in fully turbulent hydraulically rough open channel flows over gravel. Data collection methods were designed to obtain high quality data for time series analyses using spectral, quadrant, and Reynolds Decomposition methods combined with time averaged statistics.

Flow rate and slope remained constant while the location and obstruction ratio were varied to produce the desired flow conditions. The experimental conditions are summarized in Table 1, in which $Fr = U_m(gH)^{-1/2}$ is the Froude number, $\mathrm{Re}=U_m H\nu^{-1}$ is the Reynolds number, $K^+=k_s U_* \nu^{-1}$ is the shear Reynolds number. The range of flow depth H was 9.6-14.5 cm corresponding to an aspect ratio B/H of 4.2-6.4. The corresponding range of Fr and Re was 0.49 to 0.81 and $2.2\text{x}10^4$ to $5.3\text{x}10^4$ respectively. The range of K^+ was 207 to 360. Hence, the flows studied were all subcritical and turbulent over a fully rough bed.

4.3.2 Quality Control for Hydraulic Measurements

The channel bed was surfaced with angular gravel sized aggregates embedded on fiberglass-resin panels and channel side walls were acrylic plates. Particle size distributions of the bed material were measured using photogrammetric microscopy technique (Belcher 2009). Particle size analysis found the flume bed material to have D_{84} =5.7mm, standard deviation 1.38mm and D_{50}=4.4mm. The flume slope was determined

by measuring bed elevations using the Wild Nak1 survey level vertical accuracy of $\pm 10^{-5}$ m $m^{-1}$and survey rod measurement precision of 3.1mm and accuracy of $\pm 2.5\ 10^{-4}$ m m^{-1}. The survey level was placed 3 m downstream of the flume outfall and rod was positioned along the center of the flume channel at 1m increments to determine elevation. Measurement accuracy of flume elevation was approximately ±0.3mm, less than half the smallest demarcation on survey rod therefore half measurement precision on survey rod was used to assess the accuracy of flume bed elevations to be ±1.5mm. Using standard propagation of error techniques and neglecting any covariance in measurements of length and elevation the accuracy of flume slope is approximately ±0.00125 m m^{-1}. Flume slope was adjusted by elevating the flume entrance. When the slope was adjusted to 0.006 the surveyors traded jobs and the rod holder became the level operator which provided a check that flume elevations were correct.

Flow entering the flume at the channel inlet was conditioned using 127-mm long honeycomb of 6.4 mm diameter plastic tubes. Quasi-uniform flow conditions were established in the test sections approximately 6-m downstream of the inlet. To produce the maximum length of uniform flow to be used as a test section the flume outlet was equipped with semi-permeable bars to minimize drawdown effects near the free overfall. Thus prior to enforcing non-uniform flow conditions the flow developed to a quasi-uniform state for a distance of approximately 5-m. Development of quasi-uniform flow further verified consistency of flume slope throughout the testing section. Water surface elevation where measured from the bottom of the roughness elements using rulers attached the channel sidewalls.

During tests the ADV remained stationary while the downstream location of flow obstruction used to produce the desired flow conditions at the measurement location. Maintaining constant measuring location while varying downstream obstruction is opposite from previous studies were the obstruction remained constant but ADV measuring location was varied. However either procedure is expected to produce similar flow conditions at the measuring location. Flow was allowed to stabilize prior to collecting velocity measurements. Stabilization of flow properties were ensured by monitoring water temperature, maintaining consent elevation in flume reservoir and head box, and measuring flow rate through the flume supply pipe. Verification of flow stability

was confirmed by observing stabilization of the first three statistical moments of velocity prior to data collection.

The ADV remained stationary while the downstream obstruction size and location was varied similar to moving an ADV further upstream of the obstruction as was performed in previous research. Maintaining the ADV in a fixed streamwise position ensured orientation with the flow direction was consistent between measured profiles Measurements of 13 velocity profiles consisting of 18 to 34 bed normal measuring locations. Each velocity measurement is represented by 4500 instantaneous velocities. Instantaneous velocities were used to calculate turbulent statistic and were evaluated using spectral, quadrant, and Reynolds Decomposition methods. Velocimetry was performed using a 50 Hz *SonTek MicroADV*, where ADV denotes acoustic Doppler velocimeter. 4500 temporal data points were collected at each spatial location during testing to produce time series of three dimensional components of velocity recorded at 0.02 s. The ADV measures velocity in a small sampling volume (0.09 cm^3) with resolution of 0.01 cm s^{-1} and accuracy of 1% of measured velocity. Data collected with the ADV was processed with the Bureau of Reclamations software WinADV32 which was used filter data as suggested by the probe manufacturer. To ensure good quality data, filtering was performed to remove points with signal to noise ratio SNR<15 and correlation <70% as described by (Wahl 2000).

The ADV was mounted on a specially designed measurement carriage equipped with a mechanical screw mechanism for adjustment of ADV elevation. This ensured elevation of the ADV relative to the fix flume bed was estimated with high level of precision and accuracy. Prior to experimental testing the mechanical screw mechanism for adjustment of ADV elevation was determined to produce a displacement of 0.635mm/crank. The ADV elevation relative to the bed was measured before and after collection of velocity profiles and intermediate ADV positions were determined by counting the number of cranks and adding the corresponding displacement to the initial ADV elevation. The ADV mounting rod extended into the flume bed through a hole in flume bed equipped with a silicone gasket to prevent any upwelling or down welling. The combination of using a rigid ADV mounting rod and stabilizing the rod with the flume bed reduced ADV vibrations which can interfere with turbulence measurements by

producing artificially elevated velocity fluctuations (Dancey 1990). The flume was fastened to the concrete floor and isolated from the pump by connecting the flume headbox to the supply line using flexible rubber fittings to reduce flume vibrations.

The ADV was oriented down looking to obtain near bed velocity measurements without interfering with the flow. Following the collection of measurements with the probe in the down looking position, the probe was reoriented side-looking to obtain near surface measurements. Extreme care was taken to ensure proper ADV alignment with flow coordinate system. The coordinate systems of the sidelooking and down looking ADV were matched in the vertical by applying a vertical translation to one coordinate system such that discontinuities were removed from the *TKE* and V_{mag} profiles. Where TKE is the turbulent kinetic energy and V_{mag} is the magnitude of the velocity vector. This accounted for slight errors in measurements of ADV elevation during instrument installation. After ensuring that the measuring volumes corresponding to each ADV orientation were matched the vertical orientation of all measurements were adjusted such that at y=0 V_{mag}=0. The ADV coordinate system was adjusted to match the stream coordinate system by applying a series of orthogonal matrix rotations to the velocity vector to minimize the depth averaged transverse flow component.

4.3.3 Analysis of Flow

The time-averaged streamwise *U*, vertical *V*, and transverse *W* flow velocities are defined as

$$U = \frac{1}{n}\sum_{i=1}^{n} u_i, \qquad V = \frac{1}{n}\sum_{i=1}^{n} v_i, \qquad W = \frac{1}{n}\sum_{i=1}^{n} w_i \tag{1}$$

Where u_i, v_i, and w_i are instantaneous velocities and n is the total number of measurements. The root mean square of velocity fluctuations for the streamwise u, vertical v, and transverse w components, are defined as

$$U' = \left[\frac{1}{n}\sum_{i=1}^{n}\left(u_i - U\right)^2\right]^{0.5}$$
$$V' = \left[\frac{1}{n}\sum_{i=1}^{n}\left(v_i - V\right)^2\right]^{0.5} \tag{2}$$
$$W' = \left[\frac{1}{n}\sum_{i=1}^{n}\left(w_i - W\right)^2\right]^{0.5}$$

The primary Reynolds shear stress component is given as $-\overline{u'v'}$ where u'=u-U, v'=v-V and the overbar indicates a time average. For the Reynolds shear stress to be dimensionally correct we should technically multiply by the density of the fluid. The energy associated with fluctuating components of velocity is the turbulent kinetic energy (*TKE*), defined as

$$TKE = \frac{1}{2}\left(U'^2 + V'^2 + W'^2\right) \tag{3}$$

$$V_{mag} = \sqrt{U^2 + V^2 + W^2}$$

Estimation of bed shear stress used to calculation the friction velocity was found by extrapolating the primary component of Reynolds shear stress to the bed following the nonlinear distribution for decelerating flows. Bed shear stress was also estimated using the Clauser method by fitting the streamwise velocity distribution in the near bed region. Deviations in methods for estimating shear velocity were noted but extrapolation of shear stress to the bed was used for the analysis of this data as it is the preferred method in the absence of direct measurements for turbulence research. We define the shear velocity as

$$U_* = \lim_{y \to 0^+} -\overline{u'v'}(y) \tag{4}$$

Non-uniform flow by definition implies variation of the streamwise gradient of hydraulic parameters. These flows may satisfy equilibrium if the distributions of hydraulic parameters may be described by a unique relationship. Flows are in equilibrium if the pressure gradient (β) defined by Clauser remains constant in the streamwise direction as $\beta = \frac{H}{U_*^2} g\left(-S_0 + \frac{\partial H}{\partial x}\right)$. The pressure gradient parameter is used to describe the relationship of hydraulic parameters in nonuniform open channel flow.

The quadrant analysis method is a simple well established technique to identify coherent structures in single point velocimetry data (Nezu and Nakagawa, 1993). The quadrant method consists of representing the instantaneous streamwise and vertical velocity components in a (u', v') coordinate system. The first quadrant both the u' and v' signals are positive, representing outward interactions. The second quadrant represents low momentum fluid moving away from the bed (ejection like events). The third quadrant consisting of negative u' and v', consists of inward interacting fluid. The fourth

quadrant represents high momentum fluid moving toward the bed (sweep like events). The second and forth quadrants with $-u'v'$ contribute to the generation of primary Reynolds shear stress component. The first and third quadrants do not contribute to generation of the primary Reynolds shear stress component and occur less frequently. In flow regions with high shear, namely the near bed region, the joint probability function is expected to be narrow, centrally symmetric about the origin, and reside primarily in the second and fourth quadrants. Further away from the bed the shear stress is decreased and flow tends toward isotropic the joint probability becomes more circular as events in the first and third quadrants contribute negatively toward production of shear stress.

Conditional averaging of instantaneous fluctuating velocity vectors is used in quadrant analyses to identify ejection and sweep events as strong contributors to shear stress generation. A simple method for conditionally averaging involves selection of a threshold level, H' referred to as the "hole size" is defined as $H' = |u'v'|/U'V'$. The hole size separates strong motions from random or weak velocity variations and thus ejections and sweeps events are as $H' < |u'v'|/U'V'$ (Lu & Willmarth 1972). The hole size $H'=2$ was selected to be consistent with previous studies in gravel bed rivers (Buffin-Belanger & Roy 1998; Lacey & Roy 2008). The average ejection and sweep angles were determined as the average of $-\tan^{-1}(u' v'^{-1})$ for the events greater than H' in second and fourth quadrant events respectively.

Spectral analysis of the time-series signal was performed to quantify the energy frequency scales of the turbulence. The spectrum was estimated using the discrete Fourier transform of u and v with the fast Fourier transform (FFT) method as

$$S_Z(\omega) = \sum_{j=1}^{n} Z_j e^{(-2\pi i)(j-1)(\omega n/25-1)/n} \tag{5}$$

where the input variable Z represents the *u, v or w* time series. The velocity spectra in variance preserving form consists of the spectral energy density multiplied by the frequency $S_z(\omega)\omega$ ($cm^2\ s^{-2}\ Hz^{-1}$). When plotted in variance-preserving form broad spectral peaks correspond to the frequency of an energetic mean or dominant eddy passing the velocity sensor (Boppe & Neu 1995; Venditti & Bennett 2000; Venditti & Bauer 2005). The area under the variance preserving spectra represents the total variance (Venditti &

Bennett 2000). The variance associated with macroturbulence is quantified by determining the area under the spectra in the frequency range identified as containing macroturbulence.

Velocity time-series can be decomposed into a mean velocity component and two fluctuating components representing low frequency macroturbulence and fast fluctuating high frequency small-scale eddies (Fox et al. 2005). This classification of eddies constitutes the Triple Decomposition Theorem introduced by Hussain & Reynolds (1972) expressed for the streamwise velocity as

$$u(t) = U + u'(t) + u''(t) \tag{6}$$

where u and U are the instantaneous signal and temporal mean. u' is the low frequency, large-scale signal used to isolate macroturbulence. u" is the remaining high frequency, small-scale associated with shedding. u' was isolated using the moving-average over a time-step T_s as

$$U + u'(t) = \frac{1}{T_s} \int_{t-\frac{T_s}{2}}^{t+\frac{T_s}{2}} u'(t')dt' \tag{7}$$

Selection of an appropriate value for T_s where the small-scale is removed was performed using visual inspection of smoothed time-series for varying values of T_s (Fox et al. 2005; Lacey and Roy 2008; Fox & Patrick 2008). Note when T_s is zero u' represents the total fluctuating component of the time series. Triple decomposed velocity signal enables visual inspection of the respective fluctuating component for qualitatively describing the imprint of turbulent on the velocity time series.

Turbulent energy is produced by Reynolds stress components acting on mean velocity gradients, in open channel flows primary production of turbulent energy is derived from the vertical gradient of streamwise velocity given by Nezu & Nakagawa (1993) as

$$G = -\overline{u'v'}\left(\frac{dU}{dy}\right) \tag{8}$$

For 2-dimensional uniform flow this is the only mechanism the flow has to produce turbulence and is responsible for the bulk of turbulence production in gradually varied open channel flow. For gradually varied 2-dimensional flow turbulent energy can be

produced from the vertical gradient of expansion velocity given as

$$F = \overline{v'v'}\left(\frac{dV}{dy}\right) = V'^2\left(\frac{dV}{dy}\right) \tag{9}$$

The vertical velocity induced by flow expansion in gradually decelerating 2-dimensional flow can be determined by integrating the continuity equation and applying boundary conditions to derive the expansion velocity as

$$V_{\exp} = U\frac{y}{H}\frac{dH}{dx} \tag{10}$$

Equ (10) shows V_{exp} is zero in uniform flows and positive in decelerating flows as the flow depth H increases in the streamwise direction.

4.4 RESULTS

Streamwise time-averaged velocity, U, scaled with bed shear velocity, U_*, is shown in Fig1a and U is shown in dimensional form in Fig 1b. U decreases as flow depth increases consistent with the decelerating nature of the open channel flow and continuity. Scaling U with U_* reduces the variation in distributions by approximately 15%, however still Fig 1a shows the wake effect in the outer region of the decelerating flow for $U\,U_*^{-1}$. The wake effect is attributed to inertial effects within the flow (Guo et al. 2005; MacVicar & Rennie 2012) and has been shown exhibit dependence upon the adverse pressure gradient as defined by Clauser (Nezu et al. 1994; Song & Graf 1994; Kironoto & Graf 1995; Song & Chiew 2001; Onitsuka 2009). To account for the wake effect, we plot the modified Log Wake Law for an adverse pressure gradient (Nezu et al. 1994; Song & Graf 1994; Kironoto & Graf 1995; Song & Chiew 2001; Onitsuka 2009). For our experimental data and the result is shown for each test case as solid lines in Fig 1b. The modified Log Wake Law was plotted as

$$\frac{U}{U_*} = \frac{1}{\kappa}\ln\left(\frac{y}{k_s}\right) + b + \frac{2\Pi}{\kappa}\sin^2\left(\frac{\pi y}{2H}\right) \quad , \tag{11}$$

where the von Karman constant κ =0.41, the equivalent roughness height k_s=2D_{84}=1.12cm, the constant of integration b=8.5, and the wake strength Π is determined by the functional dependence on the adverse pressure gradient, β. For the latter, we use the linear fit between Π and β recently by Onitsuka et al. (2009). The

linear fit is given by Onitsuka et al. (2009) as

$$\Pi = 0.07\beta + 0.27 \,. \tag{12}$$

The relationship given by Onitsuka et al (2009) includes new data along with the data collected by Nezu et al. (1994) and Song & Graf (1994) and extends the applicability to a wider range of aspect ratios, pressure gradients β, and relative roughness.

Fig 1b shows that $U\,U_*^{-1}$ is well described by the modified Log Wake Law where Coles wake strength is determined by β. This finding is consistent with previous research and extends our dataset at higher Froude numbers than previously reported to show the wake strength increases in the presence of adverse pressure gradient as the outer layer is subjected to inertial effects (Song & Graf 1994). Development of the wake region identified as increased velocity gradients in the outer region attributed to increased shearing caused by macroturbulence structures in this region. Enhancement of the strength and spatial coherence of macroturbulence in the outer region transfers fluid and momentum between the core of the flow and near the bed to increase shear between these regions. The enhancement of shear by coherent turbulent structures prompted the development of mixing length and eddy viscosity theory to account for turbulence as an increase in the fluids viscosity. The enhancement of outer region macroturbulence in turbulent boundary layer flows suggest that similar alterations of turbulent structure in decelerating open channel flows may explain the wake development as pressure gradient is increased.

Figure 1c shows the streamwise turbulent intensity ($U'\,U_*^{-1}$) and Figure 1d shows the standard deviation of streamwise velocity fluctuations, i.e., not normalized by U_*. Figure 1c includes a solid line indicating the expected profile for $U'U_*^{-1}$ in uniform flows as defined by Nezu and Nakagawa (1993) and given as

$$U'/U_* = D_u \exp(-y/H) \tag{13}$$

where the empirical coefficient D_u = 2.3 in uniform flow irrespective of *Re* or *Fr* (Nezu 2005). As shown in Figure 1c, the nonuniform gradually decelerating open channel flow over gravel deviates from the uniform flow equation, which tends to agree with previous studies (Song & Graf 1994; Kironoto & Graf 1995; Song & Chiew 2001. The lack of agreement has been attributed to increase in Reynolds shear stress resulting from expansion velocity (Song & Chiew 2001; Yang & Chow 2008), the presence of

macroturbulence (Papanicolaoa & Hilldale 2002) and large roughness elements (Stone & Hotchkiss 2007). Commonly, the empirical coefficient D_u in Equation 13 has been fitted to the experimental results by others (Song & Graf 1994; Kironoto & Graf 1995; Song & Chiew 2001; Carollo et al. 2005). In Figure 1d, we show Equation (13) with D_u fitted to our data, as similarly performed by others (Song & Graf 1994; Kironoto & Graf 1995; Song & Chiew 2001). Measurements presented here of streamwise turbulence intensity are slightly amplified as compared to uniform flow with average D_u=2.66. Our increased D_u fit are in close agreement with the empirical fits for the coefficient reported by Song & Chiew (2001) for the nonuniform flow case. Song and Chiew (2001) report that D_u is a function of the pressure gradient parameter, β. Figure 3 shows our results for D_u as a function of β as well as the empirical equation by Song and Chiew (2001) given as

$$D_u = 0.6(0.1\beta^2 + \beta) + 3 \tag{14}$$

In this sense, we see close agreement between our results and that of others. Equation 14 is somewhat misleading as it was determined for both accelerating and decelerating flows, if only the decelerating flows of Song & Graf (1994), Kironoto & Graf (1995) and Song & Chiew 2001 are considered D_u estimated in the current study are within the experimental scatter of the previous research. The close agreement likely reflects that primary production of steamwise turbulent fluctuations, e.g. the bursting process, is driven by the vertical U gradient which was shown in Figure 1b to closely agree with the previous research. The effects of decelerating flow reduced U' by approximately 25% across the entire flow depth for the flow studied here.

The primary Reynolds shear stress ($-\overline{u'v'}$) distribution is shown in Fig (1e,f). $-\overline{u'v'}$ increases from the bed to the maximum value attained around y/H=0.2 then decreases as the free surface is approached. The location of maximum Reynolds shear stress remained fairly consistent for the present study which contradicts previous findings by Afzalimehr & Anctil (1999) and Emadzadeh et al. (2010) where the location of maximum shear stress moved away from the wall in their decelerating flows. The experiments of Afzalimehr & Anctil (1999) and Emadzadeh et al. (2010) were conducted at much lower aspect ratio (3 and 2.2) and at much lower Fr (0.287 and 0.2) which may explain the difference in our results. While Papanicolaou & Hilldale (2002) attribute additional turbulent production mechanism in the outer flow region to the shift in location

of maximum primary Reynolds shear stress. However, in general our primary shear stress results are consistent with roughbed open channel decelerating flows in that the distribution shows pronounced nonlinearity thus diverging from the uniform case (Song & Graf 1994; Kironoto & Graf 1995; Song & Chiew 2001; Afzalimehr 2010; Afzalimehr et al. 2012). Song & Chiew (2001) empirical fit the streamwise velocity distribution to derive the nonlinearity of the primary Reynolds shear stress in nonuniform gradually decelerating open channel flow over gravel, and we test that equation for our data. The Reynolds stress collapses when scaled by the square shear velocity with the outer region being well described by a slightly non-linear relationship shown as a solid line in Fig (1e,f) given by Song & Chiew (2001) as

$$\frac{\overline{u'v'}(y)}{\overline{u'v'}(0)} = 1 + \beta\frac{y}{H} - (\beta+1)\frac{(1+m)^2}{m(m+2)}\left(\frac{y}{H}\right)^{(m+2)/m} \tag{15}$$

The coefficient m is found by fitting a power law to the measured streamwise velocity distribution (Song & Chiew 2001)

$$\frac{U}{U_{avg}} = \frac{1+m}{m}\left(\frac{y}{D}\right)^{1/m} \tag{16}$$

Where U_{avg} is the cross-sectional mean velocity providing the corresponding average m value of 4.1. As can be shown, the empirical fit of Song & Chiew (2001) using Equ (15) is an excellent fit with our data. The empirical power law Equ (16) describes the velocity distribution reasonably well and Equ (16) is relatively insensitive to m over the range found to fit our data. The excellent fit of Equ (15) to the present data likely reflects the non-linearity in this equation is introduced by the expansion velocity primary production of primary Reynolds shear stress is derived from the near velocity gradients by producing bursting motions. Flow deceleration reduced $-\overline{u'v'}$ by approximately 25% across the entire flow depth. Consequently the greatest reduction in shear occurs near y/H=0.2 where shear stress attains its maximum.

Figure 2a shows the vertical turbulence intensity ($V' U_*^{-1}$) normalized with U_* and in Figure 2b shows the standard deviation of wall normal velocity fluctuations V', i.e., not normalized by U_*. Figure 2a includes a solid line indicating the expected profile for $V' U_*^{-1}$ in uniform flows as defined by Nezu and Nakagawa (1993) and given as

$$V'/U_* = D_v \exp(-y/H) \quad (17)$$

where the empirical coefficient D_v = 1.27 in uniform flow (Nezu & Nakagawa 1993). As shown in Figure 2a, the nonuniform gradually decelerating open channel flow over gravel causes an amplification of vertical turbulence intensities as compared to uniform flow consistent with previous findings (Song & Graf 1994; Kironoto & Graf 1995; Song & Chiew 2001; Afzalimehr 2010). Figure 2b shows decelerating flow reduced V' by 20% at the normalized bed distance y/H=0.2 while reduction in the near surface region y/H=0.8 was negligible. The location of maximum V' occurs near y/H=0.2 for nearly unobstructed flows while the most obstructed measured profiles maximum V' occurred near y/h=0.5 (Figure 2b). This result is consistent with Song & Graf (1994) and Afzalimehr (2010) in which location of maximum V' shifted away from the bed in more decelerated flows. Commonly, the empirical coefficient D_v in Equation (17) has been fitted to the experimental results by others (Song & Graf 1994; Kironoto & Graf 1995; Song & Chiew 2001). Measurements presented here of wall normal turbulence intensity are slightly amplified as compared to uniform flow with average D_v=1.39. The inability of U_* to collapse V' has lead previous researcher to parameterize D_v in equation 17 as a function of β to account for redistribution of Reynolds stress caused by the expansion velocity (Song & Graf 1994; Kironoto & Graf 1994; Song & Chiew 2001). Figure 3 shows our results for D_v as a function of β as well as the empirical equation by Song and Chiew (2001) given as

$$D_v = 0.3(0.1\beta^2 + \beta) + 1.5 \quad (18)$$

In this sense, we see close agreement between our results and that of others. Also, we see in Fig 2a that U_* does not collapse V' well. The shift in location of maximum V' distorts the profiles such that Equ 17 for uniform flow is of the incorrect form to properly describe the distribution. This finding is consistent with previous research in that the distribution of V' is not well described by exponential decay toward the free surface (Kironoto & Graf 1995). Shift in the location of maximum V' and amplification of V' U_*^{-1} has been attributed to additional turbulence production mechanisms including macroturbulence (Papanicolaoa & Hilldale 2002), large roughness elements (Stone & Hotchkiss 2007; Afzalimehr 2010) and increased Reynolds shear stress due the expansion velocity (Song & Chiew 2001; Yang & Chow 2008). Additionally amplification of V' U_*^{-}

[1] in the current study may be an artifact of fluctuating water surface elevation for these higher *Fr* number flows resulting in *V'* to be non-zero at the time averaged free surface. The shift in maximum *V'* location likely causes $V'U_*^{-1}$ to deviate from Equation (18). These results show vertical turbulence intensity in decelerating flows is not well predicted by a model assuming exponential decay of turbulence from a near bed production source

Figure 2b shows the transverse turbulence intensity ($W'\ U_*^{-1}$) normalized with U_* and in Figure 2d shows the standard deviation of wall normal velocity fluctuations *W'*, i.e., not normalized by U_*. *W'* increased rapidly from the bed to a maximum around y/H=0.2 then steadily decreases toward the free surface for the remainder of measurements. Figure 2a includes a solid line indicating the expected profile for $W'U_*^{-1}$ in uniform flows as defined by Nezu and Nakagawa (1993) and given as

$$W'/U_* = D_w \exp(-y/H) \tag{19}$$

where the empirical coefficient D_w = 1.51 in uniform flow (Nezu & Nakagawa 1993). As shown in Figure 2c, the nonuniform gradually decelerating open channel flow over gravel causes an amplification of transverse turbulence intensities as compared to uniform flow consistent with previous findings (Song & Chiew 2001; Afzalimehr 2010). The lack of agreement has been attributed to increase in Reynolds shear stress resulting from expansion velocity (Song & Chiew 2001) the presence of macroturbulence (Papanicolaoa & Hilldale 2002) and large roughness elements (Stone & Hotchkiss 2007). Commonly, the empirical coefficient D_w in Equation (19) has been fitted to the experimental results by others (Song & Chiew 2001). Figure (2c) shows that as the flow becomes more decelerated Equ (19) becomes less effective at describing the distribution of $W'U_*^{-1}$. In Figure 1d, we show *W'* is most reduced by decelerating flows in the region where bursting process is most active. Measurements presented here of transverse turbulence intensity are significantly amplified as compared to uniform flow with average D_w=1.77. Our increased D_w fit are in close agreement with the empirical fits for the coefficient reported by Song & Chiew (2001) for the nonuniform flow case. Song and Chiew (2001) report that D_w is a function of the pressure gradient parameter, β to account for failure of U_* to collapse *W'*. Figure 3 shows our results for D_w as a function of β as well as the empirical equation by Song and Chiew (2001) given as

$$D_w = 0.45(0.1\beta^2 + \beta) + 2.25 \quad (20)$$

In this sense, we see close agreement between our results and that of others. Equation (20) is somewhat misleading as it was determined for both accelerating and decelerating flows, if only the decelerating flows of Song & Chiew 2001 are considered D_w estimated in the current study are within the experimental scatter of the previous research. Differences likely reflect the strength of macroturbulence for these flow conditions.

Figure 2e shows the anisotropy of turbulence in the wall normal and transverse directions scaled by the shear velocity ($(\overline{W'^2}-\overline{V'^2})U_*^{-1}$) and Figure 2f shows the anisotropy of turbulence, i.e., not normalized by U_*. Anisotropy increased from the bed to a maximum value at y/H=0.2 then steady decreases to y/H>0.6 and remains approximately constant toward the free surface for the remainder of the measurements. Figure 2f indicates the magnitude of anisotropy is decreased by decelerating flow, however, anisotropy scaled by the shear velocity shows a slight increase for the highly decelerated case. Description and investigation of turbulence anisotropy within nonuniform gradually decelerating open channel flow over gravel has not been a focal point of past research studies. However, our results for turbulence anisotropy are somewhat consistent with that shown by Alfzalimehr et al. (2012) for low *Fr* decelerating flows over a rough bed with vegetated banks. Also, measured wall normal and transverse turbulent intensities in previous research show these values differ in the outer region and thus indicate some similarity to this study indicate the presence of anisotropy (Song & Chiew 2001; Afzalimehr 2010). Anisotropy of turbulence is responsible for the production of streamwise vorticity in straight uniform open channel flows and indicates the presence of three dimensional rotating turbulence structures (Nezu 2005). While the vorticity equation for straight non-uniform open channels contains additional vorticity production terms (i.e. vortex stretching and turbulence inhomogeneity) the anisotropy of turbulence suggests the occurrence of three dimensional rotating turbulence in all flow conditions examined here. The presence of three dimensional turbulence structures in fully turbulent hydraulically rough open channel flow is consistent with theory and previous findings in uniform flows (Adrian et al 2000; Hurther et al. 2007; Belcher & Fox 2009; Adrian & Marusic 2012).The enhancement of turbulence anisotropy relative to

the bed shear velocity indicates increased vorticity generation for the decelerated flow case and suggests that anisotropy is not fully controlled by the near bed shear induced bursting process.

The general effect of decelerating flow on mean velocity and Reynolds stresses scaled by shear velocity is that quantities either collapse or are increased relative to uniform flow. The near bed mean velocity distribution which scales nicely with bed shear velocity is in large part determined by shear stresses related to the near bed bursting process. The outer region velocity distribution does not collapse with bed shear stress and was accounted for with additional wake strength in decelerated flows. This indicates disconnect between the bed shear stress and outer region macroturbulent structures responsible for wake formation. Anisotropy between the vertical and transverse velocity fluctuations indicates the presence of 3-dimensional vortical turbulent structures throughout the flow. The primary component of Reynolds shear stress collapsed reasonably well when scaled by bed shear velocity yet was amplified in the outer region. The normal Reynolds stress components underwent the greatest reduction in the near bed region and remained relatively unaffected near the free surface. Turbulent intensities are enhanced for the decelerated flow conditions particularly in the outer region. Combined the results from analyzing Reynolds stress components for decelerated flows suggests outer region macroturbulence is not fully controlled by the near bed shear induced bursting process. Cumulatively these results show enhancement of outer region turbulence relative to shear velocity in decelerating flows. This suggests turbulent mechanisms other than near bed bursting is responsible for turbulent energy generation in the outer region of decelerated flows.

Angles of ejections and sweeps relative to the bed determined from quadrant analysis of the streamwise and wall normal velocity components is shown in Fig (4a and 4b), respectively. This figure shows that sweeps and ejections occur at approximately 180^{o} to one another as these two events occur in combination to create the bursting process. The bursting angle is minimum near the bed and increases toward the free surface consistent with research in roughbed uniform open channel flows at high Reynolds number (Adrian et al. 2000; Lelouvetal et al. 2007). The most decelerated flow examined here shows an increase in bursting angle for the entire flow depth except in the

very near bed roughness region. To the best of our knowledge a dependence of bursting angle on flow deceleration has not be reported for gradually varying open channel flows over a rough bed. These results indicate the bursting process changes to become more aligned in the wall normal direction in decelerating flows. This result was expected after observing that U' decreased and V' remained relatively unchanged in the decelerated flows (see Fig 1d and 2b). The change in bursting angle reflects that U' is controlled by shearing and V' is greatly enhanced by the expansion velocity in decelerating flows.

The frequency of ejection and sweep events is shown in Fig (4a,b) respectively. Ejection and sweep events represent the majority of turbulent interactions. Somewhat surprisingly, these processes are not significantly affected by flow deceleration despite the fact that the bursting period defined using outer variables (T_B=3 H V^{-1}) doubles from H=10 cm to H=14.3 cm. This result is consistent with the findings reported by Alfzalimehr (2012) in which frequency of ejections and sweeps did not show significant difference in non-uniform flows while the shape of joint probability distributions of turbulent fluctuations was affected; the latter of which agrees with the consistent decrease in U' and lack of decrease in V' found in our study. We relate the consistency of ejections and sweeps across the decelerating region to the consistency of the macroturbulence which in turn impacts the bursting process, which we discuss later.

Figure 5 shows stream wise velocity spectra multiplied by frequency, i.e. variance-preserving from. When plotted in variance-preserving form broad spectral peaks correspond to the frequency of an energetic mean or dominant eddy passing the velocity sensor (Boppe & Neu 1995; Venditti & Bennett 2000; Venditti & Bauer 2005). The turbulence structure of fully turbulent hydraulically rough open channel flows with low relative submergance have been well documented and described using particle image velocimeter and ADV spectral methods (Fox et al. 2005; Fox and Patrick 2008; Rodribguez & Garcia 2008; Belcher & Fox 2009; Fox & Belcher 2011). The dominant turbulence features of these flows include the bursting process consisting high frequency fast velocity fluctuation from eddies shed by individual roughness elements and bursting process and low-frequency slower velocity fluctuations associated with macroturbulence. The bursting period conservatively estimated using outer variables as (T_B=3 H V^{-1}) does not typically vary with *Re*, *Fr* or wall roughness (Nezu & Nakagawa 1993; Tamburrino

& Gulliver 2007). For our flow conditions the mean bursting frequency is approximately 1.2 Hz, the frequency of eddies shed from bed particles will be much higher than the bursting frequency therefore we select 1Hz as the frequency used to distinguish between macroturbulence and near bed shear induced bursting process. The area under the streamwise velocity spectra decreases as the flow becomes more obstructed (left to right Figure 5) consistent with the trends in U' showing a decreases in energy associated with streamwise velocity fluctuations. The streamwise spectral energy is greatest near the bed and decreases as the freesurface is approached (bottom to top Figure 5), showing that toward the freesurface velocity fluctuations are occurring less often or the magnitude of fluctuations is decreasing. Figure 8a shows the integral of streamwise velocity spectra across the macroturbulent frequency range (0.1-1 Hz) decreases as the flow becomes more decelerated. The average integral in the outer region of S_u over the macroturbulent frequency range shows energy associated with these structures is reduced by approximately 30% in decelerated flows (Figure 8b). The total reduction in streamwise velocity variance is approximately 50% (Figure 1b). This indicates more streamwise turbulent energy is lost by high frequency fluctuations associated with bursting and dissipation scales than is lost by low frequency macroturbulence.

Figure 6 shows vertical velocity spectra multiplied by frequency, i.e. variance-preserving form. The vertical spectra decrease as flow becomes more decelerated (left to right Figure 6) however the decrease is less obvious than was observed for streamwise spectra. The greatest reduction in vertical spectral energy comes at the normalized bed distance y/H=0.2 while in flow core and near surface region less spectral energy is lost. The decrease in vertical spectral energy as the free surface is approached is not as significant as observed for streamwise spectra (bottom to top Figure 6). The vertical spectral energy for the most decelerated flow shows little decrease as the free surface is approached (right column Figure 6). This result indicates turbulent energy associated with vertical velocity fluctuations in decelerated flows is near uniformly distributed in the wall normal direction. Vertical velocity spectra near the free surface shows energy reduction occurs at high frequencies (ω>1Hz) while energy at low frequency increases as the flow becomes more decelerated (Figure 6 top row). Figure 8c shows the integral of vertical velocity spectra across the macroturbulent frequency range (0.1-1 Hz) decreases

as the flow becomes more decelerated for the lower half of the flow, while in the upper half of the flow macroturbulence contains more energy. The average integral of S_v over the macroturbulent frequency range in the outer region shows energy associated with these structures is increased slightly in decelerated flows (Figure 8b). These results indicate the vertical velocity fluctuations associated with macroturbulence become more energetic in the outer region particularly near the free surface. High frequency velocity fluctuations related to the bursting process are reduced in decelerating flows.

Figure 7 shows transverse velocity spectra multiplied by frequency, i.e. variance-preserving from. The transverse spectra decrease as flow becomes more decelerated (left to right Figure 7) however the decrease is less obvious than was observed for streamwise spectra. The greatest reduction in transverse spectral energy comes at the normalized bed distance y/H=0.2 while the near surface region less spectral energy is lost. The decrease in transverse spectral energy as the free surface is approached is not as significant as observed for streamwise spectra (bottom to top Figure 6). Transverse velocity spectra in the flow core and near the free surface shows energy reduction occurs at high frequencies (ω>1Hz) while energy at low frequency increases as the flow becomes more decelerated (Figure 7 top and middle rows). Figure 8e shows the integral of transverse velocity spectra across the macroturbulent frequency range (0.1-1 Hz) increases in the outer region as the flow becomes more decelerated. The average integral of S_w over the macroturbulent frequency range in the outer region shows energy associated with these structures is increased by approximately 50% in decelerated flows (Figure 8b). These results indicate the transverse velocity fluctuations associated with macroturbulence become more energetic throughout the outer region.

Results of the spectral analysis reveal turbulent energy is lost from all velocity components in decelerating flows. The turbulent energy being lost is primarily at high frequencies associated with bursting process and dissipative scales. The relative contributions of macroturbulence to the total turbulent energy increase in the decelerated flows. The results of energy spectra show dominant energy containing frequencies shifts from high to low frequency fluctuations in decelerating flow. Comparison of spectra analyzed here with previous research is limited, however, this data set displays the inertial sub-range characterized by the Kolmogorov -5/3 law (not shown) which is

consistent with findings of Kironoto & Graf (1995). Similar findings have been reported for turbulent boundary layer flows subject to adverse pressure gradient in that the large scale turbulent features become more active in adverse pressure gradient flows (Lee & Sung 2008; Harun et al. 2013). To the best of our knowledge the scale dependent effects of decelerating flow on turbulence has not previously been reported for open channels. These results show flow deceleration affects turbulence in a manner somewhat consistent with low pass filtering which may have important implications for predicting flow fields of decelerating open channel flows using numerical modeling techniques. It would be interesting to see if this is an artifact of moderately high Froude number flows studied here or if the low Froude number flows previously studied in the literature show similar development of turbulence structure as flow is decelerated.

Figure 9 shows selected streamwise velocity time series smoothed according to the triple decomposition method with T_s equal to 0.2 s used to isolate low frequency large scale turbulent features. The smoothing timestep used here does not completely remove fast fluctuating velocity component from the timeseries however the large scale turbulent features become readily identifiable none the less. The magnitude of velocity fluctuations is reduced however prominent features of large scale turbulence are evident in the decelerated flow. This result agrees with the spectral analysis and provides visual confirmation of the persistence of large scale turbulent features in decelerated flows.

Figure 10a shows the production of turbulent energy from the vertical velocity gradient through the vertical velocity variance (Equ 9), solid symbols are calculated from measured values and the hollow symbols represent turbulent energy production by the stabilization of macroturbulence, i.e. the contribution from expansion velocity has been subtracted from total energy production. Turbulent energy production by the expansion velocity were calculated using the theoretical expansion velocity V_{exp} (Equ 10) for 2-dimensional flow. Figure 10a shows turbulent energy production occurs due to the vertical expansion velocity, this mechanism is not present in two-dimensional uniform flows (see Church et al. 2012 pp7). This analysis shows the expansion velocity is responsible for over 40% of this production term in the core of the flow. The remaining turbulence production of this term is likely due to the presence of secondary currents in the flow which are known to produce non-zero wall normal velocities and affect the

distribution of turbulence. Figure 10b shows primary production of turbulent energy for selected flows. The production of turbulent energy from the expansion velocity is two orders of magnitude less than primary production. The expansion velocity in non-uniform flows is shown to produce turbulent energy thus providing a mechanism to increase vertical velocity fluctuations particularly in the outer region.

4.5 DISCUSSION

Our results suggest that turbulent kinetic energy produced at the bed from the bursting process is dampened as the fluid decelerates and the mean streamwise velocity decreases (Fig 10b). The net result of dampened bursting on turbulent kinetic energy is highly evident as all three components of the energy show pronounced decreases of their maximum values in the near bed region (Fig 1d, 2b, 2d). The reduction in bursting associated turbulent energy is not surprising as the net streamwise velocity gradient in the vertical decreases, and this idea has been shown by others for decelerating flows through the use of time-averaged analyses (e.g., Yang and Chow, 2008). Further, the impact of flow deceleration on decreasing turbulent energy production through bed derived bursting is consistent with the collapse of streamwise velocity, streamwise normal stresses and the primary Reynolds shear when scaled with the friction velocity (see Fig 1 a, c, d). A few additional points regarding effects of the deceleration on bursting. It is interesting that the temporal distribution of bursting, i.e., ejection and sweep frequency, tends to remain consistent throughout the decelerating flow (Fig 4 c, d) despite the fact that the bursting period calculated using outer variables (T_B=3 H V^{-1}, Nezu and Nakagawa, 1993) doubles from 0.43 s to 0.82 s when flow depth increases from H=10 cm to H=14.5 cm. The result tends to point towards a connectivity between bursting and macroturbulence, and we discuss this idea in more detail later in reference to macroturbulence. The expansion velocity and thus net positive wall normal velocity is suggested to impact bursting to some degree since the ejection angle increases as the flow decelerates (see Fig 4a).

Evidence of the presence of a macroturbulence structure within the flow is identified in the results of this study for the first time for nonuniform, hydraulically rough open channel flow over gravels. Evidence of macroturbulence is shown by the large scale fluctuations remaining in the velocity time signal after the Triple Decomposition Theorem is applied and by the broad low frequency peaks in the spectral energy density

plots (see Fig 5, 6, 7, 9). Our results elucidate that macroturbulence has a role to redistribute turbulent kinetic energy for the nonuniform gradually decelerating open channel flow over gravel. Results suggest that the streamwise component of the macroturbulent energy decreases as the flow decelerates, although the decreased macroturbulent energy is most pronounced near the bed and is less pronounced as the free surface is approached (see Fig 8 a,b). The net weakening of the streamwise macroturbulent energy is consistent with the idea that high connectivity exists between macroturbulence and bursting, and dampening of the bursting process in turn lessens the amount of energy associated with the streamwise macroturbulence.

Somewhat surprisingly, the vertical and transverse macroturbulent energy show net increases especially in the upper half of the flow as the flow decelerates, suggesting a strengthening of the cross sectional plane of the three dimensional macroturbulent structure (see Fig 8 c,d,e,f). Increased vertical and transverse components of macroturbulent energy are attributed to: (i) secondary energy production associated with the wall normal velocity of the vertical expansion that supplies energy to the macroturbulence and (ii) the existence of the three dimensional macroturbulence which provides a mechanism for energy redistribution *via* generated vorticity. The first point is illustrated through calculation of the secondary turbulent production in the vertical (see Fig 10a) where the vertical turbulent energy production term calculated with the expansion velocity is shown to explain the excess energy production measured in the outer region. The second point is illustrated by the fluid anisotropy throughout the flow depth in the decelerating flow (Fig 2f), which provides the mechanism for vorticity generation (Nezu, 2005). When coupled with the generation term, the macroturbulent cells are conceptualized to redistribute the vertically supplied energy to the transverse components; and our understanding of the mean kinetic energy budget provides the physically-based mechanics for this concept (e.g., see Nikora and Roy, 2012). Finally, the redistribution mechanisms associated with the macroturbulent structure and the suggested interaction of the macroturbulent structure with the vertical expansion are further corroborated with the results of the vertical profiles for the secondary turbulent intensities (see Fig 2a, c). The lack of collapse of the secondary turbulent intensities with the friction velocity and the increased magnitudes in the upper half of the flow depth

suggests that the dampened bursting process at the near bed region associated with the decreased streamwise mean velocity does not well explain the secondary energy terms. Rather, the vertical and transverse turbulent intensities in the upper half of the flow depth are suggested to be heavily impacted by energy production from the vertical expansion and vorticity of the macrotubulence.

As another point, the lack of deviation of bursting frequencies (Fig 4 c, d), despite the fact that the bursting period calculated using outer variables (T_B=3 H V^{-1}) doubles from 0.43 s to 0.82 s when the flow depth increases from H=10 cm to H=14.3 cm suggests that perhaps the bursting process dynamically evolves with the macroturbulent structure without changing the spatial organization of vortices which produce ejection/sweep events. This result implies that bursting is less intense due to less bulk fluid shear at the boundary but that spatial distribution is determined by macroturbulence and hence spatial distribution of bursting is much slower to change. Previous research has suggested that the bursting process could be organized by macroturbulence sweeping motions such that bursting occurs at the edge of macroturbulence for turbulent boundary layer flows (Kline et al. 1967; Schoppa & Hussain 2002; Marusic et al. 2010) and for wall bounded flows (Adrian, 2007;Adrian & Murasic 2012). The persistence of macroturbulence and its close relationship to bursting process formation may explain the consistency displayed by the bursting frequency. The macroturbulence persistence in the decelerating flow provides a consistent mechanism to initiate the bursting process in that the dynamics have evolved to obey the constraints of continuity and decreased shear available to produce bursts. However, the connectivity between the macroturbulent structure and bursting raises the question of the usefulness of current approaches to estimate the bursting period either using outer variables, inner variables or a mixture of the two (e.g., Cao et al., 2003; Nezu and Nakagaw, 1993) as none of these methods capture the three dimensional nature of the macroturbulent flow.

As a secondary point of discussion that tends to extend beyond our currently presented dataset, a now commonly held view is that stabilization of macroturbulence produces what is known as secondary currents identifiable using time-averaged equations of motion (Nezu 2005; Belcher & fox 2009; Albayrak & Lemmin 2011; Adrian & Marusic 2012; Nikora & Roy 2012). One viewpoint is that the organization of

macroturbulence into secondary currents identifiable in the time average sense requires an external forcing perhaps provided by the turbulence-generated near-bank secondary currents (Rodriquez & Garcia 2008; Blanckaert et al. 2010). Recent findings suggest that secondary currents scale with channel depth and are present over the entire width in open channels regardless of aspect ratio, however as aspect ratio increases they are temporally less stable and have been shown to meander in the transverse direction (Nezu 2005; Albayak & Lemmin 2011). While we did not collect cross sectional measurements of secondary currents for the nonuniform flow cases, the presence of secondary currents is likely given our previous measurements of secondary flow characteristics for the uniform case with the similar conditions as those presented here (Belcher and Fox, 2009) and measurements of secondary current characteristics by others for similar uniform conditions (Rodriquez & Garcia, 2008). In summary, the presence of secondary currents in these flow conditions is generally likely given our measured vertical velocity component and recent findings in the literature that secondary currents have been identified for aspect ratios up to *B/H*=20 (Albayrak & Lemmin 2011).

In future research, the effect of nonuniform flow on stabilizing or destabilizing macroturbulence, and hence secondary currents, such that they are readily identifiable by time averaged techniques should be studied, since this topic has yet to be considered in the literature. Future work should investigate the effects of flow deceleration using the nonuniform flow vorticity equation (Nikora & Roy 2012) given as

$$\frac{D\Omega_x}{Dt} \equiv \frac{d\Omega_x}{dt} + \overbrace{U\frac{d\Omega_x}{dx} + V\frac{d\Omega_x}{dy} + W\frac{d\Omega_x}{dz}}^{A1} = \overbrace{\nu\nabla^2\Omega_x}^{A2} + \overbrace{\left(\frac{dU}{dx}\Omega_x + \frac{dU}{dy}\Omega_y + \frac{dU}{dz}\Omega_z\right)}^{A3} + \overbrace{\frac{\partial^2}{\partial y\partial z}\left(\overline{v^2} - \overline{w^2}\right)}^{A4} + \overbrace{\left(\frac{\partial^2}{\partial y^2} - \frac{\partial^2}{\partial z^2}\right)\left(-\overline{vw}\right)}^{A5} + \overbrace{\frac{\partial}{\partial x}\left[\frac{\partial}{\partial y}\left(-\overline{uw}\right) - \frac{\partial}{\partial z}\left(-\overline{uv}\right)\right]}^{A6} \tag{21}$$

With respect to Equation (21), research on secondary currents in straight channels has mostly been confined to uniform flows where vorticity production from anisotropy of turbulence (Equ 21 A4) is nearly balanced by gradients of the vertical-transverse Reynolds shear stresses (Equ 21 A5) which act to dissipate vorticity (Einstein & Li 1958; Nezu & Nakagawa 1993). These arguments imply viscous dissipation of vorticity (Equ

21 A2) is negligible away from the channel boundary. For straight river reaches or flumes with uniform flow, the vortex stretching/tilting term (Equ 21 A3) diminishes and streamwise gradients are identically zero such that the vorticity change due to non-uniformity (Equ 21 A6) disappears. That is to say, there is a balance between vorticity fed between the streamwise velocity and secondary currents, and the energy dissipated by secondary circulation. In the case of nonuniform flow, the assumptions that A2, A3 and A6 in Equation (21) are zero are no longer valid. Therefore, a number of open questions arise in terms of the production and redistribution of vorticity that lead to secondary currents via vortex stretching and non-uniformities in all directions.

As a second method to understand secondary currents and their relationship to macroturbulence, the mean kinetic energy equation for decelerating flow shows that turbulence production from the expansion velocity offers the potential to transfer mean flow energy into turbulent energy (Nikora & Roy 2012). The mean kinetic energy equation for the primary flow and for the secondary flow is given in Equation (22) and Equation (23), respectively as

$$\frac{d}{dt}\left(\frac{U^2}{2}\right)+U\frac{d}{dx}\left(\frac{U^2}{2}\right)+V\frac{d}{dy}\left(\frac{U^2}{2}\right)+W\frac{d}{dz}\left(\frac{U^2}{2}\right)=gU-\overbrace{\frac{U}{\rho}\left(\frac{dP}{dx}\right)}^{A1}$$
$$-\overbrace{\frac{dU\overline{u'u'}}{dx}+\frac{dU\overline{u'v'}}{dy}+\frac{dU\overline{u'w'}}{dz}}^{A2}+\overbrace{\overline{u'u'}\frac{dU}{dx}+\overline{u'v'}\frac{dU}{dy}+\overline{u'w'}\frac{dU}{dz}}^{A3} \tag{22}$$
$$+\overbrace{\nu\frac{d}{dx}\left(\frac{d}{dx}\frac{U^2}{2}\right)+\nu\frac{d}{dy}\left(\frac{d}{dy}\frac{U^2}{2}\right)+\nu\frac{d}{dz}\left(\frac{d}{dz}\frac{U^2}{2}\right)}^{A4}+\overbrace{\nu\left(\frac{dU}{dx}\right)^2+\nu\left(\frac{dU}{dy}\right)^2+\nu\left(\frac{dU}{dz}\right)^2}^{A5}$$

$$\frac{d}{dt}\left(\frac{V^2+W^2}{2}\right)+U\frac{d}{dx}\left(\frac{V^2+W^2}{2}\right)+V\frac{d}{dy}\left(\frac{V^2+W^2}{2}\right)+W\frac{d}{dz}\left(\frac{V^2+W^2}{2}\right)+W\frac{d}{dz}\left(\frac{U^2}{2}\right)$$
$$=-\overbrace{\left(\frac{V}{\rho}\left(\frac{dP}{dy}\right)+\frac{W}{\rho}\left(\frac{dP}{dz}\right)\right)}^{A1}-\overbrace{\frac{dV\overline{v'u'}}{dx}+\frac{dV\overline{v'v'}}{dy}+\frac{dV\overline{v'w'}}{dz}+\frac{dW\overline{w'u'}}{dx}+\frac{dW\overline{w'v'}}{dy}+\frac{dW\overline{w'w'}}{dz}}^{A2}$$
$$+\overbrace{\overline{u'v'}\frac{dV}{dx}+\overline{v'v'}\frac{dV}{dy}+\overline{v'w'}\frac{dV}{dz}+\overline{u'w'}\frac{dW}{dx}+\overline{w'v'}\frac{dW}{dy}+\overline{w'w'}\frac{dW}{dz}}^{A3} \tag{23}$$
$$+\overbrace{\nu\frac{d}{dx}\left(\frac{d}{dx}\frac{V^2}{2}\right)+\nu\frac{d}{dy}\left(\frac{d}{dy}\frac{V^2}{2}\right)+\nu\frac{d}{dz}\left(\frac{d}{dz}\frac{V^2}{2}\right)+\nu\frac{d}{dx}\left(\frac{d}{dx}\frac{W^2}{2}\right)+\nu\frac{d}{dy}\left(\frac{d}{dy}\frac{W^2}{2}\right)+\nu\frac{d}{dz}\left(\frac{d}{dz}\frac{W^2}{2}\right)}^{A4}$$

$$+\overbrace{\nu\left(\frac{dV}{dx}\right)^2+\nu\left(\frac{dV}{dy}\right)^2+\nu\left(\frac{dV}{dz}\right)^2+\nu\left(\frac{dV}{dx}\right)^2+\nu\left(\frac{dV}{dy}\right)^2+\nu\left(\frac{dV}{dz}\right)^2}^{A5}$$

The external energy source which supplies mean flow and subsequently turbulence is the gravitational term g*U* and the pressure gradient term A1. The A2 terms in Equation 22 and 23 represent the transport of mean flow energy by turbulence. The A2 terms of Equation 23 are likely responsible for the transfer of energy between secondary flow components in uniform flow as they are active only when secondary currents are present. The A2 terms of Equation 23 in nonuniform flow provide a mechanism for the expansion velocity to produce secondary flows through the transfer turbulent energy. The A3 terms in Equations 22 and 23 represent the coupling of turbulence and mean flow energy. The A3 terms include the traditional term responsible for the production of turbulence from the primary flow component in uniform flows. The A3 terms show turbulence feeds on the gradient of expansion velocity to produce secondary currents and are likely significant in nonuniform flow. Time averaged quantities in Equations 22 and 23 preclude direct determination of the source of secondary currents in nonuniform flows it appears that the expansion velocity is responsible for a portion of the secondary flow production and transfer of turbulent energy.

The source of secondary circulation associated with secondary currents has long been believed to originate at the wall where vertical and transverse derivatives of Reynolds stress are non-negligible (Einstein & Li 1958; Nezu & Nakagawa 1993; Yang 2009). However, in wide channels with water worked beds the strongest secondary currents may occur as a pair of counter-rotating cells found along the channel centerline (McLelland, 2013). This work by McLelland (2013) with experiments for narrow, intermediate, and wide channels with mobile beds with patterns of secondary current development tend to suggest mechanisms for the generation of secondary currents other than corner vortices such as relatively rougher zone produced by secondary currents reworking bed topography. In the case of the nonuniform flow, we show that it is highly likely that the expansion velocity further feeds mean energy directly into macroturbulence that is manifested in the time average sense as secondary circulations. Also, as the flow depth increases in decelerating flow, additional shearing surface at the

channel boundary becomes available to produce turbulence. The vorticity equation indicates compression of the streamwise vortex occurs as flow decelerates (Equ 21 A3) causing the vortex to expand to scale with the flow depth as is typically observed of stabilized macroturbulence, at least for narrow and wide channels. The lateral expansion of the vortex would act to stabilize the macroturbulent features as aspect ratio decreases. The vertical and transverse expansion of streamwise vorticity due to the streamwise compression will aid the production of strain $\overline{u'w'}$ which acts to dissipate vorticity. Modified 3-dimensional quadrant analysis in rapidly decelerating flows has shown that away from the channel centerline ejections become more oriented toward the channel center and sweeps are angled toward the sidewall (MacVicar & Rennie 2012). Our results show that at the channel center line the bursting angle becomes more aligned with the wall normal direction. Combined, these results may indicate the macroturbulence becomes better oriented to produce secondary velocities in decelerating flow.

The production of additional strain is indicated by the bursting angles, away from the channel centerline, becoming oriented toward the channel sidewall, and at the channel centerline V' enhancement causes the bursting angle to become oriented in the bed normal direction. The effects of flow deceleration on macroturbulence is 1) additional turbulence production by the expansion velocity 2) increased shear surface to produce turbulence 3) stream wise compression of streamwise oriented vorticity leading to lateral stabilization and increased dissipation of turbulence by shearing (Equ21 A6). These competing influences on strength and stabilization of macroturbulence make inferences on secondary currents for these flow conditions unclear at this time, but provide the mechanisms that might impact the stabilization.

More quantitative analysis of the strength and stabilization of macroturbulence in decelerating flows will require spatial correlations that cannot be inferred by time averaging procedures. The time averaging procedures smear instantaneous streamlines of macroturbulent cells that are known to fluctuate considerably (Hutchins & Marusic 2007). It is not readily apparent using the time averaged equations of motion how vertical velocities typically less than 5% of the mean streamwise velocity are capable of producing the differences observed in turbulence statistics for decelerating flows. The structure of the turbulence field resolved for consecutive instances in time should provide

a better description of the cause and effect relationship between bursting, macroturbulence, and energy transfers in relation to decelerating open channel flows.

To further illustrate the possibility of macroturbulence stabilization into depth scale structures identifiable in the time average velocity signature. The vertical velocity component resulting from the combined effects of flow expansion and macroturbulence stabilization is estimated as the linear summation of each induced component. The vertical velocity induced by secondary currents for a straight uniform channel is given as

$$\frac{V}{U_*} = -\frac{6A_b}{\kappa\pi^2} cos\left(\pi\frac{z}{H}\right)\left(\left(2\frac{y}{H}-1\right)cos\left(\pi\frac{y}{H}\right)+1\right) \quad (24)$$

The expansion velocity is estimated using Equation (10) and velocity resulting from macroturblence stabilization is estimated using Equation (24). The linear combination of Equations 10 and 24 is shown as lines in Figure 11 with measured vertical velocities shown as point symbols. Equation (24) can be derived by invoking the constant eddy viscosity model to relate shear stress to mean velocity gradients and simplifying Equation (21) for straight uniform flow such that the production of vorticity from turbulence anisotropy is balanced by the shear stress dissipation of vorticity (Nezu & Nakagawa 1993). The constant eddy viscosity model and assumption of equal flow division across the channel produces a vertical velocity induced by secondary currents which is symmetrical in the vertical direction about the channel centerline. The nature of stabilized macroturbulence is more complex than the description provided by Equation (24) which predicts uniform secondary flow strength across the channel, however, the general form of the distribution is similar. For narrow channels secondary flow strength is known to decrease away from the wall while it remains relatively uniform in intermediate depth channels and the strongest secondary flows are found in the channel center of wide channels (McLelland, 2013). The pattern of secondary flow cannot be definitively ascertained by the centerline measurements shown in Figure (11). However, Figure (11) shows that vertical velocity persists in the decelerated flows through some combination of flow expansion and stabilized macroturbulence.

4.6 CONCLUSIONS

The study objective is to present the statistical distributions of velocity and describe the structure of turbulence in gradually varied decelerating open channel flow over a fully rough gravel bed with respect to bursting process and macroturbulence. The

positive streamwise gradient of flow depth represents a decrease in external energy supplied to the mean flow which subsequently reduces the energy supplied from mean primary flow into turbulence. Reduction in all time averaged statistical measures of turbulent energy occurs as energy supplied from the mean flow is decreased (see Figures 1,2). However reduction of turbulent energy is not evenly distributed across all components and certain measures of turbulence when scaled with bed shear stress become more energetic in decelerated flows. Time series analysis using spectra and triple decomposition show high frequency fluctuations diminish while macroturbulence persists in decelerated flow. The relative increase of energy associated with macroturbulence is confirmed by comparing the integral of spectra across the macroturbulence timescales with that of all energetic frequencies. Within the outer region of the decelerating flow, the vertical expansion velocity initially acts on the vertical velocity fluctuations to produce and transport turbulent energy, which

is subsequently redistributed into the streamwise and transverse velocity components *via* the macroturbulence.

The near bed bursting turbulence processes generated by shearing forces are not significantly affected by flow deceleration. Thus the frequency of ejection and sweep processes remains unchanged in decelerating flow. The effect of flow deceleration on bursting angle arises due to the combination of decreasing streamwise fluctuations and maintenance of vertical fluctuations through the expansion velocity. The interaction between the near bed bursting process and outer layer macroturbulence remains an open question even in uniform open channel flows.

The mechanisms responsible for the persistence of macroturbulence in these flows are considered. The two mechanisms considered for the persistence of macro scale turbulence were the streamwise advection of macro turbulence and turbulent production resulting from flow non uniformity. The advection hypothesis is consistent with the finding of Lacey & Roy (2007) where macro scale turbulence in the outer layer was found to persist despite abrupt localized changes in the near bed shedding possesses associated with an isolated pebble cluster. This theory is reminiscent of Taylors frozen hypothesis in that turbulence structures evolve on a timescale much larger than the advection time scale and localized effects from near bed turbulence on the advecting

macro turbulence will display a temporal or spatial lag. A lag in the reaction time of macro turbulence to the changing bursting process in gradually varied flow is likely to only partially explain the persistence of these structures under the flow conditions studied. The macro scale of turbulence is hypothesized to be closely linked to the bursting process (Shvidchenko & Pender 2001). Thus it should be expected that decreasing primary turbulent energy production near the bed should yield decreased energy across all turbulent scales if the dynamical influences evolve together. However the decreased primary production in decelerating flows is accompanied by transfer of mean streamwise flow energy into the wall normal velocity component due to fluid expansion.

4.7 ACKNOWLEDGEMENTS

We would like to thank all of the people who worked on this project including the both the graduate and undergraduate students. We acknowledge National Science Foundation project #0918856 and the University of Kentucky, Department of Civil Engineering for financial support of students. We would also like to thank the Kentucky NSF EPSCoR Research Scholar's Program for partial support of the graduate stipend.

4.8 LIST OF SYMBOLS

A_b = Amplitude factor for secondary currents

B = channel width

B/H = Aspect ratio

D_u = empirical coefficient for estimating streamwise turbulent intensity

D_v = empirical coefficient for estimating wall normal turbulent intensity

D_w = empirical coefficient for estimating transverse turbulent intensity

D_{50} = particle diameter for which 50% of particles are finer

D_{84} = particle diameter for which 84% of particles are finer

F = production of turbulent energy by the vertical velocity gradient

Fr = $U_m(gH)^{-1/2}$ is the Froude number

G = primary production of turbulent energy

H = Flow depth

H' = hole size used to separate strong motions from velocity fluctuations

K^+ = $k_s U_* \nu^{-1}$ is the shear Reynolds number

Re = $U_m H v^{-1}$ is the Reynolds number

S_u = streamwise velocity spectrum estimated using fast Fourier transform method

S_v = wall normal velocity spectrum estimated using fast Fourier transform method

S_w = transverse velocity spectrum estimated using fast Fourier transform method

T_B = $3\ H\ V^{-1}$ bursting period defined on outer variables

TKE = turbulent kinetic energy

T_s = moving average time-step used to isolate macroturbulence

U = Time averaged streamwise velocity component

U_{avg} = cross-sectional mean velocity

U' = root mean square of streamwise velocity fluctuations

U_* = Shear velocity

V = Time averaged wall normal velocity component

V_{mag} = magnitude of the time average velocity vector

V_{exp} = expansion velocity induced by flow nonuniformity

V' = root mean square of wall normal velocity fluctuations

W = Time averaged transverse velocity component

W' = root mean square of transverse velocity fluctuations

b = log-law constant of integration for hydraulically rough flows

k_s = equivalent roughness height

m = empirical coefficient used to fit power law to velocity distribution

u = instantaneous streamwise velocity component

u' = instantaneous fluctuating component of streamwise velocity

$\overline{u'v'}$ = primary Reynolds shear stress component

v = instantaneous wall normal velocity component

v' = instantaneous fluctuating component of wall normal velocity

w = instantaneous transverse velocity component

w' = instantaneous fluctuating component of transverse velocity

x = stream wise direction

y = wall normal direction

z = transverse direction

β = Clauser pressure gradient parameter $\beta = \frac{H}{U_*^2} g\left(-S_0 + \frac{\partial H}{\partial x}\right)$

Π = Coles wake strength

Ω_x = streamwise vorticity

Ω_y = vertical vorticity

Ω_z = transverse vorticity

κ = von Karman constant

ω = frequency

4.9 REFERENCES:

Adrian, R. J. (2007). Hairpin vortex organization in wall turbulencea). *Physics of Fluids (1994-present)*, *19*(4), 041301.

Adrian, R. J., Meinhart, C. D., and Tomkins, C. D. (2000). "Vortex organization in the outer region of the turbulent boundary layer." Journal of Fluid Mechanics, 422: 1–54.

Adrian, R. J., & Marusic, I. (2012). Coherent structures in flow over hydraulic engineering surfaces. *Journal of Hydraulic Research*, *50*(5), 451-464.

Afzalimehr, H., & Anctil, F. (1999). Velocity distribution and shear velocity behaviour of decelerating flows over a gravel bed. *Canadian Journal of Civil Engineering*, *26*(4), 468-475.

Afzalimehr, H., & Rennie, C. D. (2009). Determination of bed shear stress in gravel-bed rivers using boundary-layer parameters. *Hydrological sciences journal*, *54*(1), 147-159.

Afzalimehr, H. (2010). Effect of non-uniformity of flow on velocity and turbulence intensities over a cobble-bed. *Hydrological processes*, *24*(3), 331-341.

Afzalimehr, H., Najafabadi, E. F., & Gallichand, J. (2012). Effects of accelerating and decelerating flows in a channel with vegetated banks and gravel bed. *International Journal of Sediment Research*, *27*(2), 188-200.

Albayrak, I., & Lemmin, U. (2011). Secondary currents and corresponding surface velocity patterns in a turbulent open-channel flow over a rough bed. *Journal of Hydraulic Engineering*, *137*(11), 1318-1334.

Belcher, B. (2009). “Vortex model of open channel flows with gravel beds.” Electronic dissertation, Univ. of Kentucky, Lexington, KY.

Belcher, B., and Fox, J. 2009 (Discussion). Rodriguez, J.F., and Garcia, M.H., 2008, Rodriguez, J. F., and Garcia, M. H. (2008). Laboratory measurements of 3-D flow patterns and turbulence in straight open channel with rough bed. J. Hydraul. Res., 46(4): 454–465, J.Hydraul. Res., 47(5):685-688.

Blanckaert, K., Duarte, A., & Schleiss, A. J. (2010). Influence of shallowness, bank inclination and bank roughness on the variability of flow patterns and boundary shear stress due to secondary currents in straight open-channels. *Advances in Water Resources*, *33*(9), 1062-1074.

Boppe, R. S., and W. L. Neu, (1995). Quasi-coherent structures in the marine atmospheric surface layer. J.Geophys Res., 100 (C10): 20 635–20 648

Buffin-Bélanger, T., & Roy, A. G. (1998). Effects of a pebble cluster on the turbulent structure of a depth-limited flow in a gravel-bed river. *Geomorphology*, *25*(3), 249-267.

Cao, Z. 1997. Turbulent bursting based sediment entrainment function. *J. Hyd. Engr* 123(3):233-236

Carollo, F. G., Ferro, V., & Termini, D. (2005). Analyzing turbulence intensity in gravel bed channels. *Journal of Hydraulic Engineering*, *131*(12), 1050-1061.

Church, M., Biron, P., & Roy, A. (Eds.). (2012). *Gravel Bed Rivers: Processes, Tools, Environments*. John Wiley & Sons.

Coles, D. (1956). The law of the wake in the turbulent boundary layer. *Journal of Fluid Mechanics*, *1*(02), 191-226.

Dancey, C. L. (1990). Measurements of second order turbulence statistics in an axial flow compressor via 3-component LDA. AIAA J., 90: 2017.

Duncan, W.J. (1970). Mechanics of fluids. Elsevier, New York.

Einstein, H. A., & Li, H. (1958). Secondary currents of turbulent flow over smoot and rough boundaries. *Transactions of the American Society of Civil Engineers*, *39*(1), 1085-1088

Emadzadeh, A., Chiew, Y. M., & Afzalimehr, H. (2010). Effect of accelerating and decelerating flows on incipient motion in sand bed streams. *Advances in Water*

Resources, *33*(9), 1094-1104.

Fox, J.F. and Belcher, B.J. (2011). Comparison of macroturbulence measured using decomposition of PIV, ADV and LSPIV data. Journal of Hydraulic Research, 49(1): 122-126.

Fox, J. F., Papanicolaou, A. N., and Kjos, L. (2005). Eddy taxonomy methodology around a submerged barb obstacle within a fixed rough bed. Journal of Engineering Mechanics, 131: 1082–1101.

Fox, J.F., and Patrick, A. (2008). Large-scale eddies measured with large scale particle image velocimetry. Flow Measurement and Instrumentation 19: 283–291

Guo, J., Julien, P. Y., & Meroney, R. N. (2005). Modified log-wake law for zero-pressure-gradient turbulent boundary layers. *Journal of Hydraulic Research*, *43*(4), 421-430.

Harun, Z., Monty, J. P., Mathis, R., & Marusic, I. (2013). Pressure gradient effects on the large-scale structure of turbulent boundary layers. *Journal of Fluid Mechanics*, *715*, 477-498.

Hauer, F.R., and Lamberti, G.A. (2006), Methods in stream ecology. Amsterdam, The Netherlands: Academic press

Hurther, D., Lemmin, U., and Terray, E. A. (2007). Turbulent transport in the outer region of rough-wall open-channel flows: The contribution of large coherent shear stress structures (LC3S). J. Fluid Mech., 574: 465–493.

Hussain, A. K., and Reynolds, W. (1972). The mechanics of an organized wave in turbulent shear flow. Journal of Engineering Mechanics, 54: 241–261.

Hutchins, N., & Marusic, I. (2007). Large-scale influences in near-wall turbulence. *Philosophical Transactions of the Royal Society A: Mathematical, Physical and Engineering Sciences*, *365*(1852), 647-664.

Kironoto, B. A., & Graf, W. H. (1995). Turbulence characteristics in rough non-uniform open-channel flow. *Proceedings of the ICE-Water Maritime and Energy*, *112*(4), 336-348.

Kline, S. J., Reynolds, W. C., Schraub, F. A., & Runstadler, P. W. (1967). The structure of turbulent boundary layers. *Journal of Fluid Mechanics*, *30*(04), 741-773.

Lacey. R.W.J., and Roy, A.G. (2008). Fine-Scale Characterization of the Turbulent Shear

Layer of an Instream Pebble Cluster. Journal of Hydraulic Engineering 134(7): 925-936

Lee, J. H., & Sung, H. J. (2008). Effects of an adverse pressure gradient on a turbulent boundary layer. *International Journal of Heat and Fluid Flow*, *29*(3), 568-578.

Lelouvetel, J., F. Bigillon, D. Doppler, I. Vinkovic, and J.-Y. Champagne (2009), Experimental investigation of ejections and sweeps involved in particle suspension, Water Resour. Res., 45, W02416, doi:10.1029/2007WR006520.

Papanicolaou, A. N., & Hilldale, R. (2002). Turbulence characteristics in gradual channel transition. *Journal of engineering mechanics*, *128*(9), 948-960.

MacVicar, B. J., & Rennie, C. D. (2012). Flow and turbulence redistribution in a straight artificial pool. *Water Resources Research*, *48*(2).

Marusic, I., McKeon, B. J., Monkewitz, P. A., Nagib, H. M., Smits, A. J., & Sreenivasan, K. R. (2010). Wall-bounded turbulent flows at high Reynolds numbers: Recent advances and key issues. *Physics of Fluids (1994-present)*, *22*(6), 065103.

McLelland, S., A., (2013). Coherent Secondary flows over water-worked rough bed in a straight channel. *Coherent Flow Structures at Earth's Surface*, 275-288

Nezu, I. (2005). Open-Channel Flow Turbulence and Its Research Prospect in the 21st Century. Journal of Hydraulic Engineering:229-246

Nezu, I., Kadota, A., Nakagawa, H. (1994), Turbulent structures in accelerating and decelerating open-channel flows with laser Doppler anemometer. 9th Cong. of APD-IAHR, Singapore, Vol. 1, 413–420.

Nezu, I., and Nakagawa, H. (1993). Turbulence in open channel flows, A. A. Balkema, Rotterdam, The Netherlands.

Nikora, V., & Roy, A. G. (2012). Secondary flows in rivers: Theoretical framework, recent advances, and current challenges. *Gravel Bed Rivers: Processes, Tools, Environments*, 3-22.

Onitsuka, K., Akayama, J., and Matsuoka, S. (2009), Prediction of velocity profiles and Reynolds stress distributions in turbulent open-channel flows with adverse pressure gradient, Journal of Hydraulic Research, 47(1):58-65

Rodriquez, J.F., and Garcia, M.H. (2008). Laboratory measurements of 3-D flow patterns and turbulence in straight open channel with rough bed. Journal of Hydraulic Research

46(4): 454-465

Roy, A. G., Buffin-Bélanger, T., Lamarre, H., and Kirkbride, A. D. (2004). Size, shape and dynamics of large-scale turbulent flow structures in a gravel-bed river. Journal of Fluid Mechanics, 500: 1–27.

Schoppa, W., & Hussain, F. (2002). Coherent structure generation in near-wall turbulence. *Journal of fluid Mechanics*, *453*, 57-108.

Shvidchenko, A. B., and Pender, G. (2001). "Macroturbulent structure of open-channel flow over gravel beds." *Water Resour. Res.*, 37(3), 709–719.

Singh, A., Porté-Agel, F. and Foufoula-Georgiou, E. (2010) On the influence of gravel bed dynamics on velocity power spectra. Water Resources Research, 46, W04509.

Song, T., and Graf, W.H. (1994), Non-uniform open-channel flow over a rough bed. Journal of Hyroscience and Hydraulic Engineering, 12(1): 1-25

Song, T., and Chiew, Y.M. (2001). Turbulence measurement in nonuniform open-channel flow using acoustic Doppler velocimeter (ADV). Journal of Engineering Mechanics, 127(3): 219-232

Stone, M. C., & Hotchkiss, R. H. (2007). Turbulence descriptions in two cobble-bed river reaches. *Journal of Hydraulic Engineering*, *133*(12), 1367-1378.

Sukhodolov, A. N., Nikora, V. I., & Katolikov, V. M. (2011). Flow dynamics in alluvial channels: the legacy of Kirill V. Grishanin. *Journal of Hydraulic Research*, *49*(3), 285-292.

Tamburrino, A., & Gulliver, J. S. (2007). Free-surface visualization of streamwise vortices in a channel flow. *Water Resources Research*, *43*(11).

Townsend AA. (1976). *The Structure of Turbulent Shear Flow*. Cambridge: Cambridge Univ. Press

Venditti, J. G., and S. J. Bennett (2000), Spectral analysis of turbulent flow and suspended sediment transport over dunes, J. Geophys. Res., 105: 22,035– 22,047.

Venditti, J. G., & Bauer, B. O. (2005). Turbulent flow over a dune: Green River, Colorado. *Earth Surface Processes and Landforms*, *30*(3), 289-304.

Venditti, J. G., Hardy, R. J., Church, M., & Best, J. L. (2013). What is a Coherent Flow Structure in Geophysical Flow?. *Coherent Flow Structures at Earth's Surface*, 1-16.

Wahl TL. (2000). Analyzing ADV data using WinADV. *Proceedings Joint Conference*

on Water Resources Engineering and Water Resources Planning and Management, American Society of Civil Engineers, Minneapolis, 30 July–2 August. www.usbr.gov/wrrl/twahl/winadv.

Willmarth, W. W., & Lu, S. S. (1972). Structure of the Reynolds stress near the wall. *Journal of Fluid Mechanics*, *55*(01), 65-92.

Yang, S. Q., & Chow, A. T. (2008). Turbulence structures in non-uniform flows. *Advances in Water resources*, *31*(10), 1344-1351.

Yang, S. Q. (2009). Mechanism for initiating secondary currents in channel flows. *Canadian Journal of Civil Engineering*, 36(9), 1506-1516.

Yang, S. Q., Xu, W. L., & Yu, G. L. (2006). Velocity distribution in a gradually accelerating free surface flow. *Advances in water resources*, *29*(12), 1969-1980.

4.10 TABLES AND FIGURES

Table 4.1. Hydraulic conditions for the experimental tests. Note that *dH/dx* is that which was calculated with St. Venant equation.

Run	k_s^+	H (cm)	B/D	H/D_{84}	U_{avg} (cm s^{-1})	Re	Fr	dH/dx	β	U^* (cm s^{-1})
1	319	13.3	4.6	24	60	8.0E+04	0.60	0.0062	0.11	4.6
2	296	13.7	4.5	24	58	8.0E+04	0.59	0.0064	0.22	4.65
3	306	13.9	4.4	25	59	8.2E+04	0.59	0.0064	0.26	4.5
4	288	14.3	4.3	26	57	8.2E+04	0.58	0.0066	0.44	4.25
5	294	14.5	4.2	26	53	7.7E+04	0.58	0.0066	0.47	4.25
6	416	10.4	5.9	19	71	7.4E+04	0.74	0.0045	-0.43	5.85
7	377	10.9	5.6	19	67	7.3E+04	0.71	0.0049	-0.38	5.5
8	375	11.2	5.4	20	67	7.5E+04	0.65	0.0052	-0.32	5.3
9	367	11.6	5.3	21	66	7.6E+04	0.64	0.0055	-0.19	5.26
10	354	11.7	5.2	21	64	7.5E+04	0.62	0.0058	-0.10	5.25
11	436	9.5	6.4	17	71	6.8E+04	0.81	0.0025	-0.87	6.15
12	414	10	6.1	18	70	7.0E+04	0.78	0.0038	-0.59	6
13	415	10.1	6.0	18	69	7.0E+04	0.77	0.0043	-0.49	5.9

Figure 4.1. Statistical measures of velocity that conform to bed shear velocity **a** and **b** streamwise velocity component normalized by bed shear velocity and shown in dimensional form. **c** and **d** root mean square of streamwise velocity component *U'* normalized by bed shear velocity and shown in dimensional form. **e** and **f** primary component of Reynolds shear stress $-\overline{u'v'}$ normalized by squared shear velocity and shown in dimensional form.

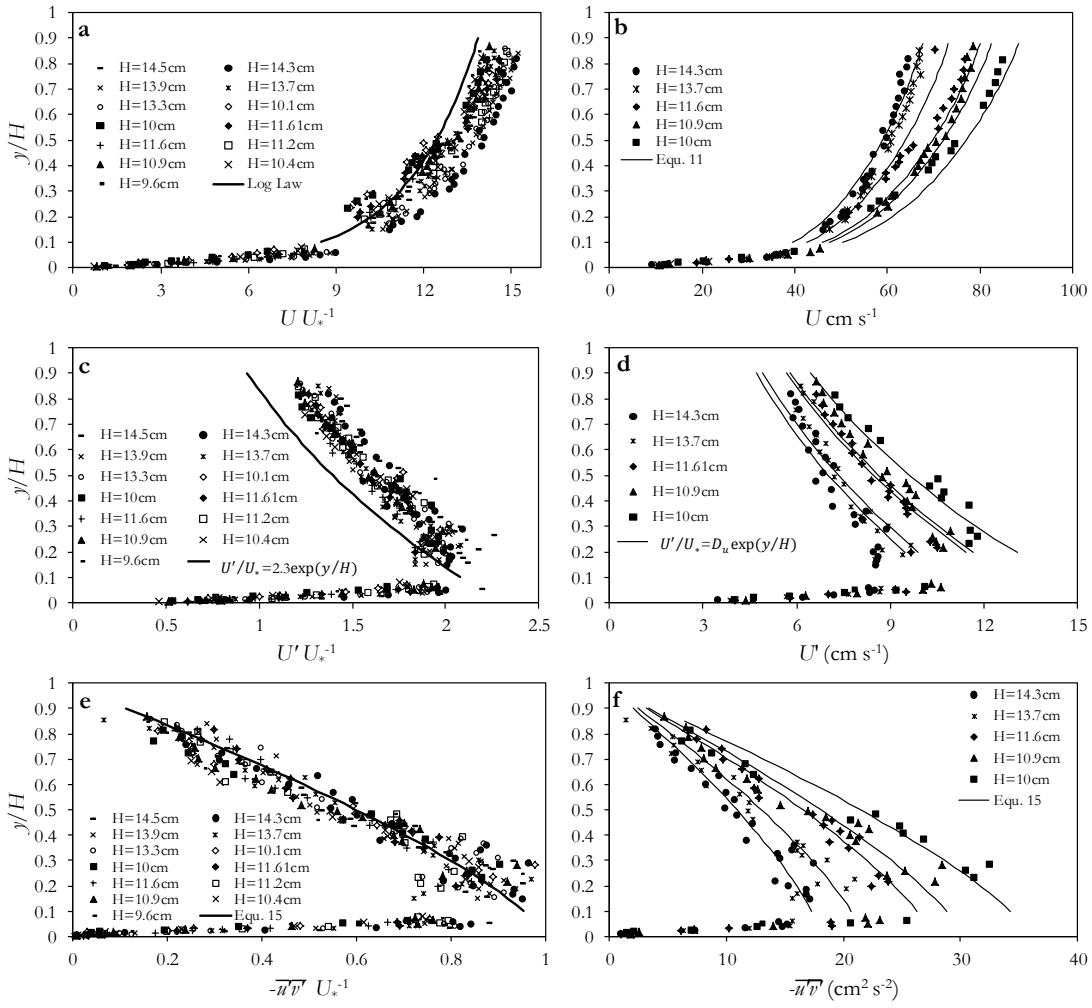

Figure 4.2. Turbulence quantities resilient to APG **a** and **b** root mean square of vertical velocity component *V'* normalized by bed shear velocity and shown in dimensional form. **c** and **d** root mean square of transverse velocity component *W'* normalized by bed shear velocity and shown in dimensional form. **e** and **f** anisotropy of turbulence in the vertical and transverse directions normalized by bed shear velocity and shown in dimensional form.

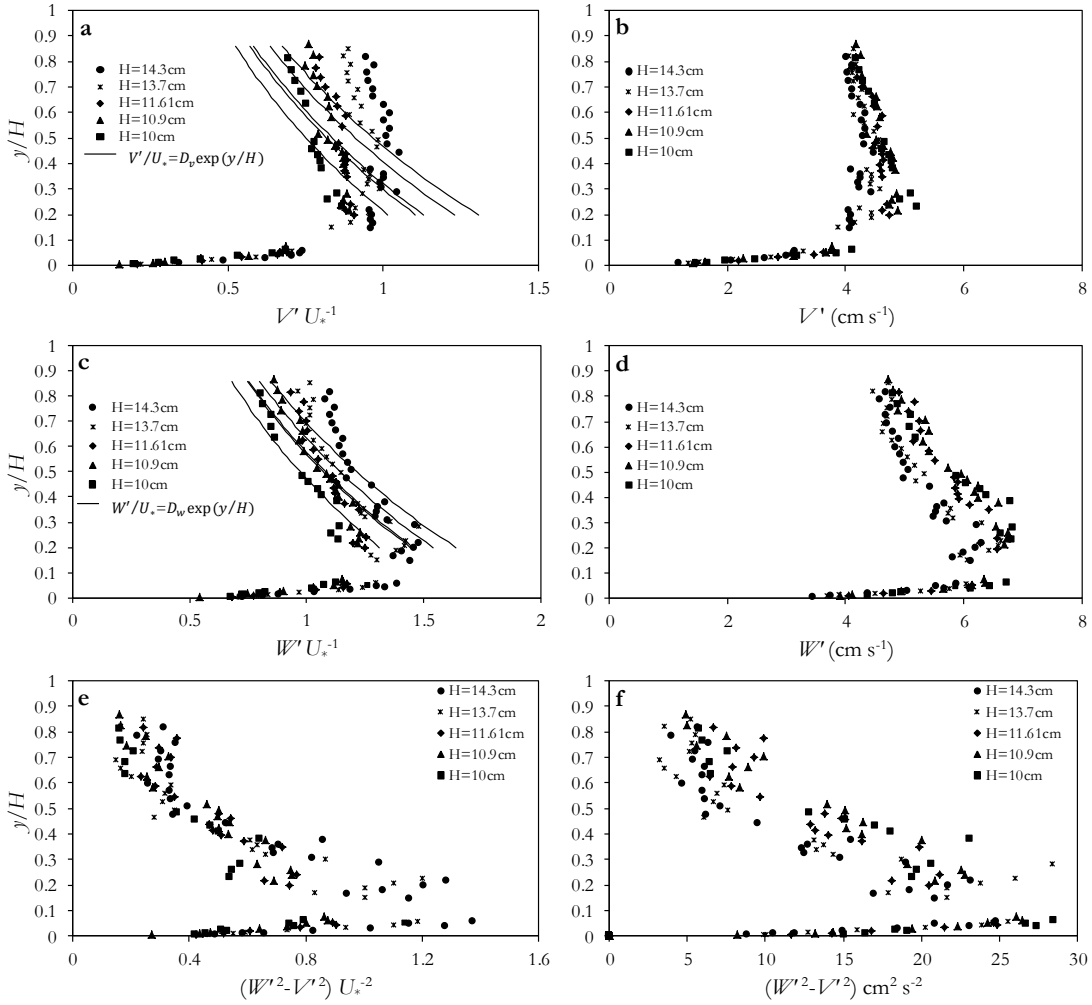

Figure 4.3 The distribution of turbulent intensity coefficients as a function of the Clauser pressure gradient parameter alongside coefficients determined using the equations given by Song & Chiew 2001.

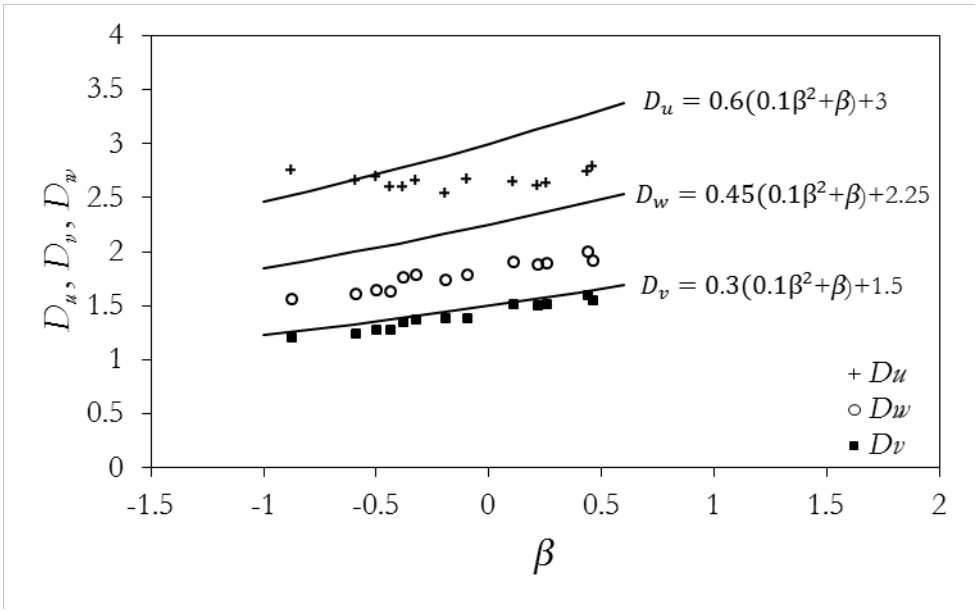

Figure 4.4. Quadrant analysis with hole size H=2 for selected velocity profiles. **a** and **b** angles relative to the bed of ejections and sweeps respectively . **c** and **d** depicts the frequency of ejections and sweeps respectively.

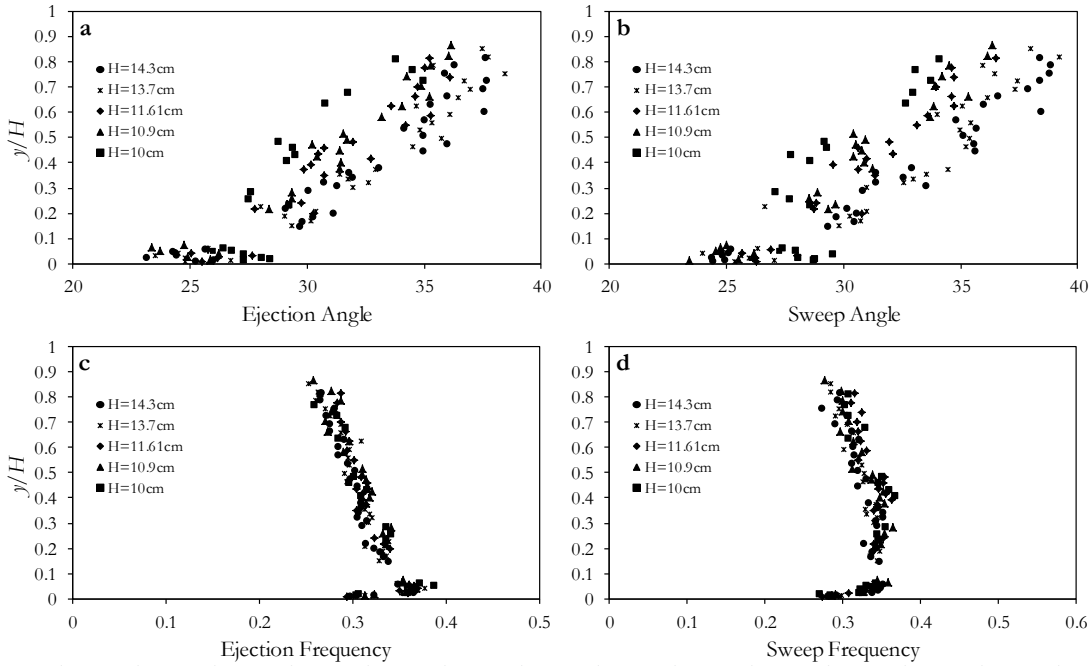

Figure 4.5 Spectral analysis of selected streamwise velocity in variance preserving form normalized by variance. Flow depth and normalized measuring location shown in the upper left corner.

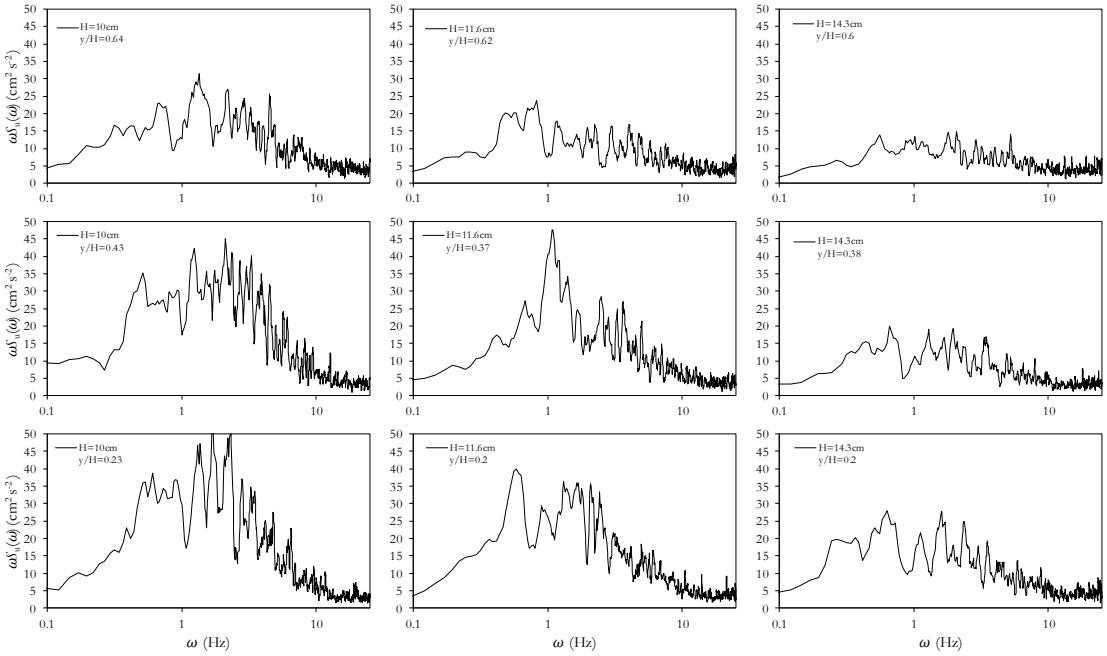

Figure 4.6 Spectral analysis of selected wall normal velocity in variance preserving form. Flow depth and normalized measuring location shown in the upper left corner.

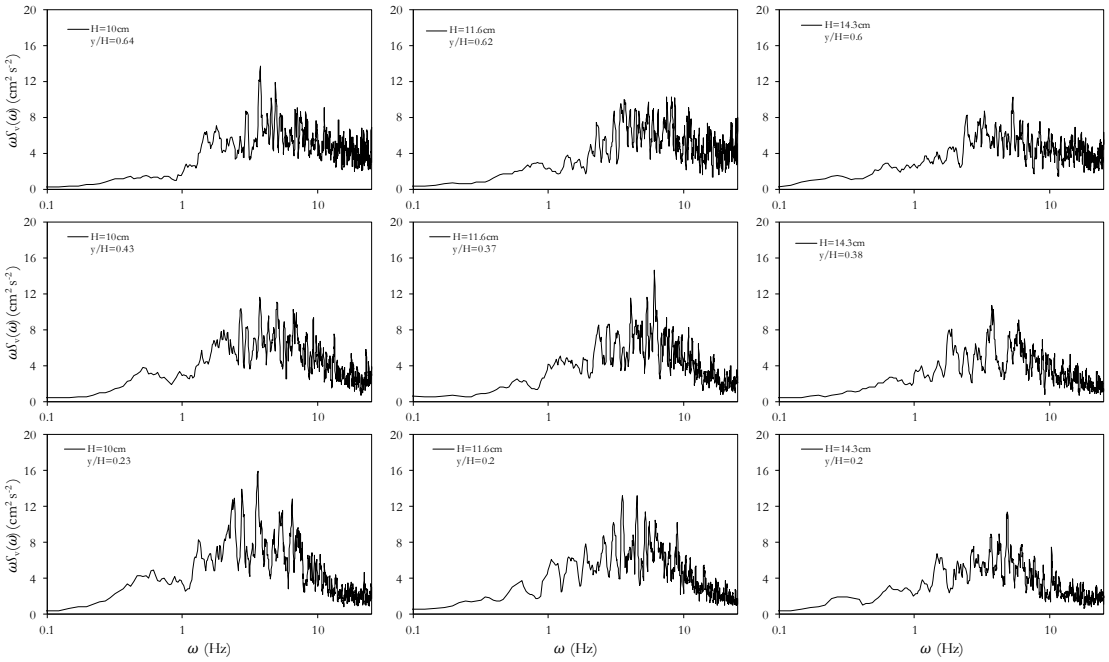

Figure 4.7 Spectral analysis of selected transverse velocity in variance preserving form. Flow depth and normalized measuring location shown in the upper left corner.

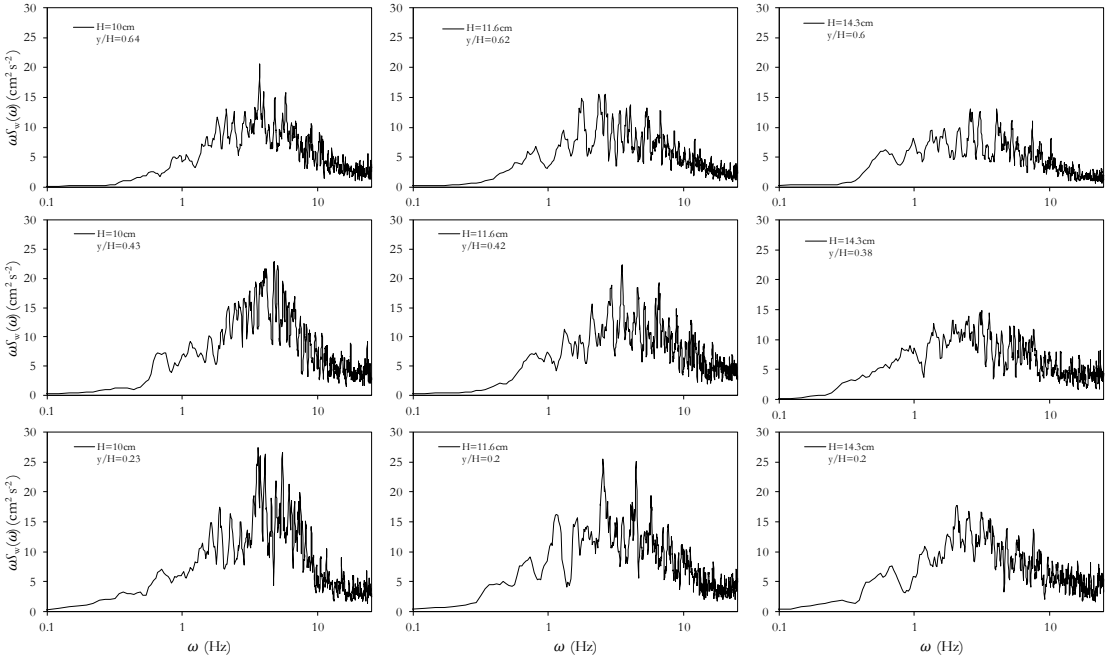

Figure 4.8. Integral of velocity power spectral densities showing energy between 0.1-1Hz . **a** and **b** energy associated with streamwise macro turbulence normalized by the total energy between 0.1-10 Hz **c** and **d** energy associated with wall normal macro turbulence normalized by the total energy between 0.1-10 Hz **e** and **f** energy associated with wall normal macro turbulence normalized by the total energy between 0.1-10 Hz

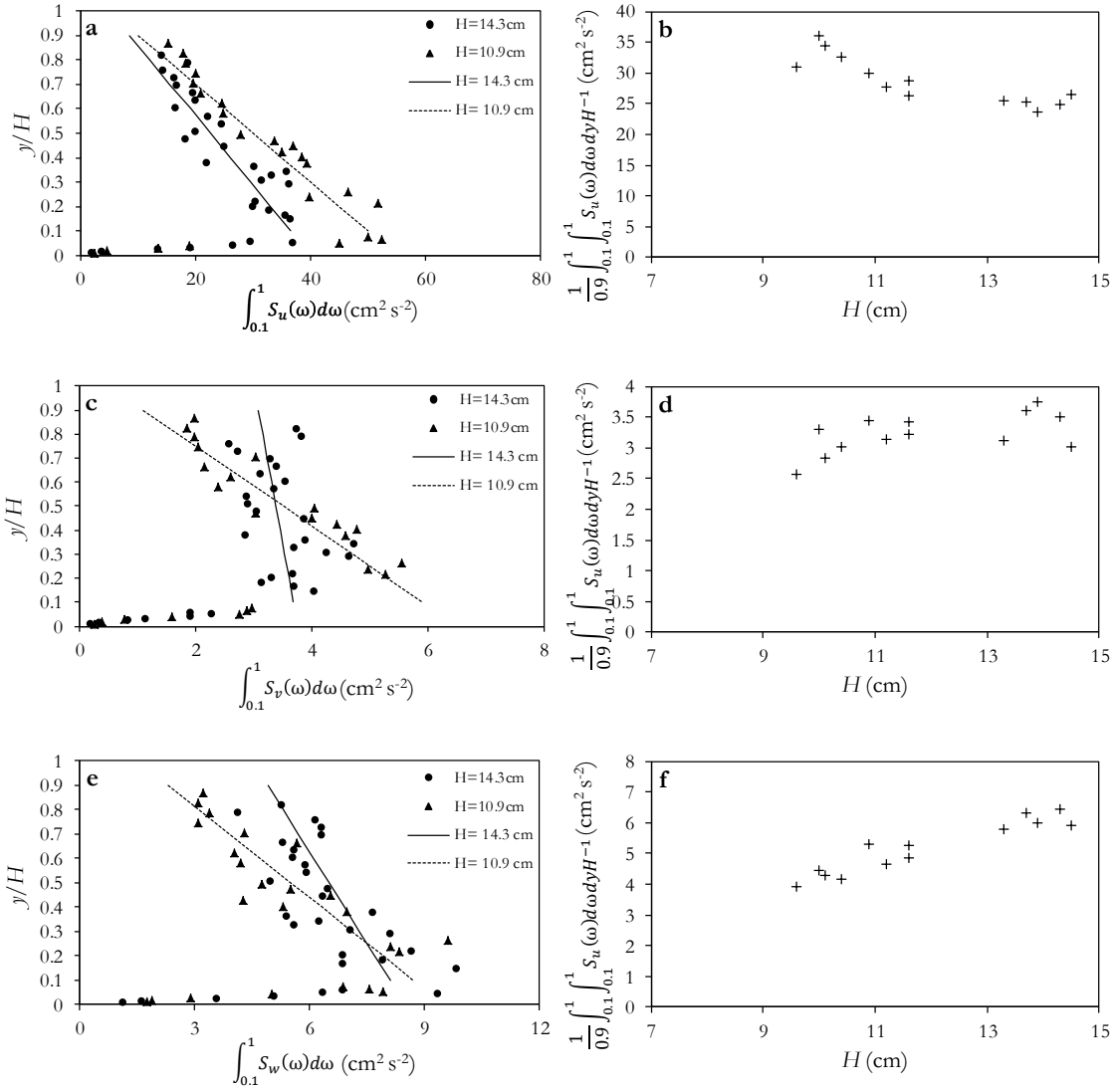

Figure 4.9. The slow fluctuating stream wise velocity component isolated with T_s equal to 0.2 s.

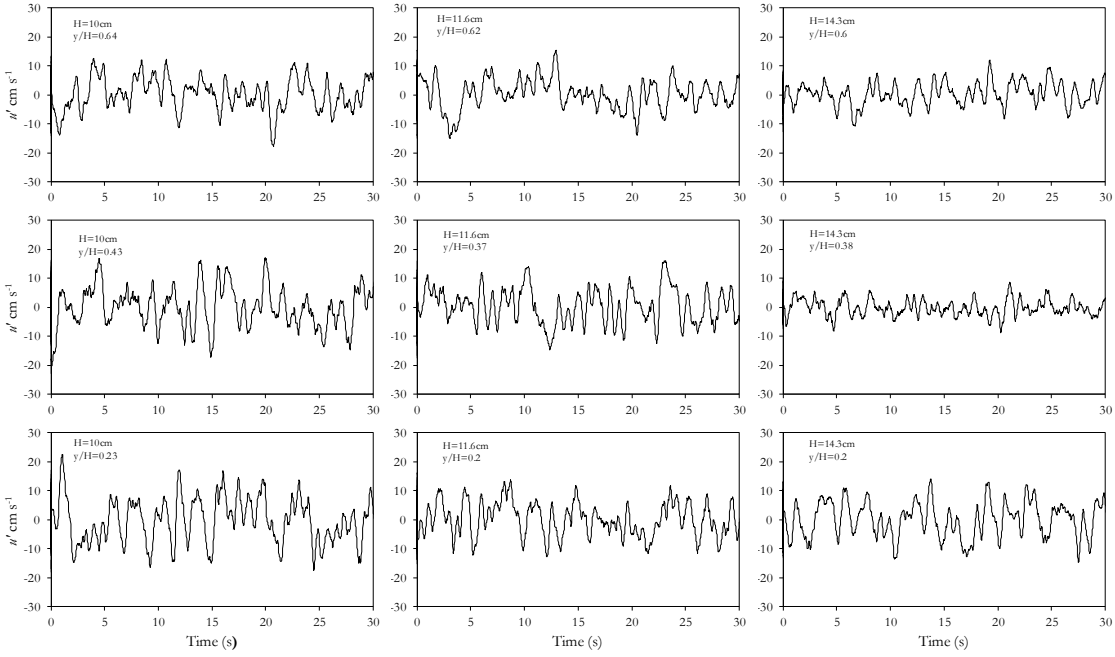

Figure 4.10. Turbulent energy production **a** from vertical velocity solid symbols are from measured data, open symbols are calculated using the theoretical expansion velocity **b** turbulent energy production in the streamwise direction

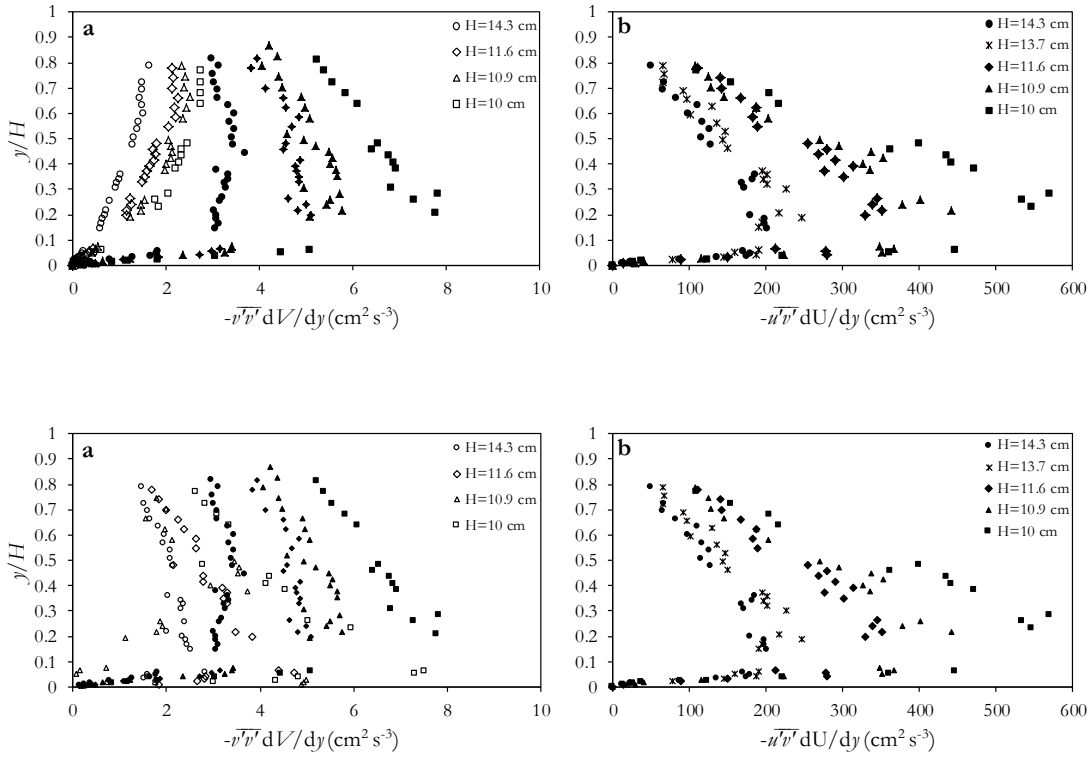

Figure 4.11. Measured vertical velocity and vertical velocity predicted by superimposing velocity induced by secondary currents onto the expansion velocity.

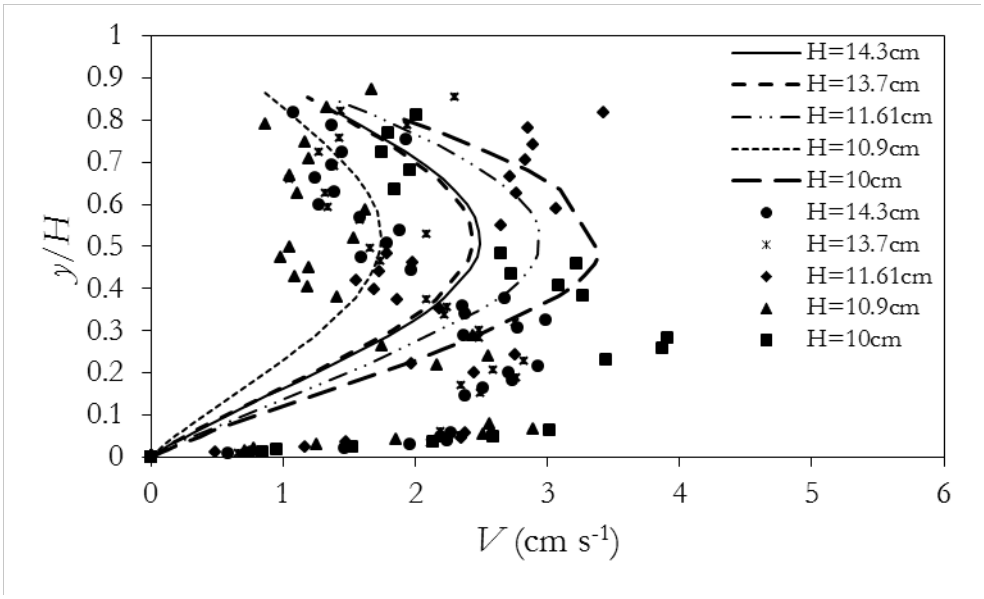

Chapter 5: Time-Average Velocity and Turbulence Measurement Using Wireless Bend Sensors in Open Channel with Rough Bed

Text extract with permission from Stewart, R. L., Fox, J. F., and Harnett, C. K. (2013) Time-Average Velocity and Turbulence Measurement Using Wireless Bend Sensors in Open Channel with Rough Bed, *Journal of Hydraulic Engineering* ASCE, 139(7): 696-706.

5.1 SUMMARY

This paper is motivated by the need to develop low cost, wireless velocity sensors for hydraulic research and application in streams. Velocity bend sensors (VBSs) are a flexible plastic polyimide substrate sheet with an electronic resistor connected to a voltage divider. Drag of a moving fluid bends the sensor, changes the electronic resistance, and produces a voltage drop that can be related to the time-average freestream velocity of the fluid. VBS were tested in a recirculating hydraulic flume with a gravel bed. The VBS show transition from rigid to elastic bending with increasing freestream velocity, which can be described using dimensionless fluid and beam bending properties. The relationship between stream velocity and voltage drop across the circuit is nonlinear. A semi-theoretical approach to estimate time-average streamwise velocity from the voltage drop based on fluid drag, elastic member bending, and circuit principles is applied and shows good agreement with experimentally derived calibration curves. The Triple Decomposition Theorem and spectral analysis are performed on VBS and acoustic Doppler velocimeter (ADV) time-series. Results show that the VBS captures low frequency characteristics of macroturblence present within the turbulent open channel flow but is unable to measure smaller-scale characteristics of eddy shedding for these hydraulic conditions. Turbulent intensity calculated using VBS data is 12% of that from the ADV attributed to the lack of detection of shedding sized eddies. But, the linear fit between turbulent intensity from the VBS and ADV suggest that the VBS can be used as a proxy for more detailed turbulent measurements when applied in streams.

5.2 INTRODUCTION

The present research is motivated by the need to develop low cost, wireless velocity sensors for hydraulic measurements within highly-sensed stream monitoring networks. We place emphasis upon velocity sensor measurements of time-average velocity and turbulence in hydraulically rough open channel flow with a gravel bed, which are typical hydraulic conditions in streams. It is recognized that inexpensive sensors and sensor networks show promise for stream measurements such as mean velocity and turbulence parameters. Inexpensive sensor networks could potentially assist with measuring the mean velocity spatially in a cross-section for stage-discharge relationships, which would decrease the need for manual collected measurements under dangerous flooding conditions. Inexpensive, wireless sensors also show promise for measuring the mean flow and turbulence in pools and transition zones in streams in order that aquatic biologists can link hydraulic diversity with fish habitat conditions and functioning (Hauer and Lamberti, 2006). Further, spatially distributed sensors will be useful for verifying the hypothesized double-layer of turbulence in streams that includes connected vortex packets that eject from the bed and macroturbulence in the outer region (Duncan 1970; Adrian et al. 2000; Roy et al. 2004; Hurther et al. 2007; Fox and Belcher, 2011) as well as measure large three-dimensional eddies induced by channel bathymetry and large obstructions (Kwan, 1988; Fox et al., 2005; Nezu, 2005). Finally, as computational fluid dynamics modeling becomes more sophisticated and applied, sensor network measurements of the flow field could be used to calibrate model parameters (Maier et al 2010).

The existing need for inexpensive hydraulic sensors is met by recent advancement in electronics and sensing. Recent technological developments in the miniaturization of electronics and wireless communication have begun a revolution in Environmental Sensor Networks (Hart and Martinez, 2006; Yick et al., 2008; Rundel et al., 2009). Recent advancement in sensor network technology promotes inexpensive measurements of environmental parameters in space and time in order that fluxes operating at the process-scale can be integrated to the large scale (Hart and Martinez 2006; Horsburg etal 2010). New sensor technologies are focusing on wireless due to low cost, small size, low power requirements, and faster installation (Wang et al., 2006). Wireless sensors offer

researchers the ability to monitor remote or dangerous environments where many processes have rarely been studied due to their inaccessibility (Hart and Martinez, 2006). Field measurements with automated mobile wireless velocity sensors combined with georeferencing technology have the possibility to reduce errors and time delays associated with manual monitoring techniques (Vivoni and Camilli, 2003).

While it appears the need for inexpensive hydraulic sensors is fulfilled with new sensor network technology, very few studies have reported detailed investigations of applicable sensors. Mechanical meters such as the propeller meter have been widely used for some time but angular momentum of the propeller affects their ability to measure turbulence within sensor networks (Rehmel, 2007). For velocity and turbulence measurements in shallow streams the predominant instruments used are the acoustic Doppler velocimeter (ADV) and electromagnetic current meter (ECM) (Buffin-Belanger and Roy 2005). The ADV and ECM provide accurate measurements of velocity and turbulence but are relatively expensive for use within sensor networks. Mobile transmission technology is revolutionizing the way in which water velocity measurements are being transferred from the field, however, many of these measurements are still being obtained manually (Vivoni and Camilli 2003). Inexpensive, wireless, low power velocity sensors are needed that offers the possibility of taking measurements at temporal and spatial scales necessary for highly-sensed stream monitoring networks.

The objective of this research is to present, investigate and verify inexpensive wireless velocity sensors for hydraulic measurements. The newly developed velocity sensors are called velocity bend sensors (VBS) (Harnett et al., 2011). In the following paper, we provide a detailed study of VBSs and their ability to measure time-averaged velocity and turbulence characteristics of open channel flow with a rough bed typical of stream conditions where the VBS can be implemented. We provide the following in this paper: (1) Full description of the VBS mechanical, electrical and wireless transmission characteristics, and fabrication of the VBS from commercially available components. (2) Experimental Method to calibrate and verify the VBS for use in open channel flow with a rough bed is described. (3) Experimentally derived calibration curves are presented for the VBS that relate time-average stream velocity to sensor voltage, and the behavior of

the sensor in bending is related to dimensionless fluid and bending properties. A semi-theoretical approach based on fluid drag and elastic member bending is used to continuously estimate time-average stream velocity using VBS measurements. (4) The ability of the VBS to measure prominent turbulent scales and turbulence intensity of open channel flow over a rough bed is examined through the use of eddy decomposition *via* the triple decomposition theorem, spectral analysis and turbulence statistics.

5.3 VELOCITY BEND SENSORS

The newly developed wireless sensors are called velocity bend sensors (VBSs) due to their operating mechanism (see Figure 1a). Water velocity causes the sensor, which acts as a strain gage, to bend and change the electrical resistance of the sensor (Figure 1b). The basic circuit of the VBS is depicted in Figure 1a and consists of a voltage divider. A fixed (10 $k\Omega$) resistor is placed in series with a variable resistor (e.g., Flexpoint brand "Bend Sensor") and is powered by a 5 volt power source (Harnett et al 2011). The bend sensor has a base resistance of approximately 4 $k\Omega$ and increases up to 30 $k\Omega$ when deflected. The voltage drop across the bend sensor is measured and used as the calibration voltage. The VBS can be interfaced with an onboard A/D chip (e.g., the Maxim DS2450) which converts the analog voltage read to a digital format. Wireless communication with the VBS is made possible using a wireless sensor node (e.g., the Crossbow Technology TelosB) which is connected to the onboard A/D chip using the 1-wire protocol. Data can be collected on a PC or data storage hub from approximately 30 m away using a second node.

Fabrication of the VBS can be performed by purchasing commercially available parts from home improvement stores and an electronics supplier. Assembling the electronic components requires some basic knowledge of circuits and the capability to solder. The housing for electronic components is constructed from polyvinyl chloride to prevent the electronics from contacting water and provides a means to deploy the sensors in the stream. The 4-AA battery pack and the wireless node are housed in the top of the polyvinyl chloride housing which is above the free surface. Wires connect the sensors to the wireless node and are contained within the polyvinyl chloride housing. A more detailed description of the construction of the VBS can be found at http://salamandersensors.org/.

The VBS are designed to be deployed across a stream network to meet the needs of researchers for high temporal and spatial data resolution. The VBS have a low hardware cost of approximately $20 US per sensor. The low cost of the VBS allow deployment in large numbers and reduce the cost associated with lost or damaged sensors. The VBS were designed using components that have a small power demand, which allows VBS deployment for reasonable amounts of time using a self-contained battery power supply. The VBS battery life is a function of power demand per location and the frequency at which data is collected; but for reference VBS that samples once every 2 minutes can operate for at least a week in the field. The wireless communication capabilities provided by the wireless node enables multiple VBS to send data to a localized data storage unit which makes data retrieval from a stream network time efficient (Harnett et al., 2011). The wireless signal can also be relayed to a long-range communication device so that researchers can view data without ever physically going to the field. The quasi-real-time data provided by the wireless capabilities of the VBS allows researchers to remotely quality check the health of the sensor network.

5.4 EXPERIMENTAL METHOD

The Experimental Method was designed to test (i) time-average velocity and (ii) turbulence measurement capabilities of the VBS. A range of mean streamwise velocity conditions typical of a stream were sought after. To represent a wide range of conditions, two experimental apparatuses were used during testing, including a water tunnel and hydraulic flume. A total of 18 tests were performed. In Table 1, the test apparatus and hydraulic conditions are indicated. Tests 1-9 were low flow conditions and testing was performed in a water tunnel. Tests 10-14 were for the intermediate flow case and were performed in a zero gradient hydraulic flume. Tests 15-18 were the highest stream velocity conditions and were performed in the hydraulic flume with the bed slope equal to 0.006 m m^{-1}. In Table 1, S is the bed gradient of the flume. H is the average flow depth. Fr is the Froude number ($Fr=U_{bulk}(gH)^{-0.5}$, where U_{bulk} is the bulk velocity and g is gravity). U_* is the shear or friction velocity. Re is the channel Reynolds number ($Re=U_{bulk}H\nu^{-1}$, where ν is kinematic viscosity of the fluid). k_s^+ is the roughness Reynolds number ($k_s^+=k_s U_*\nu^{-1}$, where k_s is the bed roughness height). All tests were used to assess time-averaged VBS output and its ability to measure the time-average

approach velocity, U. Tests 10 through 18 in the hydraulic flume were used for assessing the turbulent flow characteristics of the VBS. These tests represent hydraulically rough, low relative submergence of bed particles and moderate Froude number conditions, which are turbulent flow conditions typical of a stream.

For the relatively low flow Tests 1-9, a low speed flow visualization water tunnel was used. The water tunnel was a Model 501-6" low speed flow visualization water tunnel manufactured by Engineering Laboratory Design, Inc. The water tunnel is a closed circuit unit with a free water surface test section. The test section is 15.2 cm wide by 15.2 cm high by 45.7 cm long and constructed of type SAR, clear, acrylic which allows for observation of the VBS during testing. Flow conditioning upstream of the test section is provided by a perforated cylinder to distribute the flow followed by stainless steel, perforated plates that act as head loss baffles. The settling length, upstream of the contraction to the test section is fitted with a tubular cell plastic honeycomb section. Three 60% porosity, stainless steel screens are mounted upstream of the test section. Twin turning vane cascades in the return direct flow leaving the test section. Flow velocity is variable in increments of approximately 0.6 cm s^{-1} from 0-35 cm s^{-1}. The maximum deviation in measured approach velocities to the VBS (±4%) was used as uncertainty bounds on the estimated water tunnel velocities.

To obtain the intermediate and high range velocities and test the turbulence measuring capabilities of the VBS in Tests 10-18, a 12 m long by 0.61 m wide closed circuit hydraulic flume with a fixed bed roughness, i.e., d_{84} equal to 5.6 mm, was used (Belcher and Fox, 2009; Belcher and Fox, 2011; Fox and Belcher, 2011). Tests were performed 9 m downstream of the headbox and 3 m upstream of the flume outfall. Rods were placed at the outfall of the flume to reduce the hydraulic slope and force quasi-uniform flow in the test section. Approach velocities for the intermediate tests ranged from approximately 25 to 50 cm s^{-1} which provided some overlap with the velocities tested for the low velocity tests. Approach velocities for the high flow tests ranged from 59 to 72 cm s^{-1}.

During testing, the VBS were placed on a 2.1 cm polyvinyl chloride mounting device with the same connections that would be used in the field. The mounting device was fastened to the top of the flume using a clamp and also stabilized at the bed to

prevent flow-induced vibrations. After mounting the VBS, its elevation above the bed was measured. In the hydraulic flume, the elevation was referenced to halfway between the troughs and crests of the roughness elements to the centerline of the VBS. The data acquisition rate of the VBS is variable up to 200 Hz, and was set at 50 Hz during testing. Flow stabilization was confirmed in both apparatuses prior to data collection. The output from the VBS was the voltage drop that occurs across the bent resistor in the voltage divider circuit and has units of volts. The voltages reported here are relative to a zero velocity voltage (V_0), which is the voltage reading taken when the sensor is unbent in stagnant conditions.

During the highest flow hydraulic flume Tests 15-18 (i.e., S = 0.006 m m^{-1}), the VBS mounting device produced a gradually varied flow upstream of the VBS. For these four tests, the time-average approach velocity at the VBS bending element was estimated using a modified log wake law for gradually varied flow and verified using velocity profiles measured upstream of the VBS. The modified log wake law was used to model the time-averaged streamwise velocity profile in decelerating hydraulically rough open channel flow where the shear velocity (U_*) and Cole's wake strength (Π) were adjusted for flow non-uniformity (Song and Graf 1994; Song and Chiew 2001; Onitsuka etal. 2009). The modified log wake law is given as

$$\frac{U}{U_*} = \frac{1}{k}\ln\left(\frac{y}{k_s}\right) + B + \frac{2\Pi}{k}\sin^2\left(\frac{y\pi}{2H}\right) \tag{1}$$

where k is the von Karman constant taken to be 0.4, k_s is the roughness height taken equal to d_{84}, which was 5.6 mm, B is the constant of integration for rough bed flows 8.5, and H is the flow depth. U_* was found using turbulence measurements with an acoustic Doppler velocimeter and the Clauser method (Kirkgoz, 1989; Nezu & Nakagawa 1993), which were in close agreement. Π is a function of the pressure gradient parameter, β (Song and Graf, 1994; Onitsuka et al, 2009), which is given as

$$\beta = \frac{H}{\tau_0} g\rho\left(-S + \frac{dH}{dx}\right) \tag{2}$$

where τ_0 is the bed shear stress and dH/dx is the hydraulic gradient. We described Π as a function of β (Nezu et al., 1994; Song & Graf, 1994; Onitsuka et al., 2009) given as

$$\Pi = 0.07\beta + 0.27 \tag{3}$$

dH/dx in Equation (2) was both measured and modeled in our analysis. We modeled *dH*/*dx* using the St. Venant equation as

$$\frac{dH}{dx} = \frac{S - \frac{U_*^2}{gH}}{\left(1 - Fr^2\right)} \tag{4}$$

We verified the estimates for U using measured velocity profiles with an ADV at (10, 15, 40, and 90 cm) upstream of the VBS. RMSE was 2.1 cm s^{-1} for data collected within the sampling volume of the VBS providing uncertainty bounds for our method. The sampling volume for estimate of the approach velocity U was the same as that of the VBS (4 mm in the y-direction), and U was estimated by integrating across the modified log-wake law for this location.

To assess turbulence measurement of the VBS, its results were compared with acoustic Doppler velocimeter (ADV) results. The ADV used for comparison was a SonTek acoustic Doppler velocimeter (ADV) (16MHz) which has a sampling rate of 50Hz, velocity resolution 0.01 cm/s, and accuracy 1% of the measured velocity. The ADV has a small sampling volume (approximately 0.1 cm^3) that is located 5 cm from the transmitting transducer. The ADV was mounted on a rigid rod that was attached to the top of the flume and stabilized by the flume bed to avoid flow-induced vibrations; such vibrations may cause elevated intensity readings (Dancey 1990). The ADV was positioned 2 cm upstream of the VBS so that any flapping of the bend sensor did not impact the ADV signal. The 2 cm streamwise difference in locations was justifiable to be representative of freestream turbulence characteristics unaffected by local flow disturbances around the VBS. This location is representative with regards to measuring turbulence characteristics' of the flow in the streamwise *u*-direction because: the vertical location of the sensors above the bed was the same; the flow depth did not change over the 2 cm streamwise distance; flow was hydraulically rough (k^+>70); flow did not have pronounced secondary velocities at this location; and we were well above the roughness region at y=6d_{84}. We have extensively studied the structure of turbulence and its imprint on the mean velocity in this flume for these hydraulic conditions, and at this vertical *y*-location the turbulent structure advects with the streamwise velocity rather than being

connected to the bed (Belcher and Fox, 2009; Fox and Belcher, 2011; Belcher and Fox, 2011). In post-processing of the ADV data, we found that the velocity datasets were statistically stationary which was verified using the first, second, third, and forth statistical moments of velocity. We performed spectral analysis of the velocity data using 4800 ADV measurements. The ADV power spectral density exhibited a region with a -5/3 slope (in log-log scale) that exhibit the inertial subrange (see Fig 3) (e.g., Singh et al., 2010).

5.5 RESULTS OF TIME-AVERAGE VELOCITY

The general relationship between VBS shape and velocity is shown in Figure 1b; as velocity increases the VBS bends and the tip becomes more aligned with the flow. The greatest amount of curvature for the deflected shapes occurs near the connection location. Figure 2 provides the time-average approach velocity versus output voltage for the tests shown in Table 1. Voltage output from the VBS in Figure 2 is shown to be non-linear due to the non-linear bending response to velocity and the non-linear relationship between resistance and radius of curvature. A transition velocity is shown to exist at around 35 cm s^{-1} in Figure 2. Below the transition, deflections are small due to the large storage of elastic potential energy within the VBS as compared to the kinetic energy of the flow. The region above the transition is characterized by fluid kinetic energy that is larger than the elastic potential energy of the VBS. Large deflections result and the shape becomes asymptotically quasi-parabolic.

We use a semi-theoretical approach to relate the measured VBS voltage to the time-average approach velocity. The semi-theoretical approach logically follows from the fact that the fluid approach velocity deflects the VBS and causes its shape to be curvilinear due to fluid drag on the elastic member (see Fig 1b). In turn, the deflected shape increases electrical resistance in the member and increases the net voltage difference across the divider. Prediction of the deflected shape follows the fundamental work by Alben et al. (2002) and Alben et al. (2004). Harnett et al. (2011) applied the fundamental work to bend sensors and provides the relationships between the deflected shape and electrical resistance. Our approach builds off of the earlier work and provides a calibration method for the VBS. In addition, we improve the past methods by changing the spatial scale used for the VBS, adding a parameter to account for turbulent flow

conditions, modifying the equation used for element radius of curvature, and calibration of the predicted bent shape of the VBS using experimental photographs.

During bending by the approach fluid, the VBS is connected at one end and behaves as a cantilever beam. The shape of the member can be quantified using the dimensionless freestream speed, η (Alben et al., 2002, Alben et al., 2004). η is the ratio of fluid kinetic energy to the elastic potential energy of the member and can be formulated for the VBS as

$$\eta = C_t \sqrt{\frac{4\rho w L^3 U^2}{EI}} \tag{5}$$

where C_t is a turbulence coefficient, ρ (1g/cm^3) is the fluid density, L and w are the length and width, E is the modulus of elasticity, and I is the beam moment of inertia. In principle, η describes the fluid forces versus elastic forces in the beam and was derived using potential flow theory. The bending theory accounts for the fact that the projected area of the bend sensor changes with velocity magnitude (Alben et al., 2002, Alben et al., 2004), and the turbulent coefficient can be used to adjust experimental data in hydraulically rough flow. Alben et al. (2004) found that shape self-similarity emerges when the bending element actual coordinates are properly scaled to η. Using η, the shape of the VBS scaled coordinates can be described by

$$Y = 1.34 X^{1/2} \tag{6}$$

where the scaled coordinates (X and Y) are the actual coordinates (x and y) scaled by $\eta^{2/3}$ as

$$X = x\eta^{2/3} \text{ and } Y = y\eta^{2/3} \tag{7a,b}$$

Equations (7a,b) can be substituted into Equation (6), and using geometry it is found that the parabolic shape of the deflected VBS's actual coordinates can be written as

$$x = \frac{y^2}{2r_0} \tag{8}$$

where r_0 is the radius of curvature at the base of the parabola given as

$$r_0 = \frac{1.34^2}{2(\eta)^{2/3}} \tag{9}$$

Harnett et al. (2011) related the deflected VBS shape in bending to electrical

resistance. The total resistance in the VBS bending element, R_{total}, can be found by integrating the resistance per unit length as a function of the local radius of curvature as

$$R_{total} = \int_0^{y_{end}} R'(r_{local}(y))ds(y) \tag{10}$$

where y_{end} is the coordinate for the end of the resistive strip, R' is the resistance per unit length, r_{local} is the local radius of curvature, and the local arc length is $ds(y)$. y_{end} can be found analytically by integrating the local arc length as

$$l = \int_0^{y_{end}} ds(y) = \int_0^{y_{end}} \sqrt{1 + \left(\frac{y}{r_0}\right)^2}\, dy \tag{11}$$

where l is the length of the VBS bending element. Integration of Equation (11) yields

$$l = \frac{1}{|2r_0|}\left[r_0^2 \ln\left(\frac{\sqrt{r_0^2 + y_{end}^2} + y_{end}}{|r_0|}\right) + y_{end}\sqrt{r_0^2 + y_{end}^2}\right] \tag{12}$$

Since l is known and r_0 is given by Equation (9), y_{end} is calculated with the zero crossing as

$$\left[r_0 \ln\left(\frac{\sqrt{r_0^2 + y_{end}^2} + y_{end}}{|r_0|}\right) + y_{end}\sqrt{r_0^2 + y_{end}^2}\right] - 2l = 0 \tag{13}$$

In Equation, (10), R' is a function of the radius of curvature and can be estimated empirically (Harnett et al., 2011) as

$$R' = e^{C_{VBS-1}} r^{C_{VBS-2}} + \frac{10V_0}{l(5 - V_0)} \tag{14}$$

where r is the radius of curvature, $C_{\text{VBS-1}}$ and $C_{\text{VBS-2}}$ are calibration parameters specific to an individual VBS. $\frac{10V_0}{l(5 - V_0)}$ is the resistance per unit length of the non-deflected VBS found by measuring the resistance of individual non-deflected bending elements, V_0, and dividing by its length, l. r_{local} is found from calculus (Stewart, 2008) to be

$$r_{local}(y) = r_0\left(1 + \left(\frac{y}{r_0}\right)^2\right)^{3/2} \tag{15}$$

and can be calculated for the deflected VBS shape using Equations (8) and (9). After calculating R_{total} with Equation (10), the voltage divider law can be used to calculate the

voltage, V, for the fixed 10 kΩ resistor as

$$V = 5\left(\frac{R_{total}(r_0)}{R_{total}(r_0)+10k\Omega}\right) \tag{16}$$

The semi-theoretical approach was applied to the VBS element used in testing and to estimate the time-average approach velocity versus output voltage relationship shown in Figure 2. Table 2 compiles the measured inputs and calibrated coefficients used in the analyses. The approach was applied in two stages. First, C_t was adjusted to fit the theoretical potential flow shape of the bending element proposed by Alben et al. (2002, 2004) to the actual VBS shape found in the turbulent flow experiments. Second, the two calibration coefficients, $C_{\text{VBS-1}}$ and $C_{\text{VBS-2}}$, used to empirically estimate resistance per unit length were found by minimizing the sum of square errors between the estimated output voltage and the measured output voltage.

In the first stage of calibration, Equations (5) and (9) were substituted into Equation (8) as

$$x = \left[0.9C_t^{2/3}\left(\frac{\rho w L^3 U^2}{EI}\right)^{1/3}\right] y^2 \tag{17}$$

Photographs of the VBS bending during the experiments (see Fig 4a-c) were digitized to provide the experimental shapes. Figure 4d-f shows calibrated results with the digitized, experimental shape and the estimated shape for C_t equal to 28. In general, the calibrated shape compares well. The need for imposing C_t due to lack of exact agreement between the theoretical, self-similar shape described using η and the bending shape during experimentation is reflective of the idealized conditions under which η was derived. η was formulated in the absence of viscosity *via* potential flow theory (Alben et al., 2002). Bending in the potential flow case is caused by the pressure difference between the leading and trailing edge of the bending element. In practice, pressure along the trailing edge is set as the free stream pressure since the streamline at the trailing edge cannot be calculated. Alben et al. (2004) suggested η be further scaled to account for the actual wake pressure. In the present case, it is recognized that both viscous effects and the wake pressure difference require C_t. Zhu (2007) recently showed that a bending element in viscous flow experiences increased bending due to viscous effects. In addition, Gosselin et al. (2010) recently highlights differences in the wake pressure loss that would further

increase bending. Further testing using photographs similar to Figure 4 will be helpful in future research in order to understand how C_t varies under non-idealized cases.

Figure 5 shows results of the second stage of calibration where the voltage calculated with Equation (16) is compared to the measured output voltage. Relative VBS voltage is plotted against nondimensional velocity, η, and the time average approach velocity, U. As can be seen, the semi-theoretical approach compares well for the calibrated $C_{\text{VBS-1}}$ and $C_{\text{VBS-2}}$. Harnett et al. (2011) found $C_{\text{VBS-1}}$ to range between 6.7 to 7.9 and $C_{\text{VBS-2}}$ to range between -2.6 and -2.7, which is in fairly good agreement with the testing performed here. However, the small differences and the sensitivity of $C_{\text{VBS-1}}$ especially highlights the need to calibrate individual bending sensors prior to application. In further application and practice, the relationship U given V can be solved implicitly using a fairly small dataset due to the use of the semi-theoretical approach. We recommend verification of C_t for specific flow cases, for example using an underwater camera in the field, and thereafter a minimum of two measurements could be used to parameterize $C_{\text{VBS-1}}$ and $C_{\text{VBS-2}}$ for individual VBS. Additionally, it should be pointed out that once calibrated to the flow configuration, the semi-theoretical approach predicts the output voltage well and provides a tool for calibrating other bending type sensors in other fluids.

5.6 TURBULENCE MEASUREMENTS

Post-processing of the VBS signal was performed to investigate its ability to provide information about turbulence characteristics of open channel flow over a rough bed. Because the VBS provides only one-dimensional velocity, turbulence measurements of the VBS were compared with the streamwise velocity component measured by the ADV. Testing was compared for the stream-associated hydraulic conditions including hydraulically rough, low relative submergence of bed particles and moderate Froude number. The turbulent structure of the flow has been well measured and described for these hydraulic conditions using digital particle image velocimetry, large-scale particle image velocimetry, and acoustic Doppler velocimetry measurements (Fox et al., 2005; Fox and Patrick, 2008; Rodriguez and Garcia, 2008; Belcher and Fox, 2009; Fox and Belcher, 2011). The structure of turbulence for these conditions consists of connected vortex packets that shed from gravel particles and eject away from the bed to form

alternating high momentum/low momentum cells termed macroturbulence in the outer region of the flow (Duncan 1970; Adrian et al. 2000; Roy et al. 2004; Hurther et al. 2007; Fox and Belcher, 2011). Turbulence for these conditions tend to make two general imprints on the instantaneous streamwise velocity signal including: (i) high frequency fast velocity fluctuations associated with vortices shed at the bed and (ii) low frequency slower velocity fluctuations associated with macroturbulence.

We used scale decomposition and spectral analysis to isolate the imprint of shed vortices and macrotubulence upon the instantaneous velocity time-series of VBS and ADV data. Scale decomposition *via* the Triple Decomposition Theorem (TDT) (Hussain and Reynolds 1972) was employed to separate the velocity signal into components having different scales of time as

$$u(t) = U + u'(t) + u''(t) \tag{18}$$

where u and U are the instantaneous signal and temporal mean. u' is the low frequency, large-scale signal used to isolate macroturbulence. u" is the remaining high frequency, small-scale associated with shedding. u' was isolated using the moving-average over a time-step T_s as

$$U + u'(t) = \frac{1}{T_s} \int_{t-\frac{T_s}{2}}^{t+\frac{T_s}{2}} u'(t')dt' \tag{19}$$

Selection of an appropriate value for T_s where the small-scale is removed was performed using visual inspection of smoothed time-series as well as the skew of u' for varying values of T_s (Fox et al. 2005; Lacey and Roy 2008; Fox & Patrick 2008). The skew, S_k was calculated as

$$S_k = \frac{\frac{1}{n}\sum_{i=1}^{n}\left(u_i - U\right)^3}{\left(\sqrt{\frac{1}{n}\sum_{i=1}^{n}\left(u_i - U\right)^2}\right)^3} \tag{20}$$

Spectral analysis of the time-series signal was performed to quantify the energy frequency scales of the turbulence. The spectrum was estimated using the discrete Fourier transform of u and v with the fast Fourier transform (FFT) method as

$$X(f) = \sum_{j=1}^{n} Z_j e^{(-2\pi i)(j-1)(fn/25-1)/n} \tag{21}$$

where the input variable Z was the v or u time series. When plotted in variance-preserving form, broad peaks in the spectral energy density correspond to the frequency of an energetic mean or dominant eddy passing the velocity sensor (Boppe and Neu, 1995; Venditti and Bennett, 2000).

Results of scale decomposition and spectral analysis for the VBS and the ADV signals are shown in Figure 6. Figure 6 a and b shows unfiltered VBS (left column) and ADV (right column) 15 s segment of the total datasets. It should be pointed out that the VBS and ADV datasets in the left and right columns are not synchronized to show the matching of individual, instantaneous fluctuations but rather show how fluctuations compare in general. The VBS is in general smoother than the ADV data showing less fast fluctuations associated with smaller-scale turbulent processes. The VBS time-series shows low frequency velocity fluctuations that agree with the ADV time-series and are indicative of passing macroturbulent cells. Results of the Triple Decomposition analysis agree with the time-series observations. u' under varying T_s (Fig 6 c, d, e, f, g, and h) shows the low frequency, large-scale signal associated with macroturbulence for both the VBS and ADV results. u" variation (Fig 6 i, j) is much smaller in magnitude for the VBS as compared to the ADV indicating the lack of ability to capture the high frequency, small-scale turbulent signal associated with shedding for these hydraulic conditions. Figure 6 k and l shows results of the skew analysis. Skew of u' for varying values of T_s has shown the ability to aid in the identification of T_s where fast fluctuations within the velocity signal are effectively removed, which occurs when the skew plot displays significant changes (Fox et al. 2005; Lacey and Roy 2008; Fox & Patrick 2008). The ADV skew plot reaches a maximum around T_s 0.08s which corresponds to the visual interpretation from the moving average time plot with T_s of 0.10s which appears to eliminate the fast fluctuating component of velocity. The VBS is unable to measure the small-scale fast fluctuating component of velocity and the skew plot lacks indicators for the threshold T_s. The spectra of the VBS and the ADV show a broad peak on the order of 2 Hz, which indicates the frequency of an energetic mean or dominant eddy size passing the sensor (Boppe and Neu, 1995; Venditti and Bennett, 2000). In this case, the 2 Hz

peak are indicative of the passing of macrotubulence seen visually in the time-series results. The ADV spectrum shows energy at frequencies above 10 Hz associated with the fast fluctuating components of velocity indicative of small scale turbulence. The inability of the VBS to measure the fast fluctuating component of velocity results in the lack of energy above 10Hz. The VBS spectrum agrees with the conclusions drawn from the moving average and skew analysis in that the VBS is unable to measure small scale turbulence but has the capability to capture the low frequency macroturblence present in the flow.

A final analysis was performed to look at the turbulent intensity of the flow as an overall measure of the fluids turbulent nature. Turbulence intensity is calculated as

$$I_i = \frac{1}{Z}\left[\frac{1}{n}\sum_{i=1}^{n}\left(z_i - Z\right)^2\right]^{0.5} \tag{22}$$

where *i* indicates turbulent intensity calculated for the VBS or ADV and the variable Z is a placeholder for *V* or *U*. The non-dimensional relative turbulent intensity (Equation 22) is used for comparison between the ADV and VBS because it does not depend strongly on calibration parameters of the velocimeter (Nezu and Nakagawa 1993 pg 59). It is realized that the non-linearity of the velocity voltage relationship will cause error in the relative turbulent intensity predicted by the VBS. It is assumed that the voltage velocity relationship near the time averaged velocity being measured is approximately linear. Figure 7 provides a scatter plot of turbulence intensity calculated for the VBS and ADV at the same location in the flow. As can be seen, measurements of turbulent intensity with the VBS is approximately 12% of that recorded with the ADV. The discrepancy between the VBS and ADV measurements is reflective of the inability of the VBS to measure the smaller scale turbulence for these conditions. At the same time, the correlation between $I_{x,VBS}$ and $I_{x,ADV}$ is promising and reflects the ability of the VBS to capture the underlying structure of the turbulent flow. The linear fit between $I_{x,VBS}$ and $I_{x,ADV}$ suggest that the VBS could be used as a proxy for more detailed turbulent measurements and could provide some indication of the overall turbulent nature of the flow.

5.7 CONCLUSIONS

The mechanical, electrical, and wireless transmission characteristics of the newly

developed inexpensive wireless velocity bend sensors (VBS) were presented here. Thereafter, we tested the capability of the VBS to measure (i) streamwise time-average approach velocity and (ii) turbulence in a hydraulically rough open channel flow.

The VBS tests showed that the sensors were capable of measuring the streamwise time-averaged approach velocity. Only small voltage differences existed for velocities below a threshold velocity where deflections were small, however above the threshold velocity an appreciable voltage output is measured that will allow field application. A semi-theoretical calibration approach based on fluid drag and elastic member bending was been developed to estimate the streamwise time-average approach velocity from the VBS voltage output. The shape parameter of the semi-theoretical approach agreed well with measurements of the deflected VBS shape during experiments after correcting for viscous flow and wake pressure effects. Further, experimental results agreed well with the semi-theoretical approach after calibrating empirical parameters for resistance per unit length of the VBS. In further application and practice, the relationship between velocity and voltage for individual VBS can be solved implicitly using a fairly small dataset due to the use of the semi-theoretical approach.

The ability of the VBS to measure turbulence of hydraulically rough bed flow were analyzed using eddy decomposition *via* the Triple Decomposition Theorem, spectral analysis and turbulence statistics. The results show that the VBS could not resolve small scale turbulence associated with vortex shedding off of gravel particles at the streambed, but were capable of measuring low frequency macroturbulence. The streamwise turbulent intensity measured by the VBS was found to be approximately linear and 12% of that recorded with the ADV for the tested flow conditions. The turbulence results suggest that the VBS can be helpful as a proxy for more detailed turbulent measurements and could provide some indication of the overall turbulent nature of the flow in the streams.

Advancements in technology have made the development of these sensors possible which when integrated into environmental stream monitoring efforts will provide a wealth of velocity and turbulence data for researchers. The newly developed inexpensive wireless VBS capable of measuring time-average velocity and turbulence will be a valuable tool for highly-sensed stream monitoring efforts were multiple velocity

measurements are necessary to span the spatial scales relevant to environmental parameters of interest. Figure 8 conceptualizes field deployment of the VBS for measuring turbulence and time-average flow conditions in a stream. The wireless capabilities of the sensors will enable faster installation of hydraulic measurement networks. The low cost of the sensors make deployment possible across spatial scales that have previously been cost prohibitive. Low cost and wireless capabilities provide researchers the ability to monitor remote and dangerous environments that would be difficult to monitor with other sensors. And, the use of inexpensive sensors is especially attractive because of the potential for losing the sensors during high flow events.

While field deployment of sensor networks is promising, we highlight potential limitations of the VBS that should be considered during field deployment. VBS fatigue or creep the irreversible increase in the sensor dimensions due to temperature or loading conditions is a potential limitation in future field deployment. Assessment of creep for the polyimide material used in the VBS has been extensive due to the use of polyimide in electronics nowadays for flexible circuit boards. In our VBS experiments, temperature conditions were low (room temperature) and we reached a maximum loading on the sensors equal to 12.5 MPa. Using the elongation ratio as a measure of creep, these temperature and loading conditions would provide an elongation ratio less than 0.5% for our 200 μm polyimide VBS far below the proportional limit (see Figures 5, 9, and 10 in Chang et al., 2008 for polyimide materials), which is negligible creep. During field deployment, water temperature of streams is not expected to induce creep of the polyimide VBS. However, extreme loading *via* high magnitude hydrologic events would have the potential to cause creep of the polyimide sensors. Further, solid debris (e.g., large woody debris) transported during hydrologic events could potentially destroy the bend sensors. The VBS sensors also have limitations at the upper end of their range (i.e., high velocities) and should include an appropriate U_{max} setting. This was also pointed out in bend sensor research by Harnett et al. (2011). The resolution of the bend sensor decreases asymptotically to zero as the sensor element aligns with the flow. Resolution is given by $\Delta V / \Delta U$ where ΔU is the change in flow rate, and ΔV is the change in output voltage. Reduced sensitivity occurs at U_{max} because the sensor aligns nearly completely with the flow, its shape changes very little at these high velocities, and its output voltage

is a function of the sensor shape. An appropriate U_{max} setting will be particularly important in field deployment where hydrologic conditions can be highly variable. U_{max} can be increased if a thicker polyimide VBS is used, and the semi-theoretical model presented in this paper can be used as a predictive method for U. To this end, field deployment might benefit from numerous VBS with varying thickness to accurately capture a wide range of hydrologic events. Like many field deployable sensors, the VBS is subject to fouling by organic debris such as leaves or algae if deployed for long periods of time, and the VBS should be properly installed in-stream to measure streamwise velocity. Routine maintenance of field deployed VBS should be included in future field methods.

5.8 ACKNOWLEDGMENTS:

We would like to thank Alex Thompson, Bill Ford, Ben Zinninger, Thomas Lawrence, and Cory Franklin for building the VBS and their help with data collection. We thank Prof. Sean Bailey, Mechanical Engineering at the University of Kentucky and Mark Miller for use of, and assistance with, the water tunnel. We acknowledge support from National Science Foundation award No0918856. We thank two anonymous reviewers and the associate editor, whose comments helped improve the quality of this paper.

5.9 SYMBOLS

B = log-law constant of integration for hydraulically rough flows

C_t = turbulence coefficient

$C_{\text{VBS-1}}$ = exponential coefficient in empirical resistance

$C_{\text{VBS-2}}$ = power coefficient in empirical resistance

d_{84} = diameter of bed particles for which 84% are finer

$ds(y)$ = local arc length

E = modulus of elasticity

f = spectral frequency

Fr = Froude number

g = gravitational constant

H = mean flow depth

$\frac{dH}{dx}$	=	hydraulic gradient
I	=	beam moment of inertia
$I_{x,ADV}$	=	turbulence intensity measure with the ADV
$I_{x,VBS}$	=	turbulence intensity measure with the VBS
j	=	index in fast Fourier transform
k	=	index in fast Fourier transform
k_s^+	=	roughness Reynolds number
k_s	=	bed roughness height
L	=	length of the VBS
l	=	length of the VBS resistive element
n	=	number of data points used during the spectral analysis
$P(f)$	=	spectrum of time series
R'	=	resistance per unit length
Re	=	channel Reynolds number
r_{local}	=	local radius of curvature
r_0	=	radius of curvature at the base of the deflected VBS
R_{total}	=	total resistance of the VBS bending element
S	=	bed slope
S_k	=	skew, 3rd statistical moment
T_s	=	moving-average timestep
U	=	streamwise time average approach velocity
u	=	instantaneous velocity
u'	=	loww frequency velocity fluctuations associated with macroturbulence
u''	=	high frequency velocity fluctuations associated with vortex shedding
U_{bulk}	=	bulk velocity
U_*	=	shear or friction velocity
V	=	time average voltage output from the VBS
v	=	instantaneous voltage output from the VBS
V_0	=	voltage reading for un-deflected, stagnant conditions
w	=	width of the VBS

X = scaled streamwise coordinate of the VBS

x = actual streamwise coordinate of the VBS

Y = scaled lateral coordinate of the VBS

y = actual lateral coordinate of the VBS

y_{end} = y coordinate for the end of the resistive strip

β = pressure gradient parameter

η = dimensionless freestream speed

k = von Karman constant

ν = kinematic viscosity of the fluid

Π = Cole's wake strength

ρ = fluid density

τ_0 = bed shear stress

5.10 REFERENCES

Adrian, R. J., Meinhart, C. D., and Tomkins, C. D. 2000. "Vortex organization in the outer region of the turbulent boundary layer." Journal of Fluid Mechanics, 422: 1–54.

Alben, S., Shelley, M., Zhang, J. 2004. How flexibility induces streamlining in a two dimensional flow. Physics of Fluids, 16(5): 1694-1713.

Alben, S., Shelley, M., Zhang, J. 2002. Drag reduction through self-similar bending of a flexible body. Letters to Nature 420(5): 479-481.

Belcher, B.J., and Fox, J.F. 2011. Outer Scaling for Open Channel Flow over a Gravel Bed. Journal of Engineering Mechanics 137(1): 40-46

Belcher, B., and Fox, J. 2009 (Discussion). Rodriguez, J.F., and Garcia, M.H., 2008, Rodriguez, J. F., and Garcia, M. H. 2008. Laboratory measurements of 3-D flow patterns and turbulence in straight open channel with rough bed. J. Hydraul. Res., 46(4): 454–465, J.Hydraul. Res., 47(5):685-688.

Boppe, R. S., and W. L. Neu, 1995. Quasi-coherent structures in the marine atmospheric surface layer. J.Geophys Res., 100 (C10): 20 635–20 648

Buffin-Belanger, T., and Roy, A.G. 2005. 1min in the life of a river: selecting the optimal record length for the measurement of turbulence in fluvial boundary layers. Geomorphology 68: 77-94

Chang, W.Y., Fang, T.H. and Lin, Y.C. (2008) “Physical characteristics of polyimide films for flexible sensors.” *Applied Physics A*, 92: 693–701.

Dancey, C. L. 1990. Measurements of second order turbulence statistics in an axial flow compressor via 3-component LDA. AIAA J., 90: 2017.

Duncan, W.J. 1970. Mechanics of fluids. Elsevier, New York.

Fox, J.F. and Belcher, B.J. 2011. Comparison of macroturbulence measured using decomposition of PIV, ADV and LSPIV data. Journal of Hydraulic Research, 49(1): 122-126.

Fox, J. F., Papanicolaou, A. N., and Kjos, L. 2005. Eddy taxonomy methodology around a submerged barb obstacle within a fixed rough bed. Journal of Engineering Mechanics, 131: 1082–1101.

Fox, J.F., and Patrick, A. 2008. Large-scale eddies measured with large scale particle image velocimetry. Flow Measurement and Instrumentation 19: 283–291

Gosselin, f., Langre, E., and Machado-Almeida, B.A. 2010. Drag reduction of flexible plates by reconfiguration. Journal of Fluid Mechanics 650: 319-341

Harnett, C. K., Schueler, M. T., Blumenthal, N. R., Hopf, K. L., Fox, J. F., and Pulugurtha, S. (2011). Calibration and field deployment of low-cost fluid flow-rate sensors using a wireless network. IEEE Transactions on Instrumentation and Measurement, 60(2): 633-641

Hart, J.K., and Martinez, K. 2006. Environmental Sensor Networks: A revolution in the earth system science? Earth-science Reviews 78:177-191

Hauer, F.R., and Lamberti, G.A. 2006, Methods in stream ecology. Amsterdam, The Netherlands: Academic press

Horsburgh, J.S., Jones, A.S., Stevens, D.K., Tarboton, D.G., and Mesner, N.O. 2010. A sensor network for high frequency estimation of water quality constituent fluxes using surrogates. Environmental Modelling & Software. 25:1031-1044

Hurther, D., Lemmin, U., and Terray, E. A. 2007. Turbulent transport in the outer region of rough-wall open-channel flows: The contribution of large coherent shear stress structures (LC3S). J. Fluid Mech., 574: 465–493.

Hussain, A. K., and Reynolds, W. 1972. The mechanics of an organized wave in turbulent shear flow. Journal of Engineering Mechanics, 54: 241–261.

Kirkgoz, M.S., 1989, Turbulent velocity profiles for smooth and rough open channel flow. Journal of Hydraulic Engineering, 115(11): 1543-1561

Kwan, T.F. 1988. A study of abutment scour. Rep. No. 451, Dept. of Civil Engineering, Univ. of Auckland, Auckland, New Zealand.

Lacey. R.W.J., and Roy, A.G. 2008. Fine-Scale Characterization of the Turbulent Shear Layer of an Instream Pebble Cluster. Journal of Hydraulic Engineering 134(7): 925-936

Maier, H.R., Jain, A., Dand, G.C., and Sudheer, K.P., 2010, Methods used for the development of neural networks for the prediction of water resource variables in river systems: Current status and future directions, Environmental Modelling and Software 25: 891-909

Nezu, I. 2005. Open-Channel Flow Turbulence and Its Research Prospect in the 21st Century. Journal of Hydraulic Engineering:229-246

Nezu, I., Kadota, A., Nakagawa, H. 1994, Turbulent structures in accelerating and decelerating open-channel flows with laser Doppler anemometer. 9th Cong. of APD-IAHR, Singapore, Vol. 1, 413–420.

Nezu, I., and Nakagawa, H. 1993. Turbulence in open channel flows, A. A. Balkema, Rotterdam, The Netherlands.

Onitsuka, K., Akayama, J., and Matsuoka, S. 2009, Prediction of velocity profiles and Reynolds stress distributions in turbulent open-channel flows with adverse pressure gradient, Journal of Hydraulic Research, 47(1):58-65

Rehmel, M. 2007. Application of Acoustic Doppler Velocimeters for Streamflow Measurements. Journal of Hydraulic Engineering 133(12) 1433-1438

Rodriquez, J.F., and Garcia, M.H. 2008. Laboratory measurements of 3-D flow patterns and turbulence in straight open channel with rough bed. Journal of Hydraulic Research 46(4): 454-465

Roy, A. G., Buffin-Bélanger, T., Lamarre, H., and Kirkbride, A. D. 2004. Size, shape and dynamics of large-scale turbulent flow structures in a gravel-bed river. Journal of Fluid Mechanics, 500: 1–27.

Rundel, P.W., Graham, E.A., Allen, M.F., Fisher, J.C., and Harmon, T.C. 2009. Environmental sensor networks in ecological research. New Phytologist 182(3): 589-

607.

Singh, A., Porté-Agel, F. and Foufoula-Georgiou, E. (2010) On the influence of gravel bed dynamics on velocity power spectra. Water Resources Research, 46, W04509.

Song, T., and Graf, W.H. 1994, Non-uniform open-channel flow over a rough bed. Journal of Hyroscience and Hydraulic Engineering, 12(1): 1-25

Song, T., and Chiew, Y.M. 2001. Turbulence measurement in nonuniform open-channel flow using acoustic Doppler velocimeter (ADV). Journal of Engineering Mechanics, 127(3): 219-232

Stewart, J. 2008. Calculus Early Transcendentals-Custom edition for University of Kentucky 6th edition Cengage Learning

Venditti, J. G., and S. J. Bennett (2000), Spectral analysis of turbulent flow and suspended sediment transport over dunes, J. Geophys. Res., 105: 22,035– 22,047.

Vivoni, E.R., and Camilli, R. 2003. Real-time streaming of environmental field data. Computers & Geosciences 29: 457-468

Wang, N., Zhang, N., and Wang, M. 2006. Wireless sensors in agriculture and food industry-Recent development and future perspective. Computers and Electronics in Agriculture 50:1-14

Yick, J., Mukherjee, B., and Ghosal, D. 2008. Wireless sensor network survey. Computer Networks 52: 2292-2330

Zhu, H. 2007, Viscous flow past a flexible fibre tethered at its centre point: vortex shedding, Journal of Fluid Mechanics, 587: 217-234

5.11 TABLES AND FIGURES

Table 5.1. Hydraulic conditions for experimental tests.

Test #	Test Apparatus[£]	S (m m^{-1})	U (cm s^{-1})	H (cm)	Fr	U_* (cm s^{-1})	Re ($\times 10^4$)	k_s^+
1	WT	0	1.6	6	0.01	0.1	0.1	n/a
2	WT	0	6.0	6	0.05	0.4	0.4	n/a
3	WT	0	11.9	6	0.10	0.7	0.7	n/a
4	WT	0	17.7	6	0.14	1.1	1.1	n/a
5	WT	0	23.6	6	0.19	1.4	1.4	n/a
6	WT	0	26.5	6	0.22	1.5	1.5	n/a
7	WT	0	29.4	6	0.24	1.6	1.8	n/a
8	WT	0	32.4	6	0.26	1.8	1.9	n/a
9	WT	0	35.3	6	0.29	1.9	2.1	n/a
10	HF	0	25.6	7.9	0.28	1.9	2.1	109
11	HF	0	32.7	9.8	0.33	2.5[§]	3.2	139
12	HF	0	35.9	10.7	0.36	2.7	3.9	154
13	HF	0	43.3	12.6	0.40	3.2	5.6	182
14	HF	0	47.9	14.0	0.43	3.6	7.1	201
15	HF	0.006	61.1	8.5	0.64	4.6	5.0	258
16	HF	0.006	65.5	9.8	0.66	5.0	6.4	278
17	HF	0.006	69.6	11.4	0.68	5.3	8.3	298
18	HF	0.006	73.0	14.0	0.68	5.7	11.2	318

Notes: [£]WT is water tunnel and HF is hydraulic flume. [§]Interpolated value since calibrated ADV incomplete, and thus results of this test are not included in Figure 6.

Table 5.2. Measured inputs and calibration coefficients in the VBS bending analysis.

Symbol	Description	Value	Units	Means of Acquisition
C_t	Turbulence coefficient	28	Dimensionless	Calibrated
E	Young's modulus of elasticity	2.55	GPa	Constant
f	Width	8	mm	Measured
L	Length of VBS	41.2	mm	Measured
l	Length of resistive strip	36.5	mm	Measured
$C_{VBS\text{-}1}$	Exponent coefficient in R'	20.6	Dimensionless	Calibrated
$C_{VBS\text{-}2}$	Power coefficient in R'	-6.4	Dimensionless	Calibrated
ρ	Fluid density	1	g cm^{-3}	Constant
V_0	Voltage reading taken when the sensor is un-deflected in stagnant conditions	3.0	Volts	Measured

Figure 5.1. (a) Photograph of a VBS with a depiction of electronic behavior. **(b)** Approximate deflected shape of the VBS in bending when increasing from 0 to 80 cm s^{-1} in 5 cm s^{-1} increments.

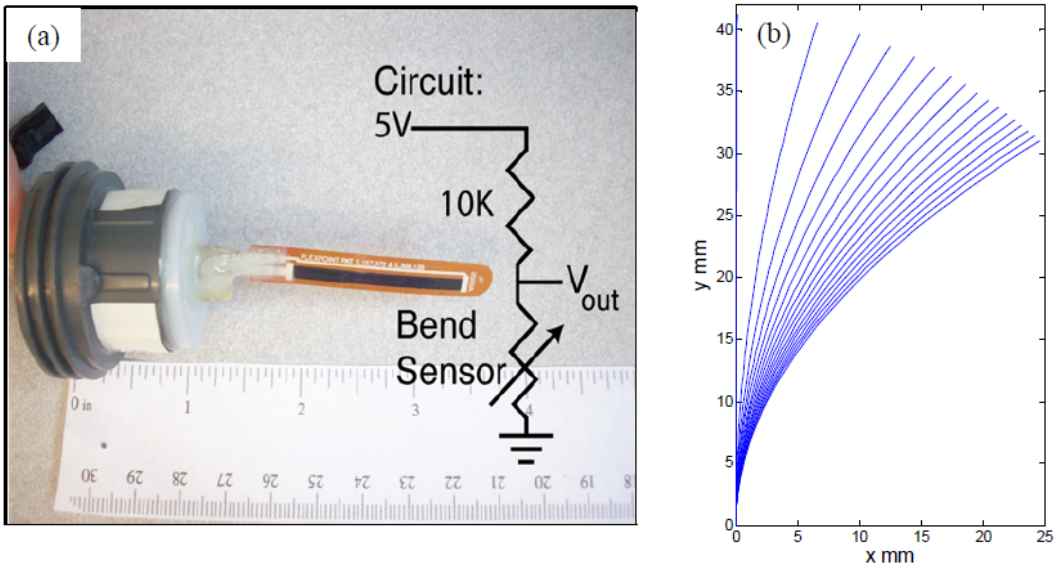

Figure 5.2. Time-average approach velocity versus output voltage.

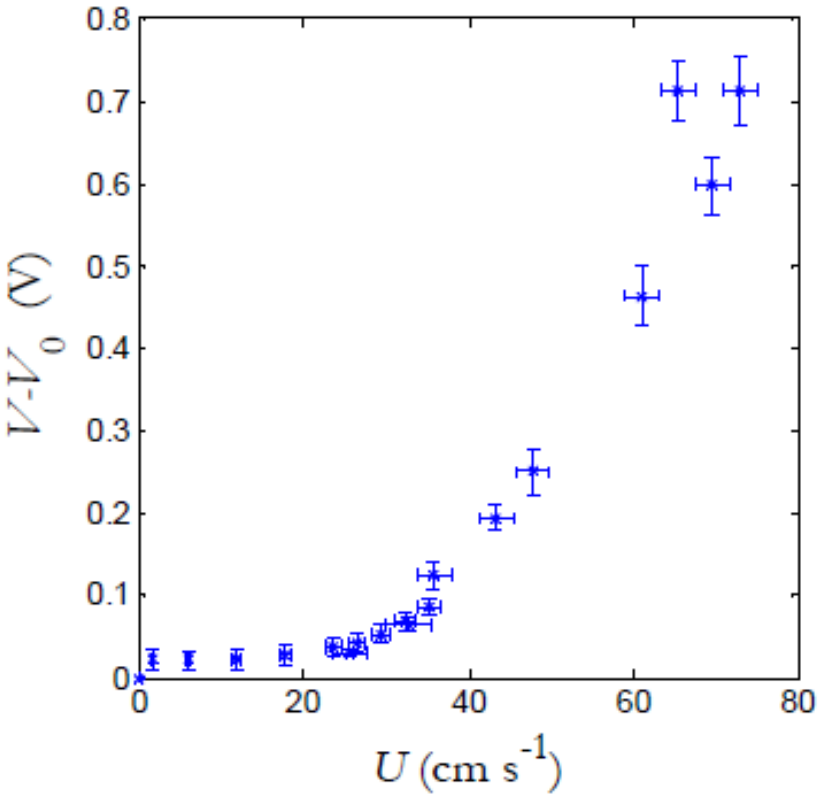

Figure 5.3. Power spectral density of the ADV data.

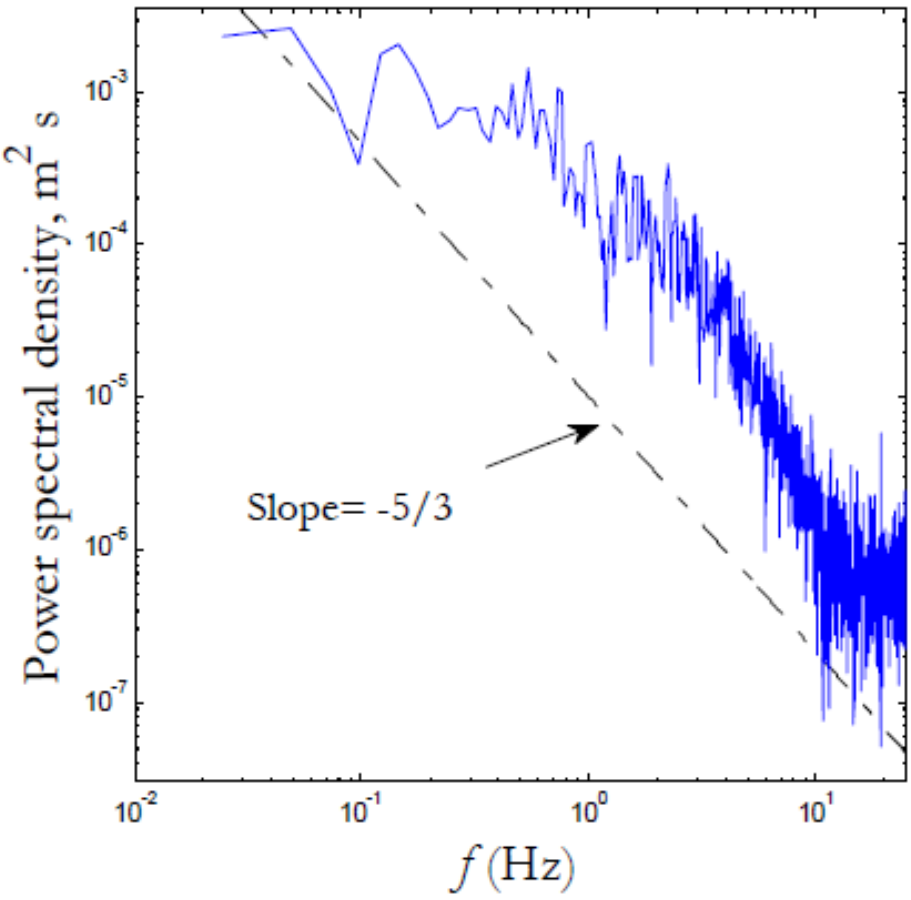

Figure 5.4. (a-c) Photographs of the VBS in bending for U equal to 6.0, 29.4, and 35.3 cm s^{-1}, respectively. **(d-f)** Digitized VBS shape in bending and predicted VBS shapes (solid line) using Equations 6-8.

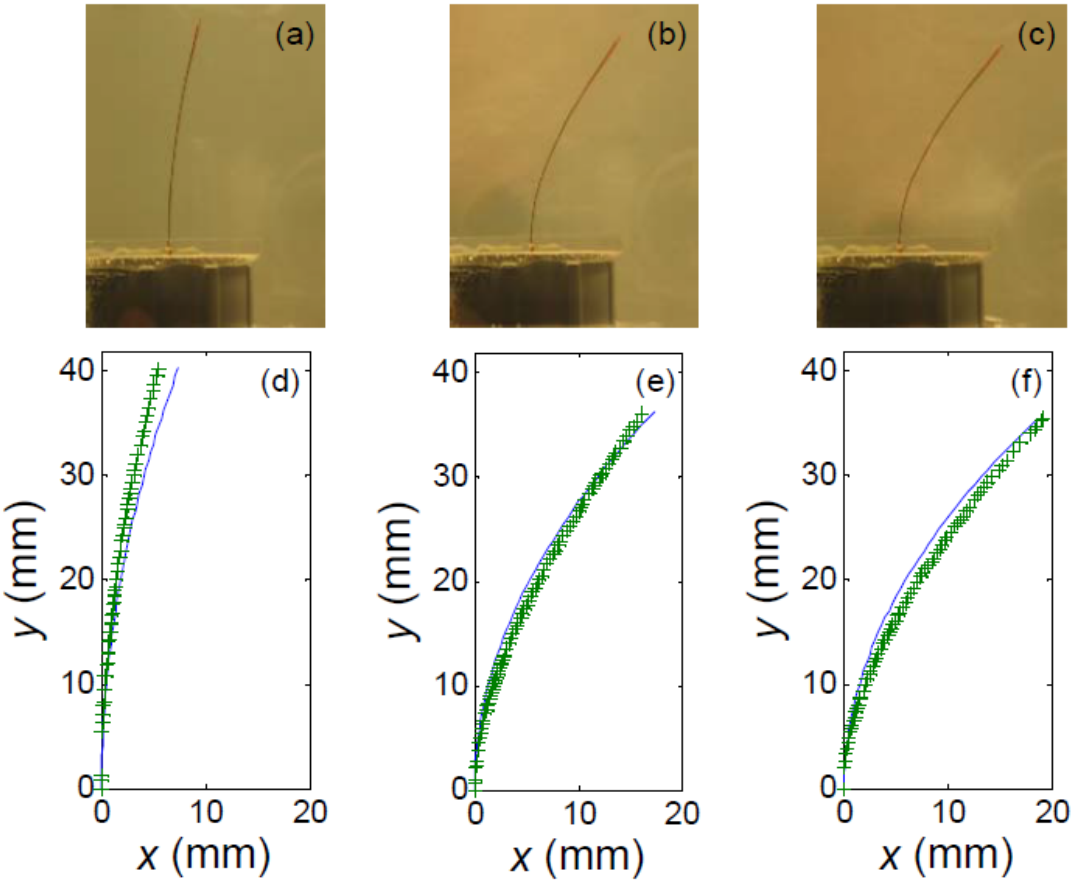

Figure 5.5 (a) VBS voltage is plotted against nondimensional velocity η. **(b)** VBS voltage plotted against time average approach velocity.

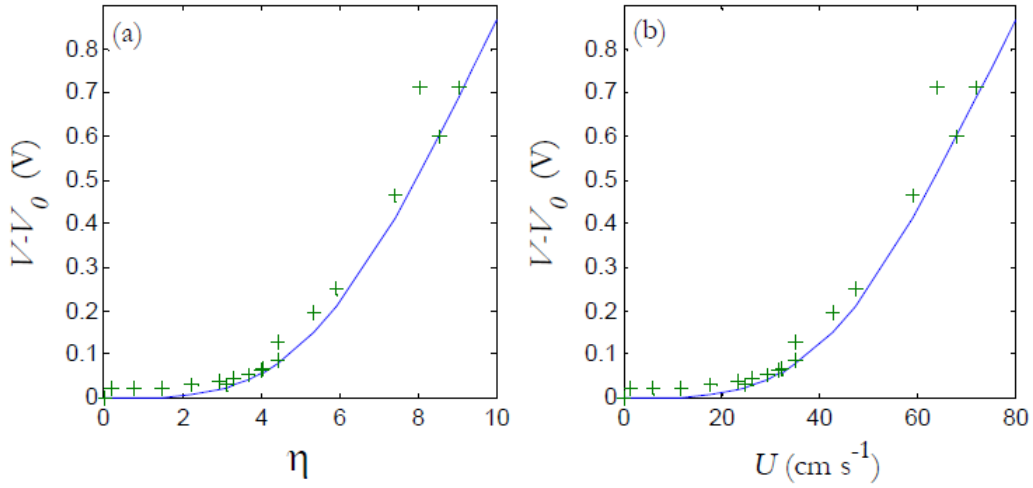

Figure 5.6. Time-series analysis for the VBS (left column) and ADV (right column). **(a,b)** Unfiltered time-series data for Test 17. **(c-h)** Results of slow fluctuating component of the Triple Decomposition Theorem for successive moving-average times-steps. **(i,j)** Results of the fast fluctuating component of the Triple Decomposition Theorem for T_s equal to 0.10 s. **(k,l)** Skew curves for VBS voltage and ADV streamwise velocity as a function of T_s. **(m,n)** Spectral plots of the VBS voltage and ADV streamwise velocity in variance preserving form.

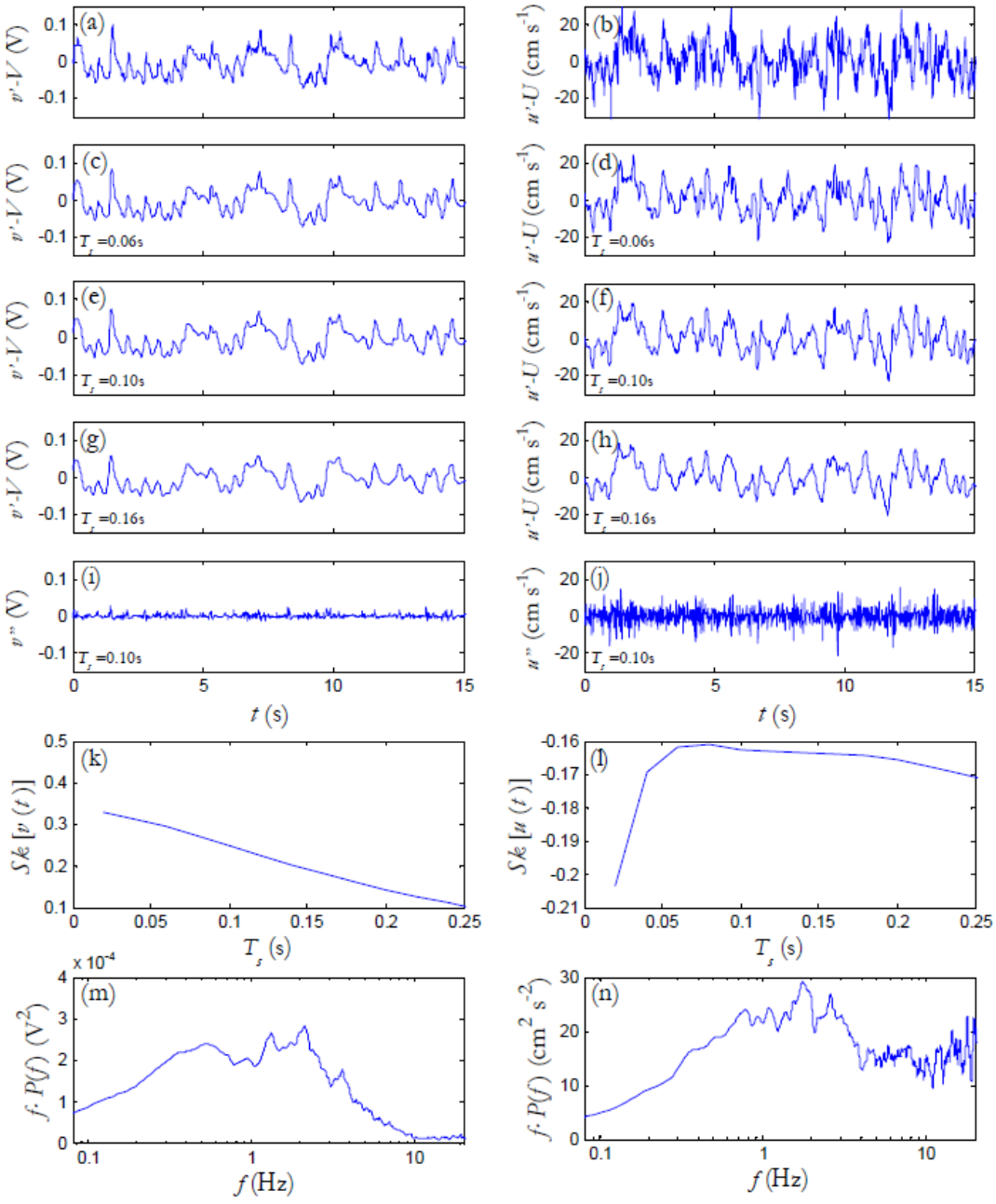

Figure 5.7. Turbulent intensity comparison for VBS voltage and ADV streamwise velocity.

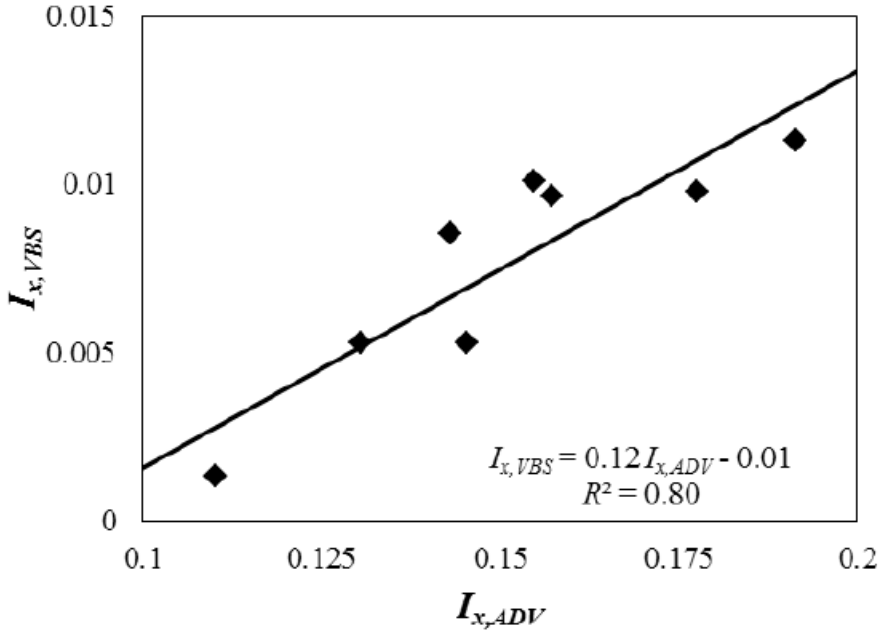

Figure 5.8 (a) Depiction of VBS measuring macroturbulence in a stream. (b) VBS measuring time-average flow to construct *U* isovels in cm s^{-1} for a cross-section.

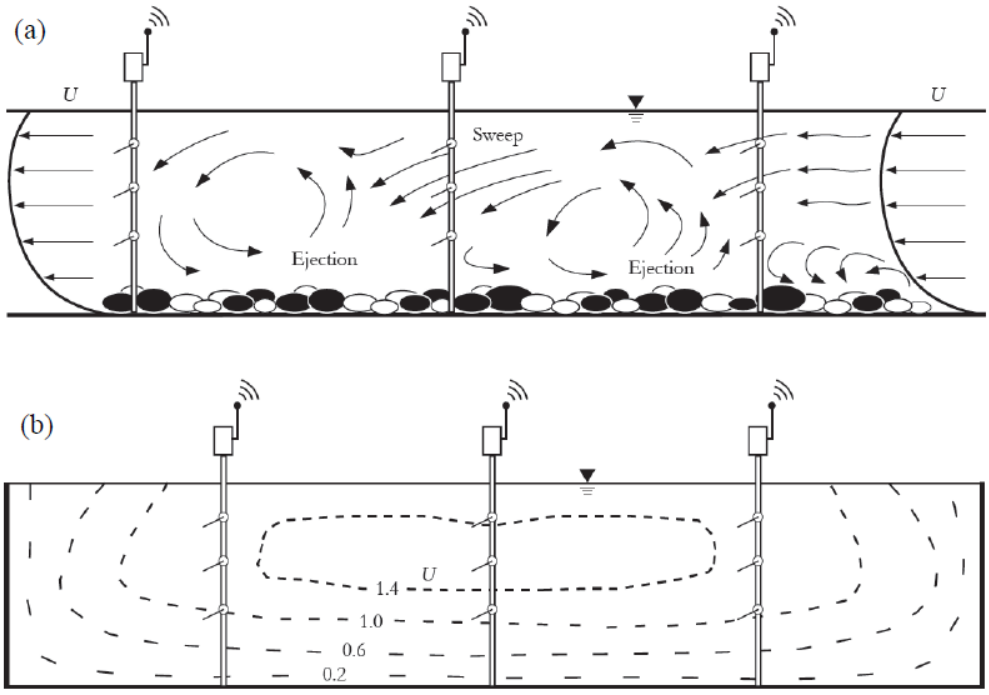

Chapter 6: Estimating Suspended Sediment Concentration in Streams by Diffuse Light Attenuation

Text extract with permission from Stewart, R. L., Fox, J. F., Harnett, C. K., (2014) Estimating Suspended Sediment Concentration in Streams by Diffuse Light Attenuation, *Journal of Hydraulic Engineering* ASCE,140(8), 0414033

6.1 SUMMARY

A light attenuation sensor system (LASS) for measurements in waters is described. The LASS records irradiance at multiple levels in the water column to provide a measure of the diffuse light attenuation coefficient which is strongly affected by suspended sediment. Dimensional analysis and geometric optical theory are used to relate the irradiance attenuation to sediment properties through a dimensionless product. The latter is termed a light attenuation number for suspended sediment in waters. The LASS and dimensional analysis results are validated in the laboratory using fluvial sediments collected from a third order stream as well as mono-disperse quartz sediment. The attenuation coefficient estimated with LASS data varied non-linearly with total suspended sediment concentration due to particle shadowing and multiple scattering at large optical depths. The light attenuation coefficient for each sediment type is well described as a function of total suspended sediment concentration by empirical power law relationships, which provides confidence in the functioning of LASS. Light attenuation curves for different sediment types collapsed onto a single curve when replotted according to dimensionless numbers arising from the dimensional analysis, which confers confidence in the analysis for future research and application. A successful field demonstration of LASS over a hydrological event in a small stream highlights its potential application in hydraulic and ecological research as well as future avenues of research to improve the sensor.

6.2 INTRODUCTION

It is well recognized that spatially distributed stream monitoring will benefit from the use of inexpensive, wireless sensors and sensor networks. Recent advancement in wireless electronic technology offers the potential for inexpensive measurements of

environmental parameters in space and time using miniaturized electronic sensors and wireless communication that focus on low cost, low power requirements, and fast installation (Glasgow et al. 2004; Hart and Martinez 2006; Wang et al. 2006; Yick et al. 2008; Rundel et al. 2009; Horsburg et al. 2010; Larios et al. 2012; Sunita et al. 2012). Application of the new sensor technology to stream network monitoring is attractive because a sensed system could be used to identify hot spots of high sediment and pollutant flux, be useful for calibrating numerical models, and generally provide a better understanding of stream network connectivity and geomorphology under different flow regimes. Further, the use of miniaturized, inexpensive sensors offers the practicality of deployment within remote, dangerous, and high discharge settings where the sensors could be destroyed. Application of these technologies offer several advantages over traditional monitoring techniques by streamlining the data collection process, minimizing human errors and time delays, reducing overall cost of data collection, and increasing the quantity and quality of data on temporal and spatial scales (Glasgow et al. 2004).

While the advancement of sensor networks and the potential usefulness of the technology in streams is well recognized, few studies have been published with regards to inexpensive, wireless sensors that will be useful for suspended sediment transport measurements. Traditional methods for suspended sediment transport monitoring in streams rely on manually or automated sampling equipment, which requires substantial effort in the laboratory to determine the sediment concentrations of the samples and significant manpower in the field to assist with sampling, equipment servicing and maintenance (Walling et al. 2006). More recently, turbidity sensors and beam transmissometers are increasingly used as proxies of suspended sediment concentration in order to increase the temporal resolution of traditional techniques and reduce manpower (Walling et al. 2006; Davies-Colley and Nagels, 2008). The use of wireless communications technology and automatic data processing further reduces the manpower resources to operate large data-collection networks (Glasgow et al. 2004). Turbidity sensors and beam transmissometers offer advantages over traditional concentration measurements but would be very expensive to deploy in a highly distributed sensor network (see Table 1).

We introduce and experimentally study the light attenuation sensor system (LASS) for measuring suspended sediment concentration in streams. LASS are inexpensive wireless optical sensors that measure diffuse light (irradiance), which is strongly affected by suspended sediment concentration and thus LASS along with measurement of velocity is useful for suspended sediment transport measurement in streams. Aquatic ecologists frequently use diffuse optical sensors in large standing waters to estimate natural light availability for photosynthesis by aquatic plants (Kirk 1994; Davies-Colley et al. 2003). LASS are different from other optical sensors primarily in the low cost of the device and the miniature size and wireless communications that make them ideal for sensor networks. Table 1 shows that the price of LASS is a fraction of other instruments that measure surrogates of total suspend sediment concentration. While it is recognized that the price of some off-the-shelf instruments has risen due to product upgrades from user feedback and the availability of additional measurements (see Tab 1), the potential of the low-cost LASS for distributed stream sensor networks is realized. Further, LASS can operate using an artificial or natural external light source to reduce energy consumption making them well suited for deployment in remote stream locations. LASS can be sensed within a wireless network using hardware that automatically identifies and transmits data allowing the addition or removal of sensors to meet changing application requirements without disrupting network communication organizations.

Prior to application of LASS within inexpensive wireless networks for sediment transport research and consulting, there is a need to develop modeling methods that relate light attenuation to the concentration and physical properties of suspended sediment in streams. Models that relate suspended sediment properties to light attenuation will be useful for calibrating sensors such as the LASS. Theory from optical physics provides arguments for estimating the likelihood of photon interactions with opaque particles (van de Hulst 1981; Bohren and Huffman 2008; Kirk 1994), and previous light attenuation studies in water bodies provide an understanding of the probable factors impacting light attenuation in streams (Davies-Colley & Nagels 2008; Julian et al. 2008a; Stavn 2012). However, little published work is available that relates light attenuation to a set of sediment properties in low order streams. We seek to define dimensionless light, water

and sediment associated parameters that can be useful for calibrating the LASS and other light attenuation sensors for sediment transport measurements.

The present research is motivated by the need to develop low cost, wireless sensors that measure suspended sediment concentrations within highly-sensed stream monitoring networks. Specifically, we place emphasis upon the use of newly developed wireless LASS to measure the concentration of fine sediments with diameters ranging from approximately 1 to 100 μm and suspended concentrations on the order of 0 to 1 g L^{-1}. The suspended sediment diameter and concentration range represent fine sediment transported by low order stream systems. Based on the research needs to develop inexpensive sensors for suspended sediment concentration measurements in streams and light attenuation prediction methods, the objectives of this paper are: (1) to describe the LASS, their functioning, and their fabrication; (2) to perform dimensional analysis to provide a model of light attenuation in streams based on dimensionless water and sediment variables; (3) to measure the sensitivity of LASS and test our results from dimensional analysis using fluvial sediments collected from a third order stream as well as quartz grained sediments; and (4) to show a field demonstration of LASS and highlight its future application in hydraulic and ecological research as well as future avenues of research to improve the sensor.

6.3 DESCRIPTION OF LASS

LASS consists of a vertical array of photo sensors which measure down welling, diffuse irradiance, *E*, using a voltage divider circuit. In order to explain the functioning of LASS in a stream, Figure 1 depicts the vertical distribution of light impacted by sediment absorption and scattering and numerous LASS measuring *E* at multiple locations in the water column. Absorption by sediment directly removes light from the water column by converting the absorbed light into other forms of energy while scattering by sediment either removes light directly by backscattering or causes light to take a tortuous path increasing the probability of absorption (Davies-Colley & Smith 2001; Van Duin et al. 2001). LASS measures the resultant *E* using a voltage divider circuit and a cadmium sulfide light dependent resistor, or photocell, placed in series with a fixed resistor. The resistance of the off-the-shelf photocell (manufactured by Jameco ValuePro) decreases with increasing incident irradianceThe spectral response of the photocells is right skewed

and has a relative response of 10% at 350 nm and 780 nm as compared to the peak response at 530 nm. In the LASS, E is converted to a digital format with an analog to digital chip and transmitted from the sensor to a central data logger *via* wireless nodes. E measured with LASS can then be used to estimate the concentration of suspended sediment (*TSS*) that absorbs and scatters light in the water column. The light attenuation coefficient, K_d, can be calculated from measured E as

$$K_d = \frac{-1}{z} \ln\left(\frac{E}{E_0}\right) , \quad (1)$$

where E is the light irradiance when the light has traveled a distance z through water, and E_0 is light irradiance when z is zero (see Figure 1). K_d has been found to depend primarily upon *TSS* in flowing fresh water bodies although it is now recognized that a number of secondary variables can significantly impact K_d (Kirk 1994; Davies-Colley & Smith 2001; Squires and Lesack 2003; Mishra et al. 2005; Davies-Colley and Nagels 2008; Julian et al. 2008b). As part of this study, we work towards relating K_d to *TSS* and secondary variables for use of the LASS in streams.

LASS have been designed and fabricated to meet researcher's needs for high temporal and spatial data resolution within stream network monitoring efforts. The LASS have a low hardware cost of approximately $225 US per sensor. The low cost of the LASS allow deployment in large numbers and reduce the cost associated with lost or damaged sensors. The wireless communication capabilities provided by the wireless node enables multiple LASS to send data to a localized data storage unit which makes data retrieval from a stream network more time efficient (Glasgow et al. 2004; Harnett et al. 2011). The wireless signal can also be relayed to a long-range communication device for remote data viewing and health monitoring of the network. Fabrication of the LASS can be performed by purchasing commercially available parts from home improvement stores and an electronics supplier. Assembling the electronic components requires some basic knowledge of circuits and soldering capabilities. The housing for electronic components is constructed from polyvinyl chloride to prevent the electronics from contacting water and provides a means to deploy the sensors in the stream. Wires connect the sensors to the wireless node and are contained within the polyvinyl chloride housing.

The measuring volume of LASS can be approximated as the cone determined by

sensor depths (z_1 and z_2) and Snell's law of refraction. Snell's law of refraction describes the bending of light transmitted across a boundary of mediums as a function of refractive indices and incident light angle. Snell's law and the refractive indices of water and air limit the apex angle of this cone to an approximate maximum value of 97^0 in freshwater. The measuring volume of LASS is estimated as the volume of the cone defined by twice the maximum refracted angle. For example, for a 20 cm sensor spacing with z_1 and z_2 placed at flow depths of 30 and 50 cm, respectively, the sampling volume will be 6275 cm^3.

6.4 DIMENSIONAL ANALYSIS

Dimensional analysis can be performed to provide a semi-empirical model that relates K_d measured with optical sensors such as LASS to properties of suspended sediment in streams. Light attenuation in natural waters is attributed to water, chromophoric dissolved organic matter, inorganic suspended sediment, non-algal particulate organic matter, and phytoplankton (Kirk 1994; Davies-Colley & Nagels 2008; Julian et al. 2008b; Stavn 2012) as

$$K_d = fn\left[\{\alpha, \lambda\}, \{K_w, e, CDOM, POM, PHYTO\}, \{ISS, \rho_s, d, n\}\right]. \quad (2)$$

The three sets of variables shown in Equation (2) represent the properties of the light, properties of the water, and properties of sediment, respectively. α and λ are the light angle to the fluid surface and wavelength of the incident light in free space. K_w is the light attenuation caused by clear water; e is entrained air; *CDOM* is chromophoric dissolved organic matter; *POM* is particulate organic matter; and *PHYTO* is phytoplankton. *ISS* is the total inorganic suspended sediment concentration; ρ_s is the suspended sediment density; and d is the size distribution of suspended sediment, and n the refractive index.

Water settings that have received the most K_d research include estuaries and continental shelf, which are optically complex due to large variability in concentration and composition of the particulate and dissolved organic matter (Wozniak et al. 2010). Less published work is available that relates light attenuation to sediment transport in streams, but it is recognized that streams are less optically complex due to low hydraulic retention time that reduces suspended biologic activity (Vannote et al. 1980; Davies-Colley & Nagels 2008; Julian et al. 2008b). Published research on light attenuation in low-order streams due to suspended sediments is likely less abundant since shading from

riparian vegetation largely limits light availability for photosynthesis (Julian et al., 2008b).Equation (2) can be reduced for the case of a diffuse light source in low order streams based on a number of considerations. While K_d is an apparent optical property of the medium and dependent upon the light field, it has been shown that the apparent optical properties of open water are impacted little by the angle of a diffuse light source (Kirk 1994; Davies-Colley and Smith 2001); thus the functional dependence of K_d on α can be relaxed. Omitting flow regions of a stream with very high entrainment, e.g., flow over partially submerged obstacles or spillways, the dependence of K_d on e can be removed. Further, low order streams in watersheds have less connectivity to their flood plains and lower retention times not allowing for an abundant growth of phytoplankton (Naiman and Bilby 1998; Julian et al. 2008b). Thus, the dependence on *PHYTO* is removed. If streams with high CDOM concentrations are not considered, including those draining standing waters, inundated floodplains, and wetlands than the contribution of CDOM to light attenuation will be negligible. Light attenuation in streams is typically dominated by the inorganic, as opposed to the organic, fraction of particulate matter decreasing the importance of *POM* (Davies-Colley & Smith 2001; Julian et al 2008). Further, *POM* will generally be low, i.e., <5 g OM per 100 g sediment, for low order stream systems and the influence of *POM* will be at least partially reflected in sediment density (Williams et al. 2008). Reduction of variables in Equation (2) provides

$$K_d = fn\left[\{\lambda\},\{K_w\},\{TSS,\rho_s,d,n\}\right] . \quad (3)$$

Equation (3) represents the functional dependence of K_d upon light, water and sediment properties in low order streams with suspended sediments. *ISS* is replaced by *TSS* in Equation (3) reflecting that measurement of total suspended solids, in low order streams during transport events, will be comprised primarily of inorganic suspended solids.

From Equation (3), we select λ as a repeating variable and produce the following dimensionless products

$$K_d\lambda = fn\left[\{K_w\lambda\},\{n\},\left\{\frac{TSS\lambda}{\rho_s d}\right\}\right] . \quad (4)$$

The result in Equation (4) relates the dimensionless light attenuation coefficient to dimensionless products including the dimensionless light attenuation by water, the refraction index, and the dimensionless number for light attenuation by sediment. The last

term in Equation (4) represents a dimensionless sediment surface area available to interact with light. λ accounts for the dependence of absorption and scattering by water and sediments upon the energy of light(Kirk 1994; Babin and Stramski 2004; Stramski et al. 2007; Doxaran et al. 2009; Wozniak et al. 2010). The semi-empirical result from the dimensional analysis in Equation (4) qualitatively agrees with numerous empirical studies that show direct dependence of *TSS* upon K_d and inverse dependence of ρ_s and d upon K_d (Bunt et al. 1999; Neukermans et al. 2012).

6.5 DATA COLLECTION

To measure the sensitivity of LASS and test the semi-empirical result in Equation (4), data collection was performed to estimate K_d with the LASS. The experiments were conducted by placing the LASS in suspensions of known suspended sediment concentrations to collect measurements of E used with Equation 1 to calculate K_d. Figure 2 shows the experimental testing apparatus designed to test diffuse optical sensors which was a modified version of the optical sensor testing apparatus designed and published by Downing and Beach (1989). The testing chamber was designed to produce uniform mixing of suspended sediments within a 45 cm test section of the chamber. Water and sediment were circulated upward *via* a propeller through the testing section. A baffle provided flow conditioning downstream of the propeller to reduce large scale secondary currents and assist with sediment mixing. Lighting within the tank was provided by three banks of light emitting diode lights that produced three different intensities (i.e., Color 3100K at 2 Lumens each) placed above the test section to provide even light distribution. LASS were placed within the test section during data collection (see Fig 2). During measurements, a vacuum line was attached to the LASS mounting rod to collect 500 ml water samples for *TSS* analysis *via* filtration method using 0.7 micron glass filters (see Fig 2). Estimates of K_d and measurements of *TSS* at different depths within the test section revealed no significant systematic bias, which provided confidence in the apparatus functioning and uniform suspended sediment conditions. In addition, uniform suspended sediment concentration in the test section was verified using turbidity measurements with a 90° near infrared turbidity meter (e.g. the Yellow Stone Intsruments 6136 turbidity probe). The turbidity meter was positioned throughout the test section and gave similar readings throughout; for example the standard deviation was less than 1% of

the mean readings for 250 NTU readings.

K_d data were collected in the experimental apparatus for a range of sediment types with varying *TSS*, *d* and ρ_s parameters shown in Table 2. Three different types of sediment were used including quartz grains with a median diameter equal to 27.2 μm, quartz grains with a median diameter equal to 14.2 μm, and fluvial sediment with a median diameter equal to 10.5 μm (see Figure 3). The quartz grains were primarily SiO_2 and termed ground silica by the manufacturer U.S. Silica Company. The fluvial sediments were collected from the South Elkhorn Creek located in central Kentucky, United States. South Elkhorn Creek is a low order stream with sediment impairment and represents the type of stream for which sensor networks that use LASS will be useful. The fluvial sediments were collected during three high flow discharge events when the sediments were suspended and transported in the water column.

A total of 102 experimental tests were performed to measure *E* to calculate K_d using Equation (1), and the tests were grouped into repetitions for the range of test 25 conditions described in Table 2. Repetitions were performed by varying both the vertical location of the LASS in the test section and by varying the lighting conditions, i.e., *z* and E_0 in Equation (1). No significant bias of K_d due to *z* or E_0 was found. No systematic bias was observed for the *TSS* before, during and after testing which verified that *TSS* was uniform during testing. After completing measurements at a fixed *TSS*, sediment slurry was added to the tank to provide a successively higher *TSS*. The Yellow Stone Instruments 6136 turbidity probe was used to monitor suspended sediment uniformity and once the turbidity readings stabilized, the next set of *E* and *TSS* measurements were collected.

6.6 SENSITIVITY OF LASS

As a first step to the investigating the sensitivity of LASS, statistical distributions including the sample mean and variance of the sensor readings were analyzed. The voltage values measured by LASS were approximately normally distributed thus central tendency was estimated as the mean of all sample readings. To estimate the standard uncertainty on a function, *f*, of several variables, first-order error propagation (Neukermans et. al. 2012) was used as

$$\sigma(f) = \left(\sum_{i=1}^{n} \sum_{j=1}^{n} \frac{\partial f}{dx_i} \frac{\partial f}{dx_j} \operatorname{cov}\left(x_i, x_j\right) \right)^{1/2} \tag{5}$$

The uncertainty was estimated for relative irradiance, T_E=E E_0^{-1} ,as

$$\sigma\left(K_d\right) = z \frac{\sigma\left(T_E\right)}{\left(T_E\right)} = z \frac{T_E \left(\left(\frac{\sigma(I)}{I} \right)^2 + \left(\frac{\sigma(I_0)}{I_0} \right)^2 \right)^{1/2}}{\left(T_E\right)} \tag{6}$$

Equation (6) is the upper bound on the uncertainty estimate since the variables are positively correlated and the correlation coefficient was omitted. The standard deviation of K_d relative to the mean K_d generally decrease as *TSS* increases. The standard deviation associated with *TSS* is typically of the same order of magnitude as that associated with K_d. The exception is extremely clear waters where water surface fluctuations can significantly impact under water irradiance distribution.

Figure 4 shows K_d plotted against *TSS* for the three types of sediments tested with error bars (±1 standard deviation). Figure 4 illustrates that K_d is closely related to *TSS* and the dependence of K_d on *TSS* is non-linear. Separate non-linear relationships fit each sediment type well. We preformed non-linear regression to fit power laws to each for each sediment type of the form

$$K_d = K_w + c_1 (TSS)^{c_2} \tag{7}$$

Coefficients, K_w, c_1 and c_2, in Equation (7) were found by minimizing the sum of squared error (*RMSE*) between the estimated and predicted K_d. Figure 4 depicts data for each of the three sediment types plotted on log-log scales along with the regressed power law relationships, which describe the data well. The intercept is approximately the origin for these data sets indicating that light attenuation by water K_w is small as measured by LASS. In past research and application of light attenuation instruments, e.g., turbidity meters, empirical fits as shown in Figure 4 are commonly used for calibration of measured optical properties to *TSS* (Van Duin et al. 2001; Liu et al. 2005; Chao et al. 2009); and LASS shows the ability to meet this goal. However, such empirical sediment specific relationships fail to account for variability between sediment types emphasizing the need to theoretically account for the effects of secondary variable. To this end, notice that the distributions of light attenuation in Figure 4 increase in K_d magnitude as particle

size and density decrease, which agree well with the dimensional dependence in Equation (4).

6.7 DIMENSIONLESS MODEL EVALUATION

In order to evaluate our semi-theoretical model, our collected LASS data were compared for the dimensionless products in Equation (4). Figure 5 shows the dimensionless light attenuation coefficient plotted against the dimensionless number for light attenuation by sediment. The results show that including the secondary sediment variables to rescale the data into the dimensionless product provides a collapse of $K_d\lambda$ between the different sediment types used in this study. In this manner, light attenuation is more predictable when parameterized as a function of the projected area of sediment particles rather than *TSS* alone, as suggested by Equation (4). A two parameter power law (i.e., c_1, c_2) was found to describe the relationship well. The power-law equation in Figure 5 was fit to the datasets by minimizing the sum of square errors during *k*-fold cross validation to provide a stable estimate of the coefficients and error (Kohavi 1995). Note that the $K_w\lambda$ term in Equation (4) was not present in the power law equations in Fig 5 or Fig 4. In general, $K_w\lambda$ is reflective of light attenuation by any dissolved constituents or water itself. An intercept (K_w) was not found for either the fluvial or quartz grained sediments indicating no appreciable light attenuation by water or by dissolved constituents. Dissolved constituents were not present in the water used during laboratory testing and thus did not contribute to light attenuation. Water that is free of dissolved constituents is only a weak attenuator of light for the wavelength range corresponding to the peak sensitivity of LASS (i.e., K_d at 530nm<0.05 m^{-1}) (Mobley, 1994).

The non-linear nature of the power-law relationship in Figure 5 requires some discussion, especially in comparison with the forth pi term of Equation (4). The dimensional analysis technique used to arrive at Equation (4) implies that a relationship exists between the dimensionless products while making no assumption on form the relationship. A simple 2D geometric arrangement of the optics problem implies the linear relationship reported to hold for many studies of light attenuation. The linear relationship arises from the assumption that each sediment particle absorbs or scatters an incoming portion of the light field. In this manner, each particle removes a small percentage of the light field proportional to the particles projected area. However, as the depth of the

particle layer or the number particles in the layer are increased, secondary processes of particle shadowing and backscattering occur and cause light attenuation to be less than predicted by linear relationships (Clifford et al. 1995; Hill et al. 2011). Some particles are shadowed by other particles in the layer causing less absorption, less scattering out of the layer, and ultimately less light is attenuated than would be predicted using a linear relationship calibrated at low concentrations. Further, scattered light that attempts to exit the particle layer can backscatter after interacting with surrounding particles, which effectively reduces the amount of light lost from the layer. This idea is reflected in the results of Figure 5; the relationship behaves as linear for low values of the light attenuation number, which reflects a relatively small amount of particles in the sediment layer. As the light attenuation number increases, so too does the number of particles and the opportunity for shadowing and backscattering, and a non-linear decay in light attenuation results. This non-linear dependence of K_d on *TSS* has been noted to exist, when λ, ρ_s, and d are held constant, and thus we might expect the first and forth terms of Equation (4) to be related by a power law with an exponent between 0.5 and unity. This concept is broadly consistent with the optical Monte Carlo stochastic modelling of Kirk (1981). Kirk (1981 and 1984) shows that K_d is nearly linearly dependent on light absorption and the square root of light scattering.

We provide some further discussion of two assumptions of the derivation presented here including (i) opaque and (ii) spherical particles. Our analysis assumed opaque particles and made no use of the imaginary part of the refractive index, which is the measure of light transmissivity through a particle. The assumption of opaque particles is reasonable for sufficiently large sediment particles and densely compacted sediment aggregates as those found in low order streams with large imaginary index, however when this assumption is not valid light attenuation would not be expected to scale proportional to area of particle, and a more complete description of this idea is explained by Bohren and Huffman (2008). For most optically significant particles encountered in natural waters these assumptions are reasonable and geometric optical theory explains light attenuation (Kirk 1994). To accentuate the opaque assumption note that the fluvial sediments plot higher that the 14.2 μm quartz grains suggesting the potential for error when using the power law equation beyond the sediments for this study. Also, it cannot

necessarily be assumed that natural sediment particles will be spherical in nature, however, this assumption likely has little impact on our results. Pollack and Cuzzi (1980) and Clavano et al. (2007) took the shape factor as a known constant, and implied that particles might behave like spherical particles of equivalent volume, which they showed was a good approximation for a concentration of randomly oriented, non-absorbing, irregular particles. Suspended irregular sediment particles transported in turbulent streams should behave as spherical particles of equivalent volume due to random particle orientation resulting from high Reynolds number flows (Clifford et al. 1995).

6.8 FIELD DEMONSTRATION OF LASS

The field location selected for the demonstration of LASS for measuring suspended sediment concentration and suspended sediment load was the South Elkhorn Creek, a third order stream located in the central Bluegrass Region of Kentucky (see Fox et al., 2010 and Ford and Fox, 2012). The field measurements were collected using three individual LASS as shown in Figure 6A, paired to provide three combinations of two sensors for calculating K_d. LASS sampling frequency was set to collect two measurements per minute. Sensor spacing remained constant during field deployment which enabled sensors near the free surface to account for variable ambient light conditions. In this manner, the topmost sensor accounts for ambient conditions and is compared to readings from lower sensors to calculate T_E between sensors, which is then used to calculate K_d. Figure 6B shows the stream flow rate Q as measured by the USGS gage station (03289000). Figure 6C shows underwater irradiance at the three vertical locations measured by LASS, and it can visually be seen that the measurements covary over time. Irradiance measured by LASS lower in the water column (i.e., 10 cm and 25cm above the bed) decreases dramatically from 5:00 pm to approximately 5:10 pm while irradiance closer to the free surface (i.e., 45 cm above the bed) decreases only marginally during this same time period. The change in irradiance corresponded with transport of a plume of sediment that the graduate researchers could see visually in the stream. Maximum turbidity was seen in the stream at approximately 5:10 pm which coincided with an increase in water discharge. The graduate researchers also observed an increase in turbidity and the amount of debris for the time period from 5:35 pm to the end of sampling which coincided with an additional increase in water discharge.

In order to further demonstrate the utility of the LASS instruments, we calculated suspended sediment discharge, *Qss*, for the event shown in Figure 6. As the first step, *TSS* was calculated using the laboratory derived relation for the fluvial sediments tested (see Fig 4), which were also suspended sediments from South Elkhorn Creek. Figure 6D shows *TSS* increased significantly during the time period 5:00 pm to 5:10 pm and then increased slightly at the end of the sampling period, corresponding to the decreases in irradiance measured by LASS. *Qss* was estimated for the sampling period *via* the Einstein approach (Chang 1988, pp. 150) by integrating a logarithmic velocity distribution with the suspended sediment concentration profile estimated using the Rouse equation. The Rouse Equation estimates nonuniform sediment concentration profile for sediment with non-negligible fall velocity in turbulent open channel flow (Chang 1988, pp149). The Rouse equation was fitted at each time step using least squared error minimization with the *TSS* derived from LASS. *Qss* in Figure 6E corresponds well with the irradiance measurements and *TSS* estimates, and *Qss* increases from 5:00 pm until 5:10 pm then decreases until about 5:35 pm and continues to increase until the end of the sampling period.

Independent field measurements of *TSS* (i.e. grab samples) that were collected during the field demonstration compared very well with the power law in Figure 5. One grab sample had *TSS* equal to 38.5 mg l^{-1} and was collected simultaneously with the field deployed LASS measurements that estimated K_d equal to 1.53 m^{-1}. The power law scaling in Figure 5 provided a K_d estimate equal to 1.51 (± 0.9) m^{-1} when *TSS* is equal to 38.5 mg l^{-1}, showing very good agreement between the power law and the field deployed LASS. Similarly, a second grab sample had a *TSS* value equal to 74 mg l^{-1} and was collected simultaneously with the field deployed LASS measurements that estimated K_d equal to 2.3 m^{-1}. The power law scaling in Figure 5 provided a K_d estimate equal to 2.4 (± 0.9) m^{-1} when *TSS* is equal to 74 mg l^{-1}, again showing very good agreement between the power law and the field deployed LASS. However, further validation of LASS for a wider range of flow conditions as presented in the Field Demonstration will be important in future work, and the results presented in this paper suggest the efficacy of LASS for such conditions.

The field demonstration results show the utility of the LASS method for future

application, but we also point out that the demonstration allowed us to see some potential limitations of LASS that should be further considered in future applications. First, the rising limb of the hydrograph was accompanied by a notable increase in debris including limbs, leaves, and trash which fouled the sampling equipment and sensors. In the future, better precautions including angling the LASS mounts are necessary to prevent sensor fouling, especially in watersheds dominated by deciduous trees during autumn sampling routines. Second, high flow events pose a threat to the equipment as was evident by the loss of sensors during a subsequent event not reported here. Often the most costly aspect of field deployment is the personnel cost associated with sensor deployment and maintenance. That said, loss of instrumentation during extreme events poses a problem to hydraulic field measurement in general and the inexpensive cost of the LASS (see Table 1) at least partially alleviates the monetary losses. Future field deployment of LASS offers the possibility to study a wide variety of hydraulic engineering topics including suspended sediment transport in river confluences, and it is our intent to pursue a research agenda in this topic area.

6.9 CONCLUSIONS

The major findings of this study were as follows. (1) The light attenuation coefficient measured by LASS shows utility for measuring *TSS* in streams and is promising for future field application. (2) A dimensionless relationship for light attenuation by sediment is derived and verified, and suggests that the diffuse light attenuation coefficient can be estimated for conditions such as that in streams using properties of light, water and sediment.

The inexpensive light attenuation sensor for sediment (LASS) presented here shows the ability to estimate suspended sediment concentration and transmit measurements wirelessly. The inexpensive wireless LASS are well suited for use within highly instrumented stream monitoring networks. The inexpensive sensor allows LASS to monitor at finer spatial resolution than is possible with traditional monitoring techniques, and monitoring could be conducted from the smallest tributary catchments within the watershed allowing quantification of sediment sources. The inexpensive nature of LASS is an obvious advantage of the sensors, and other commercially available sensors that provide a surrogate of suspended sediment concentration are one to two

orders of magnitude more expensive than the LASS (see Table 1). The wireless capabilities of LASS are another possible advantage and make it easier to integrate data collected at fine spatial scales across different levels of resolution to meet the goals of watershed monitoring efforts. Another potential advantage of LASS is related to its relatively large sampling volume. The small measuring volume of turbidity probes and optical backscatter sensors enables these sensors to provide at-a-point surrogate measurement to *TSS*, which may not be representative of the mean cross-sectional TSS (Gray and Gartner, 2009). The larger measuring volume of LASS provides a potential alternative and a more representative measurement for estimating suspended sediment flux.

One limitation of LASS is its dependence on an ambient light source to measure the attenuation of diffuse light. Practically speaking, this problem could be corrected by adding an artificial light source located above the free surface for nighttime measurements. That said, hydraulic sampling networks will likely be coupled with numerical modeling, so highly distributed daytime measurements may provide ample amounts of data for model calibration and validation. Another limitation of LASS is potential damage or fouling by debris during sampling in any stream however certain site specific characteristics may tend to embody this problem. To circumvent these limitations, the field deployment of LASS should consider site selection and sensor arrangement within the flow to avoid impact with debris.

The results of Figure 5 suggest that a more general formulation for light attenuation by sediment is found when calibrating to the dimensionless parameter that represents sediment area concentration, for the conditions tested. LASS is shown to be capable of measuring *TSS* up to approximately 1000 mg l^{-1}, which is often near the maximum suspended load in small order streams. Low order streams tend to be characterized by highly turbulent flows that transport primarily tightly bound or disaggregated inorganic sediment particles with characteristics similar to that of the parent soil. To this end, we point out that the dimensional analysis and subsequent experiments were conducted assuming a negligible contribution to light attenuation by dissolved substances.. Extrapolation of the analysis and results presented in this paper to waters with high concentrations of dissolved matter, e.g., humic or fulvic substances,

may not be applicable without further validation beyond the experimental conditions in this study. Sediments tested during experiments contained small amounts of organic matter (<3 gC/100g sed) tightly bound to the inorganic sediment particles within sediment aggregates, and the applicability of the dimensionless scaling in Equation (4) to include organic-dominated sediments and biologic particles is currently untested.

Light attenuation is significantly affected by high concentrations of dissolved and particulate organic matter, and future work to examine the dimensionless relationship in Figure 5 for these conditions will be welcomed.. Low order streams, especially those draining standing water, inundated floodplains and wetlands, may have high concentrations of CDOM requiring further investigation of the relationship between light attenuation, water and sediments. For example researchers have found *CDOM* to account for most of the attenuated light in large blackwater rivers such as St. John's River (Phlips et al., 2000). *POM* in lakes or estuaries may be the dominant light attenuating constituent where large phytoplankton populations exist and inorganic particulates have mostly settled out of the water column (Phlips et al., 1995a; Phlips et al., 1995b; Christian and Sheng, 2003). To this end, the refractive index in Equation (4) might be used to provide a set of curves or nomograph for varying levels of organic constituents. Organic-dominated sediment particles and flocs are expected to have lower density and lower refractive index causing them to interact with light mainly through absorption. Inorganic-dominated sediment particles and aggregates are expected to be denser, have higher refractive index, and scatter more light than biologic particles. For example, recent research on beam attenuation and scattering by particles conducted by Neukermans et al. (2012) found that inorganic particles have about three times greater scattering efficiency than organic particles. We are hopeful that the dimensional analysis provided here can lead to further investigations of such scenarios. The inexpensive LASS presented here offer the possibility for high density measurements for estimating light attenuation, which will be useful to engineers for modelling suspended sediment transport and aquatic ecologists modelling light availability for photosynthesis in streams. As the understanding of light attenuation principles continue to improve, LASS may fulfill the growing need for inexpensive high frequency measurements within densely sensed stream monitoring efforts.

6.10 ACKNOWLEDGEMENTS

We would like to thank all of the people who worked on this project including the both the graduate and undergraduate students. We are thankful for the comments of one of the anonymous reviewers and the Associate Editor, which have greatly improved the quality of this paper. We acknowledge National Science Foundation project #0918856 and the University of Kentucky, Department of Civil Engineering for financial support of students.

6.11 LIST OF SYMBOLS

A_j = the projected area of each particle available to intercept light

c_1 = first coefficient of the power law

c_2 = exponent coefficient in the power law

CDOM= chromophoric dissolved organic matter

d = size distribution of suspended sediment

e = entrained air

f = function

E = irradiance

E_0 = irradiance when the light path is zero

Q = stream flow rate

Q_{ss} = suspended sediment flux

ISS = total inorganic suspended sediment concentration

j = number of particle size classes

K_d = downward vertical diffuse light attenuation coefficient

K_w = the light attenuation coefficient due to water and dissolved substances

z = vertical distance between measurements of E

z_1 = depth of top most sensor below water surface

z_2 = depth of 2nd sensor below water surface

LASS = light attenuation sensors for sediments

n = refractive index of sediment particles relative to water

POM = particulate organic matter

PHYTO= the concentration of phytoplankton

T_E = relative irradiance $E\ E_0^{-1}$

TSS = total suspended sediment concentration

Q_j = dimensionless attenuation efficiency factor

α = angle of incident light relative to the free surface

λ = wavelength of the incident light in free space

ρ_s = suspended sediment density

σ = standard deviation

6.12 REFERENCES

Babin, M., & Stramski, D. (2004). Variations in the mass-specific absorption coefficient of mineral particles suspended in water. *Limnology and Oceanography*, 49(3), 756-767.

Bohren, C. F., & Huffman, D. R. (2008). *Absorption and scattering of light by small particles*. (Wiley, 2008).

Bunt, J. A., Larcombe, P., & Jago, C. F. (1999). Quantifying the response of optical backscatter devices and transmissometers to variations in suspended particulate matter. *Continental Shelf Research*, 19(9), 1199-1220.

Chang, H. H. 1988. *Fluvial processes in river engineering*, Wiley, New York.

Chao, X., Jia, Y., Shields, D. F., Wang, S. S., & Cooper, C. M. (2009). Numerical simulation of sediment-associated water quality processes for a Mississippi delta lake. *Ecohydrology*, 2(3), 350-359.

Christian, D., & Sheng, Y. P. (2003). Relative influence of various water quality parameters on light attenuation in Indian River Lagoon. *Estuarine, Coastal and Shelf Science*, 57(5), 961-971.

Clavano, W.R., Boss, E., & Karp-Boss, L., (2007). Inherent Optical Properties of Non-Spherical Marine-Like Particles- From Theory to Observation. *Oceanography and Marine Biology: An Annual Review*, 45, 1-38

Clifford, N. J., Richards, K. S., Brown, R. A., & Lane, S. N. (1995). Laboratory and field assessment of an infrared turbidity probe and its response to particle size and variation in suspended sediment concentration. *Hydrological Sciences Journal*, 40(6), 771-791.

Davies-Colley, R.J. Vant, W.N. and Smith, D.G. 2003: Colour and clarity of natural waters. Science and management of optical water quality. Blackburn Press, New Jersey. 310p.

Davies-Colley, R. J., & Smith, D. G. (2001). Turbidity, suspended sediment, and water clarity: a review. *JAWRA Journal of the American Water Resources Association*, 37(5), 1085-1101.

Davies-Colley, R.J. and J.W. Nagels 2008. Predicting Light Penetration Into River Waters. *Journal of Geophysical Research-Biogeosciences* 113:G03028, doi: 03010.01029/02008JG000722.

Downing, J. P., & Beach, R. A. (1989). Laboratory apparatus for calibrating optical suspended solids sensors. *Marine Geology*, 86, 243-249.

Doxaran, D., Ruddick, K., McKee, D., Gentili, B., Tailliez, D., Chami, M., & Babin, M. (2009). Spectral variations of light scattering by marine particles in coastal waters, from visible to near infrared. *Limnology and oceanography*, 54(4), 1257-1271.

Fox, James F., Charles M. Davis, and Darren K. Martin, 2010. "Sediment Source Assessment in a Lowland Watershed Using Nitrogen Stable Isotopes." Journal of the American Water Resources Association (JAWRA) 46(6):1192-1204. DOI: 10.1111 / j.1752 1688.2010.00485.x

Ford, W. I., & Fox, J. F. (2014). Model of particulate organic carbon transport in an agriculturally impacted stream. *Hydrological Processes*. 28(3), 662-675, DOI: 10.1002/hyp.9569

Glasgow, H. B., Burkholder, J. M., Reed, R. E., Lewitus, A. J., & Kleinman, J. E. (2004). Real-time remote monitoring of water quality: a review of current applications, and advancements in sensor, telemetry, and computing technologies. *Journal of Experimental Marine Biology and Ecology*, 300, 409-448.

Gray, J. R., and J. W. Gartner (2009), Technological advances in suspended-sediment surrogate monitoring, *Water Resources Research*, 45, W00D29, doi:10.1029/2008WR007063.

Harnett, C. K., Schueler, M. T., Blumenthal, N. R., Hopf, K. L., Fox, J. F., & Pulugurtha, S. (2011). Calibration and field deployment of low-cost fluid flow-rate sensors using a wireless network. *Instrumentation and Measurement, IEEE Transactions on*, 60(2), 633-641.

Hart, J. K., & Martinez, K. (2006). Environmental Sensor Networks: A revolution in the earth system science?. *Earth-Science Reviews*, 78(3-4), 177-191.

Hill, P. S., Boss, E., Newgard, J. P., Law, B. A., & Milligan, T. G. (2011). Observations of the sensitivity of beam attenuation to particle size in a coastal bottom boundary layer. *Journal of Geophysical Research: Oceans* 116, (C02023), doi:10.1029/2010JC006539.

Horsburgh, J. S., Spackman Jones, A., Stevens, D. K., Tarboton, D. G., & Mesner, N. O. (2010). A sensor network for high frequency estimation of water quality constituent fluxes using surrogates. *Environmental Modelling & Software*, 25(9), 1031-1044.

Julian, J. P., Doyle, M. W., Powers, S. M., Stanley, E. H., & Riggsbee, J. A. (2008). Optical water quality in rivers. *Water Resources Research*, 44, W10411, doi:10.1029/2007WR006457.

Julian, J. P., M. W. Doyle, and E. H. Stanley (2008b), Empirical modeling of light availability in rivers, *Journal of Geophysical Research*, 113, G03022, doi:10.1029/2007JG000601.

Kirk, J. T. O., (1981). A Monte Carlo study of the nature of the underwater light field in, and the relationships between optical properties of, turbid yellow waters. *Australian Journal of Marine and Freshwater Research*, 32(4) 533-9.

Kirk, J. T. O. (1984). Dependence of relationship between inherent and apparent optical properties of water on solar altitude. *Limnology and Oceanography*, 29(2), 350-356

Kirk, J. T. O. _1994_ *Light and photosynthesis in aquatic ecosystems*, Cambridge University Press, Cambridge, U.K.

Kohavi, R. (1995). A study of cross-validation and bootstrap for accuracy estimation and model selection. In *Prodeedings of the Fourteenth International Joint Conference on Artificial Intelligence* (Vol. 14, No. 2, pp. 1137-1145)

Larios, D. F., Barbancho, J., Sevillano, J. L., Molina, F. J., & Leon, C. (2012). Energy efficient wireless sensor network communications based on computational intelligent data fusion for environmental monitoring. Communications, IET, 6(14), 2189-2197, doi: 10.1049/iet-com.2011.0809

Liu, Wen-Cheng, Ming-Hsi Hsu, Shu-Yi Chen, Chi-Ray Wu, and Albert Y. Kuo, 2005. Water Column Light Attenuation in Danshuei River Estuary, Taiwan. *Journal of the American Water Resources Association* (JAWRA) 41(2):425-435.

Mishra, D. R., Narumalani, S., Rundquist, D., & Lawson, M. (2005). Characterizing the

vertical diffuse attenuation coefficient for downwelling irradiance in coastal waters: Implications for water penetration by high resolution satellite data. Journal of Photogrammetry and Remote Sensing (ISPRS), 60(1), 48-64. doi:10.1016/j.isprsjprs.2005.09.003

Mobley, C. D. (1994). *Light and water: Radiative transfer in natural waters* (Academic press, San Diego).

Naiman, R. J., & Bilby, R. E. (Eds). (1998). *River ecology and management: lessons from the Pacific coastal ecoregion*. (Springer, New York).

Neukermans, G., Loisel, H., Mériaux, X., Astoreca, R., & McKee, D. (2012). In situ variability of mass-specific beam attenuation and backscattering of marine particles with respect to particle size, density, and composition. *Limnology and Oceanography*, 57(1) 124-144.

Phlips, E. J., Lynch, T. C., & Badylak, S. (1995a). Chlorophyll a, tripton, color, and light availability in a shallow tropical inner-shelf lagoon, Florida Bay, USA. *Marine ecology progress series*, 127(1), 223-234.

Phlips, E. J., Aldridge, F. J., Schelske, C. L., & Crisman, T. L. (1995b). Relationships between light availability, chlorophyll a, and tripton in a large, shallow subtropical lake. *Limnology and Oceanography*, 40(2), 416-421.

Phlips, E. J., Cichra, M., Aldridge, F. J., Jembeck, J., Hendrickson, J., & Brody, R. (2000). Light availability and variations in phytoplankton standing crops in a nutrient-rich blackwater river. *Limnology and Oceanography*, 45(4), 916-929.

Pollack, J. B., & Cuzzi, J. N. (1980). Scattering by non-spherical particles of size comparable to a wavelength: A new semi-empirical theory and its application to tropospheric aerosols. *Journal of the Atmospheric Sciences*, 37(4), 868-881.

Rundel, P. W., Graham, E. A., Allen, M. F., Fisher, J. C., & Harmon, T. C. (2009). Environmental sensor networks in ecological research. *New Phytologist*, 182 (3), 589-607.

Squires, M. M., & Lesack, L. F. (2003). Spatial and temporal patterns of light attenuation among lakes of the Mackenzie Delta. *Freshwater Biology*, 48(1), 1-20.

Stavn, R. H. (2012). Mass-specific scattering cross sections of suspended sediments and aggregates: theoretical limits and applications. *Optics Express*, 20(1), 201-219.

Stramski, D., Babin, M., & Wozniak, S. B. (2007). Variations in the optical properties of terrigenous mineral-rich particulate matter suspended in seawater. *Limnology and Oceanography*, 52(6), 2418-2433.

Sunita, M., Malik, J., & Mor, S. (2012). Comprehensive Study of Applications of Wireless Sensor Network. *International Journal of Advanced Research in Computer Science and Software Engineering,* 2 (11), 56-60

van de Hulst, H. C., (1981). *Light scattering: by small particles*. (Dover, New York).

Van Duin, E. H. S., Blom, G., Los, F. J., Maffione, R., Zimmerman, R., Cerco, C. F., Dortch, M., & Best, E. P. H. (2001). Modeling underwater light climate in relation to sedimentation, resuspension, water quality and autotrophic growth. *Hydrobiologia*, 444, 25-42.

Vannote, R. L., Minshall, G. W., Cummins, K. W., Sedell, J. R., & Cushing, C. E. (1980). The river continuum concept. *Canadian Journal of Fisheries and Aquatic Sciences*, 37, 130-137.

Walling, D. E., Collins, A. L., Jones, P. A., Leeks, G. J. L., & Old, G. (2006). Establishing fine-grained sediment budgets for the Pang and Lambourn LOCAR catchments, UK. *Journal of Hydrology*, 330, 126-141.

Wang, N., Zhang, N., & Wang, M. (2006). Wireless sensors in agriculture and food industry—Recent development and future perspective. *Computers and Electronics in Agriculture*, 50(1), 1-14.

Williams, N. D., Walling, D. E., & Leeks, G. J. L. (2008). An analysis of the factors contributing to the settling potential of fine fluvial sediment. *Hydrological Processes*, 22(20), 4153-4162.

Wozniak, S. B., Stramski, D., Stramska, M., Reynolds, R. A., Wright, V. M., Miksic, E. Y., Cichocka, M., & Cieplak, A. M. (2010). Optical variability of seawater in relation to particle concentration, composition, and size distribution in the nearshore marine environment at Imperial Beach, California. *Journal of Geophysical Research: Oceans,* 115, C08027.

Yick, J., Mukherjee, B., & Ghosal, D. (2008). Wireless sensor network survey. *Computer Networks*, 52(12), 2292-2330.

6.13 TABLES AND FIGURES

Table 6.1. Measurements Comparing the Price of LASS with Other Instruments

Sensor	Cost	Manufacturer	TSS Surrogate	Other Measurement†
Dual Li-Cor LI-192	$18,522	YSI/Li-Cor	Light attenuation	*T*, *Cond*,
ECO-PAR	$5,835	WETLabs	Light attenuation	n/a
LASS*	$225	Current Study	Light attenuation	n/a
ECO NTU	$6,975	WETLabs	Turbidity	n/a
AQ703 Multi-Probe	$6,595	ISCO	Turbidity	*T*, *H*, *Cond*, *pH*, *DO*
2100Q	$1,010	HACH	Turbidity	n/a

† *T* is temperature; *Cond* is conductivity; *H* is water depth; and *DO* is dissolved oxygen concentration.

*Note: LASS price includes 3 irradiance sensors, 3 temperature sensors, and wireless data transmitter.

Table 6.2. Tests Grouped into Repetitions for the Range of 25 Test Conditions

Test	d (µm)	$TSS \pm 1$STD (mg l^{-1})	$K_d \pm 1$STD (m^{-1})	Repetitions
1	10.5	2 ± 1	0.10 ± 0.61	3
2	10.5	3 ± 1	0.30 ± 0.92	3
3	10.5	31 ± 13	0.83 ± 0.26	7
4	10.5	40 ± 2	2.45 ± 0.09	2
5	10.5	50 ± 10	2.26 ± 0.38	9
6	10.5	51 ± 3	1.75 ± 0.10	2
7	10.5	66 ± 3	3.74 ± 0.10	2
8	10.5	75 ± 13	2.53 ± 0.29	9
9	10.5	112 ± 8	3.63 ± 0.73	2
10	10.5	186 ± 4	5.60 ± 0.13	3
11	10.5	349 ± 10	7.11 ± 0.34	3
12	10.5	353 ± 15	8.61 ± 0.39	3
13	10.5	480 ± 25	9.74 ± 0.56	3
14	14.2	20 ± 9	0.15 ± 0.32	6
15	14.2	47 ± 11	0.69 ± 0.29	6
16	14.2	92 ± 12	1.12 ± 0.28	6
17	14.2	187 ± 9	2.54 ± 0.24	6
18	14.2	347 ± 11	3.37 ± 0.26	6
19	14.2	672 ± 54	4.48 ± 0.20	4
20	27.2	30 ± 14	0.11 ± 0.25	3
21	27.2	42 ± 2	0.44 ± 0.21	3
22	27.2	63 ± 5	0.92 ± 0.18	2
23	27.2	140 ± 9	1.63 ± 0.20	3
24	27.2	272 ± 21	2.28 ± 0.19	3
25	27.2	535 ± 26	3.09 ± 0.19	3

Note: ρ_s of 10.5 µm sediments is 1,800 kg m^{-3} ;ρs of 14.5- and 27.2 µm sediments is 2,650 kg m-3

Figure 6.1. (a) A vertical distribution of irradiance measured by LASS and the calculation used to estimate Kd; (b) a photograph of a LASS photocell; (c) the schematic of the LASS circuit diagram

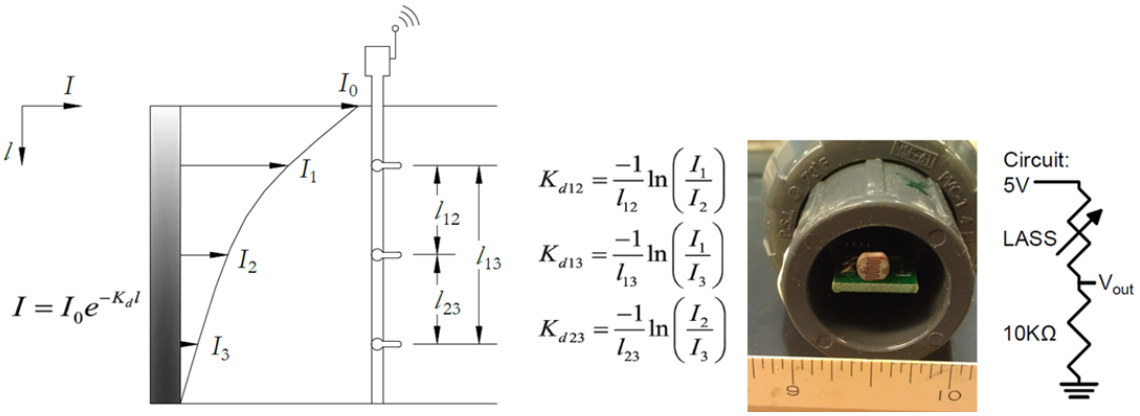

Figure 6.2 The LASS testing apparatus

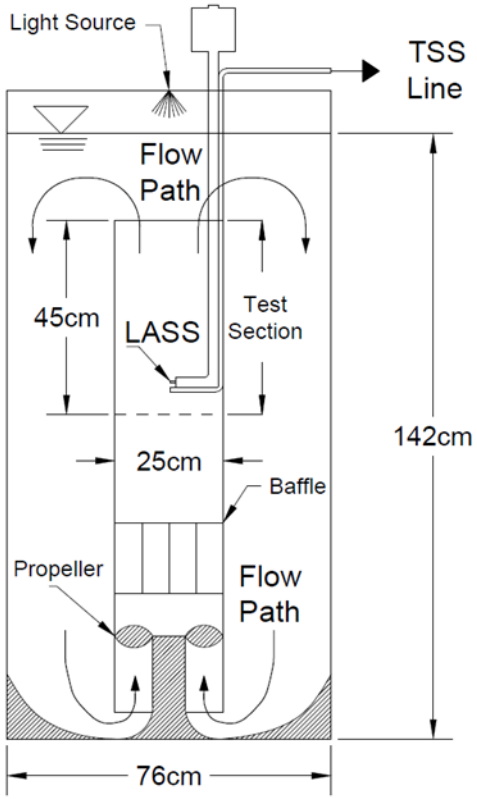

Figure 6.3 Particle size distributions of laboratory tested sediments

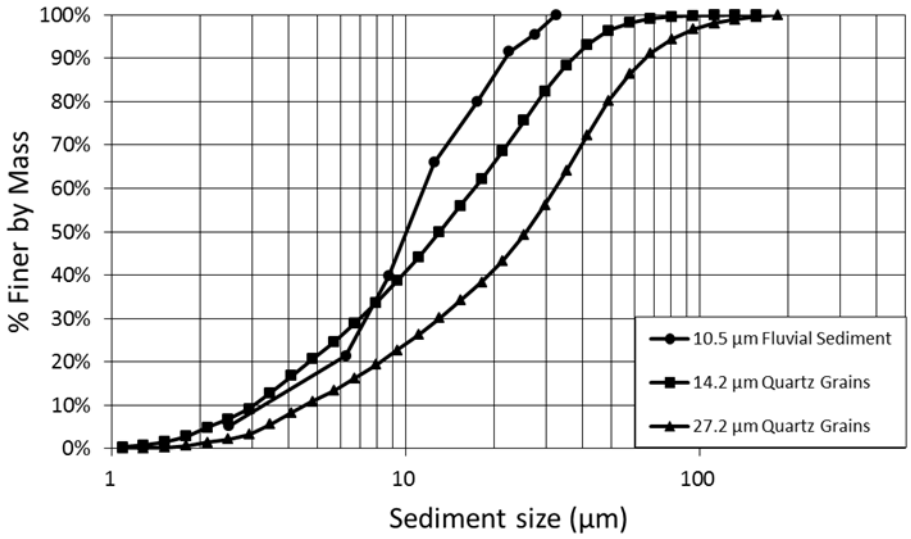

Figure 6.4 Distribution of Kd versus TSS for laboratory experiments (data shown with ±1 standard deviation)

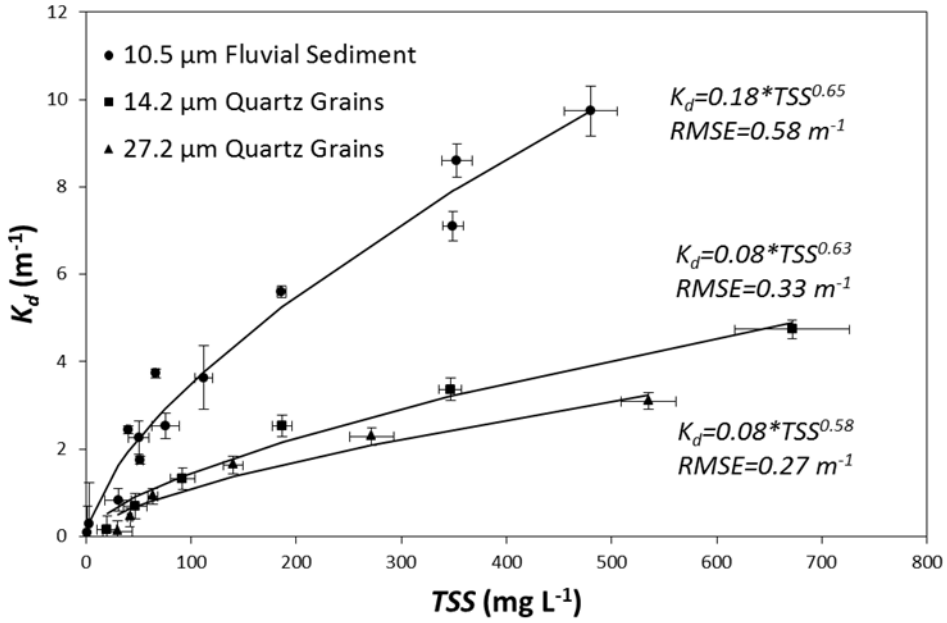

Figure 6.5 Collapse of Kd due to the dimensionless scaling (depicts light attenuation data presented in dimensionless form along with the power law equation 8 fit using the k-fold cross validation with k equal to 5)

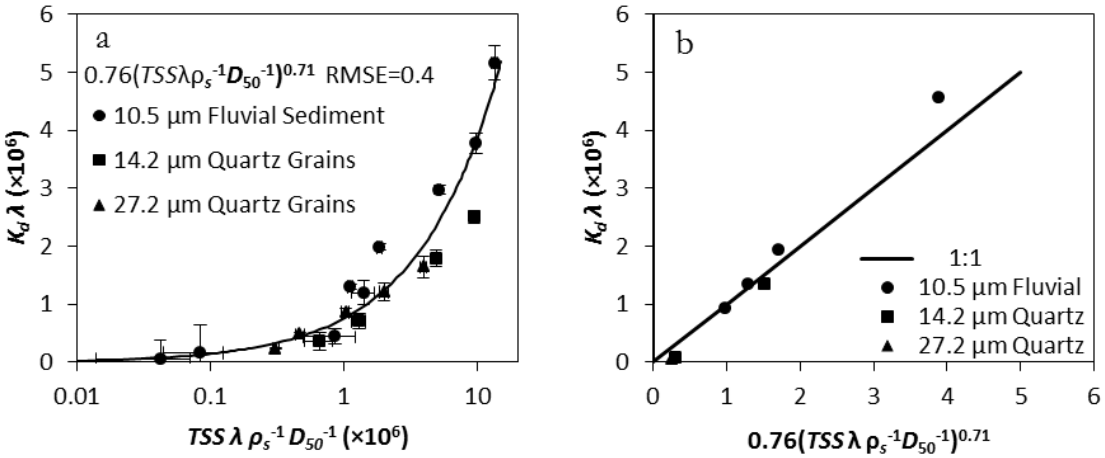

Figure 6.6 Field demonstration of LASS: (a) graduate researchers conducting field measurements and schematic of the field-deployed LASS (an offset was used for the field-deployed LASS to reduce potential shadowing at very low TSS); (b) stream flow rate; (c) LASS output at specified distance above the bed; (d) TSS calculated from LASS measurements using the laboratory calibration curve; (e) calculated suspended sediment load using LASS measurements

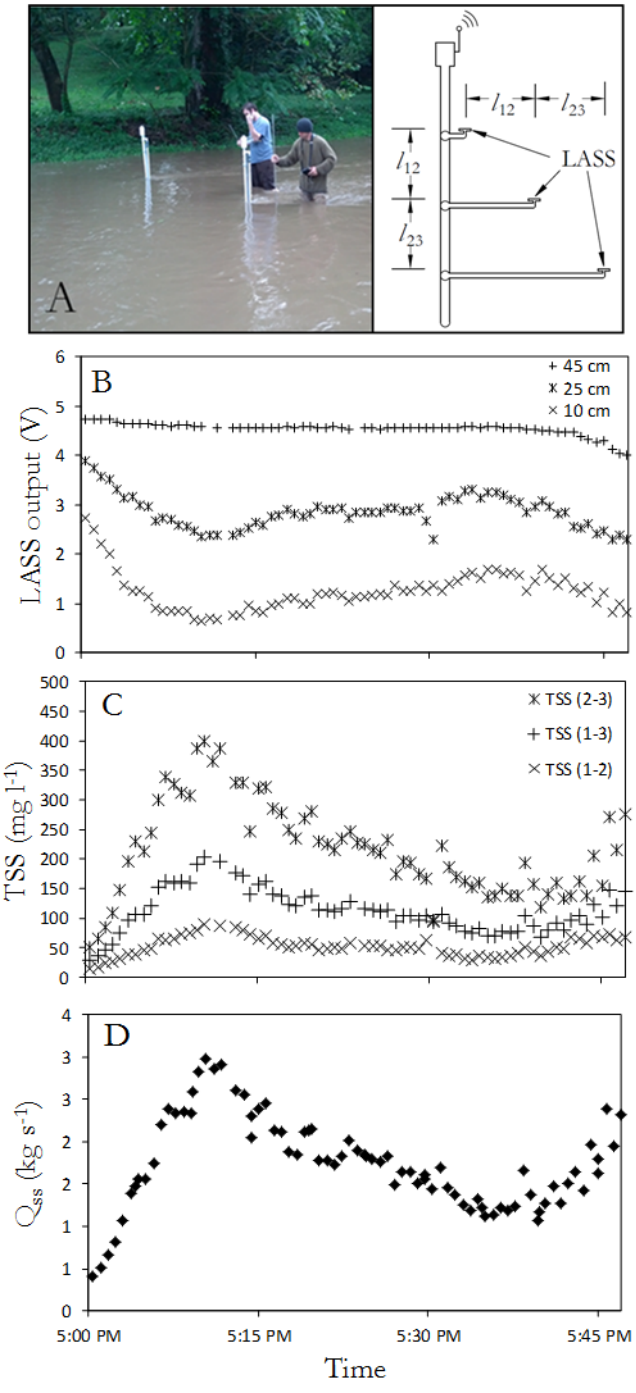

Chapter 7: Dimensionless Scaling of Diffuse Light Attenuation by Suspended Sediment

7.1 SUMMARY

Primary production in some of the world's most diverse and productive aquatic ecosystems is governed by the concentration and physical properties of suspended sediments that absorb and scatter light. However, there is a lack of prediction models that relate light attenuation to concentration and physical properties of suspended sediments. We test scaling of the dimensionless light attenuation coefficient against the dimensionless number for light attenuation by sediment using 13 published datasets including 1341 data points from rivers, lakes and estuaries. The data was clearly divided into two functions: one linear and one non-linear, both of which collapse the data well. 90% of the data falls within the linear region, which includes data from lakes and estuaries where sediments likely have low refractive indices and absorb light well. An analytical approach is formulated to provide a linear equation for the light attenuation by sediments that agrees exactly with our empirical scaling in the linear region and provides confidence that our scaling can be used for future applications in lakes and estuaries. The non-linear region includes data from rivers, lakes, and an estuary suggests secondary process of shadowing and backscattering associated with scattering properties of inorganic suspended sediments. Future research of this latter process is needed to provide a predictive nomograph for highly scattering sediments based on the dimensionless number for light attenuation by sediments.

7.2 INTRODUCTION

Diffuse optical sensors that estimate attenuation of natural light by particles in water have been widely used to study light availability for biologic activities due to its impact on aquatic ecosystem health and nutrient cycling (Cloern 1987; Kirk 1994; Mobley 1994; Davies-Colley et al. 2003; Chao et al., 2010; Stewart et al. 2014). Diffuse light in the PAR (400-700nm) wavelength spectrum is most commonly studied as these wavelengths of light are relevant for photosynthesis by algae and macrophytes (Kirk, 1994, Hauer and Lamberti, 2006). Often the objective of these ecohydrology studies is to estimate light levels in the aquatic ecosystem from available data sets of suspended sediment concentration which is commonly measured and regularly cited as being the

most significant light attenuating constituent in turbid waters (Cloern 1987; Lawson et al., 2007; Painting et al., 2007; Devlin et al., 2009). Because light attenuation by sediment in turbid waters limits photosynthetic production in lakes, estuaries and rivers, modeling tools that couple hydrodynamic and biological processes will be useful to ascertain new knowledge regarding topics such as hydrologic extremities and their impact on primary producers in lakes and estuaries and CO_2 degassing under conditions with high sediment loads. A model of the interactions between water, its constituents and light is essential when using diffuse optical sensor measurements to estimate system wide photosynthetic conditions. Despite the water resources research community's interest in light attenuation, there is a lack of reliable models to assist with estimating diffuse light attenuation by sediments in water and researchers must typically rely on a site specific relationship (Lund-Hansen et al. 2010). The motivation of this paper is appropriate dimensionless scaling of the diffuse light attenuation problem that works towards a dimensionless relationship that will be useful in future application and research.

Light attenuation in water is described by the exponential function derived theoretically by van de Hulst (1981) and verified experimentally (Gordon, 1989) as

$$E(z) = E_0 e^{-K_d z} \tag{1}$$

Equation (1) describes the propagation of light in water where E and E_0 are the irradiances at depth z and just below the surface respectively, and K_d is the diffuse light attenuation coefficient. Previous work provides an understanding of parameters likely to impact light attenuation by sediment in water; and thus impact K_d (Kirk 1994; Mobley 1994; Davies-Colley and Nagels, 2008; Julian et al., 2008; Stavn 2012). For example, a number of authors have shown mass specific optical measurements of scattering and beam attenuation to depend on particle diameter (Baker and Lavelle, 1984; Bunt et al., 1999; Wozniak et al. 2010). Further, a number of recent studies suggest that variability in mass specific absorption and scattering is almost entirely explained by the product of particle density and diameter (Boss et al., 2009; Bowers et al., 2009; Neukermans et al., 2012; and Stavn, 2012). While previous research of diffuse light attenuation in water recognizes the importance of sediment size and density (Biggs et al. 1983; Liu et al. 2005; Lawson et al. 2007, Lund-Hansen et al. 2010), few studies have investigated the proper dimensionless scaling of K_d in order to provide a more widely usable model of the

attenuation process. Typically, field studies rely on site specific, empirical parameterization of K_d as a function of total suspended sediment load (*TSS*).

Recently, Stewart et al. (2014) performed dimensional analysis and provided a dimensionless light attenuation coefficient and dimensionless number for light attenuation by sediments that may be useful in scaling K_d based on sediment and light properties. In their study, Stewart et al. (2014) found a consistent relationship between their datasets and showed the ability of the dimensionless numbers to collapse the data to a single curve, however, the experimental dataset was heavily limited with respect to the sediment conditions. Our objective in this paper was to test the dimensionless scaling of light attenuation by sediments for a wide range of published datasets from rivers, lakes and estuaries in order to work towards a consistent set of curves that may be useful for application and future research.

7.3 METHODS

7.3.1 Dimensional Analysis

We revisit and briefly describe the dimensional analysis by Stewart et al. (2014), and we make some revisions with regards to relaxing assumptions and better defining light attenuation by sediment in order to provide a more robust model. The light attenuation coefficient, K_s, associated with organic and inorganic particulates, i.e., sediments, in the water column can be isolated as

$$K_s = K_d - K_w \,, \tag{2}$$

where K_d is the total light attenuation coefficient as measured with an optical sensor and K_w is light attenuation coefficient associated with water and its dissolved constituents. In this manner, K_w includes attenuation due to entrained air, transported dissolved gases, benthic derived dissolved organic matter, water color and chromophoric dissolved organic matter. K_d and hence K_s is an apparent optical property of the medium and dependent upon the light field However it has been shown that the apparent optical properties of open water are impacted little by the angle of a diffuse light source and rather depend primarily on the wavelength, λ, of the incident light in free space (Kirk 1994; Davies-Colley and Smith 2001). Therefore, K_s can be expressed as a functional dependence of light and sediment variables as

$$K_s = fn\left[\{\lambda\},\{TSS,\rho_s,d,n\}\right], \quad (3)$$

where the first bracket is the light term and second bracket includes sediment parameters. *TSS* in Equation (3) is the total suspended sediment concentration in water (kg m^{-3}); ρ_s is the suspended sediment density; d is the diameter of suspended sediment, and n is the refractive index of the sediment particles.

From Equation (3), we select λ, as a repeating variable due to the consideration that λ accounts for the dependence of absorption and scattering by water and sediments upon the energy of light (Kirk 1994; Babin and Stramski 2004; Stramski et al. 2007; Doxaran et al. 2009; Wozniak et al. 2010). We use dimensional analysis to produce the following dimensionless products

$$K_s\lambda = fn\left[\{n\},\left\{\frac{TSS\lambda}{\rho_s d}\right\}\right]. \quad (4)$$

Equation (4) relates the dimensionless light attenuation coefficient to dimensionless numbers including the refractive index and the dimensionless number for light attenuation by sediment. This last term in Equation (4) represents the dimensionless sediment surface area available to interact with light. The semi-empirical result from the dimensional analysis qualitatively agrees with numerous empirical studies that show direct dependence of *TSS* upon K_d and inverse dependence of ρ_s and d upon K_d (e.g., Bunt et al. 1999; Neukermans et al. 2012).

Stewart et al. (2014) showed the relationship between the terms in Equation (4) to behave as a non-linear function for a small set of primarily inorganic dominated sediments, however the form of Equation (4) for different sediment types in water remains an open question. For example, the constituents of inorganic suspended sediment, non-algal particulate organic matter and phytoplankton within the sediment mixture would be expected to impact both n and ρ_s and perhaps provide a set of relationships. This idea stems from the fact that suspended sediments can exist in aquatic ecosystems as individual grains termed primary particles, water stable soil aggregates formed in the uplands, or flocs formed in situ (Droppo et al. 2005). Light typically interacts with the surface of these particles leaving the internal matter shadowed (Latimer, 1985; Boss et al. 2009), and interactions with particles are the result of the

coupled scattering and absorption processes (Bohren and Huffman, 1998). The degree at which particles scatter light relative to absorption is determined by the particulate composition which controls the refractive index n. Primary particles and water stable aggregates composed of mostly dense inorganic material with high refractive index n scatter light strongly. Flocs formed in the water column by incorporating organic material into a loosely packed matrix with low refractive index attenuate light more strongly through absorption. Therefore, the functional behavior of Equation (4) is expected to reflect compositional and structural variations between primary particles, water stable aggregates, and flocs.

7.3.2 Data Meta-analysis

We gathered diffuse light attenuation datasets from the peer-reviewed literature to test the functional dependence of the scaling in Equation (4). A total of 55 peer-reviewed articles were found within the broad topic of light attenuation in water within the body of literature encompassing estuary, lakes, rivers and coastal sciences and engineering. From the published articles, we were able to find 13 datasets that had sufficient information for estimating central values from distributed spatial or temporal samples for K_s, λ, TSS, ρ_s, and d and thus test the dimensionless scaling in Equation (4). Unfortunately we did not find any published studies that measured n for their samples.

1341 samples were used in this analysis and were from a range of stream, lake, and estuary studies. The characteristics of the studies are compiled in Table 1. The data were all collected in the northern hemisphere and mostly from subtropical and temperate climates with the exception of two data sets coming from the arctic regions of Canada and Greenland. Data were from Biggs et al., (1983) abbreviated as Bi, Cloern (1987) as Cl, Colijn (1982) as Co, Devlin et al. (2008) as De, Lund-Hansen et al. (2010) as LH, Stump and Pennock (1991) as SP, Chao et al. (2010) as Ch, Squires and Lesack (2003) as SL, Stewart et al. (2014) as St and Zhang et al. (2007) as Zh.

Two data sets from Biggs et al., (1983) included 113 points collected longitudinally throughout the Delaware Estuary in Delaware and New Jersey, USA during 1978-1981. The Biggs et al. (1983) datasets are distinguished by two separate relationships between K_d and TSS resulting from a difference in particle size. The Bi1 data set from Biggs et al. (1983) was collected from the lower turbidity maximum where

sediments were comprised of larger particles. The other subset, Bi2 was collected from the river and lower bay where sediments were comprised of smaller particles.

The dataset from Chao et al., (2010) consisted of 17 points collected at three locations approximately every two weeks from January to March, 2004 in Deep Hollow Lake Mississippi, USA. Deep Hollow Lake is a shallow oxbow lake located on alluvial flood plain with the majority of its suspended sediment derived from agricultural lands.

The dataset from Cloern (1987) contained 417 points collected at 30 fixed sites sampled twice monthly during 1980 from the San Francisco Bay, in central California USA. The San Francisco Bay comprises two distinct estuaries: the northern reach is representative of partially mixed estuaries with well-developed gravitational circulation and a turbidity maximum during summer; the southern reach is a lagoon-type estuary with no large, direct source of freshwater.

The dataset from Colijn (1982) consisted of eight temporally averaged data points collected at eight locations in the Ems-Dollard estuary. The estuary is located on the border of western Germany and the eastern Netherlands. The Ems river basin is located in the North-German Plain where agriculture accounts for about 62% of the land use and groundwater accounts for about 20-40% of the total runoff (Gommann et al. 2005).

The dataset from Devlin et al. (2008) consisted of 382 spatially distinct data points collected between August 2004 and December 2005 from transitional, coastal, and offshore waters near the United Kingdom. These samples were predominantly obtained from coastal waters (approximately 70%) and the remaining samples were collected from transitional waters and offshore waters. Devlin et al. (2008) described transitional waters in the vicinity of river mouths which are partly saline in character, the typical salinity range is between freshwater and 30 ppt. Coastal waters were defined as waters within 1 nautical mile of the coast excluding transitional. The Thames Estuary and surrounding coastal region was heavily sampled; the sampling pattern then traverses north along the coast to Sunderland then moves offshore into the north and head south remaining in offshore waters until moving back into the transitional and coastal waters near Portsmouth. The coastal area around Portland England was included in the sampling. There is a cluster of sampling points around Isles of Scilly located off the south west corner of England. Coastal sampling was also performed between Milford Haven and

River Loughor located on the north side of the Bristol Channel. St George's Channel and the Irish Sea were part of the offshore samples. Additional coastal and transitional water sampling occurred on the Firth of Clyde and waters near Oban Scotland.

One dataset from Lund-Hansen et al. (2010) consisted of 12 spatially distinct data points obtained during a four day cruise between the 6^{th} and 9^{th} of August 2007 from an arctic fjord-type estuary in west Greenland. The sampling locations extend from the estuary mouth inland to the town of Kangerlussauq where the Watson River carries melt water from Greenland Inland Ice.

One data set from Squires and Lesack (2003) consisted of 254 data points collected from six spatially distinct locations during the summers of 1998 and 1999 from chain set lakes in the Mackenzie River delta located in the western Canadian Arctic. The chain set lakes where interconnected with flow rate controlled by river flow depth.

Three data sets from Stewart et al. (2014) consisted of 25 data points collected in laboratory tests in a suspended sediment chamber and field sampling in Kentucky USA. One dataset St1 consisted of fluvial sediment from the South Elkhorn Creek, a low order stream located in the central Bluegrass region of Kentucky. Two of the datasets where obtained using cleaned quartz grain sediments purchased from the U.S. Silica Company.

A single dataset from Stump and Pennock (1991) consisting of 46 data points collected on four occasions during 1987 from multiple locations in the lower portion of the Delaware Bay. The bay is located on the border of eastern Delaware and western New Jersey USA.

The dataset from Zhang et al., (2007) consisted of 67 spatially distinct data points collected during a 9 day cruse between 20 and 29 October 2004 from the large shallow Lake Taihu. The lake is located on the border of eastern Anhul and western Jiangsu provinces in China.

Table 1 reports K_d, *TSS*, λ, ρ_s, and d for the 13 datasets used in the analysis. In the studies K_d was typically measured using a submersible diffuse optical sensor either by vertical profiling or with a pair of matched sensors separated by a known vertical displacement. *TSS* was measured by passing a known volume of sample through pre-weighed filters, oven drying the filters overnight and measuring the mass retained on the filter. Water samples for *TSS* analysis were obtained from the water column in close

proximity to optical sensor profiles used to estimate K_d. Determination of sediment particle size simultaneous with measurements of K_d were carried out and reported in four of the manuscripts Colijn (1982) using a coulter counter, Biggs et al. (1983) using an inverted microscope, Lund-Hansen et al. (2010) using laser diffraction and Stewart et al. (2014) using laser diffraction and inverted microscope. Particles sizes for the remaining data sets were estimated from average published literature values for the water bodies sampled during the same time period. In this study estimations of floc and primary particle sizes were used within the floc model of Khelifa and Hill (2006) to estimate particle density as

$$\rho_{floc} - \rho_w = (\rho_s - \rho_w)\left(\frac{D_f}{d_{50}}\right)^{F-3}\phi \tag{5}$$

Where ρ_{floc}, ρ_s, and ρ_s represent the density of floc, component particles within the floc, and water respectively, D_f represents floc diameter, d_{50} is the primary particles median diameter, φ assumed to be 1 accounts for primary particle size distribution and F is the critical fractal floc dimension defined as

$$F = \alpha\left(\frac{D_f}{d_{50}}\right)^{\beta} \tag{6}$$

Where α and β are coefficients relating fractal dimension to floc size where α assumes the value 3 and β as

$$\beta = \frac{\log(F_c/3)}{\log(D_{fc}/d_{50})} \tag{7}$$

Where the subscript c denotes the parameter at characteristic floc size. The appropriate density, $\rho_{optical}$, for optical modeling of suspended sediments is the ratio of *TSS* to floc volume defined as

$$\rho_{optical} = \left(\frac{\rho_{floc} - \rho_w}{\rho_s - \rho_w}\right) \times \rho_s = \rho_s\left(\frac{D_f}{d_{50}}\right)^{F-3}\phi \tag{8}$$

The most sensitive parameter of the Khelifa and Hill model is d_{50}, which may affect density estimates by almost two orders of magnitude. Varying F_c from 1.6-2.4 may affect density estimates by as much as a factor of 7 for very large flocs. However this variability is constrained significantly for most datasets by using literature estimates of primary

particle size. K_w represents light attenuation when the filterable solids concentration *TSS* is zero and was estimated using linear regression and extrapolating to the intercept. The wavelength of light λ is determined by the optical instrument used to obtain measurements. The analyzed datasets measured wavelengths in the PAR range (400-700nm). For this analysis the centroid of the measured wavelength range was used as an estimate of λ.

7.3.3 Statistical Analysis:

Statistical regression analysis based on minimization of residual errors was used to estimate empirical coefficients. For linearly related data, the method of least squares was used to estimate the regression coefficients in the linear regression model such that the sum of the squares of the errors was minimized (Montgomery, 2005). The significance of individual regression coefficients was determined using the *t* test statistic calculated as the ratio of the regression coefficient to the standard error of the regression coefficient (Montgomery, 2005). For the linear data, ordinary linear regression and R^2 calculation techniques were used. Regression coefficients of power equations may be found by linearization of the data using a logarithmic transformation followed by ordinary least squares regression however this guarantees unbiased estimates of parameters only in the logarithmic domain (McCuen et al. 1990). The regression coefficients of the non-linear relationships were determined by minimizing the sum of the absolute errors using the Leven-Marquardt algorithm. Non-linear least absolute error regression was selected to provide an unbiased estimate of regression coefficients robust toward outliers (Pandey and Nguyen 1999).

7.4 RESULTS/DISCUSSION:

The data is clearly divided into two groups: one group showing linear dependence of the dimensionless light attenuation coefficient upon the light attenuation number and the second group showing non-linearity (see Figure 1b). Linear and power law regression lines further emphasize the differences between the two groups of plotted data.

90% of the data points fall within the linear relationship in Figure 1b. We isolate a subset of the data in Figure 1 c,d to further illustrate that the datasets with different *d* and ρ_s collapse to a single line. The linear results suggests a true exponential

dependence of $TSS\lambda d_{50}^{-1}\rho_s^{-1}$ upon irradiance with depth, $E(z)$, in the water column (see Eqn 1) and thus that absorption dominates over scattering for these field studies. To explain the linear behavior, we consider the interaction between light and sediments as light photons attempt to traverse a sediment layer where absorption dominates. The probability that a photon of light passes through the sediment layer is proportional to the particle-free cross-sectional area relative to the entire cross-sectional area of the layer. Equivalently, the percent of light attenuated while attempting to traverse the sediment layer is proportional to the ratio of particle cross sectional area to that of the layer. This single particle layer concept with linear dependence of irradiance attenuation on particle concentration works well provided that the concentrations of particles are low and the layer is thin. The linear dependence suggests that interaction between irradiance and net projected sediment surface area remains constant in the water and that absorption dominates the light attenuation process.

To formalize the concept that the surface area of sediments results in the linear relationship in Figure (1), we use an analytical approach to show that the linear empirical result of our macro-analysis can be explained exactly. Bohren and Huffman (1998) performed a theoretical analysis to study light passing through a layer of opaque particles in order to model the absorption of light based on net projected particle surface area in the layer. Our approach is adopted from Bohren and Huffman (1998) and made specific to suspended sediment in water with diffuse light. The light attenuation coefficient associated with opaque particles in the layer, K_p, is expressed based on the probability that a photon of light is attenuated while attempting to traverse the particle layer as

$$K_p = QAN \tag{9}$$

where Q is the dimensionless attenuation efficiency factor dependent upon the particle size relative to the wavelength of incident light, λ (van de Hulst 1981; Kirk 1994), A is the projected cross sectional area of the particle, and N is the number of particles per unit area. To parameterize the Bohren and Huffman (1998) equation for the case of suspended sediments in water, we parameterize A assuming spherical particles as

$$A = \frac{\pi d^2}{4} \tag{10}$$

and the number of suspended sediments can be estimated as a function of *TSS* and particle mass as

$$N = \frac{TSS}{\rho_s \pi d^3 / 6} \tag{11}$$

Substituting equations (5) and (6) into (4) and simplifying, we obtain

$$K_p = \frac{3QTSS}{2\rho_s d} \tag{12}$$

which provides the physical dependence of K_p upon sediment properties. For large particles the efficiency factor Q accounts for the scattering of light impingent on the particle surface area and diffraction of light near the particle. The area surrounding the particle diffracting light is proportional to the particles surface area. The angle of diffracted light will be small and will maintain a forward trajectory similar to that prior to diffraction by the particle. A sensor measuring diffuse irradiance will detect the vast majority of diffracted light and Q will essentially be equal to 1. Considering these additional assumptions, we see that Equation (12) becomes

$$K_p = 1.5\frac{TSS}{\rho_s d} \tag{13}$$

Note that Equation (13) agrees exactly with the linear scaled relationship in Figure 1 since λ is a repeating variable in the dimensionless numbers and K_d-K_w in the figure removes the influence of water and thus isolates the sediment and light interaction.

The linear behavior of the dimensionless attenuation coefficient upon $TSS\lambda d_{50}^{-1}\rho_s^{-1}$ suggests that the percent of light attenuated by a sediment layer will be proportional to the ratio of projected area of sediment and surface area of the layer. The result should be placed in the context of the datasets exhibiting linearity in the macro-analysis. Eight of the 13 datasets in Table 1 fell in the linear region. Of the eight linear datasets, six datasets were from estuary or continental shelf studies that encompassed arctic, temperate and subtropical climates. The remaining two datasets were from lake studies

in locations where sediments derived from rivers had been transported into the lakes. The particle size ranged across the eight datasets from approximately 10 to 100 μm, and the range of $TSS\lambda d_{50}^{-1}\rho_s^{-1}$ within each individual dataset was generally due to either spatial variability of samples typically with the highest suspended sediment concentration near river inputs and temporal variability in suspended sediment concentration due to either riverine inputs across a hydrologic event or resuspension of bottom sediments due to wave action increasing with the tidal cycle. It is not fully clear the percentage of riverine versus marine or autochthonous lake derived sediment in these individual studies, but given the nature of these studies to sample riverine inputs it is likely that sediments are dominated by primarily lithogenous matter derived from land sources and phytoplankton/seston transported by large rivers. Given the probable riverine origin, it is unlikely that the sediments are organic dominated (e.g., OM>50% by mass), however, the inorganic mineral particles are likely stained with organic substances and held in matrices of sediment flocs or aggregates that include both organic and inorganic particles. The likely presence of organics within the sediment layer leads to the process of absorption given that organic matter contained sediments are expected to have lower refractive index causing them to interact with light mainly through absorption.

Comparison of the results in Equation (13) with the linear results in Figure 1 suggests that our assumptions of sediment particles as spheres and sediment opaqueness are reasonable. Natural sediments in lakes and estuaries are not likely spheres, however, previous studies by Pollack and Cuzzi (1980) and Clavano et al. (2007) investigated the shape factor of particles and showed that the net effect of irregular particles is that they attenuate light similarly to spherical particles of equivalent volume when all particles within the concentrated mixture are randomly oriented. Given the turbulent nature of river and near shore flows the suspended irregular sediment particles should behave as spherical particles of equivalent volume due to random particle orientation resulting from the flow conditions (Clifford et al. 1995). Kirk (1994) suggests that for most optically significant particles encountered in natural waters opaqueness is reasonable and geometric optical theory explains light attenuation.

The non-linear data is also collapsed using the dimensionless scaling, $TSS\lambda d_{50}^{-1}\rho_s^{-}$

^{1}, which is further illustrated with the non-linear subset of data in Figure 1f. While the linear behavior suggests that each sediment particle or sediment aggregate removes a small percentage of the light field proportional to the particles projected area, the non-linear behavior suggests that secondary processes such as particle shadowing and backscattering occur and that irradiance is not truly an exponential function of $TSS\lambda d_{50}^{-1}\rho_s^{-1}$. Shadowing and backscattering can cause light attenuation to be less than that predicted by linear relationships and in general are attributed to the sediment's size and reflective properties (Clifford et al. 1995; Hill et al. 2011). Particle shadowing results in less light absorption per particle and ultimately less light is attenuated than would be predicted assuming linear dependence between K_d and sediments. Further, scattered light that might be attenuated within the particle layer can backscatter, which effectively reduces the amount of light lost within the layer. This concept is broadly consistent with the optical Monte Carlo stochastic modelling of Kirk (1981). Kirk (1981 and 1984) showed that K_d is nearly linearly dependent on light absorption and the square root of light scattering.

The concept of scattering can be explained using a thick sediment layer or multiple thin sediment layers with high area concentration of scattering particles where scattered light may not be attenuated in the downward direction. Light attenuation by the first sediment layer is proportional to area occluded by sediments. However, the light attenuated by the second sediment layer is less than the amount of light interacting with sediment while attempting to traverse this sediment layer due to multiple scattering. The second sediment layer absorbs one photon of light and scatters two others. Unlike the first layer; all scattered light is not lost in the downward direction as some portion of the light scattered by the second sediment layer is scattered back into the downward direction by the above sediment. This simple multi-layer example illustrates how multiple scattering reduces attenuation as compared to the single layer linear model. In this manner, an additional sediment layer does not occlude in an additive manner the cross sectional area of the plane light is attempting to traverse. That said the non-linear attenuation from highly scattering sediments is still expected to properly scale with the dimensionless scaling of Equation 4,as the particle area is responsible for the scattering of irradiance by sediments.

The non-linear data in Figure 1f can be further divided into subsets that in turn reflect the properties of the sediment to shadow and scatter light. Among the collapsed datasets, three sub-groups were clearly evident including (see Figure 2): the Colijn (1982) dataset; the Squires and Lesasck (2003) and Stewart et al. (2014) St1 data; and the Stewart et al. (2014) quartz grains. Power law functions showed increasingly pronounced non-linearity across the sub-groups with the quartz grains showing the most non-linearity. These subgroups suggest scattering is dependent on the organic matter content and particle assemblage. Inorganic mineral particles have a higher refractive index (quartz 1.16) than organic material (variable, 1.04 is typical) (Davies-Colley et al. 2001, Twardowski et al. 2001) and are more effective at scattering light. Sediments sampled by Co are believed by the authors to contain inorganic matter concentrations that greatly exceed the organic portion indicating the tendency to scatter light. Sediments sampled by Squires and Lesack 2003 contained <10% of *TSS* as volatile suspended sediments; further the authors suggest that absorption by humics bound to sediments and by detritus represent a small part of irradiance attenuation. It is interesting that St1 a natural sediment assemblage plotted closer to the theoretical linear model while St2 and St3 plotted further away. It is likely that the quartz grains in St2 and St3 absorb less light than the stream aggregates in St1 due to their lack of pigmentation. Natural sediment assemblages are likely to be pigmented due to organic materials bound to their surfaces or contain pigmented inorganic compounds such as iron. Additionally a floc comprised of many fractured purely inorganic sediments will not likely have optical properties that resemble that of the heterogeneous parent material due the state of aggregation.

The results in Figure 2 provide the basis for a nomograph to describe the non-linear relationship between the dimensionless light attenuation coefficient and dimensionless number for light attenuation by sediments. Sediment particles and aggregates that primarily absorb light are indicated by linear behavior while sediments that increasing attenuate light through scattering are indicated by the increasingly non-linear curves. To this end, the refractive index might be used within Figure 2 to provide a set of curves for varying levels of organic and inorganic constituents. Organic-dominated sediment particles and flocs are expected to have lower refractive index

causing them to interact with light mainly through absorption. Inorganic-dominated sediment particles and aggregates are expected to have higher refractive index and scatter more light than biologic particles. For example, recent research on beam attenuation and scattering by particles conducted by Neukermans et al. (2012) found that inorganic particles have about three times greater scattering efficiency than organic particles. Unfortunately, none of the samples in this meta-analysis reported values for n (refractive index), and future functional dependence of $K_s\lambda$ on n is needed.

We point out that there are additional explanations and instances that can muddle the non-linear curves in Figure 2. Non-linearity between $\lambda(K_d\text{-}K_w)$ and $TSS\lambda d^{-1}\rho_s^{-1}$could result from non-constant sediment properties during sampling that were assumed to be constant (e.g. artificial non-linearity). Sediment transport processes in rivers, estuaries and lakes may result in d and ρ_s being codependent upon TSS in both space and time. High energy flows associated with high TSS have the ability to transport larger, denser sediments. In this manner, non-linearity could be interpreted as larger, denser sediments associated high energy, high TSS events that will attenuate less light per mass; and thus explain the decreasing gradient. We point out that the results of Colijn (1982) and Squires and Lesack (2003) display a lower mass specific light attenuation coefficient at high TSS, which might suggest some artificial non-linearity. However, without corresponding d and ρ_s estimates for each TSS and K_d data point in Colijn (1982) and Squires and Lesack (2003), it is not possible to know whether the non-linearity is artificial or pronounced scattering; given the above discussion, we suggest it is likely that both come into play for the Colijn (1982) and Squires and Lesack (2003) datasets. In the case of the Stewart et al. (2014) fluvial sediments and quartz grains, the non-linearity can be limited to the scattering, backscattering, and shadowing processes given that the sampling conditions did not produce changes in d and ρ_s. The potential for artificial non-linearity resulting from a coarsening of particle size distribution suggests the need to collect information that allows for estimating K_d, TSS, d and ρ_s when working towards revising the relationships in Figure 2.

7.5 CONCLUSIONS

For the majority of sediments light attenuation is linearly related to the dimensionless number for light attenuation by sediments as shown by the meta-analysis

performed for light attenuation by suspended sediments. Light attenuation for the remaining sediment compositions is related through power law equations. Dimensional analysis performed using sediment characteristics provides a scaling by which light attenuation by sediments collapses onto a nomograph of curves distinguished by the degree to which sediments scatter light. The linear relationship between dimensionless light attenuation and the light attenuation number exactly matches the result from the analytical analysis providing a clear physical explanation of the empirical dimensionless scaling. We can conclude that the attenuation of diffuse light by suspended sediments occurs through interactions regulated by the sediment surface area. Further work is needed to relate the sediments refractive index to the nomograph of curves believing to result from light scattering. The variability of light attenuating constituents that influence the degree of scattering by sediments in field studies has hindered the development of a physically based model that relates sediment properties to irradiance attenuation. The recent laboratory experiments conducted by Stewart et al. (2014) maintained constant sediment properties over the entire range of TSS, these experiments show non-linearity in the relationship between irradiance attenuation of highly scattering particles. Future research of light attenuation by sediments should strive to provide fundamental relationships describing the physical processes by which light and sediments interact. Field measurements of *TSS* along with organic content and particle size information such as those conducted by Lund-Hansen et al. (2010) will be valuable for further refinement of the nomograph of curves which separate certain sediments. Beyond the size and density of sediments further work to characterize the refractive index of flocculated sediments would be beneficial to determine the effect of scattering on the non-linear light attenuation relationship.

7.6 ACKNOWLEDGEMENTS

We would like to thank all of the people who worked on this project including both the graduate and undergraduate students. We would like to thank Dr. Agouridis for help with data analysis. We acknowledge National Science Foundation project #0918856 and the University of Kentucky, Department of Civil Engineering for financial support of students.

7.7 LIST OF SYMBOLS

A = cross sectional area of sediment particles

c = denotes floc parameter at characteristic size

d = sediment diameter

d_{50} = Median diameter of primary particles

F = Three-dimensional critical fractal dimension of flocs

E = irradiance

E_0 = irradiance when the light path length is zero

K_d = downward vertical diffuse light attenuation coefficient

K_p = the light attenuation coefficient associated with an layer of opaque particles

K_s = the light attenuation coefficient associated with sediments

K_w = the light attenuation coefficient due to water and dissolved substances

z = vertical coordinate

n = refractive index of sediment particles relative to water

N = number of particles in sediment layer

TSS = total suspended sediment concentration

α, β = coefficients relating fractal dimension to floc size

ϕ = Factor to account for the size distribution of primary particles when estimating density

λ = wavelength of the incident light in free space

$\rho_{optical}$ = The dry mass of sediment divided by the volume of the floc that contains that sediment.

ρ_{floc} = density of floc predicted using Khelifa Hill model

ρ_s = suspended sediment density

ρ_w = density of water

7.8 REFERENCES

Babin, M., & Stramski, D. (2004). "Variations in the mass-specific absorption coefficient of mineral particles suspended in water." *Limnology and Oceanography*, 49(3), 756-

767.

Baker, E. T., & Lavelle, J. W. (1984). "The effect of particle size on the light attenuation coefficient of natural suspensions." *Journal of Geophysical Research: Oceans*, 89(C5), 8197-8203.

Biggs, R. B., Sharp, J. H., Church, T. M., & Tramontano, J. M. (1983). "Optical properties, suspended sediments, and chemistry associated with the turbidity maxima of the Delaware Estuary." *Canadian Journal of Fisheries and Aquatic Sciences*, 40(S1), 172-179.

Bohren, C. F., & Huffman, D. R. (1998). *Absorption and scattering of light by small particles*. Wiley New York

Boss, E., Slade, W., & Hill, P. (2009). "Effect of particulate aggregation in aquatic environments on the beam attenuation and its utility as a proxy for particulate mass." *Optics Express*, 17(11), 9408-9420.

Bowers, D. G., Braithwaite, K. M., Nimmo-Smith, W. A. M., & Graham, G. W. (2009). "Light scattering by particles suspended in the sea: The role of particle size and density." *Continental Shelf Research*, 29(14), 1748-1755.

Bunt, J. A., Larcombe, P., & Jago, C. F. (1999). "Quantifying the response of optical backscatter devices and transmissometers to variations in suspended particulate matter." *Continental Shelf Research*, 19(9), 1199-1220.

Chao, X., Jia, Y., Shields Jr, F. D., Wang, S. S., & Cooper, C. M. (2010). Three-dimensional numerical simulation of water quality and sediment-associated processes with application to a Mississippi Delta lake. *Journal of environmental management*, 91(7), 1456-1466.

Clavano, W.R., Boss, E., & Karp-Boss, L., (2007). Inherent Optical Properties of Non-Spherical Marine-Like Particles- From Theory to Observation. *Oceanography and Marine Biology: An Annual Review*, 45, 1-38

Clifford, N. J., Richards, K. S., Brown, R. A., & Lane, S. N. (1995). Laboratory and field assessment of an infrared turbidity probe and its response to particle size and variation in suspended sediment concentration. *Hydrological Sciences Journal*, 40(6), 771-791.

Cloern, J. E. (1987). Turbidity as a control on phytoplankton biomass and productivity in estuaries. *Continental Shelf Research*, 7(11/12), 1367-1381.

Colijn, F. (1982). “Light absorption in the waters of the Ems-Dollard estuary and its consequences for the growth of phytoplankton and microphytobenthos.” *Netherlands Journal of Sea Research*, 15(2), 196-216.

Davies-Colley, R. J., Vant, W. N., & Smith, D. G. (2003). Colour and clarity of natural waters: Science and management of optical water quality. Blackburn Press Caldwell New Jersey

Davies-Colley, R.J., & Smith, D. G. (2001). “Turbidity, suspended sediment, and water clarity: a review.” *JAWRA Journal of the American Water Resources Association*, 37(5), 1085-1101. DOI: 10.1111/j.1752-1688.2001.tb03624.x

Davies-Colley, R.J. and J.W. Nagels 2008. Predicting Light Penetration Into River Waters. *Journal of Geophysical Research-Biogeosciences* 113 (G3), G03028

Devlin, M. J., Barry, J., Mills, D. K., Gowen, R. J., Foden, J., Sivyer, D., & Tett, P. (2008). Relationships between suspended particulate material, light attenuation and Secchi depth in UK marine waters. *Estuarine, Coastal and Shelf Science*, 79(3), 429-439.

Devlin, M. J., Barry, J., Mills, D. K., Gowen, R. J., Foden, J., Sivyer, D., Greenwood, N., Pearce, D., & Tett, P. (2009). “Estimating the diffuse attenuation coefficient from optically active constituents in UK marine waters.” *Estuarine, Coastal and Shelf Science*, 82(1), 73-83.

Doxaran, D., Ruddick, K., McKee, D., Gentili, B., Tailliez, D., Chami, M., & Babin, M. (2009). “Spectral variations of light scattering by marine particles in coastal waters, from visible to near infrared.” *Limnology and oceanography*, 54(4), 1257-1271.

Droppo, I. G., Nackaerts, K., Walling, D. E., & Williams, N. (2005). “Can flocs and water stable soil aggregates be differentiated within fluvial systems?.” *Catena*, 60(1), 1-18.

Gordon, H. R. (1989). Can the Lambert-Beer law be applied to the diffuse attenuation coefficient of ocean water?. *Limnology and Oceanography*, 34(8), 1389-1409.

Hauer, F. R., & Lamberti, G. A. (2006). *Methods in stream ecology*. Academic Press, Amsterdam.

Hill, P. S., Boss, E., Newgard, J. P., Law, B. A., & Milligan, T. G. (2011). Observations of the sensitivity of beam attenuation to particle size in a coastal bottom boundary

layer. *Journal of Geophysical Research: Oceans* 116, (C02023), doi:10.1029/2010JC006539.

van de Hulst, H. C., (1981). *Light scattering: by small particles*. Dover, New York.

Julian, J. P., Doyle, M. W., Powers, S. M., Stanley, E. H., & Riggsbee, J. A. (2008). Optical water quality in rivers. *Water Resources Research*, 44(10), W10411.

Khelifa, A., & Hill, P. S. (2006). "Models for effective density and settling velocity of flocs." *Journal of Hydraulic Research*, 44(3), 390-401.

Kirk, J. T. O. (1994). *Light and photosynthesis in aquatic ecosystems*. Cambridge University press New York New York.

Kirk, J. T. O., (1981). A Monte Carlo study of the nature of the underwater light field in, and the relationships between optical properties of, turbid yellow waters. *Australian Journal of Marine and Freshwater Research*, 32(4) 533-9.

Kirk, J. T. O. (1984). Dependence of relationship between inherent and apparent optical properties of water on solar altitude. *Limnology and Oceanography*, 29(2), 350-356

Lawson, S. E., Wiberg, P. L., McGlathery, K. J., & Fugate, D. C. (2007). Wind-driven sediment suspension controls light availability in a shallow coastal lagoon. *Estuaries and Coasts*, 30(1), 102-112.

Latimer, P. (1985). "Experimental tests of a theoretical method for predicting light scattering by aggregates." *Applied optics*, 24(19), 3231-3239.

Lund-Hansen, L. C., Andersen, T. J., Nielsen, M. H., & Pejrup, M. (2010). Suspended matter, Chl-a, CDOM, grain sizes, and optical properties in the Arctic fjord-type estuary, Kangerlussuaq, West Greenland during summer. *Estuaries and coasts*, 33(6), 1442-1451. DOI 10.1007/s12237-010-9300-7

McCuen, R. H., Leahy, R. B., & Johnson, P. A. (1990). Problems with logarithmic transformations in regression. *Journal of Hydraulic Engineering*, 116(3), 414-428.

Mobley, C. D. (1994). *Light and water: Radiative transfer in natural waters* (Academic press, San Diego).

Montgomery, D.C. (2005). *Design and Analysis of Experiments* (John Wiley & Sons, New Jersey) pg 390-391.

Neukermans, G., Loisel, H., Mériaux, X., Astoreca, R., & McKee, D. (2012). "In situ variability of mass-specific beam attenuation and backscattering of marine particles

with respect to particle size, density, and composition." *Limnology and Oceanography*, 57(1) 124-144.

Painting, S. J., Devlin, M. J., Malcolm, S. J., Parker, E. R., Mills, D. K., Mills, C., Tett, P., Wither, A., Bert, J., Jones, R., & Winpenny, K. (2007). Assessing the impact of nutrient enrichment in estuaries: susceptibility to eutrophication. *Marine pollution bulletin*, *55*(1), 74-90. doi:10.1016/j.marpolbul.2006.08.020

Pandey, G. R., & Nguyen, V. T. V. (1999). A comparative study of regression based methods in regional flood frequency analysis. *Journal of Hydrology*, 225(1), 92-101.

Pollack, J. B., & Cuzzi, J. N. (1980). Scattering by non-spherical particles of size comparable to a wavelength: A new semi-empirical theory and its application to tropospheric aerosols. *Journal of the Atmospheric Sciences*, 37(4), 868-881.

Sorensen, C. M. (2001). Light scattering by fractal aggregates: a review. *Aerosol Science & Technology*, 35(2), 648-687.

Squires, M. M., & Lesack, L. F. (2003). "Spatial and temporal patterns of light attenuation among lakes of the Mackenzie Delta." *Freshwater Biology*, 48(1), 1-20.

Stavn, R. H. (2012). "Mass-specific scattering cross sections of suspended sediments and aggregates: theoretical limits and applications." *Optics Express*, 20(1), 201-219.

Stewart, R. L., Fox, J. F., & Harnett, C. K. (2014). Estimating Suspended Sediment Concentration in Streams by Diffuse Light Attenuation. *Journal of Hydraulic Engineering,* ##(#), ##-##

Stramski, D., Babin, M., & Wozniak, S. B. (2007). "Variations in the optical properties of terrigenous mineral-rich particulate matter suspended in seawater." *Limnology and Oceanography*, 52(6), 2418-2433.

Stumpf, R. P., & Pennock, J. R. (1991). "Remote estimation of the diffuse attenuation coefficient in a moderately turbid estuary." *Remote Sensing of Environment*, 38(3), 183-191.

Twardowski, M. S., Boss, E., Macdonald, J. B., Pegau, W. S., Barnard, A. H., & Zaneveld, J. R. V. (2001). A model for estimating bulk refractive index from the optical backscattering ratio and the implications for understanding particle composition in case I and case II waters. *Journal of Geophysical Research: Oceans* (2001), 106(C7), 14,129-14,142.

Wozniak, S. B., Stramski, D., Stramska, M., Reynolds, R. A., Wright, V. M., Miksic, E. Y., Cichocka, M., & Cieplak, A. M. (2010). "Optical variability of seawater in relation to particle concentration, composition, and size distribution in the nearshore marine environment at Imperial Beach, California." *Journal of Geophysical Research: Oceans,* 115(C8), C08027.

Zhang, Y., Zhang, B., Ma, R., Feng, S., & Le, C. (2007). "Optically active substances and their contributions to the underwater light climate in Lake Taihu, a large shallow lake in China." *Fundamental and Applied Limnology/Archiv für Hydrobiologie*, 170(1), 11-19.

7.9 TABLES AND FIGURES

Table 7.1 Table with sediment sensor characteristics

Data set	Number of samples	d μm	Specific Gravity	Sizing method	TSS mg l^{-1}	K_d m^{-1}	λ nm
DE	273	90	0.239	LISST 100S	0-290	0.5-18	400-700
Bi-1	20	9	2.08	Photographs	5.1-80	0.5-7	400-700
Bi-2	93	36	0.95	Photographs	5.1-80	0.5-7	400-700
Cl	417	55	0.46	LISST 100X	0-200	0.5-12.5	400-700
Co	8	24	0.8	Coulter Counter	0-193	1.7-6.7	400-700
SP	46	33	0.689	Photographs	3-63	0.6-4.9	400-700
LH	12	varies	varies	LISST	2-372	0.12-15.34	400-700
St-1	13	10.5	1.8	Inverted Microscope	0-480	0.1-9.7	530
St-2	6	14	2.65	LISST	0-670	0.1-4.48	530
St-3	6	27	2.65	LISST	0-535	0.1-3.09	530
Ch	17	26	1.23	NA	160-280	7.9-14	400-700
SI	254	8.2	0.876	Inverted Microscope	25-500	0-13	400-700
Zh	67	20	0.9	Image Analysis	3-170	0.87-12.43	400-700

Figure 7.1. (a) all data plotted in dimensional form Kd; (b) all data scaled into dimensionless variables photocell; (c) linear data plotted in dimensional form; (d) linear data plotted as scaled dimensionless parameters; (e) non-linear data plotted in dimensional form; (f) non-linear data plotted as scaled dimensionless parameters

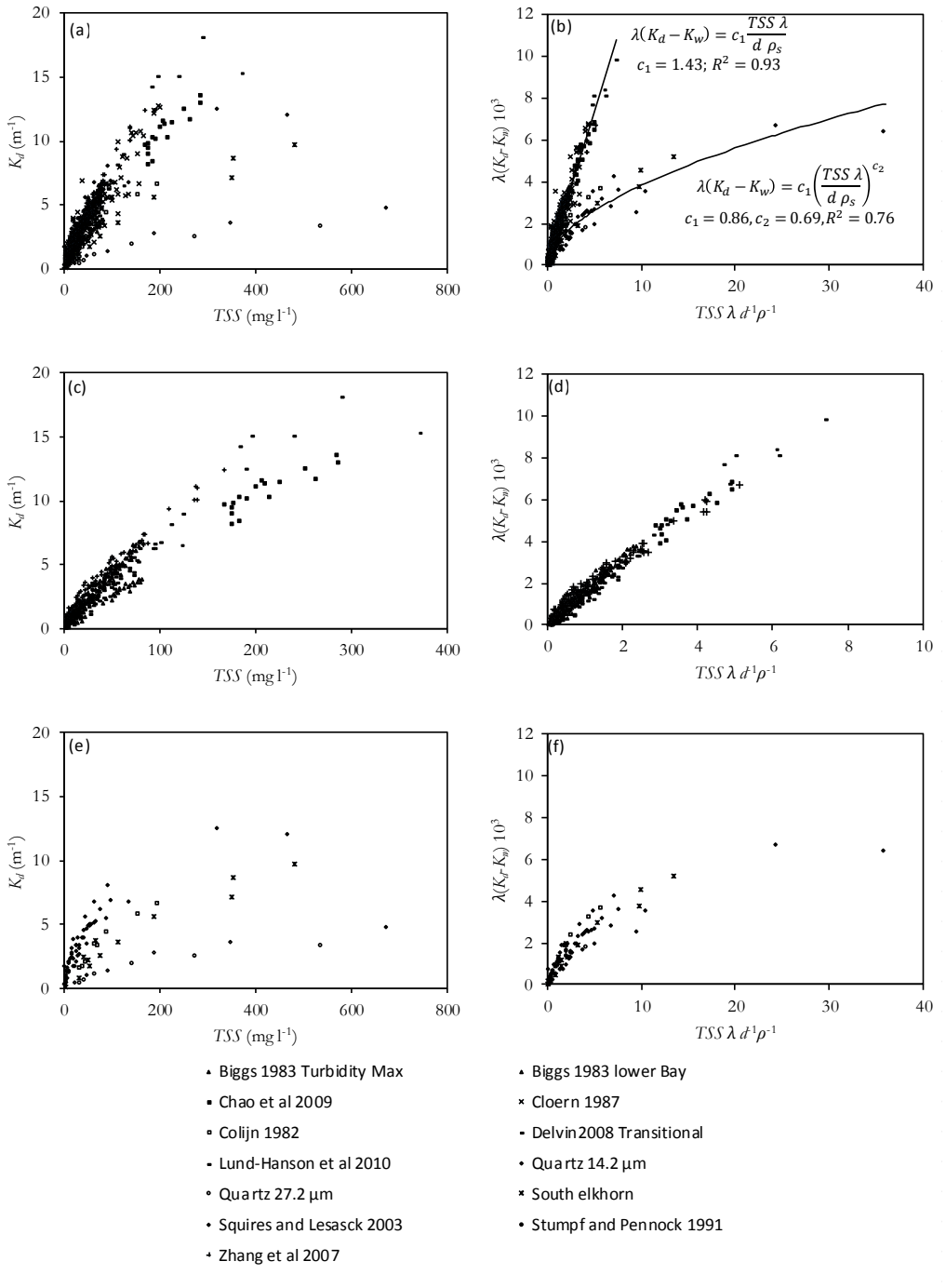

Figure 7.2. shows varying degrees of non-linearity arising due to the scattering properties of the sediments.

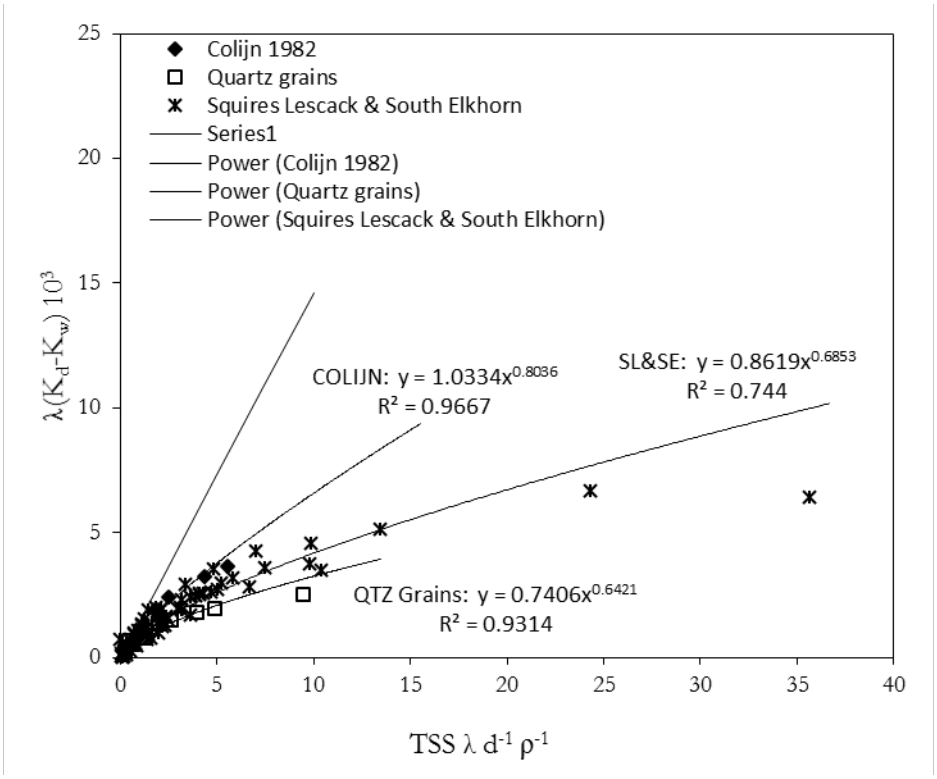

APPENDIX A

List of all data used for analysis – Chapter 3

Data Set	U (cm s^{-1})	U_∞ (cm s^{-1})	δ (cm)	δ^* (cm)	y (cm)
PS-1.1	68.0	68.5	11.1	1.9	11.4
PS-1.1	68.5	68.5	11.1	1.9	11.1
PS-1.1	67.1	68.5	11.1	1.9	10.8
PS-1.1	67.8	68.5	11.1	1.9	10.4
PS-1.1	66.8	68.5	11.1	1.9	9.9
PS-1.1	66.3	68.5	11.1	1.9	9.5
PS-1.1	66.7	68.5	11.1	1.9	9.0
PS-1.1	65.4	68.5	11.1	1.9	8.6
PS-1.1	64.7	68.5	11.1	1.9	8.1
PS-1.1	65.1	68.5	11.1	1.9	7.7
PS-1.1	63.4	68.5	11.1	1.9	7.2
PS-1.1	64.0	68.5	11.1	1.9	6.8
PS-1.1	62.3	68.5	11.1	1.9	6.4
PS-1.1	11.1	68.5	11.1	1.9	0.1
PS-1.1	12.8	68.5	11.1	1.9	0.2
PS-1.1	17.8	68.5	11.1	1.9	0.2
PS-1.1	21.4	68.5	11.1	1.9	0.3
PS-1.1	27.2	68.5	11.1	1.9	0.4
PS-1.1	34.7	68.5	11.1	1.9	0.6
PS-1.1	36.8	68.5	11.1	1.9	0.7
PS-1.1	39.9	68.5	11.1	1.9	0.8
PS-1.1	49.9	68.5	11.1	1.9	2.1
PS-1.1	49.7	68.5	11.1	1.9	2.3
PS-1.1	50.8	68.5	11.1	1.9	2.6
PS-1.1	52.4	68.5	11.1	1.9	2.9
PS-1.1	51.7	68.5	11.1	1.9	3.1
PS-1.1	0.0	68.5	11.1	1.9	3.4
PS-1.1	0.0	68.5	11.1	1.9	3.6
PS-1.1	56.1	68.5	11.1	1.9	3.9
PS-1.1	56.9	68.5	11.1	1.9	4.1
PS-1.1	57.1	68.5	11.1	1.9	4.4
PS-1.1	58.6	68.5	11.1	1.9	4.6
PS-1.1	59.0	68.5	11.1	1.9	4.9
PS-1.1	58.3	68.5	11.1	1.9	5.1
PS-1.1	61.3	68.5	11.1	1.9	5.4
PS-1.2	60.0	67.2	10.4	1.8	6.4
PS-1.2	60.6	67.2	10.4	1.8	6.8

PS-1.2	60.8	67.2	10.4	1.8	7.2
PS-1.2	62.4	67.2	10.4	1.8	7.7
PS-1.2	63.2	67.2	10.4	1.8	8.1
PS-1.2	64.0	67.2	10.4	1.8	8.6
PS-1.2	64.8	67.2	10.4	1.8	9.0
PS-1.2	65.2	67.2	10.4	1.8	9.5
PS-1.2	65.6	67.2	10.4	1.8	9.9
PS-1.2	67.2	67.2	10.4	1.8	10.4
PS-1.2	66.4	67.2	10.4	1.8	10.8
PS-1.2	67.0	67.2	10.4	1.8	11.2
PS-1.2	67.0	67.2	10.4	1.8	11.7
PS-1.2	56.9	67.2	10.4	1.8	5.1
PS-1.2	56.6	67.2	10.4	1.8	4.9
PS-1.2	55.4	67.2	10.4	1.8	4.6
PS-1.2	56.0	67.2	10.4	1.8	4.4
PS-1.2	55.1	67.2	10.4	1.8	4.1
PS-1.2	54.1	67.2	10.4	1.8	3.9
PS-1.2	0.0	67.2	10.4	1.8	3.6
PS-1.2	0.0	67.2	10.4	1.8	3.4
PS-1.2	51.3	67.2	10.4	1.8	3.1
PS-1.2	50.3	67.2	10.4	1.8	2.9
PS-1.2	50.8	67.2	10.4	1.8	2.6
PS-1.2	47.0	67.2	10.4	1.8	2.3
PS-1.2	47.6	67.2	10.4	1.8	2.1
PS-1.2	38.3	67.2	10.4	1.8	0.8
PS-1.2	36.7	67.2	10.4	1.8	0.7
PS-1.2	34.7	67.2	10.4	1.8	0.6
PS-1.2	29.7	67.2	10.4	1.8	0.4
PS-1.2	21.4	67.2	10.4	1.8	0.3
PS-1.2	13.1	67.2	10.4	1.8	0.2
PS-1.2	10.5	67.2	10.4	1.8	0.1
PS-1.2	5.7	67.2	10.4	1.8	0.1
PS-1.2	5.9	67.2	10.4	1.8	0.1
PS-1.3	68.6	68.6	11.7	2.2	11.7
PS-1.3	67.7	68.6	11.7	2.2	11.2
PS-1.3	67.4	68.6	11.7	2.2	10.8
PS-1.3	67.3	68.6	11.7	2.2	10.4
PS-1.3	65.8	68.6	11.7	2.2	9.9
PS-1.3	65.2	68.6	11.7	2.2	9.5
PS-1.3	64.6	68.6	11.7	2.2	9.0
PS-1.3	64.1	68.6	11.7	2.2	8.6
PS-1.3	63.4	68.6	11.7	2.2	8.1
PS-1.3	63.2	68.6	11.7	2.2	7.7

PS-1.3	62.0	68.6	11.7	2.2	7.2
PS-1.3	61.6	68.6	11.7	2.2	6.8
PS-1.3	60.2	68.6	11.7	2.2	6.4
PS-1.3	5.2	68.6	11.7	2.2	0.1
PS-1.3	9.6	68.6	11.7	2.2	0.1
PS-1.3	12.9	68.6	11.7	2.2	0.2
PS-1.3	20.6	68.6	11.7	2.2	0.3
PS-1.3	26.5	68.6	11.7	2.2	0.4
PS-1.3	33.7	68.6	11.7	2.2	0.6
PS-1.3	36.4	68.6	11.7	2.2	0.7
PS-1.3	39.6	68.6	11.7	2.2	0.8
PS-1.3	47.7	68.6	11.7	2.2	2.1
PS-1.3	48.2	68.6	11.7	2.2	2.3
PS-1.3	49.3	68.6	11.7	2.2	2.6
PS-1.3	50.1	68.6	11.7	2.2	2.9
PS-1.3	51.4	68.6	11.7	2.2	3.1
PS-1.3	0.0	68.6	11.7	2.2	3.4
PS-1.3	0.0	68.6	11.7	2.2	3.6
PS-1.3	54.2	68.6	11.7	2.2	3.9
PS-1.3	54.9	68.6	11.7	2.2	4.1
PS-1.3	54.9	68.6	11.7	2.2	4.4
PS-1.3	55.6	68.6	11.7	2.2	4.6
PS-1.3	56.1	68.6	11.7	2.2	4.9
PS-1.3	57.2	68.6	11.7	2.2	5.1
PS-1.3	58.5	68.6	11.7	2.2	5.4
PS-1.3	58.1	68.6	11.7	2.2	5.4
PS-1.4	57.1	64.5	11.7	1.9	6.4
PS-1.4	59.5	64.5	11.7	1.9	6.8
PS-1.4	59.9	64.5	11.7	1.9	7.2
PS-1.4	59.1	64.5	11.7	1.9	7.7
PS-1.4	61.2	64.5	11.7	1.9	8.1
PS-1.4	61.6	64.5	11.7	1.9	8.6
PS-1.4	61.9	64.5	11.7	1.9	9.0
PS-1.4	62.6	64.5	11.7	1.9	9.5
PS-1.4	63.8	64.5	11.7	1.9	9.9
PS-1.4	63.1	64.5	11.7	1.9	10.4
PS-1.4	0.0	64.5	11.7	1.9	10.8
PS-1.4	64.3	64.5	11.7	1.9	11.2
PS-1.4	64.5	64.5	11.7	1.9	11.7
PS-1.4	56.9	64.5	11.7	1.9	5.4
PS-1.4	55.7	64.5	11.7	1.9	5.1
PS-1.4	55.1	64.5	11.7	1.9	4.9
PS-1.4	55.4	64.5	11.7	1.9	4.6

PS-1.4	54.7	64.5	11.7	1.9	4.4
PS-1.4	52.7	64.5	11.7	1.9	4.1
PS-1.4	0.0	64.5	11.7	1.9	3.9
PS-1.4	52.9	64.5	11.7	1.9	3.6
PS-1.4	51.6	64.5	11.7	1.9	3.4
PS-1.4	50.6	64.5	11.7	1.9	3.1
PS-1.4	50.1	64.5	11.7	1.9	2.9
PS-1.4	47.9	64.5	11.7	1.9	2.6
PS-1.4	46.6	64.5	11.7	1.9	2.3
PS-1.4	46.2	64.5	11.7	1.9	2.1
PS-1.4	38.3	64.5	11.7	1.9	0.8
PS-1.4	36.0	64.5	11.7	1.9	0.7
PS-1.4	33.9	64.5	11.7	1.9	0.6
PS-1.4	28.6	64.5	11.7	1.9	0.4
PS-1.4	21.0	64.5	11.7	1.9	0.3
PS-1.4	12.3	64.5	11.7	1.9	0.2
PS-1.4	9.3	64.5	11.7	1.9	0.1
PS-1.4	4.8	64.5	11.7	1.9	0.1
PS-1.5	62.3	62.5	11.7	2.4	11.7
PS-1.5	62.5	62.5	11.7	2.4	11.2
PS-1.5	61.5	62.5	11.7	2.4	10.8
PS-1.5	60.7	62.5	11.7	2.4	10.4
PS-1.5	60.0	62.5	11.7	2.4	9.9
PS-1.5	59.5	62.5	11.7	2.4	9.5
PS-1.5	57.7	62.5	11.7	2.4	9.0
PS-1.5	58.3	62.5	11.7	2.4	8.6
PS-1.5	57.8	62.5	11.7	2.4	8.1
PS-1.5	56.3	62.5	11.7	2.4	7.7
PS-1.5	56.4	62.5	11.7	2.4	7.2
PS-1.5	54.8	62.5	11.7	2.4	6.8
PS-1.5	55.7	62.5	11.7	2.4	6.4
PS-1.5	0.0	62.5	11.7	2.4	6.4
PS-1.5	3.7	62.5	11.7	2.4	0.1
PS-1.5	6.2	62.5	11.7	2.4	0.1
PS-1.5	9.5	62.5	11.7	2.4	0.2
PS-1.5	15.7	62.5	11.7	2.4	0.3
PS-1.5	21.2	62.5	11.7	2.4	0.4
PS-1.5	27.3	62.5	11.7	2.4	0.6
PS-1.5	29.5	62.5	11.7	2.4	0.7
PS-1.5	32.0	62.5	11.7	2.4	0.8
PS-1.5	40.6	62.5	11.7	2.4	2.1
PS-1.5	43.0	62.5	11.7	2.4	2.3
PS-1.5	43.6	62.5	11.7	2.4	2.6

PS-1.5	43.7	62.5	11.7	2.4	2.9
PS-1.5	44.1	62.5	11.7	2.4	3.1
PS-1.5	0.0	62.5	11.7	2.4	3.4
PS-1.5	0.0	62.5	11.7	2.4	3.6
PS-1.5	48.8	62.5	11.7	2.4	3.9
PS-1.5	47.7	62.5	11.7	2.4	4.1
PS-1.5	48.8	62.5	11.7	2.4	4.4
PS-1.5	48.9	62.5	11.7	2.4	4.6
PS-1.5	50.3	62.5	11.7	2.4	4.9
PS-1.5	52.6	62.5	11.7	2.4	5.1
PS-1.5	51.7	62.5	11.7	2.4	5.4
PS-1.6	78.3	80.5	7.7	1.5	6.4
PS-1.6	79.3	80.5	7.7	1.5	6.8
PS-1.6	79.8	80.5	7.7	1.5	7.2
PS-1.6	80.5	80.5	7.7	1.5	7.7
PS-1.6	0.0	80.5	7.7	1.5	8.1
PS-1.6	0.0	80.5	7.7	1.5	8.6
PS-1.6	0.0	80.5	7.7	1.5	9.0
PS-1.6	0.0	80.5	7.7	1.5	5.4
PS-1.6	75.2	80.5	7.7	1.5	5.1
PS-1.6	76.4	80.5	7.7	1.5	4.9
PS-1.6	73.8	80.5	7.7	1.5	4.6
PS-1.6	72.5	80.5	7.7	1.5	4.4
PS-1.6	73.0	80.5	7.7	1.5	4.1
PS-1.6	0.0	80.5	7.7	1.5	3.9
PS-1.6	0.0	80.5	7.7	1.5	3.6
PS-1.6	0.0	80.5	7.7	1.5	3.4
PS-1.6	65.3	80.5	7.7	1.5	3.1
PS-1.6	63.1	80.5	7.7	1.5	2.9
PS-1.6	61.3	80.5	7.7	1.5	2.6
PS-1.6	60.2	80.5	7.7	1.5	2.3
PS-1.6	59.2	80.5	7.7	1.5	2.1
PS-1.6	45.7	80.5	7.7	1.5	0.8
PS-1.6	44.9	80.5	7.7	1.5	0.7
PS-1.6	39.9	80.5	7.7	1.5	0.6
PS-1.6	33.5	80.5	7.7	1.5	0.4
PS-1.6	22.7	80.5	7.7	1.5	0.3
PS-1.6	13.6	80.5	7.7	1.5	0.2
PS-1.6	11.1	80.5	7.7	1.5	0.1
PS-1.6	4.2	80.5	7.7	1.5	0.1
PS-1.7	0.0	78.4	9.5	1.8	9.9
PS-1.7	78.4	78.4	9.5	1.8	9.5
PS-1.7	77.2	78.4	9.5	1.8	9.0

PS-1.7	77.9	78.4	9.5	1.8	8.6
PS-1.7	76.7	78.4	9.5	1.8	8.1
PS-1.7	76.3	78.4	9.5	1.8	7.7
PS-1.7	75.9	78.4	9.5	1.8	7.2
PS-1.7	74.8	78.4	9.5	1.8	6.8
PS-1.7	74.0	78.4	9.5	1.8	6.4
PS-1.7	4.4	78.4	9.5	1.8	0.1
PS-1.7	10.8	78.4	9.5	1.8	0.1
PS-1.7	12.9	78.4	9.5	1.8	0.2
PS-1.7	21.0	78.4	9.5	1.8	0.3
PS-1.7	30.1	78.4	9.5	1.8	0.4
PS-1.7	38.4	78.4	9.5	1.8	0.6
PS-1.7	43.4	78.4	9.5	1.8	0.7
PS-1.7	45.4	78.4	9.5	1.8	0.8
PS-1.7	58.1	78.4	9.5	1.8	2.1
PS-1.7	57.9	78.4	9.5	1.8	2.3
PS-1.7	60.2	78.4	9.5	1.8	2.6
PS-1.7	59.6	78.4	9.5	1.8	2.9
PS-1.7	0.0	78.4	9.5	1.8	3.1
PS-1.7	0.0	78.4	9.5	1.8	3.4
PS-1.7	0.0	78.4	9.5	1.8	3.6
PS-1.7	0.0	78.4	9.5	1.8	3.9
PS-1.7	65.7	78.4	9.5	1.8	4.1
PS-1.7	66.5	78.4	9.5	1.8	4.4
PS-1.7	67.0	78.4	9.5	1.8	4.6
PS-1.7	67.9	78.4	9.5	1.8	4.9
PS-1.7	68.7	78.4	9.5	1.8	5.1
PS-1.7	70.4	78.4	9.5	1.8	5.4
PS-1.7	72.6	78.4	9.5	1.8	5.6
PS-1.8	74.2	78.8	9.5	1.9	6.4
PS-1.8	74.1	78.8	9.5	1.9	6.8
PS-1.8	74.9	78.8	9.5	1.9	7.2
PS-1.8	76.4	78.8	9.5	1.9	7.7
PS-1.8	77.8	78.8	9.5	1.9	8.1
PS-1.8	77.3	78.8	9.5	1.9	8.6
PS-1.8	78.4	78.8	9.5	1.9	9.0
PS-1.8	78.8	78.8	9.5	1.9	9.5
PS-1.8	0.0	78.8	9.5	1.9	9.9
PS-1.8	68.7	78.8	9.5	1.9	5.4
PS-1.8	68.7	78.8	9.5	1.9	5.1
PS-1.8	65.9	78.8	9.5	1.9	4.9
PS-1.8	65.5	78.8	9.5	1.9	4.6
PS-1.8	66.5	78.8	9.5	1.9	4.4

PS-1.8	65.6	78.8	9.5	1.9	4.1
PS-1.8	64.2	78.8	9.5	1.9	3.9
PS-1.8	0.0	78.8	9.5	1.9	3.6
PS-1.8	0.0	78.8	9.5	1.9	3.4
PS-1.8	59.6	78.8	9.5	1.9	3.1
PS-1.8	58.1	78.8	9.5	1.9	2.9
PS-1.8	57.7	78.8	9.5	1.9	2.6
PS-1.8	55.7	78.8	9.5	1.9	2.3
PS-1.8	52.9	78.8	9.5	1.9	2.1
PS-1.8	42.0	78.8	9.5	1.9	0.8
PS-1.8	41.3	78.8	9.5	1.9	0.7
PS-1.8	38.2	78.8	9.5	1.9	0.6
PS-1.8	32.8	78.8	9.5	1.9	0.4
PS-1.8	25.4	78.8	9.5	1.9	0.3
PS-1.8	20.5	78.8	9.5	1.9	0.2
PS-1.8	17.3	78.8	9.5	1.9	0.2
PS-1.8	11.9	78.8	9.5	1.9	0.1
PS-1.9	78.9	78.9	9.5	2.0	9.5
PS-1.9	77.1	78.9	9.5	2.0	9.0
PS-1.9	77.4	78.9	9.5	2.0	8.6
PS-1.9	76.6	78.9	9.5	2.0	8.1
PS-1.9	75.5	78.9	9.5	2.0	7.7
PS-1.9	75.1	78.9	9.5	2.0	7.2
PS-1.9	75.0	78.9	9.5	2.0	6.8
PS-1.9	73.5	78.9	9.5	2.0	6.4
PS-1.9	12.6	78.9	9.5	2.0	0.1
PS-1.9	17.7	78.9	9.5	2.0	0.2
PS-1.9	21.6	78.9	9.5	2.0	0.2
PS-1.9	25.2	78.9	9.5	2.0	0.3
PS-1.9	29.5	78.9	9.5	2.0	0.4
PS-1.9	36.4	78.9	9.5	2.0	0.5
PS-1.9	39.9	78.9	9.5	2.0	0.6
PS-1.9	41.7	78.9	9.5	2.0	0.8
PS-1.9	0.0	78.9	9.5	2.0	2.0
PS-1.9	53.6	78.9	9.5	2.0	2.3
PS-1.9	53.4	78.9	9.5	2.0	2.5
PS-1.9	55.2	78.9	9.5	2.0	2.8
PS-1.9	56.4	78.9	9.5	2.0	3.0
PS-1.9	0.0	78.9	9.5	2.0	3.3
PS-1.9	0.0	78.9	9.5	2.0	3.5
PS-1.9	0.0	78.9	9.5	2.0	3.8
PS-1.9	61.1	78.9	9.5	2.0	4.1
PS-1.9	62.1	78.9	9.5	2.0	4.3

PS-1.9	62.8	78.9	9.5	2.0	4.6
PS-1.9	64.2	78.9	9.5	2.0	4.8
PS-1.9	65.2	78.9	9.5	2.0	5.1
PS-1.9	66.1	78.9	9.5	2.0	5.3
PS-1.9	67.0	78.9	9.5	2.0	5.6
PS-1.10	70.9	76.6	9.5	2.0	6.4
PS-1.10	70.8	76.6	9.5	2.0	6.8
PS-1.10	72.0	76.6	9.5	2.0	7.2
PS-1.10	74.0	76.6	9.5	2.0	7.7
PS-1.10	74.4	76.6	9.5	2.0	8.1
PS-1.10	76.0	76.6	9.5	2.0	8.6
PS-1.10	76.4	76.6	9.5	2.0	9.0
PS-1.10	76.6	76.6	9.5	2.0	9.5
PS-1.10	0.0	76.6	9.5	2.0	9.9
PS-1.10	65.7	76.6	9.5	2.0	5.6
PS-1.10	64.5	76.6	9.5	2.0	5.3
PS-1.10	62.8	76.6	9.5	2.0	5.1
PS-1.10	62.4	76.6	9.5	2.0	4.8
PS-1.10	61.8	76.6	9.5	2.0	4.6
PS-1.10	59.6	76.6	9.5	2.0	4.3
PS-1.10	59.5	76.6	9.5	2.0	4.1
PS-1.10	59.4	76.6	9.5	2.0	3.8
PS-1.10	59.0	76.6	9.5	2.0	3.5
PS-1.10	54.8	76.6	9.5	2.0	3.3
PS-1.10	54.3	76.6	9.5	2.0	3.0
PS-1.10	53.6	76.6	9.5	2.0	2.8
PS-1.10	51.5	76.6	9.5	2.0	2.5
PS-1.10	51.1	76.6	9.5	2.0	2.3
PS-1.10	39.4	76.6	9.5	2.0	0.8
PS-1.10	36.9	76.6	9.5	2.0	0.6
PS-1.10	35.0	76.6	9.5	2.0	0.5
PS-1.10	25.8	76.6	9.5	2.0	0.4
PS-1.10	18.9	76.6	9.5	2.0	0.2
PS-1.10	10.9	76.6	9.5	2.0	0.1
PS-1.10	6.1	76.6	9.5	2.0	0.1
PS-1.11	85.4	85.4	8.1	1.8	8.1
PS-1.11	85.3	85.4	8.1	1.8	7.7
PS-1.11	83.7	85.4	8.1	1.8	7.2
PS-1.11	83.1	85.4	8.1	1.8	6.8
PS-1.11	83.1	85.4	8.1	1.8	6.4
PS-1.11	6.2	85.4	8.1	1.8	0.1
PS-1.11	12.0	85.4	8.1	1.8	0.1
PS-1.11	15.8	85.4	8.1	1.8	0.2

PS-1.11	21.8	85.4	8.1	1.8	0.3
PS-1.11	30.8	85.4	8.1	1.8	0.4
PS-1.11	36.7	85.4	8.1	1.8	0.6
PS-1.11	40.7	85.4	8.1	1.8	0.7
PS-1.11	56.7	85.4	8.1	1.8	2.1
PS-1.11	60.2	85.4	8.1	1.8	2.3
PS-1.11	61.3	85.4	8.1	1.8	2.6
PS-1.11	63.0	85.4	8.1	1.8	2.9
PS-1.11	65.7	85.4	8.1	1.8	3.1
PS-1.11	66.7	85.4	8.1	1.8	3.4
PS-1.11	0.0	85.4	8.1	1.8	3.6
PS-1.11	74.4	85.4	8.1	1.8	3.9
PS-1.11	72.9	85.4	8.1	1.8	4.1
PS-1.11	76.5	85.4	8.1	1.8	4.4
PS-1.11	77.5	85.4	8.1	1.8	4.6
PS-1.12	80.8	84.9	8.1	1.9	6.4
PS-1.12	82.2	84.9	8.1	1.9	6.8
PS-1.12	83.3	84.9	8.1	1.9	7.2
PS-1.12	83.8	84.9	8.1	1.9	7.7
PS-1.12	84.9	84.9	8.1	1.9	8.1
PS-1.12	0.0	84.9	8.1	1.9	8.6
PS-1.12	74.6	84.9	8.1	1.9	4.9
PS-1.12	73.9	84.9	8.1	1.9	4.6
PS-1.12	70.4	84.9	8.1	1.9	4.4
PS-1.12	69.7	84.9	8.1	1.9	4.1
PS-1.12	68.9	84.9	8.1	1.9	3.9
PS-1.12	0.0	84.9	8.1	1.9	3.6
PS-1.12	0.0	84.9	8.1	1.9	3.4
PS-1.12	0.0	84.9	8.1	1.9	3.1
PS-1.12	61.7	84.9	8.1	1.9	2.9
PS-1.12	58.4	84.9	8.1	1.9	2.6
PS-1.12	56.4	84.9	8.1	1.9	2.3
PS-1.12	0.0	84.9	8.1	1.9	2.1
PS-1.12	39.9	84.9	8.1	1.9	0.6
PS-1.12	36.0	84.9	8.1	1.9	0.5
PS-1.12	28.7	84.9	8.1	1.9	0.4
PS-1.12	20.4	84.9	8.1	1.9	0.2
PS-1.12	15.0	84.9	8.1	1.9	0.2
PS-1.12	12.2	84.9	8.1	1.9	0.1
PS-1.12	6.5	84.9	8.1	1.9	0.1
PS-1.13	0.0	83.9	7.8	2.0	8.7
PS-1.13	0.0	83.9	7.8	2.0	8.2
PS-1.13	83.9	83.9	7.8	2.0	7.8

PS-1.13	83.8	83.9	7.8	2.0	7.3
PS-1.13	82.0	83.9	7.8	2.0	6.9
PS-1.13	80.8	83.9	7.8	2.0	6.5
PS-1.13	5.9	83.9	7.8	2.0	0.1
PS-1.13	11.0	83.9	7.8	2.0	0.2
PS-1.13	13.3	83.9	7.8	2.0	0.2
PS-1.13	19.9	83.9	7.8	2.0	0.3
PS-1.13	23.3	83.9	7.8	2.0	0.4
PS-1.13	32.0	83.9	7.8	2.0	0.5
PS-1.13	37.1	83.9	7.8	2.0	0.6
PS-1.13	40.4	83.9	7.8	2.0	0.7
PS-1.13	53.8	83.9	7.8	2.0	2.1
PS-1.13	56.1	83.9	7.8	2.0	2.4
PS-1.13	56.9	83.9	7.8	2.0	2.6
PS-1.13	59.4	83.9	7.8	2.0	2.9
PS-1.13	61.6	83.9	7.8	2.0	3.1
PS-1.13	61.9	83.9	7.8	2.0	3.4
PS-1.13	65.1	83.9	7.8	2.0	3.6
PS-1.13	66.0	83.9	7.8	2.0	3.9
PS-1.13	67.3	83.9	7.8	2.0	4.1
PS-1.13	69.0	83.9	7.8	2.0	4.4
PS-1.13	71.3	83.9	7.8	2.0	4.6
PS-1.13	70.8	83.9	7.8	2.0	4.9
PS-1.13	73.6	83.9	7.8	2.0	5.1
PS-2.1	38.2	69.8	4.6	1.1	0.6
PS-2.1	34.0	69.8	4.6	1.1	0.4
PS-2.1	26.4	69.8	4.6	1.1	0.3
PS-2.1	12.5	69.8	4.6	1.1	0.2
PS-2.1	10.7	69.8	4.6	1.1	0.1
PS-2.1	67.8	69.8	4.6	1.1	3.8
PS-2.1	68.3	69.8	4.6	1.1	3.9
PS-2.1	68.2	69.8	4.6	1.1	4.1
PS-2.1	68.1	69.8	4.6	1.1	4.2
PS-2.1	69.5	69.8	4.6	1.1	4.4
PS-2.1	69.8	69.8	4.6	1.1	4.5
PS-2.2	11.3	55.9	7.0	1.5	0.2
PS-2.2	17.6	55.9	7.0	1.5	0.3
PS-2.2	21.1	55.9	7.0	1.5	0.4
PS-2.2	21.0	55.9	7.0	1.5	0.4
PS-2.2	23.6	55.9	7.0	1.5	0.5
PS-2.2	28.1	55.9	7.0	1.5	0.6
PS-2.2	30.0	55.9	7.0	1.5	0.8
PS-2.2	46.0	55.9	7.0	1.5	3.1

PS-2.2	45.1	55.9	7.0	1.5	2.9
PS-2.2	43.7	55.9	7.0	1.5	2.8
PS-2.2	43.4	55.9	7.0	1.5	2.7
PS-2.2	43.1	55.9	7.0	1.5	2.5
PS-2.2	41.3	55.9	7.0	1.5	2.3
PS-2.2	0.0	55.9	7.0	1.5	1.9
PS-2.2	0.0	55.9	7.0	1.5	1.0
PS-2.2	30.0	55.9	7.0	1.5	0.7
PS-2.2	23.3	55.9	7.0	1.5	0.5
PS-2.2	16.2	55.9	7.0	1.5	0.3
PS-2.2	5.2	55.9	7.0	1.5	0.1
PS-2.2	11.3	55.9	7.0	1.5	0.2
PS-2.2	17.4	55.9	7.0	1.5	0.3
PS-2.2	16.3	55.9	7.0	1.5	0.3
PS-2.2	25.7	55.9	7.0	1.5	0.5
PS-2.2	55.9	55.9	7.0	1.5	7.0
PS-2.2	55.8	55.9	7.0	1.5	6.7
PS-2.2	55.3	55.9	7.0	1.5	6.4
PS-2.2	54.8	55.9	7.0	1.5	6.2
PS-2.2	54.5	55.9	7.0	1.5	5.9
PS-2.2	53.6	55.9	7.0	1.5	5.7
PS-2.2	53.4	55.9	7.0	1.5	5.4
PS-2.2	53.0	55.9	7.0	1.5	5.1
PS-2.2	52.0	55.9	7.0	1.5	4.9
PS-2.2	52.0	55.9	7.0	1.5	4.6
PS-2.2	50.5	55.9	7.0	1.5	4.4
PS-2.2	50.0	55.9	7.0	1.5	4.1
PS-2.2	49.1	55.9	7.0	1.5	3.9
PS-2.2	0.0	55.9	7.0	1.5	3.9
PS-2.2	49.0	55.9	7.0	1.5	3.7
PS-2.3	9.1	53.7	7.2	1.5	0.1
PS-2.3	11.0	53.7	7.2	1.5	0.2
PS-2.3	15.1	53.7	7.2	1.5	0.3
PS-2.3	17.3	53.7	7.2	1.5	0.3
PS-2.3	19.3	53.7	7.2	1.5	0.4
PS-2.3	22.5	53.7	7.2	1.5	0.5
PS-2.3	25.4	53.7	7.2	1.5	0.5
PS-2.3	27.6	53.7	7.2	1.5	0.6
PS-2.3	29.6	53.7	7.2	1.5	0.7
PS-2.3	28.9	53.7	7.2	1.5	0.7
PS-2.3	41.0	53.7	7.2	1.5	2.2
PS-2.3	41.0	53.7	7.2	1.5	2.4
PS-2.3	40.3	53.7	7.2	1.5	2.6

PS-2.3	43.3	53.7	7.2	1.5	2.7
PS-2.3	42.3	53.7	7.2	1.5	2.9
PS-2.3	45.1	53.7	7.2	1.5	3.1
PS-2.3	46.4	53.7	7.2	1.5	3.7
PS-2.3	47.9	53.7	7.2	1.5	4.1
PS-2.3	49.7	53.7	7.2	1.5	4.6
PS-2.3	50.2	53.7	7.2	1.5	5.0
PS-2.3	50.7	53.7	7.2	1.5	5.5
PS-2.3	52.1	53.7	7.2	1.5	5.9
PS-2.3	51.6	53.7	7.2	1.5	6.4
PS-2.3	52.6	53.7	7.2	1.5	6.8
PS-2.3	53.7	53.7	7.2	1.5	7.2
PS-2.4	45.5	53.7	7.4	1.5	3.4
PS-2.4	44.1	52.7	7.4	1.5	3.3
PS-2.4	42.3	52.7	7.4	1.5	3.1
PS-2.4	40.8	52.7	7.4	1.5	2.9
PS-2.4	40.7	52.7	7.4	1.5	2.7
PS-2.4	39.1	52.7	7.4	1.5	2.5
PS-2.4	38.9	52.7	7.4	1.5	2.3
PS-2.4	39.3	52.7	7.4	1.5	2.1
PS-2.4	29.1	52.7	7.4	1.5	0.7
PS-2.4	24.4	52.7	7.4	1.5	0.5
PS-2.4	16.0	52.7	7.4	1.5	0.3
PS-2.4	16.1	52.7	7.4	1.5	0.3
PS-2.4	11.1	52.7	7.4	1.5	0.2
PS-2.4	6.5	52.7	7.4	1.5	0.1
PS-2.4	50.8	52.7	7.4	1.5	5.7
PS-2.4	52.7	52.7	7.4	1.5	6.8
PS-2.4	52.1	52.7	7.4	1.5	6.4
PS-2.4	51.2	52.7	7.4	1.5	5.9
PS-2.4	51.1	52.7	7.4	1.5	5.5
PS-2.4	49.6	52.7	7.4	1.5	5.0
PS-2.4	48.5	52.7	7.4	1.5	4.6
PS-2.4	47.9	52.7	7.4	1.5	4.1
PS-2.4	47.3	52.7	7.4	1.5	3.7
PS-2.5	11.5	51.4	7.7	1.5	0.2
PS-2.5	14.5	51.4	7.7	1.5	0.3
PS-2.5	16.2	51.4	7.7	1.5	0.3
PS-2.5	21.6	51.4	7.7	1.5	0.4
PS-2.5	23.3	51.4	7.7	1.5	0.5
PS-2.5	26.1	51.4	7.7	1.5	0.5
PS-2.5	28.1	51.4	7.7	1.5	0.7
PS-2.5	30.5	51.4	7.7	1.5	0.8

PS-2.5	37.6	51.4	7.7	1.5	2.0
PS-2.5	37.9	51.4	7.7	1.5	2.2
PS-2.5	39.3	51.4	7.7	1.5	2.4
PS-2.5	38.8	51.4	7.7	1.5	2.5
PS-2.5	38.9	51.4	7.7	1.5	2.6
PS-2.5	39.8	51.4	7.7	1.5	2.7
PS-2.5	39.7	51.4	7.7	1.5	2.9
PS-2.5	40.6	51.4	7.7	1.5	3.0
PS-2.5	41.3	51.4	7.7	1.5	3.1
PS-2.5	43.0	51.4	7.7	1.5	3.3
PS-2.5	43.7	51.4	7.7	1.5	3.7
PS-2.5	45.2	51.4	7.7	1.5	4.0
PS-2.5	45.1	51.4	7.7	1.5	4.3
PS-2.5	46.8	51.4	7.7	1.5	4.6
PS-2.5	47.5	51.4	7.7	1.5	5.0
PS-2.5	48.2	51.4	7.7	1.5	5.3
PS-2.5	48.5	51.4	7.7	1.5	5.6
PS-2.5	49.4	51.4	7.7	1.5	5.9
PS-2.5	49.7	51.4	7.7	1.5	6.2
PS-2.5	49.7	51.4	7.7	1.5	6.5
PS-2.5	50.7	51.4	7.7	1.5	6.9
PS-2.5	51.1	51.4	7.7	1.5	7.2
PS-2.5	51.4	51.4	7.7	1.5	7.5
PS-2.6	5.4	49.9	7.8	1.8	0.1
PS-2.6	6.4	49.9	7.8	1.8	0.1
PS-2.6	12.0	49.9	7.8	1.8	0.2
PS-2.6	12.1	49.9	7.8	1.8	0.3
PS-2.6	14.4	49.9	7.8	1.8	0.3
PS-2.6	21.3	49.9	7.8	1.8	0.5
PS-2.6	22.8	49.9	7.8	1.8	0.6
PS-2.6	25.0	49.9	7.8	1.8	0.7
PS-2.6	33.9	49.9	7.8	1.8	2.4
PS-2.6	35.4	49.9	7.8	1.8	2.6
PS-2.6	34.7	49.9	7.8	1.8	2.7
PS-2.6	35.0	49.9	7.8	1.8	2.9
PS-2.6	36.8	49.9	7.8	1.8	3.1
PS-2.6	36.8	49.9	7.8	1.8	3.3
PS-2.6	49.9	49.9	7.8	1.8	7.8
PS-2.6	49.0	49.9	7.8	1.8	7.6
PS-2.6	49.3	49.9	7.8	1.8	7.3
PS-2.6	47.4	49.9	7.8	1.8	7.0
PS-2.6	48.0	49.9	7.8	1.8	6.7
PS-2.6	48.0	49.9	7.8	1.8	6.4

PS-2.6	46.6	49.9	7.8	1.8	6.0
PS-2.6	46.8	49.9	7.8	1.8	5.7
PS-2.6	45.4	49.9	7.8	1.8	5.4
PS-2.6	44.6	49.9	7.8	1.8	5.1
PS-2.6	44.0	49.9	7.8	1.8	4.8
PS-2.6	42.3	49.9	7.8	1.8	4.4
PS-2.6	42.7	49.9	7.8	1.8	4.1
PS-2.6	41.0	49.9	7.8	1.8	3.8
PS-2.6	40.0	49.9	7.8	1.8	3.7
PS-2.7	40.0	68.9	5.6	1.2	0.6
PS-2.7	34.7	68.9	5.6	1.2	0.5
PS-2.7	28.9	68.9	5.6	1.2	0.4
PS-2.7	20.6	68.9	5.6	1.2	0.2
PS-2.7	14.8	68.9	5.6	1.2	0.2
PS-2.7	62.8	68.9	5.6	1.2	3.8
PS-2.7	64.4	68.9	5.6	1.2	4.1
PS-2.7	65.6	68.9	5.6	1.2	4.4
PS-2.7	65.8	68.9	5.6	1.2	4.8
PS-2.7	67.0	68.9	5.6	1.2	5.1
PS-2.7	68.0	68.9	5.6	1.2	5.4
PS-2.7	68.9	68.9	5.6	1.2	5.7
PS-2.8	42.0	66.1	5.9	1.2	0.8
PS-2.8	39.3	66.1	5.9	1.2	0.7
PS-2.8	33.9	66.1	5.9	1.2	0.5
PS-2.8	26.1	66.1	5.9	1.2	0.4
PS-2.8	22.6	66.1	5.9	1.2	0.3
PS-2.8	20.6	66.1	5.9	1.2	0.3
PS-2.8	13.8	66.1	5.9	1.2	0.2
PS-2.8	9.3	66.1	5.9	1.2	0.1
PS-2.8	8.5	66.1	5.9	1.2	0.1
PS-2.8	66.1	66.1	5.9	1.2	5.9
PS-2.8	66.0	66.1	5.9	1.2	5.5
PS-2.8	65.5	66.1	5.9	1.2	5.1
PS-2.8	63.8	66.1	5.9	1.2	4.8
PS-2.8	62.9	66.1	5.9	1.2	4.4
PS-2.8	60.2	66.1	5.9	1.2	4.0
PS-2.8	60.7	66.1	5.9	1.2	3.8
PS-2.9	8.3	66.2	6.0	1.2	0.1
PS-2.9	8.1	66.2	6.0	1.2	0.1
PS-2.9	14.8	66.2	6.0	1.2	0.2
PS-2.9	19.5	66.2	6.0	1.2	0.3
PS-2.9	21.7	66.2	6.0	1.2	0.3
PS-2.9	26.9	66.2	6.0	1.2	0.4

PS-2.9	31.7	66.2	6.0	1.2	0.5
PS-2.9	35.8	66.2	6.0	1.2	0.6
PS-2.9	38.7	66.2	6.0	1.2	0.7
PS-2.9	0.0	66.2	6.0	1.2	0.8
PS-2.9	0.0	66.2	6.0	1.2	1.0
PS-2.9	0.0	66.2	6.0	1.2	1.9
PS-2.9	60.9	66.2	6.0	1.2	3.7
PS-2.9	61.2	66.2	6.0	1.2	4.1
PS-2.9	62.4	66.2	6.0	1.2	4.4
PS-2.9	64.0	66.2	6.0	1.2	4.7
PS-2.9	65.2	66.2	6.0	1.2	5.0
PS-2.9	64.9	66.2	6.0	1.2	5.3
PS-2.9	66.2	66.2	6.0	1.2	5.7
PS-2.10	25.3	62.1	6.3	1.3	0.4
PS-2.10	35.9	62.1	6.3	1.3	0.7
PS-2.10	34.2	62.1	6.3	1.3	0.6
PS-2.10	29.5	62.1	6.3	1.3	0.5
PS-2.10	20.4	62.1	6.3	1.3	0.3
PS-2.10	13.8	62.1	6.3	1.3	0.2
PS-2.10	9.6	62.1	6.3	1.3	0.1
PS-2.10	7.1	62.1	6.3	1.3	0.1
PS-2.10	62.1	62.1	6.3	1.3	6.3
PS-2.10	61.4	62.1	6.3	1.3	6.0
PS-2.10	61.4	62.1	6.3	1.3	5.7
PS-2.10	60.6	62.1	6.3	1.3	5.3
PS-2.10	59.9	62.1	6.3	1.3	5.0
PS-2.10	58.8	62.1	6.3	1.3	4.7
PS-2.10	58.4	62.1	6.3	1.3	4.4
PS-2.10	56.4	62.1	6.3	1.3	4.1
PS-2.10	56.6	62.1	6.3	1.3	3.7
PS-2.11	45.1	60.8	6.5	1.4	2.0
PS-2.11	0.0	60.8	6.5	1.4	1.9
PS-2.11	32.3	60.8	6.5	1.4	0.7
PS-2.11	29.9	60.8	6.5	1.4	0.5
PS-2.11	25.1	60.8	6.5	1.4	0.4
PS-2.11	17.5	60.8	6.5	1.4	0.3
PS-2.11	14.4	60.8	6.5	1.4	0.2
PS-2.11	7.4	60.8	6.5	1.4	0.1
PS-2.11	6.0	60.8	6.5	1.4	0.1
PS-2.11	3.7	60.8	6.5	1.4	0.0
PS-2.11	54.0	60.8	6.5	1.4	3.7
PS-2.11	53.1	60.8	6.5	1.4	3.9
PS-2.11	53.6	60.8	6.5	1.4	4.1

PS-2.11	55.2	60.8	6.5	1.4	4.3
PS-2.11	55.3	60.8	6.5	1.4	4.4
PS-2.11	56.2	60.8	6.5	1.4	4.6
PS-2.11	56.5	60.8	6.5	1.4	4.8
PS-2.11	57.5	60.8	6.5	1.4	5.0
PS-2.11	57.3	60.8	6.5	1.4	5.2
PS-2.11	58.6	60.8	6.5	1.4	5.4
PS-2.11	58.1	60.8	6.5	1.4	5.6
PS-2.11	58.2	60.8	6.5	1.4	5.8
PS-2.11	59.9	60.8	6.5	1.4	6.0
PS-2.11	60.0	60.8	6.5	1.4	6.2
PS-2.11	59.9	60.8	6.5	1.4	6.4
PS-2.11	60.8	60.8	6.5	1.4	6.5
PS-2.12	8.3	70.4	5.3	1.2	0.1
PS-2.12	14.0	70.4	5.3	1.2	0.2
PS-2.12	18.8	70.4	5.3	1.2	0.3
PS-2.12	21.4	70.4	5.3	1.2	0.3
PS-2.12	26.4	70.4	5.3	1.2	0.4
PS-2.12	34.5	70.4	5.3	1.2	0.5
PS-2.12	36.1	70.4	5.3	1.2	0.6
PS-2.12	40.8	70.4	5.3	1.2	0.7
PS-2.12	7.2	70.4	5.3	1.2	0.1
PS-2.12	13.6	70.4	5.3	1.2	0.1
PS-2.12	70.4	70.4	5.3	1.2	5.3
PS-2.12	68.6	70.4	5.3	1.2	5.0
PS-2.12	68.6	70.4	5.3	1.2	4.7
PS-2.12	67.5	70.4	5.3	1.2	4.4
PS-2.12	66.0	70.4	5.3	1.2	4.1
PS-2.12	65.2	70.4	5.3	1.2	3.7
PS-2.13	5.6	70.3	5.7	1.3	0.1
PS-2.13	7.4	70.3	5.7	1.3	0.1
PS-2.13	16.7	70.3	5.7	1.3	0.2
PS-2.13	19.5	70.3	5.7	1.3	0.3
PS-2.13	23.0	70.3	5.7	1.3	0.3
PS-2.13	25.7	70.3	5.7	1.3	0.4
PS-2.13	31.8	70.3	5.7	1.3	0.5
PS-2.13	36.7	70.3	5.7	1.3	0.6
PS-2.13	39.7	70.3	5.7	1.3	0.7
PS-2.13	0.0	70.3	5.7	1.3	0.8
PS-2.13	63.5	70.3	5.7	1.3	3.7
PS-2.13	65.8	70.3	5.7	1.3	4.1
PS-2.13	66.7	70.3	5.7	1.3	4.4
PS-2.13	66.6	70.3	5.7	1.3	4.7

PS-2.13	68.4	70.3	5.7	1.3	5.0
PS-2.13	69.2	70.3	5.7	1.3	5.3
PS-2.13	69.8	70.3	5.7	1.3	5.7
PS-2.14	38.9	70.0	5.5	1.6	1.4
PS-2.14	34.9	70.0	5.5	1.6	0.7
PS-2.14	28.7	70.0	5.5	1.6	0.6
PS-2.14	21.6	70.0	5.5	1.6	0.5
PS-2.14	17.0	70.0	5.5	1.6	0.3
PS-2.14	8.3	70.0	5.5	1.6	0.3
PS-2.14	7.6	70.0	5.5	1.6	0.2
PS-2.14	3.7	70.0	5.5	1.6	0.1
PS-2.14	3.1	70.0	5.5	1.6	0.1
PS-2.14	66.0	70.0	5.5	1.6	4.5
PS-2.14	64.8	70.0	5.5	1.6	4.4
PS-2.14	64.8	70.0	5.5	1.6	4.3
PS-2.14	63.9	70.0	5.5	1.6	4.1
PS-2.14	62.7	70.0	5.5	1.6	3.9
PS-2.14	62.3	70.0	5.5	1.6	3.7
PS-3.1	6.8	54.0	5.9	1.3	0.2
PS-3.1	8.9	54.0	5.9	1.3	0.2
PS-3.1	13.2	54.0	5.9	1.3	0.3
PS-3.1	17.2	54.0	5.9	1.3	0.3
PS-3.1	18.6	54.0	5.9	1.3	0.4
PS-3.1	24.3	54.0	5.9	1.3	0.5
PS-3.1	25.3	54.0	5.9	1.3	0.5
PS-3.1	28.2	54.0	5.9	1.3	0.6
PS-3.1	30.4	54.0	5.9	1.3	0.7
PS-3.1	31.5	54.0	5.9	1.3	0.7
PS-3.1	50.4	54.0	5.9	1.3	4.5
PS-3.1	49.8	54.0	5.9	1.3	4.3
PS-3.1	49.4	54.0	5.9	1.3	4.0
PS-3.1	48.6	54.0	5.9	1.3	3.8
PS-3.1	48.2	54.0	5.9	1.3	3.5
PS-3.1	42.8	54.0	5.9	1.3	2.4
PS-3.1	44.0	54.0	5.9	1.3	2.6
PS-3.1	44.7	54.0	5.9	1.3	2.9
PS-3.1	46.4	54.0	5.9	1.3	3.1
PS-3.1	47.2	54.0	5.9	1.3	3.4
PS-3.1	48.4	54.0	5.9	1.3	3.6
PS-3.1	48.7	54.0	5.9	1.3	3.9
PS-3.1	49.5	54.0	5.9	1.3	4.2
PS-3.1	50.2	54.0	5.9	1.3	4.4
PS-3.2	39.8	50.5	6.2	1.2	2.2

PS-3.2	26.8	50.5	6.2	1.2	0.6
PS-3.2	25.6	50.5	6.2	1.2	0.5
PS-3.2	23.1	50.5	6.2	1.2	0.5
PS-3.2	18.5	50.5	6.2	1.2	0.4
PS-3.2	17.2	50.5	6.2	1.2	0.3
PS-3.2	14.9	50.5	6.2	1.2	0.3
PS-3.2	9.8	50.5	6.2	1.2	0.2
PS-3.2	8.3	50.5	6.2	1.2	0.1
PS-3.2	2.8	50.5	6.2	1.2	0.1
PS-3.2	46.5	50.5	6.2	1.2	3.5
PS-3.2	46.3	50.5	6.2	1.2	3.8
PS-3.2	46.8	50.5	6.2	1.2	4.0
PS-3.2	48.5	50.5	6.2	1.2	4.3
PS-3.2	48.3	50.5	6.2	1.2	4.6
PS-3.2	48.8	50.5	6.2	1.2	4.8
PS-3.2	49.8	50.5	6.2	1.2	5.1
PS-3.2	50.4	50.5	6.2	1.2	5.3
PS-3.2	50.2	50.5	6.2	1.2	5.6
PS-3.2	50.5	50.5	6.2	1.2	5.4
PS-3.2	49.2	50.5	6.2	1.2	5.2
PS-3.2	48.8	50.5	6.2	1.2	4.9
PS-3.2	48.4	50.5	6.2	1.2	4.7
PS-3.2	48.4	50.5	6.2	1.2	4.4
PS-3.2	47.6	50.5	6.2	1.2	4.2
PS-3.2	46.4	50.5	6.2	1.2	3.9
PS-3.2	45.5	50.5	6.2	1.2	3.6
PS-3.2	45.2	50.5	6.2	1.2	3.4
PS-3.2	44.5	50.5	6.2	1.2	3.1
PS-3.2	42.9	50.5	6.2	1.2	2.9
PS-3.2	42.6	50.5	6.2	1.2	2.6
PS-3.2	40.4	50.5	6.2	1.2	2.4
PS-3.3	9.6	50.0	6.4	1.3	0.2
PS-3.3	13.5	50.0	6.4	1.3	0.3
PS-3.3	16.8	50.0	6.4	1.3	0.3
PS-3.3	17.5	50.0	6.4	1.3	0.4
PS-3.3	22.8	50.0	6.4	1.3	0.5
PS-3.3	25.0	50.0	6.4	1.3	0.5
PS-3.3	27.5	50.0	6.4	1.3	0.6
PS-3.3	28.6	50.0	6.4	1.3	0.6
PS-3.3	29.1	50.0	6.4	1.3	0.7
PS-3.3	39.9	50.0	6.4	1.3	2.3
PS-3.3	50.0	50.0	6.4	1.3	5.6
PS-3.3	49.1	50.0	6.4	1.3	5.3

PS-3.3	48.5	50.0	6.4	1.3	5.1
PS-3.3	48.0	50.0	6.4	1.3	4.8
PS-3.3	48.2	50.0	6.4	1.3	4.6
PS-3.3	46.7	50.0	6.4	1.3	4.3
PS-3.3	46.8	50.0	6.4	1.3	4.0
PS-3.3	44.5	50.0	6.4	1.3	3.8
PS-3.3	45.2	50.0	6.4	1.3	3.5
PS-3.3	39.7	50.0	6.4	1.3	2.1
PS-3.3	40.4	50.0	6.4	1.3	2.4
PS-3.3	40.7	50.0	6.4	1.3	2.6
PS-3.3	42.0	50.0	6.4	1.3	2.9
PS-3.3	42.9	50.0	6.4	1.3	3.1
PS-3.3	43.3	50.0	6.4	1.3	3.4
PS-3.3	44.7	50.0	6.4	1.3	3.6
PS-3.3	45.6	50.0	6.4	1.3	3.9
PS-3.3	46.7	50.0	6.4	1.3	4.2
PS-3.3	47.2	50.0	6.4	1.3	4.4
PS-3.3	47.9	50.0	6.4	1.3	4.7
PS-3.3	48.2	50.0	6.4	1.3	4.9
PS-3.3	49.0	50.0	6.4	1.3	5.2
PS-3.3	49.5	50.0	6.4	1.3	5.4
PS-3.4	37.1	47.0	6.6	1.3	2.5
PS-3.4	38.2	47.0	6.6	1.3	2.3
PS-3.4	37.8	47.0	6.6	1.3	2.2
PS-3.4	30.8	47.0	6.6	1.3	0.9
PS-3.4	28.7	47.0	6.6	1.3	0.8
PS-3.4	28.0	47.0	6.6	1.3	0.8
PS-3.4	27.6	47.0	6.6	1.3	0.7
PS-3.4	25.4	47.0	6.6	1.3	0.6
PS-3.4	24.1	47.0	6.6	1.3	0.6
PS-3.4	21.2	47.0	6.6	1.3	0.5
PS-3.4	17.0	47.0	6.6	1.3	0.4
PS-3.4	16.1	47.0	6.6	1.3	0.4
PS-3.4	13.8	47.0	6.6	1.3	0.3
PS-3.4	9.0	47.0	6.6	1.3	0.2
PS-3.4	41.7	47.0	6.6	1.3	3.5
PS-3.4	43.0	47.0	6.6	1.3	3.8
PS-3.4	43.4	47.0	6.6	1.3	4.0
PS-3.4	44.1	47.0	6.6	1.3	4.3
PS-3.4	45.8	47.0	6.6	1.3	4.6
PS-3.4	45.3	47.0	6.6	1.3	4.8
PS-3.4	45.0	47.0	6.6	1.3	5.1
PS-3.4	46.7	47.0	6.6	1.3	5.3

PS-3.4	46.7	47.0	6.6	1.3	5.6
PS-3.4	46.8	47.0	6.6	1.3	5.8
PS-3.4	47.0	47.0	6.6	1.3	6.1
PS-3.4	46.1	47.0	6.6	1.3	5.4
PS-3.4	46.2	47.0	6.6	1.3	5.2
PS-3.4	45.6	47.0	6.6	1.3	4.9
PS-3.4	44.7	47.0	6.6	1.3	4.7
PS-3.4	44.3	47.0	6.6	1.3	4.4
PS-3.4	43.2	47.0	6.6	1.3	4.2
PS-3.4	43.2	47.0	6.6	1.3	3.9
PS-3.4	42.5	47.0	6.6	1.3	3.6
PS-3.4	41.9	47.0	6.6	1.3	3.4
PS-3.4	41.0	47.0	6.6	1.3	3.1
PS-3.4	39.6	47.0	6.6	1.3	2.9
PS-3.4	39.4	47.0	6.6	1.3	2.6
PS-3.4	37.9	47.0	6.6	1.3	2.4
PS-3.4	36.4	47.0	6.6	1.3	2.1
PS-3.5	4.9	44.0	6.7	1.4	0.1
PS-3.5	7.2	44.0	6.7	1.4	0.2
PS-3.5	10.8	44.0	6.7	1.4	0.2
PS-3.5	13.3	44.0	6.7	1.4	0.3
PS-3.5	14.0	44.0	6.7	1.4	0.4
PS-3.5	18.0	44.0	6.7	1.4	0.4
PS-3.5	18.8	44.0	6.7	1.4	0.4
PS-3.5	21.5	44.0	6.7	1.4	0.5
PS-3.5	22.9	44.0	6.7	1.4	0.5
PS-3.5	23.7	44.0	6.7	1.4	0.6
PS-3.5	33.4	44.0	6.7	1.4	2.2
PS-3.5	33.2	44.0	6.7	1.4	2.3
PS-3.5	33.7	44.0	6.7	1.4	2.4
PS-3.5	44.0	44.0	6.7	1.4	6.1
PS-3.5	43.2	44.0	6.7	1.4	5.8
PS-3.5	43.3	44.0	6.7	1.4	5.6
PS-3.5	42.4	44.0	6.7	1.4	5.3
PS-3.5	42.5	44.0	6.7	1.4	5.1
PS-3.5	42.1	44.0	6.7	1.4	4.8
PS-3.5	40.9	44.0	6.7	1.4	4.6
PS-3.5	40.5	44.0	6.7	1.4	4.3
PS-3.5	40.6	44.0	6.7	1.4	4.0
PS-3.5	38.9	44.0	6.7	1.4	3.8
PS-3.5	38.6	44.0	6.7	1.4	3.5
PS-3.5	32.7	44.0	6.7	1.4	2.1
PS-3.5	33.2	44.0	6.7	1.4	2.4

PS-3.5	34.4	44.0	6.7	1.4	2.6
PS-3.5	36.2	44.0	6.7	1.4	2.9
PS-3.5	36.7	44.0	6.7	1.4	3.1
PS-3.5	37.7	44.0	6.7	1.4	3.4
PS-3.5	38.6	44.0	6.7	1.4	3.6
PS-3.5	38.7	44.0	6.7	1.4	3.9
PS-3.5	40.0	44.0	6.7	1.4	4.2
PS-3.5	40.1	44.0	6.7	1.4	4.4
PS-3.5	40.5	44.0	6.7	1.4	4.7
PS-3.5	41.1	44.0	6.7	1.4	4.9
PS-3.5	42.3	44.0	6.7	1.4	5.2
PS-3.5	42.3	44.0	6.7	1.4	5.4
PS-3.6	35.0	56.3	5.1	1.2	0.7
PS-3.6	32.1	56.3	5.1	1.2	0.7
PS-3.6	28.7	56.3	5.1	1.2	0.6
PS-3.6	7.8	56.3	5.1	1.2	0.5
PS-3.6	10.9	56.3	5.1	1.2	0.2
PS-3.6	15.4	56.3	5.1	1.2	0.3
PS-3.6	56.1	56.3	5.1	1.2	4.8
PS-3.6	55.1	56.3	5.1	1.2	4.6
PS-3.6	55.0	56.3	5.1	1.2	4.3
PS-3.6	54.6	56.3	5.1	1.2	4.0
PS-3.6	53.8	56.3	5.1	1.2	3.8
PS-3.6	56.3	56.3	5.1	1.2	4.4
PS-3.6	55.6	56.3	5.1	1.2	4.2
PS-3.6	54.5	56.3	5.1	1.2	3.9
PS-3.6	54.4	56.3	5.1	1.2	3.6
PS-3.6	52.5	56.3	5.1	1.2	3.4
PS-3.6	51.7	56.3	5.1	1.2	3.1
PS-3.6	49.9	56.3	5.1	1.2	2.9
PS-3.6	49.1	56.3	5.1	1.2	2.6
PS-3.7	14.8	55.2	5.3	1.1	0.2
PS-3.7	19.5	55.2	5.3	1.1	0.3
PS-3.7	23.4	55.2	5.3	1.1	0.3
PS-3.7	52.4	55.2	5.3	1.1	4.0
PS-3.7	53.7	55.2	5.3	1.1	4.2
PS-3.7	54.3	55.2	5.3	1.1	4.5
PS-3.7	55.2	55.2	5.3	1.1	4.8
PS-3.7	55.2	55.2	5.3	1.1	5.0
PS-3.7	55.1	55.2	5.3	1.1	5.3
PS-3.7	48.6	55.2	5.3	1.1	2.9
PS-3.7	49.3	55.2	5.3	1.1	3.1
PS-3.7	50.4	55.2	5.3	1.1	3.4

PS-3.7	51.2	55.2	5.3	1.1	3.6
PS-3.7	52.5	55.2	5.3	1.1	3.9
PS-3.7	53.4	55.2	5.3	1.1	4.1
PS-3.7	54.1	55.2	5.3	1.1	4.4
PS-3.8	18.2	53.5	5.5	1.2	0.4
PS-3.8	16.4	53.5	5.5	1.2	0.4
PS-3.8	13.0	53.5	5.5	1.2	0.3
PS-3.8	22.1	53.5	5.5	1.2	0.5
PS-3.8	24.2	53.5	5.5	1.2	0.5
PS-3.8	27.1	53.5	5.5	1.2	0.6
PS-3.8	30.1	53.5	5.5	1.2	0.7
PS-3.8	30.4	53.5	5.5	1.2	0.7
PS-3.8	53.5	53.5	5.5	1.2	5.3
PS-3.8	52.9	53.5	5.5	1.2	5.0
PS-3.8	52.7	53.5	5.5	1.2	4.8
PS-3.8	51.8	53.5	5.5	1.2	4.5
PS-3.8	50.9	53.5	5.5	1.2	4.2
PS-3.8	50.5	53.5	5.5	1.2	4.0
PS-3.8	50.9	53.5	5.5	1.2	4.1
PS-3.8	50.0	53.5	5.5	1.2	3.8
PS-3.8	49.5	53.5	5.5	1.2	3.6
PS-3.8	47.8	53.5	5.5	1.2	3.3
PS-3.8	48.3	53.5	5.5	1.2	3.1
PS-3.8	46.2	53.5	5.5	1.2	2.8
PS-3.8	45.1	53.5	5.5	1.2	2.6
PS-3.8	44.2	53.5	5.5	1.2	2.3
PS-3.8	43.8	53.5	5.5	1.2	2.1
PS-3.9	27.9	52.6	5.6	1.4	0.8
PS-3.9	26.5	52.6	5.6	1.4	0.8
PS-3.9	25.9	52.6	5.6	1.4	0.7
PS-3.9	23.4	52.6	5.6	1.4	0.6
PS-3.9	20.2	52.6	5.6	1.4	0.6
PS-3.9	17.0	52.6	5.6	1.4	0.5
PS-3.9	15.3	52.6	5.6	1.4	0.5
PS-3.9	49.3	52.6	5.6	1.4	3.7
PS-3.9	49.1	52.6	5.6	1.4	4.0
PS-3.9	50.0	52.6	5.6	1.4	4.2
PS-3.9	50.2	52.6	5.6	1.4	4.5
PS-3.9	50.5	52.6	5.6	1.4	4.8
PS-3.9	51.7	52.6	5.6	1.4	5.0
PS-3.9	52.1	52.6	5.6	1.4	5.3
PS-3.9	52.6	52.6	5.6	1.4	5.5
PS-3.9	41.2	52.6	5.6	1.4	2.3

PS-3.9	43.1	52.6	5.6	1.4	2.6
PS-3.9	43.7	52.6	5.6	1.4	2.8
PS-3.9	44.9	52.6	5.6	1.4	3.1
PS-3.9	45.0	52.6	5.6	1.4	3.3
PS-3.9	47.5	52.6	5.6	1.4	3.6
PS-3.9	47.8	52.6	5.6	1.4	3.8
PS-3.9	48.8	52.6	5.6	1.4	4.1
PS-3.9	49.3	52.6	5.6	1.4	4.4
PS-3.9	50.7	52.6	5.6	1.4	4.6
PS-3.10	63.3	63.3	4.8	0.9	4.8
PS-3.10	61.7	63.3	4.8	0.9	4.5
PS-3.10	61.7	63.3	4.8	0.9	4.2
PS-3.10	61.4	63.3	4.8	0.9	4.0
PS-3.10	54.3	63.3	4.8	0.9	2.3
PS-3.10	55.1	63.3	4.8	0.9	2.6
PS-3.10	57.1	63.3	4.8	0.9	2.8
PS-3.10	58.1	63.3	4.8	0.9	3.1
PS-3.10	59.2	63.3	4.8	0.9	3.3
PS-3.10	60.5	63.3	4.8	0.9	3.6
PS-3.10	61.4	63.3	4.8	0.9	3.8
PS-3.11	1.2	59.2	4.8	1.0	0.0
PS-3.11	58.6	59.2	4.8	1.0	4.0
PS-3.11	58.5	59.2	4.8	1.0	4.2
PS-3.11	59.2	59.2	4.8	1.0	4.5
PS-3.11	58.7	59.2	4.8	1.0	4.8
PS-3.11	58.8	59.2	4.8	1.0	3.8
PS-3.11	57.3	59.2	4.8	1.0	3.6
PS-3.11	55.8	59.2	4.8	1.0	3.3
PS-3.11	55.0	59.2	4.8	1.0	3.1
PS-3.11	53.4	59.2	4.8	1.0	2.8
PS-3.11	52.2	59.2	4.8	1.0	2.6
PS-3.11	49.9	59.2	4.8	1.0	2.3
So94-1	33.0	88.9	20.0	4.3	1.6
So94-1	88.9	88.9	20.0	4.3	20.5
So94-1	42.5	88.9	20.0	4.3	2.0
So94-1	47.3	88.9	20.0	4.3	2.5
So94-1	51.6	88.9	20.0	4.3	2.9
So94-1	53.5	88.9	20.0	4.3	3.2
So94-1	55.7	88.9	20.0	4.3	3.6
So94-1	58.3	88.9	20.0	4.3	4.0
So94-1	60.4	88.9	20.0	4.3	4.4
So94-1	62.0	88.9	20.0	4.3	4.8
So94-1	63.6	88.9	20.0	4.3	5.2

So94-1	64.8	88.9	20.0	4.3	5.6
So94-1	66.0	88.9	20.0	4.3	6.0
So94-1	67.0	88.9	20.0	4.3	6.4
So94-1	68.0	88.9	20.0	4.3	6.8
So94-1	69.1	88.9	20.0	4.3	7.1
So94-1	70.0	88.9	20.0	4.3	7.5
So94-1	71.0	88.9	20.0	4.3	8.0
So94-1	72.0	88.9	20.0	4.3	8.3
So94-1	73.2	88.9	20.0	4.3	8.7
So94-1	74.0	88.9	20.0	4.3	9.1
So94-1	74.9	88.9	20.0	4.3	9.5
So94-1	75.9	88.9	20.0	4.3	9.9
So94-1	76.8	88.9	20.0	4.3	10.3
So94-1	77.7	88.9	20.0	4.3	10.7
So94-1	78.5	88.9	20.0	4.3	11.0
So94-1	79.3	88.9	20.0	4.3	11.5
So94-1	80.2	88.9	20.0	4.3	11.9
So94-1	81.1	88.9	20.0	4.3	12.3
So94-1	82.1	88.9	20.0	4.3	12.6
So94-1	82.8	88.9	20.0	4.3	13.0
So94-1	83.5	88.9	20.0	4.3	13.4
So94-1	84.1	88.9	20.0	4.3	13.9
So94-1	84.9	88.9	20.0	4.3	14.2
So94-1	85.1	88.9	20.0	4.3	14.6
So94-1	85.7	88.9	20.0	4.3	15.0
So94-1	86.2	88.9	20.0	4.3	15.3
So94-1	86.8	88.9	20.0	4.3	15.7
So94-1	87.1	88.9	20.0	4.3	16.1
So94-1	87.4	88.9	20.0	4.3	16.5
So94-1	87.7	88.9	20.0	4.3	16.9
So94-1	87.9	88.9	20.0	4.3	17.3
So94-1	88.0	88.9	20.0	4.3	17.7
So94-1	88.2	88.9	20.0	4.3	18.0
So94-1	88.3	88.9	20.0	4.3	18.5
So94-1	88.5	88.9	20.0	4.3	18.9
So94-1	88.5	88.9	20.0	4.3	19.3
So94-1	88.8	88.9	20.0	4.3	19.6
So94-1	88.8	88.9	20.0	4.3	20.0
So94-2	29.8	78.3	18.0	4.7	1.9
So94-2	78.3	78.3	18.0	4.7	18.0
So94-2	78.1	78.3	18.0	4.7	17.5
So94-2	77.6	78.3	18.0	4.7	17.2
So94-2	77.4	78.3	18.0	4.7	16.7

So94-2	77.0	78.3	18.0	4.7	16.3
So94-2	76.7	78.3	18.0	4.7	15.9
So94-2	76.2	78.3	18.0	4.7	15.4
So94-2	75.8	78.3	18.0	4.7	15.1
So94-2	75.4	78.3	18.0	4.7	14.7
So94-2	74.9	78.3	18.0	4.7	14.3
So94-2	74.2	78.3	18.0	4.7	13.9
So94-2	73.4	78.3	18.0	4.7	13.5
So94-2	72.8	78.3	18.0	4.7	13.1
So94-2	71.9	78.3	18.0	4.7	12.7
So94-2	71.2	78.3	18.0	4.7	12.3
So94-2	70.3	78.3	18.0	4.7	11.9
So94-2	69.6	78.3	18.0	4.7	11.5
So94-2	68.8	78.3	18.0	4.7	11.1
So94-2	68.2	78.3	18.0	4.7	10.7
So94-2	67.3	78.3	18.0	4.7	10.3
So94-2	66.5	78.3	18.0	4.7	9.9
So94-2	65.7	78.3	18.0	4.7	9.5
So94-2	65.0	78.3	18.0	4.7	9.0
So94-2	64.1	78.3	18.0	4.7	8.7
So94-2	62.8	78.3	18.0	4.7	8.2
So94-2	62.0	78.3	18.0	4.7	7.9
So94-2	60.8	78.3	18.0	4.7	7.5
So94-2	59.5	78.3	18.0	4.7	7.1
So94-2	58.8	78.3	18.0	4.7	6.6
So94-2	57.3	78.3	18.0	4.7	6.3
So94-2	56.2	78.3	18.0	4.7	5.9
So94-2	54.7	78.3	18.0	4.7	5.5
So94-2	53.0	78.3	18.0	4.7	5.1
So94-2	50.8	78.3	18.0	4.7	4.7
So94-2	49.4	78.3	18.0	4.7	4.3
So94-2	46.9	78.3	18.0	4.7	3.9
So94-2	44.3	78.3	18.0	4.7	3.6
So94-2	43.2	78.3	18.0	4.7	3.1
So94-2	40.1	78.3	18.0	4.7	2.7
So94-2	35.5	78.3	18.0	4.7	2.3
So94-3	28.5	78.3	14.5	3.2	0.9
So94-3	36.4	78.3	14.5	3.2	1.3
So94-3	43.7	78.3	14.5	3.2	1.7
So94-3	45.5	78.3	14.5	3.2	2.0
So94-3	47.2	78.3	14.5	3.2	2.4
So94-3	49.6	78.3	14.5	3.2	2.8
So94-3	53.8	78.3	14.5	3.2	3.6

So94-3	55.7	78.3	14.5	3.2	4.0
So94-3	58.8	78.3	14.5	3.2	4.8
So94-3	57.2	78.3	14.5	3.2	4.4
So94-3	60.7	78.3	14.5	3.2	5.2
So94-3	61.8	78.3	14.5	3.2	5.6
So94-3	51.1	78.3	14.5	3.2	3.3
So94-3	78.3	78.3	14.5	3.2	14.5
So94-3	77.6	78.3	14.5	3.2	14.0
So94-3	76.7	78.3	14.5	3.2	13.2
So94-3	76.1	78.3	14.5	3.2	12.6
So94-3	75.2	78.3	14.5	3.2	12.0
So94-3	76.1	78.3	14.5	3.2	11.6
So94-3	75.2	78.3	14.5	3.2	11.3
So94-3	74.5	78.3	14.5	3.2	11.0
So94-3	73.9	78.3	14.5	3.2	10.8
So94-3	73.7	78.3	14.5	3.2	10.4
So94-3	72.6	78.3	14.5	3.2	9.9
So94-3	71.9	78.3	14.5	3.2	9.6
So94-3	71.1	78.3	14.5	3.2	9.3
So94-3	70.3	78.3	14.5	3.2	8.9
So94-3	69.4	78.3	14.5	3.2	8.4
So94-3	68.6	78.3	14.5	3.2	8.0
So94-3	67.8	78.3	14.5	3.2	7.6
So94-3	67.4	78.3	14.5	3.2	7.3
So94-3	65.9	78.3	14.5	3.2	6.9
So94-3	64.7	78.3	14.5	3.2	6.6
So94-3	63.7	78.3	14.5	3.2	6.2
So94-3	62.5	78.3	14.5	3.2	5.8
So94-3	61.7	78.3	14.5	3.2	5.5
So94-3	60.7	78.3	14.5	3.2	5.2
So94-4	33.4	95.6	16.5	4.3	1.6
So94-4	40.4	95.6	16.5	4.3	2.1
So94-4	47.1	95.6	16.5	4.3	2.4
So94-4	52.0	95.6	16.5	4.3	2.8
So94-4	54.7	95.6	16.5	4.3	3.2
So94-4	57.1	95.6	16.5	4.3	3.7
So94-4	59.2	95.6	16.5	4.3	4.0
So94-4	61.4	95.6	16.5	4.3	4.5
So94-4	63.6	95.6	16.5	4.3	4.9
So94-4	65.9	95.6	16.5	4.3	5.3
So94-4	67.7	95.6	16.5	4.3	5.6
So94-4	69.3	95.6	16.5	4.3	6.0
So94-4	71.1	95.6	16.5	4.3	6.5

So94-4	73.3	95.6	16.5	4.3	6.8
So94-4	75.2	95.6	16.5	4.3	7.3
So94-4	76.6	95.6	16.5	4.3	7.7
So94-4	78.1	95.6	16.5	4.3	8.1
So94-4	79.8	95.6	16.5	4.3	8.5
So94-4	81.5	95.6	16.5	4.3	8.8
So94-4	82.7	95.6	16.5	4.3	9.2
So94-4	83.8	95.6	16.5	4.3	9.6
So94-4	84.7	95.6	16.5	4.3	10.0
So94-4	85.6	95.6	16.5	4.3	10.5
So94-4	87.1	95.6	16.5	4.3	10.9
So94-4	87.8	95.6	16.5	4.3	11.3
So94-4	88.7	95.6	16.5	4.3	11.6
So94-4	89.5	95.6	16.5	4.3	12.0
So94-4	90.3	95.6	16.5	4.3	12.4
So94-4	91.4	95.6	16.5	4.3	12.9
So94-4	92.0	95.6	16.5	4.3	13.3
So94-4	92.8	95.6	16.5	4.3	13.7
So94-4	93.5	95.6	16.5	4.3	14.0
So94-4	93.9	95.6	16.5	4.3	14.4
So94-4	94.3	95.6	16.5	4.3	14.8
So94-4	95.1	95.6	16.5	4.3	15.2
So94-4	95.3	95.6	16.5	4.3	15.6
So94-4	95.3	95.6	16.5	4.3	16.1
So94-4	95.6	95.6	16.5	4.3	16.5
So94-5	40.1	110.5	18.5	3.3	0.5
So94-5	51.3	110.5	18.5	3.3	0.9
So94-5	57.8	110.5	18.5	3.3	1.3
So94-5	62.1	110.5	18.5	3.3	1.7
So94-5	65.0	110.5	18.5	3.3	2.1
So94-5	67.8	110.5	18.5	3.3	2.5
So94-5	70.6	110.5	18.5	3.3	2.8
So94-5	72.9	110.5	18.5	3.3	3.3
So94-5	75.2	110.5	18.5	3.3	3.8
So94-5	77.5	110.5	18.5	3.3	4.1
So94-5	79.1	110.5	18.5	3.3	4.4
So94-5	81.7	110.5	18.5	3.3	4.8
So94-5	83.2	110.5	18.5	3.3	5.3
So94-5	85.3	110.5	18.5	3.3	5.6
So94-5	86.9	110.5	18.5	3.3	6.1
So94-5	88.6	110.5	18.5	3.3	6.5
So94-5	90.0	110.5	18.5	3.3	6.9
So94-5	91.6	110.5	18.5	3.3	7.4

So94-5	92.8	110.5	18.5	3.3	7.7
So94-5	94.2	110.5	18.5	3.3	8.1
So94-5	95.5	110.5	18.5	3.3	8.5
So94-5	96.6	110.5	18.5	3.3	8.9
So94-5	98.1	110.5	18.5	3.3	9.4
So94-5	98.7	110.5	18.5	3.3	9.8
So94-5	100.0	110.5	18.5	3.3	10.1
So94-5	101.0	110.5	18.5	3.3	10.5
So94-5	102.3	110.5	18.5	3.3	11.0
So94-5	103.3	110.5	18.5	3.3	11.5
So94-5	104.1	110.5	18.5	3.3	11.9
So94-5	105.6	110.5	18.5	3.3	12.5
So94-5	107.3	110.5	18.5	3.3	13.2
So94-5	108.2	110.5	18.5	3.3	13.9
So94-5	109.5	110.5	18.5	3.3	14.6
So94-5	109.9	110.5	18.5	3.3	15.3
So94-5	109.9	110.5	18.5	3.3	16.0
So94-5	110.1	110.5	18.5	3.3	16.6
So94-5	110.2	110.5	18.5	3.3	17.0
So94-5	110.2	110.5	18.5	3.3	17.4
So94-5	110.4	110.5	18.5	3.3	17.9
So94-5	110.5	110.5	18.5	3.3	18.5
So94-6	33.1	84.5	17.0	4.5	1.9
So94-6	38.5	84.5	17.0	4.5	2.4
So94-6	43.6	84.5	17.0	4.5	2.7
So94-6	45.8	84.5	17.0	4.5	3.1
So94-6	48.4	84.5	17.0	4.5	3.5
So94-6	50.7	84.5	17.0	4.5	3.9
So94-6	53.1	84.5	17.0	4.5	4.3
So94-6	55.3	84.5	17.0	4.5	4.7
So94-6	57.4	84.5	17.0	4.5	5.2
So94-6	59.3	84.5	17.0	4.5	5.5
So94-6	61.0	84.5	17.0	4.5	5.9
So94-6	62.1	84.5	17.0	4.5	6.2
So94-6	63.8	84.5	17.0	4.5	6.7
So94-6	65.1	84.5	17.0	4.5	7.1
So94-6	66.3	84.5	17.0	4.5	7.5
So94-6	67.3	84.5	17.0	4.5	7.9
So94-6	68.6	84.5	17.0	4.5	8.3
So94-6	69.5	84.5	17.0	4.5	8.6
So94-6	70.7	84.5	17.0	4.5	9.0
So94-6	71.8	84.5	17.0	4.5	9.4
So94-6	72.7	84.5	17.0	4.5	9.8

So94-6	73.6	84.5	17.0	4.5	10.2
So94-6	74.5	84.5	17.0	4.5	10.7
So94-6	75.1	84.5	17.0	4.5	11.1
So94-6	76.0	84.5	17.0	4.5	11.4
So94-6	77.1	84.5	17.0	4.5	11.8
So94-6	77.8	84.5	17.0	4.5	12.2
So94-6	78.6	84.5	17.0	4.5	12.6
So94-6	79.3	84.5	17.0	4.5	13.0
So94-6	80.3	84.5	17.0	4.5	13.4
So94-6	80.9	84.5	17.0	4.5	13.8
So94-6	81.7	84.5	17.0	4.5	14.2
So94-6	82.3	84.5	17.0	4.5	14.5
So94-6	82.9	84.5	17.0	4.5	14.9
So94-6	83.6	84.5	17.0	4.5	15.3
So94-6	83.9	84.5	17.0	4.5	15.7
So94-6	84.1	84.5	17.0	4.5	16.2
So94-6	84.5	84.5	17.0	4.5	17.0
So94-6	84.3	84.5	17.0	4.5	16.6
So94-7	30.4	82.3	20.5	4.2	1.1
So94-7	35.2	82.3	20.5	4.2	1.4
So94-7	41.2	82.3	20.5	4.2	1.8
So94-7	44.4	82.3	20.5	4.2	2.2
So94-7	46.4	82.3	20.5	4.2	2.6
So94-7	48.4	82.3	20.5	4.2	3.1
So94-7	49.9	82.3	20.5	4.2	3.4
So94-7	51.7	82.3	20.5	4.2	3.9
So94-7	53.5	82.3	20.5	4.2	4.3
So94-7	55.1	82.3	20.5	4.2	4.6
So94-7	56.7	82.3	20.5	4.2	5.0
So94-7	58.4	82.3	20.5	4.2	5.3
So94-7	59.8	82.3	20.5	4.2	5.8
So94-7	60.9	82.3	20.5	4.2	6.2
So94-7	62.1	82.3	20.5	4.2	6.5
So94-7	63.3	82.3	20.5	4.2	7.0
So94-7	64.4	82.3	20.5	4.2	7.4
So94-7	65.4	82.3	20.5	4.2	7.7
So94-7	66.4	82.3	20.5	4.2	8.1
So94-7	67.4	82.3	20.5	4.2	8.6
So94-7	68.4	82.3	20.5	4.2	9.0
So94-7	69.0	82.3	20.5	4.2	9.4
So94-7	70.1	82.3	20.5	4.2	9.8
So94-7	70.9	82.3	20.5	4.2	10.3
So94-7	72.0	82.3	20.5	4.2	10.7

So94-7	72.9	82.3	20.5	4.2	11.1
So94-7	73.7	82.3	20.5	4.2	11.6
So94-7	74.3	82.3	20.5	4.2	12.0
So94-7	75.1	82.3	20.5	4.2	12.4
So94-7	76.1	82.3	20.5	4.2	13.0
So94-7	76.9	82.3	20.5	4.2	13.6
So94-7	77.9	82.3	20.5	4.2	14.2
So94-7	78.5	82.3	20.5	4.2	14.7
So94-7	79.1	82.3	20.5	4.2	15.1
So94-7	79.6	82.3	20.5	4.2	15.6
So94-7	80.3	82.3	20.5	4.2	16.0
So94-7	80.9	82.3	20.5	4.2	16.7
So94-7	81.3	82.3	20.5	4.2	17.2
So94-7	81.6	82.3	20.5	4.2	17.7
So94-7	81.6	82.3	20.5	4.2	18.1
So94-7	81.8	82.3	20.5	4.2	18.7
So94-7	82.2	82.3	20.5	4.2	19.2
So94-7	82.1	82.3	20.5	4.2	19.7
So94-7	82.3	82.3	20.5	4.2	20.5
So94-8	42.2	115.7	18.0	4.4	1.3
So94-8	50.1	115.7	18.0	4.4	1.6
So94-8	56.9	115.7	18.0	4.4	2.0
So94-8	61.3	115.7	18.0	4.4	2.4
So94-8	64.1	115.7	18.0	4.4	2.8
So94-8	66.7	115.7	18.0	4.4	3.2
So94-8	69.3	115.7	18.0	4.4	3.6
So94-8	71.9	115.7	18.0	4.4	4.0
So94-8	74.3	115.7	18.0	4.4	4.4
So94-8	76.5	115.7	18.0	4.4	4.8
So94-8	78.6	115.7	18.0	4.4	5.2
So94-8	80.9	115.7	18.0	4.4	5.5
So94-8	82.8	115.7	18.0	4.4	6.0
So94-8	84.5	115.7	18.0	4.4	6.3
So94-8	85.7	115.7	18.0	4.4	6.8
So94-8	87.9	115.7	18.0	4.4	7.2
So94-8	89.5	115.7	18.0	4.4	7.6
So94-8	91.0	115.7	18.0	4.4	8.0
So94-8	92.7	115.7	18.0	4.4	8.4
So94-8	94.6	115.7	18.0	4.4	8.8
So94-8	96.2	115.7	18.0	4.4	9.2
So94-8	97.4	115.7	18.0	4.4	9.6
So94-8	100.6	115.7	18.0	4.4	10.4
So94-8	101.5	115.7	18.0	4.4	10.8

So94-8	102.9	115.7	18.0	4.4	11.1
So94-8	104.1	115.7	18.0	4.4	11.6
So94-8	102.9	115.7	18.0	4.4	11.2
So94-8	101.5	115.7	18.0	4.4	10.8
So94-8	100.3	115.7	18.0	4.4	10.4
So94-8	99.0	115.7	18.0	4.4	10.0
So94-8	97.0	115.7	18.0	4.4	9.6
So94-8	115.7	115.7	18.0	4.4	18.0
So94-8	115.0	115.7	18.0	4.4	17.4
So94-8	114.6	115.7	18.0	4.4	16.9
So94-8	114.1	115.7	18.0	4.4	16.5
So94-8	113.7	115.7	18.0	4.4	16.1
So94-8	113.0	115.7	18.0	4.4	15.5
So94-8	112.7	115.7	18.0	4.4	15.0
So94-8	111.6	115.7	18.0	4.4	14.5
So94-8	110.4	115.7	18.0	4.4	14.1
So94-8	109.5	115.7	18.0	4.4	13.7
So94-8	108.3	115.7	18.0	4.4	13.2
So94-8	107.5	115.7	18.0	4.4	12.8
So94-8	106.3	115.7	18.0	4.4	12.4
So94-8	105.4	115.7	18.0	4.4	12.0
So94-8	104.5	115.7	18.0	4.4	11.6
So94-8	103.3	115.7	18.0	4.4	11.3
So94-8	102.2	115.7	18.0	4.4	11.0
So94-8	100.8	115.7	18.0	4.4	10.5
So94-8	99.1	115.7	18.0	4.4	10.1
So94-8	97.7	115.7	18.0	4.4	9.7
So94-8	96.3	115.7	18.0	4.4	9.2
So94-8	94.6	115.7	18.0	4.4	8.8
So94-8	92.7	115.7	18.0	4.4	8.4
So94-8	91.2	115.7	18.0	4.4	8.0
So94-8	89.4	115.7	18.0	4.4	7.6
Ah98-1.1	27.2	33.3	13.5	2.2	4.6
Ah98-1.1	30.7	33.3	13.5	2.2	7.7
Ah98-1.1	31.0	33.3	13.5	2.2	9.2
Ah98-1.1	31.7	33.3	13.5	2.2	10.0
Ah98-1.1	32.3	33.3	13.5	2.2	10.8
Ah98-1.1	32.9	33.3	13.5	2.2	11.6
Ah98-1.1	33.0	33.3	13.5	2.2	12.3
Ah98-1.1	33.2	33.3	13.5	2.2	13.1
Ah98-1.1	33.3	33.3	13.5	2.2	13.5
Ah98-1.1	26.6	33.3	13.5	2.2	3.8
Ah98-1.1	25.8	33.3	13.5	2.2	3.0

Ah98-1.1	19.3	33.3	13.5	2.2	1.0
Ah98-1.1	30.3	33.3	13.5	2.2	6.9
Ah98-1.1	29.0	33.3	13.5	2.2	6.1
Ah98-1.1	23.4	33.3	13.5	2.2	2.2
Ah98-1.2	9.6	25.6	13.4	2.0	0.3
Ah98-1.2	12.6	25.6	13.4	2.0	0.7
Ah98-1.2	14.3	25.6	13.4	2.0	1.0
Ah98-1.2	16.5	25.6	13.4	2.0	1.4
Ah98-1.2	18.6	25.6	13.4	2.0	2.2
Ah98-1.2	19.8	25.6	13.4	2.0	3.0
Ah98-1.2	20.7	25.6	13.4	2.0	3.8
Ah98-1.2	22.1	25.6	13.4	2.0	4.6
Ah98-1.2	23.1	25.6	13.4	2.0	5.3
Ah98-1.2	23.3	25.6	13.4	2.0	6.1
Ah98-1.2	23.6	25.6	13.4	2.0	6.9
Ah98-1.2	24.0	25.6	13.4	2.0	7.7
Ah98-1.2	24.3	25.6	13.4	2.0	8.5
Ah98-1.2	24.6	25.6	13.4	2.0	9.2
Ah98-1.2	24.9	25.6	13.4	2.0	10.0
Ah98-1.2	25.2	25.6	13.4	2.0	10.8
Ah98-1.2	25.4	25.6	13.4	2.0	11.6
Ah98-1.2	25.6	25.6	13.4	2.0	12.3
Ah98-1.2	25.5	25.6	13.4	2.0	13.0
Ah98-1.2	25.4	25.6	13.4	2.0	13.4
Ah98-1.3	11.0	28.0	14.0	2.1	0.2
Ah98-1.3	13.9	28.0	14.0	2.1	0.6
Ah98-1.3	16.5	28.0	14.0	2.1	1.0
Ah98-1.3	17.8	28.0	14.0	2.1	1.4
Ah98-1.3	20.4	28.0	14.0	2.1	2.2
Ah98-1.3	21.0	28.0	14.0	2.1	3.0
Ah98-1.3	22.7	28.0	14.0	2.1	3.8
Ah98-1.3	22.6	28.0	14.0	2.1	4.5
Ah98-1.3	24.0	28.0	14.0	2.1	5.3
Ah98-1.3	25.3	28.0	14.0	2.1	6.1
Ah98-1.3	25.1	28.0	14.0	2.1	6.9
Ah98-1.3	25.5	28.0	14.0	2.1	7.7
Ah98-1.3	26.1	28.0	14.0	2.1	8.4
Ah98-1.3	26.6	28.0	14.0	2.1	9.3
Ah98-1.3	27.1	28.0	14.0	2.1	10.0
Ah98-1.3	27.2	28.0	14.0	2.1	10.8
Ah98-1.3	27.2	28.0	14.0	2.1	11.5
Ah98-1.3	27.5	28.0	14.0	2.1	12.3
Ah98-1.3	28.0	28.0	14.0	2.1	13.1

Ah98-1.3	27.6	28.0	14.0	2.1	13.5
Ah98-1.4	13.1	28.8	14.0	2.4	0.7
Ah98-1.4	15.8	28.8	14.0	2.4	1.1
Ah98-1.4	16.3	28.8	14.0	2.4	1.4
Ah98-1.4	18.8	28.8	14.0	2.4	2.2
Ah98-1.4	20.7	28.8	14.0	2.4	3.0
Ah98-1.4	23.2	28.8	14.0	2.4	4.5
Ah98-1.4	24.5	28.8	14.0	2.4	5.3
Ah98-1.4	26.1	28.8	14.0	2.4	6.1
Ah98-1.4	25.5	28.8	14.0	2.4	6.9
Ah98-1.4	26.5	28.8	14.0	2.4	7.7
Ah98-1.4	26.7	28.8	14.0	2.4	8.5
Ah98-1.4	27.3	28.8	14.0	2.4	9.3
Ah98-1.4	27.7	28.8	14.0	2.4	10.1
Ah98-1.4	27.9	28.8	14.0	2.4	10.8
Ah98-1.4	28.2	28.8	14.0	2.4	11.6
Ah98-1.4	28.8	28.8	14.0	2.4	12.3
Ah98-1.4	28.6	28.8	14.0	2.4	13.0
Ah98-1.4	28.4	28.8	14.0	2.4	13.5
Ah98-1.5	13.7	30.1	14.0	2.4	0.6
Ah98-1.5	16.8	30.1	14.0	2.4	1.1
Ah98-1.5	18.1	30.1	14.0	2.4	1.4
Ah98-1.5	20.9	30.1	14.0	2.4	2.1
Ah98-1.5	22.1	30.1	14.0	2.4	3.8
Ah98-1.5	24.3	30.1	14.0	2.4	4.5
Ah98-1.5	25.3	30.1	14.0	2.4	5.4
Ah98-1.5	25.9	30.1	14.0	2.4	6.2
Ah98-1.5	26.3	30.1	14.0	2.4	6.9
Ah98-1.5	27.1	30.1	14.0	2.4	7.7
Ah98-1.5	27.1	30.1	14.0	2.4	8.5
Ah98-1.5	27.9	30.1	14.0	2.4	9.3
Ah98-1.5	28.9	30.1	14.0	2.4	10.1
Ah98-1.5	29.8	30.1	14.0	2.4	10.8
Ah98-1.5	29.3	30.1	14.0	2.4	11.6
Ah98-1.5	29.8	30.1	14.0	2.4	12.3
Ah98-1.5	30.1	30.1	14.0	2.4	13.1
Ah98-1.5	29.7	30.1	14.0	2.4	13.5
Ah98-1.5	21.4	30.1	14.0	2.4	3.0
Ah98-1.5	11.8	30.1	14.0	2.4	0.3
Ah98-1.6	15.0	30.8	14.0	2.2	0.6
Ah98-1.6	17.4	30.8	14.0	2.2	1.0
Ah98-1.6	25.4	30.8	14.0	2.2	4.6
Ah98-1.6	25.7	30.8	14.0	2.2	5.4

Ah98-1.6	27.0	30.8	14.0	2.2	6.2
Ah98-1.6	27.9	30.8	14.0	2.2	6.9
Ah98-1.6	28.2	30.8	14.0	2.2	7.7
Ah98-1.6	28.6	30.8	14.0	2.2	8.5
Ah98-1.6	29.0	30.8	14.0	2.2	9.3
Ah98-1.6	29.7	30.8	14.0	2.2	10.0
Ah98-1.6	29.9	30.8	14.0	2.2	10.8
Ah98-1.6	30.3	30.8	14.0	2.2	11.6
Ah98-1.6	30.3	30.8	14.0	2.2	12.3
Ah98-1.6	30.8	30.8	14.0	2.2	13.1
Ah98-1.6	30.7	30.8	14.0	2.2	13.4
Ah98-1.6	18.7	30.8	14.0	2.2	1.4
Ah98-1.6	12.1	30.8	14.0	2.2	0.3
Ah98-1.7	15.5	31.7	14.0	2.3	0.6
Ah98-1.7	17.4	31.7	14.0	2.3	1.0
Ah98-1.7	25.0	31.7	14.0	2.3	4.5
Ah98-1.7	26.2	31.7	14.0	2.3	5.3
Ah98-1.7	27.0	31.7	14.0	2.3	6.0
Ah98-1.7	29.4	31.7	14.0	2.3	7.7
Ah98-1.7	29.7	31.7	14.0	2.3	8.4
Ah98-1.7	30.5	31.7	14.0	2.3	9.2
Ah98-1.7	31.1	31.7	14.0	2.3	10.0
Ah98-1.7	31.0	31.7	14.0	2.3	10.7
Ah98-1.7	31.2	31.7	14.0	2.3	11.5
Ah98-1.7	31.3	31.7	14.0	2.3	12.3
Ah98-1.7	31.7	31.7	14.0	2.3	13.0
Ah98-1.7	31.5	31.7	14.0	2.3	13.4
Ah98-1.7	24.2	31.7	14.0	2.3	3.7
Ah98-1.7	22.7	31.7	14.0	2.3	2.9
Ah98-1.7	21.2	31.7	14.0	2.3	2.1
Ah98-1.8	25.9	32.6	14.0	2.3	4.5
Ah98-1.8	27.2	32.6	14.0	2.3	5.3
Ah98-1.8	28.9	32.6	14.0	2.3	6.9
Ah98-1.8	30.8	32.6	14.0	2.3	8.4
Ah98-1.8	31.1	32.6	14.0	2.3	10.0
Ah98-1.8	31.6	32.6	14.0	2.3	10.7
Ah98-1.8	31.7	32.6	14.0	2.3	11.5
Ah98-1.8	32.3	32.6	14.0	2.3	12.3
Ah98-1.8	32.6	32.6	14.0	2.3	13.0
Ah98-1.8	32.5	32.6	14.0	2.3	13.4
Ah98-1.8	24.7	32.6	14.0	2.3	3.7
Ah98-1.8	24.1	32.6	14.0	2.3	2.9
Ah98-1.8	18.3	32.6	14.0	2.3	1.0

AA99-1	14.8	42.4	21.1	5.1	0.9
AA99-1	20.1	42.4	21.1	5.1	1.8
AA99-1	22.4	42.4	21.1	5.1	2.5
AA99-1	22.6	42.4	21.1	5.1	3.2
AA99-1	25.3	42.4	21.1	5.1	4.2
AA99-1	26.2	42.4	21.1	5.1	5.0
AA99-1	27.4	42.4	21.1	5.1	5.3
AA99-1	30.3	42.4	21.1	5.1	7.3
AA99-1	32.3	42.4	21.1	5.1	9.1
AA99-1	34.3	42.4	21.1	5.1	11.0
AA99-1	36.4	42.4	21.1	5.1	13.1
AA99-1	38.8	42.4	21.1	5.1	14.8
AA99-1	41.4	42.4	21.1	5.1	18.1
AA99-1	39.9	42.4	21.1	5.1	16.6
AA99-1	42.4	42.4	21.1	5.1	21.1
AA99-1	42.3	42.4	21.1	5.1	19.7
SC01-1.1	25.5	51.0	16.2	2.7	0.9
SC01-1.1	28.3	51.0	16.2	2.7	1.2
SC01-1.1	32.4	51.0	16.2	2.7	1.6
SC01-1.1	33.3	51.0	16.2	2.7	2.0
SC01-1.1	35.0	51.0	16.2	2.7	2.2
SC01-1.1	35.7	51.0	16.2	2.7	2.6
SC01-1.1	36.8	51.0	16.2	2.7	3.0
SC01-1.1	37.5	51.0	16.2	2.7	3.3
SC01-1.1	38.2	51.0	16.2	2.7	3.7
SC01-1.1	39.5	51.0	16.2	2.7	4.1
SC01-1.1	40.6	51.0	16.2	2.7	4.7
SC01-1.1	41.3	51.0	16.2	2.7	5.3
SC01-1.1	42.0	51.0	16.2	2.7	5.3
SC01-1.1	43.2	51.0	16.2	2.7	6.1
SC01-1.1	43.0	51.0	16.2	2.7	5.7
SC01-1.1	44.1	51.0	16.2	2.7	7.1
SC01-1.1	43.5	51.0	16.2	2.7	6.8
SC01-1.1	44.4	51.0	16.2	2.7	7.6
SC01-1.1	44.6	51.0	16.2	2.7	7.9
SC01-1.1	45.0	51.0	16.2	2.7	8.4
SC01-1.1	45.3	51.0	16.2	2.7	8.7
SC01-1.1	45.9	51.0	16.2	2.7	9.0
SC01-1.1	46.1	51.0	16.2	2.7	9.6
SC01-1.1	46.5	51.0	16.2	2.7	10.2
SC01-1.1	46.6	51.0	16.2	2.7	10.7
SC01-1.1	46.7	51.0	16.2	2.7	11.1
SC01-1.1	47.8	51.0	16.2	2.7	11.5

SC01-1.1	48.3	51.0	16.2	2.7	12.0
SC01-1.1	48.4	51.0	16.2	2.7	12.2
SC01-1.1	48.9	51.0	16.2	2.7	12.5
SC01-1.1	49.4	51.0	16.2	2.7	13.0
SC01-1.1	49.5	51.0	16.2	2.7	13.4
SC01-1.1	50.2	51.0	16.2	2.7	13.8
SC01-1.1	50.3	51.0	16.2	2.7	14.2
SC01-1.1	50.4	51.0	16.2	2.7	14.5
SC01-1.1	50.4	51.0	16.2	2.7	15.0
SC01-1.1	51.0	51.0	16.2	2.7	16.1
SC01-1.1	50.5	50.9	16.2	2.7	15.5
SC01-1.1	50.8	50.9	16.2	2.7	16.0
SC01-1.2	25.2	50.9	14.6	2.5	0.7
SC01-1.2	27.6	50.9	14.6	2.5	1.0
SC01-1.2	29.4	50.9	14.6	2.5	1.1
SC01-1.2	33.0	50.9	14.6	2.5	1.6
SC01-1.2	34.2	50.9	14.6	2.5	1.9
SC01-1.2	34.9	50.9	14.6	2.5	2.0
SC01-1.2	36.2	50.9	14.6	2.5	2.4
SC01-1.2	37.2	50.9	14.6	2.5	2.8
SC01-1.2	37.6	50.9	14.6	2.5	3.3
SC01-1.2	38.2	50.9	14.6	2.5	3.7
SC01-1.2	39.4	50.9	14.6	2.5	4.0
SC01-1.2	40.5	50.9	14.6	2.5	4.4
SC01-1.2	41.3	50.9	14.6	2.5	4.8
SC01-1.2	41.7	50.9	14.6	2.5	5.2
SC01-1.2	42.6	50.9	14.6	2.5	5.3
SC01-1.2	42.6	50.9	14.6	2.5	5.7
SC01-1.2	43.0	50.9	14.6	2.5	6.1
SC01-1.2	44.2	50.9	14.6	2.5	7.0
SC01-1.2	45.0	50.9	14.6	2.5	7.6
SC01-1.2	45.6	50.9	14.6	2.5	8.1
SC01-1.2	45.9	50.9	14.6	2.5	8.5
SC01-1.2	46.2	50.9	14.6	2.5	9.0
SC01-1.2	46.7	50.9	14.6	2.5	9.4
SC01-1.2	47.0	50.9	14.6	2.5	9.8
SC01-1.2	47.4	50.9	14.6	2.5	10.2
SC01-1.2	47.7	50.9	14.6	2.5	10.6
SC01-1.2	48.0	50.9	14.6	2.5	11.0
SC01-1.2	48.6	50.9	14.6	2.5	11.3
SC01-1.2	49.2	50.9	14.6	2.5	11.4
SC01-1.2	49.4	50.9	14.6	2.5	12.1
SC01-1.2	49.6	50.9	14.6	2.5	12.6

SC01-1.2	50.1	50.9	14.6	2.5	13.0
SC01-1.2	50.3	50.9	14.6	2.5	13.5
SC01-1.2	50.4	50.9	14.6	2.5	13.8
SC01-1.2	50.6	50.9	14.6	2.5	14.1
SC01-1.2	50.9	50.9	14.6	2.5	14.6
SC01-1.2	50.7	50.7	14.6	2.5	14.4
SC01-1.3	26.4	50.2	13.1	2.2	1.0
SC01-1.3	28.5	50.2	13.1	2.2	1.2
SC01-1.3	30.4	50.2	13.1	2.2	1.3
SC01-1.3	32.2	50.2	13.1	2.2	1.5
SC01-1.3	33.4	50.2	13.1	2.2	1.8
SC01-1.3	34.7	50.2	13.1	2.2	2.1
SC01-1.3	35.8	50.2	13.1	2.2	2.2
SC01-1.3	37.4	50.2	13.1	2.2	3.2
SC01-1.3	37.4	50.2	13.1	2.2	2.9
SC01-1.3	36.9	50.2	13.1	2.2	2.8
SC01-1.3	36.7	50.2	13.1	2.2	2.5
SC01-1.3	38.7	50.2	13.1	2.2	3.4
SC01-1.3	40.1	50.2	13.1	2.2	3.6
SC01-1.3	40.7	50.2	13.1	2.2	4.1
SC01-1.3	41.9	50.2	13.1	2.2	4.5
SC01-1.3	42.3	50.2	13.1	2.2	4.8
SC01-1.3	43.2	50.2	13.1	2.2	5.2
SC01-1.3	43.3	50.2	13.1	2.2	5.5
SC01-1.3	43.8	50.2	13.1	2.2	5.9
SC01-1.3	44.2	50.2	13.1	2.2	6.3
SC01-1.3	44.7	50.2	13.1	2.2	6.7
SC01-1.3	45.3	50.2	13.1	2.2	7.3
SC01-1.3	45.9	50.2	13.1	2.2	7.6
SC01-1.3	46.9	50.2	13.1	2.2	8.9
SC01-1.3	47.0	50.2	13.1	2.2	9.3
SC01-1.3	47.6	50.2	13.1	2.2	9.6
SC01-1.3	48.4	50.2	13.1	2.2	10.0
SC01-1.3	48.8	50.2	13.1	2.2	10.4
SC01-1.3	49.1	50.2	13.1	2.2	10.8
SC01-1.3	49.3	50.2	13.1	2.2	11.4
SC01-1.3	49.5	50.2	13.1	2.2	11.8
SC01-1.3	49.7	50.2	13.1	2.2	12.3
SC01-1.3	50.0	50.2	13.1	2.2	12.5
SC01-1.3	50.2	50.2	13.1	2.2	13.0
MR07-1.1	75.8	222.7	65.6	21.5	4.8
MR07-1.1	116.6	222.7	65.6	21.5	15.1
MR07-1.1	130.9	222.7	65.6	21.5	25.3

MR07-1.1	169.7	222.7	65.6	21.5	35.3
MR07-1.1	178.8	222.7	65.6	21.5	45.5
MR07-1.1	222.7	222.7	65.6	21.5	65.6
MR07-1.2	40.6	187.2	75.5	32.0	5.0
MR07-1.2	62.1	187.2	75.5	32.0	15.1
MR07-1.2	89.8	187.2	75.5	32.0	25.3
MR07-1.2	111.3	187.2	75.5	32.0	35.4
MR07-1.2	124.6	187.2	75.5	32.0	45.3
MR07-1.2	141.1	187.2	75.5	32.0	55.4
MR07-1.2	153.3	187.2	75.5	32.0	65.3
MR07-1.2	187.2	187.2	75.5	32.0	75.5
MR07-1.3	39.5	166.7	105.3	30.8	5.3
MR07-1.3	62.1	166.7	105.3	30.8	15.4
MR07-1.3	88.8	166.7	105.3	30.8	25.0
MR07-1.3	111.3	166.7	105.3	30.8	35.6
MR07-1.3	125.7	166.7	105.3	30.8	45.2
MR07-1.3	139.0	166.7	105.3	30.8	55.1
MR07-1.3	144.1	166.7	105.3	30.8	65.2
MR07-1.3	157.5	166.7	105.3	30.8	75.3
MR07-1.3	154.4	166.7	105.3	30.8	85.1
MR07-1.3	153.3	166.7	105.3	30.8	95.2
MR07-1.3	166.7	166.7	105.3	30.8	105.3
MR07-1.4	12.1	170.6	113.9	51.9	14.7
MR07-1.4	41.6	170.6	113.9	51.9	24.9
MR07-1.4	69.1	170.6	113.9	51.9	34.6
MR07-1.4	91.5	170.6	113.9	51.9	44.6
MR07-1.4	111.8	170.6	113.9	51.9	54.1
MR07-1.4	131.1	170.6	113.9	51.9	64.6
MR07-1.4	153.5	170.6	113.9	51.9	74.0
MR07-1.4	168.7	170.6	113.9	51.9	84.0
MR07-1.4	163.5	170.6	113.9	51.9	94.0
MR07-1.4	161.4	170.6	113.9	51.9	103.4
MR07-1.4	170.6	170.6	113.9	51.9	113.9
AR09-1.1	76.5	108.2	27.5	3.1	2.3
AR09-1.1	80.0	108.2	27.5	3.1	3.5
AR09-1.1	83.8	108.2	27.5	3.1	4.6
AR09-1.1	86.0	108.2	27.5	3.1	5.5
AR09-1.1	89.6	108.2	27.5	3.1	6.4
AR09-1.1	92.9	108.2	27.5	3.1	7.4
AR09-1.1	94.7	108.2	27.5	3.1	8.7
AR09-1.1	108.2	108.2	27.5	3.1	27.5
AR09-1.1	108.0	108.2	27.5	3.1	25.6
AR09-1.1	107.1	108.2	27.5	3.1	23.3

AR09-1.1	106.2	108.2	27.5	3.1	21.4
AR09-1.1	105.2	108.2	27.5	3.1	19.4
AR09-1.1	104.1	108.2	27.5	3.1	17.4
AR09-1.1	102.7	108.2	27.5	3.1	16.4
AR09-1.1	99.6	108.2	27.5	3.1	14.5
AR09-1.1	97.8	108.2	27.5	3.1	11.7
AR09-1.1	96.7	108.2	27.5	3.1	10.4
AR09-1.1	96.0	108.2	27.5	3.1	9.5
AR09-1.2	67.4	113.2	31.1	5.2	2.1
AR09-1.2	71.3	113.2	31.1	5.2	3.2
AR09-1.2	73.8	113.2	31.1	5.2	4.2
AR09-1.2	78.3	113.2	31.1	5.2	6.3
AR09-1.2	84.3	113.2	31.1	5.2	8.1
AR09-1.2	89.2	113.2	31.1	5.2	10.2
AR09-1.2	93.1	113.2	31.1	5.2	11.3
AR09-1.2	104.3	113.2	31.1	5.2	17.2
AR09-1.2	106.0	113.2	31.1	5.2	19.2
AR09-1.2	107.8	113.2	31.1	5.2	21.1
AR09-1.2	109.6	113.2	31.1	5.2	23.2
AR09-1.2	109.8	113.2	31.1	5.2	25.2
AR09-1.2	110.7	113.2	31.1	5.2	27.2
AR09-1.2	112.3	113.2	31.1	5.2	29.1
AR09-1.2	113.2	113.2	31.1	5.2	31.1
AR09-1.3	50.2	90.2	17.3	3.8	2.2
AR09-1.3	54.2	90.2	17.3	3.8	3.4
AR09-1.3	57.8	90.2	17.3	3.8	4.4
AR09-1.3	66.0	90.2	17.3	3.8	5.4
AR09-1.3	70.0	90.2	17.3	3.8	6.5
AR09-1.3	83.1	90.2	17.3	3.8	10.4
AR09-1.3	85.4	90.2	17.3	3.8	11.5
AR09-1.3	87.1	90.2	17.3	3.8	13.3
AR09-1.3	89.3	90.2	17.3	3.8	15.3
AR09-1.3	90.2	90.2	17.3	3.8	17.3
AR09-1.3	79.1	90.2	17.3	3.8	9.1
AR09-1.3	75.4	90.2	17.3	3.8	7.3
AR09-1.4	46.5	86.2	69.7	14.3	3.1
AR09-1.4	49.2	86.2	69.7	14.3	5.8
AR09-1.4	52.2	86.2	69.7	14.3	9.2
AR09-1.4	59.2	86.2	69.7	14.3	16.3
AR09-1.4	60.5	86.2	69.7	14.3	19.0
AR09-1.4	62.2	86.2	69.7	14.3	21.5
AR09-1.4	63.3	86.2	69.7	14.3	25.8
AR09-1.4	64.3	86.2	69.7	14.3	30.8

AR09-1.4	75.0	86.2	69.7	14.3	41.5
AR09-1.4	78.3	86.2	69.7	14.3	46.1
AR09-1.4	80.8	86.2	69.7	14.3	53.6
AR09-1.4	83.3	86.2	69.7	14.3	60.6
AR09-1.4	86.1	86.2	69.7	14.3	66.0
AR09-1.4	86.2	86.2	69.7	14.3	69.7
AR09-1.5	63.4	97.1	34.3	4.5	2.2
AR09-1.5	72.1	97.1	34.3	4.5	5.3
AR09-1.5	74.9	97.1	34.3	4.5	6.4
AR09-1.5	77.6	97.1	34.3	4.5	7.3
AR09-1.5	79.3	97.1	34.3	4.5	8.4
AR09-1.5	80.5	97.1	34.3	4.5	9.2
AR09-1.5	81.1	97.1	34.3	4.5	10.3
AR09-1.5	83.7	97.1	34.3	4.5	11.5
AR09-1.5	84.3	97.1	34.3	4.5	12.3
AR09-1.5	85.2	97.1	34.3	4.5	13.4
AR09-1.5	86.3	97.1	34.3	4.5	14.2
AR09-1.5	88.4	97.1	34.3	4.5	16.4
AR09-1.5	89.5	97.1	34.3	4.5	18.4
AR09-1.5	90.3	97.1	34.3	4.5	20.3
AR09-1.5	91.2	97.1	34.3	4.5	22.3
AR09-1.5	92.4	97.1	34.3	4.5	24.3
AR09-1.5	93.5	97.1	34.3	4.5	26.3
AR09-1.5	94.6	97.1	34.3	4.5	28.3
AR09-1.5	95.6	97.1	34.3	4.5	30.4
AR09-1.5	96.4	97.1	34.3	4.5	32.4
AR09-1.5	97.1	97.1	34.3	4.5	34.3
AR09-1.6	65.3	161.3	44.4	11.7	3.4
AR09-1.6	70.4	161.3	44.4	11.7	4.6
AR09-1.6	77.8	161.3	44.4	11.7	5.4
AR09-1.6	79.8	161.3	44.4	11.7	6.4
AR09-1.6	82.9	161.3	44.4	11.7	7.5
AR09-1.6	89.8	161.3	44.4	11.7	8.5
AR09-1.6	93.1	161.3	44.4	11.7	9.3
AR09-1.6	97.6	161.3	44.4	11.7	10.4
AR09-1.6	108.0	161.3	44.4	11.7	11.5
AR09-1.6	116.7	161.3	44.4	11.7	14.3
AR09-1.6	122.1	161.3	44.4	11.7	16.4
AR09-1.6	124.8	161.3	44.4	11.7	18.5
AR09-1.6	127.5	161.3	44.4	11.7	20.4
AR09-1.6	127.5	161.3	44.4	11.7	22.4
AR09-1.6	130.9	161.3	44.4	11.7	24.4
AR09-1.6	136.4	161.3	44.4	11.7	26.2

AR09-1.6	139.7	161.3	44.4	11.7	28.3
AR09-1.6	142.2	161.3	44.4	11.7	30.3
AR09-1.6	145.5	161.3	44.4	11.7	32.4
AR09-1.6	145.6	161.3	44.4	11.7	34.4
AR09-1.6	148.3	161.3	44.4	11.7	36.3
AR09-1.6	152.5	161.3	44.4	11.7	38.3
AR09-1.6	153.8	161.3	44.4	11.7	40.2
AR09-1.6	161.2	161.3	44.4	11.7	42.4
AR09-1.6	161.3	161.3	44.4	11.7	44.4
AR09-1.7	45.9	62.2	13.2	2.1	2.1
AR09-1.7	47.8	62.2	13.2	2.1	3.2
AR09-1.7	51.7	62.2	13.2	2.1	4.2
AR09-1.7	52.5	62.2	13.2	2.1	5.0
AR09-1.7	54.4	62.2	13.2	2.1	6.2
AR09-1.7	55.7	62.2	13.2	2.1	7.2
AR09-1.7	57.3	62.2	13.2	2.1	9.1
AR09-1.7	60.2	62.2	13.2	2.1	11.2
AR09-1.7	62.2	62.2	13.2	2.1	13.2
AR09-1.7	61.8	62.2	13.2	2.1	15.1
AR09-1.7	61.6	62.2	13.2	2.1	17.1
AR09-1.8	61.2	88.3	25.3	3.5	2.2
AR09-1.8	63.3	88.3	25.3	3.5	3.2
AR09-1.8	66.6	88.3	25.3	3.5	4.4
AR09-1.8	69.6	88.3	25.3	3.5	5.3
AR09-1.8	71.6	88.3	25.3	3.5	6.3
AR09-1.8	74.0	88.3	25.3	3.5	7.4
AR09-1.8	76.1	88.3	25.3	3.5	9.2
AR09-1.8	78.0	88.3	25.3	3.5	11.4
AR09-1.8	80.8	88.3	25.3	3.5	13.3
AR09-1.8	82.9	88.3	25.3	3.5	15.2
AR09-1.8	83.4	88.3	25.3	3.5	17.3
AR09-1.8	83.9	88.3	25.3	3.5	19.2
AR09-1.8	85.4	88.3	25.3	3.5	21.2
AR09-1.8	86.3	88.3	25.3	3.5	23.4
AR09-1.8	88.3	88.3	25.3	3.5	25.3
AR09-1.9	74.3	120.7	37.3	4.6	2.3
AR09-1.9	76.0	120.7	37.3	4.6	3.4
AR09-1.9	83.8	120.7	37.3	4.6	4.4
AR09-1.9	90.0	120.7	37.3	4.6	5.2
AR09-1.9	92.9	120.7	37.3	4.6	6.3
AR09-1.9	97.5	120.7	37.3	4.6	7.3
AR09-1.9	99.2	120.7	37.3	4.6	8.2
AR09-1.9	100.9	120.7	37.3	4.6	9.2

AR09-1.9	102.5	120.7	37.3	4.6	10.2
AR09-1.9	104.0	120.7	37.3	4.6	11.2
AR09-1.9	105.2	120.7	37.3	4.6	12.3
AR09-1.9	106.1	120.7	37.3	4.6	13.3
AR09-1.9	107.4	120.7	37.3	4.6	14.2
AR09-1.9	109.4	120.7	37.3	4.6	15.3
AR09-1.9	110.5	120.7	37.3	4.6	17.2
AR09-1.9	111.3	120.7	37.3	4.6	19.3
AR09-1.9	112.1	120.7	37.3	4.6	21.3
AR09-1.9	114.1	120.7	37.3	4.6	23.4
AR09-1.9	115.3	120.7	37.3	4.6	25.2
AR09-1.9	117.4	120.7	37.3	4.6	27.3
AR09-1.9	118.2	120.7	37.3	4.6	29.2
AR09-1.9	119.2	120.7	37.3	4.6	31.2
AR09-1.9	120.2	120.7	37.3	4.6	33.1
AR09-1.9	120.4	120.7	37.3	4.6	35.3
AR09-1.9	120.7	120.7	37.3	4.6	37.3
AR09-1.10	78.5	128.4	36.3	4.9	2.2
AR09-1.10	83.6	128.4	36.3	4.9	3.2
AR09-1.10	86.5	128.4	36.3	4.9	4.4
AR09-1.10	90.4	128.4	36.3	4.9	5.4
AR09-1.10	93.5	128.4	36.3	4.9	6.4
AR09-1.10	96.6	128.4	36.3	4.9	7.3
AR09-1.10	99.5	128.4	36.3	4.9	8.3
AR09-1.10	103.5	128.4	36.3	4.9	9.3
AR09-1.10	106.2	128.4	36.3	4.9	10.3
AR09-1.10	110.1	128.4	36.3	4.9	11.5
AR09-1.10	112.1	128.4	36.3	4.9	12.4
AR09-1.10	114.1	128.4	36.3	4.9	13.4
AR09-1.10	115.3	128.4	36.3	4.9	14.3
AR09-1.10	116.3	128.4	36.3	4.9	15.5
AR09-1.10	117.8	128.4	36.3	4.9	16.4
AR09-1.10	118.1	128.4	36.3	4.9	18.4
AR09-1.10	119.3	128.4	36.3	4.9	20.4
AR09-1.10	120.8	128.4	36.3	4.9	22.4
AR09-1.10	122.3	128.4	36.3	4.9	24.4
AR09-1.10	123.8	128.4	36.3	4.9	26.3
AR09-1.10	124.9	128.4	36.3	4.9	28.3
AR09-1.10	126.0	128.4	36.3	4.9	30.5
AR09-1.10	127.3	128.4	36.3	4.9	32.4
AR09-1.10	128.0	128.4	36.3	4.9	34.4
AR09-1.10	128.4	128.4	36.3	4.9	36.3
AR09-1.11	66.4	98.1	29.5	4.0	2.1

AR09-1.11	68.7	98.1	29.5	4.0	3.3
AR09-1.11	72.7	98.1	29.5	4.0	4.3
AR09-1.11	77.1	98.1	29.5	4.0	6.5
AR09-1.11	79.5	98.1	29.5	4.0	7.5
AR09-1.11	81.4	98.1	29.5	4.0	8.4
AR09-1.11	82.9	98.1	29.5	4.0	9.3
AR09-1.11	84.2	98.1	29.5	4.0	10.5
AR09-1.11	85.4	98.1	29.5	4.0	11.4
AR09-1.11	86.2	98.1	29.5	4.0	12.4
AR09-1.11	86.9	98.1	29.5	4.0	13.5
AR09-1.11	88.8	98.1	29.5	4.0	15.5
AR09-1.11	90.2	98.1	29.5	4.0	17.4
AR09-1.11	90.8	98.1	29.5	4.0	19.4
AR09-1.11	92.0	98.1	29.5	4.0	21.4
AR09-1.11	94.5	98.1	29.5	4.0	23.5
AR09-1.11	95.3	98.1	29.5	4.0	25.3
AR09-1.11	97.4	98.1	29.5	4.0	27.5
AR09-1.11	98.1	98.1	29.5	4.0	29.5
AR09-1.12	74.5	137.1	39.3	5.7	2.0
AR09-1.12	81.8	137.1	39.3	5.7	3.1
AR09-1.12	85.7	137.1	39.3	5.7	4.4
AR09-1.12	92.2	137.1	39.3	5.7	5.2
AR09-1.12	99.1	137.1	39.3	5.7	6.2
AR09-1.12	103.5	137.1	39.3	5.7	7.2
AR09-1.12	106.2	137.1	39.3	5.7	8.2
AR09-1.12	111.7	137.1	39.3	5.7	9.1
AR09-1.12	113.4	137.1	39.3	5.7	10.2
AR09-1.12	115.2	137.1	39.3	5.7	11.3
AR09-1.12	117.7	137.1	39.3	5.7	13.3
AR09-1.12	119.7	137.1	39.3	5.7	15.2
AR09-1.12	120.0	137.1	39.3	5.7	17.2
AR09-1.12	123.6	137.1	39.3	5.7	19.1
AR09-1.12	124.5	137.1	39.3	5.7	21.1
AR09-1.12	126.5	137.1	39.3	5.7	23.3
AR09-1.12	128.4	137.1	39.3	5.7	25.3
AR09-1.12	130.5	137.1	39.3	5.7	27.2
AR09-1.12	132.4	137.1	39.3	5.7	29.3
AR09-1.12	133.6	137.1	39.3	5.7	31.3
AR09-1.12	134.2	137.1	39.3	5.7	33.2
AR09-1.12	135.4	137.1	39.3	5.7	35.3
AR09-1.12	136.7	137.1	39.3	5.7	37.3
AR09-1.12	137.1	137.1	39.3	5.7	39.3
AR09-1.13	65.0	104.1	35.5	4.6	2.2

AR09-1.13	75.5	104.1	35.5	4.6	5.3
AR09-1.13	79.3	104.1	35.5	4.6	6.3
AR09-1.13	83.2	104.1	35.5	4.6	7.3
AR09-1.13	85.1	104.1	35.5	4.6	8.3
AR09-1.13	87.5	104.1	35.5	4.6	9.1
AR09-1.13	89.5	104.1	35.5	4.6	10.4
AR09-1.13	90.2	104.1	35.5	4.6	11.3
AR09-1.13	92.3	104.1	35.5	4.6	13.4
AR09-1.13	93.9	104.1	35.5	4.6	15.4
AR09-1.13	94.8	104.1	35.5	4.6	17.3
AR09-1.13	95.5	104.1	35.5	4.6	19.3
AR09-1.13	96.7	104.1	35.5	4.6	21.3
AR09-1.13	97.5	104.1	35.5	4.6	23.5
AR09-1.13	98.6	104.1	35.5	4.6	25.5
AR09-1.13	99.4	104.1	35.5	4.6	27.4
AR09-1.13	100.5	104.1	35.5	4.6	29.4
AR09-1.13	102.6	104.1	35.5	4.6	31.4
AR09-1.13	103.2	104.1	35.5	4.6	33.3
AR09-1.13	104.1	104.1	35.5	4.6	35.5
AR09-1.13	104.1	104.1	35.5	4.6	37.5
AR09-1.13	103.8	104.1	35.5	4.6	39.4
AR09-1.14	62.9	87.4	25.4	2.7	2.2
AR09-1.14	72.3	87.4	25.4	2.7	5.3
AR09-1.14	70.0	87.4	25.4	2.7	4.2
AR09-1.14	67.6	87.4	25.4	2.7	3.4
AR09-1.14	75.5	87.4	25.4	2.7	6.5
AR09-1.14	77.0	87.4	25.4	2.7	7.4
AR09-1.14	78.4	87.4	25.4	2.7	8.4
AR09-1.14	79.6	87.4	25.4	2.7	9.3
AR09-1.14	80.4	87.4	25.4	2.7	11.3
AR09-1.14	81.0	87.4	25.4	2.7	13.3
AR09-1.14	81.9	87.4	25.4	2.7	15.4
AR09-1.14	84.0	87.4	25.4	2.7	17.3
AR09-1.14	84.7	87.4	25.4	2.7	19.3
AR09-1.14	86.1	87.4	25.4	2.7	21.3
AR09-1.14	86.6	87.4	25.4	2.7	23.4
AR09-1.14	87.4	87.4	25.4	2.7	25.4
AR09-1.15	71.8	108.0	32.5	3.9	2.2
AR09-1.15	76.2	108.0	32.5	3.9	3.5
AR09-1.15	80.3	108.0	32.5	3.9	4.5
AR09-1.15	82.9	108.0	32.5	3.9	5.4
AR09-1.15	86.1	108.0	32.5	3.9	6.5
AR09-1.15	90.9	108.0	32.5	3.9	7.4

AR09-1.15	92.2	108.0	32.5	3.9	8.5
AR09-1.15	93.4	108.0	32.5	3.9	9.5
AR09-1.15	94.4	108.0	32.5	3.9	10.5
AR09-1.15	95.1	108.0	32.5	3.9	11.5
AR09-1.15	97.3	108.0	32.5	3.9	12.4
AR09-1.15	97.7	108.0	32.5	3.9	14.4
AR09-1.15	98.5	108.0	32.5	3.9	16.5
AR09-1.15	100.0	108.0	32.5	3.9	18.5
AR09-1.15	101.7	108.0	32.5	3.9	20.5
AR09-1.15	102.9	108.0	32.5	3.9	22.5
AR09-1.15	104.8	108.0	32.5	3.9	24.4
AR09-1.15	105.9	108.0	32.5	3.9	26.4
AR09-1.15	107.6	108.0	32.5	3.9	28.5
AR09-1.15	107.8	108.0	32.5	3.9	30.5
AR09-1.15	108.0	108.0	32.5	3.9	32.5
AR09-1.16	68.6	102.4	29.3	3.3	2.3
AR09-1.16	73.8	102.4	29.3	3.3	3.3
AR09-1.16	80.6	102.4	29.3	3.3	4.4
AR09-1.16	84.2	102.4	29.3	3.3	5.3
AR09-1.16	86.1	102.4	29.3	3.3	6.4
AR09-1.16	88.3	102.4	29.3	3.3	7.3
AR09-1.16	89.7	102.4	29.3	3.3	8.4
AR09-1.16	90.5	102.4	29.3	3.3	9.3
AR09-1.16	91.6	102.4	29.3	3.3	10.3
AR09-1.16	92.2	102.4	29.3	3.3	11.5
AR09-1.16	92.7	102.4	29.3	3.3	12.3
AR09-1.16	93.7	102.4	29.3	3.3	13.5
AR09-1.16	94.9	102.4	29.3	3.3	14.3
AR09-1.16	94.8	102.4	29.3	3.3	15.3
AR09-1.16	96.0	102.4	29.3	3.3	17.3
AR09-1.16	96.7	102.4	29.3	3.3	19.3
AR09-1.16	98.9	102.4	29.3	3.3	21.3
AR09-1.16	100.2	102.4	29.3	3.3	23.5
AR09-1.16	100.8	102.4	29.3	3.3	25.4
AR09-1.16	102.1	102.4	29.3	3.3	27.3
AR09-1.16	102.4	102.4	29.3	3.3	29.3
AR09-1.17	57.8	80.0	22.5	2.7	2.3
AR09-1.17	60.0	80.0	22.5	2.7	3.3
AR09-1.17	63.9	80.0	22.5	2.7	4.3
AR09-1.17	67.7	80.0	22.5	2.7	5.4
AR09-1.17	69.0	80.0	22.5	2.7	6.7
AR09-1.17	69.9	80.0	22.5	2.7	7.7
AR09-1.17	70.8	80.0	22.5	2.7	8.8

AR09-1.17	71.2	80.0	22.5	2.7	9.8
AR09-1.17	72.1	80.0	22.5	2.7	11.4
AR09-1.17	74.1	80.0	22.5	2.7	12.5
AR09-1.17	80.0	80.0	22.5	2.7	22.5
AR09-1.17	78.8	80.0	22.5	2.7	18.5
AR09-1.17	77.5	80.0	22.5	2.7	16.5
AR09-1.17	75.9	80.0	22.5	2.7	14.3
AR09-1.18	59.3	89.2	22.4	2.9	2.1
AR09-1.18	64.4	89.2	22.4	2.9	3.3
AR09-1.18	72.7	89.2	22.4	2.9	5.3
AR09-1.18	75.5	89.2	22.4	2.9	6.3
AR09-1.18	77.1	89.2	22.4	2.9	7.3
AR09-1.18	78.2	89.2	22.4	2.9	8.3
AR09-1.18	78.9	89.2	22.4	2.9	9.3
AR09-1.18	82.6	89.2	22.4	2.9	11.5
AR09-1.18	83.2	89.2	22.4	2.9	12.2
AR09-1.18	84.6	89.2	22.4	2.9	14.2
AR09-1.18	86.4	89.2	22.4	2.9	16.4
AR09-1.18	87.2	89.2	22.4	2.9	18.5
AR09-1.18	88.6	89.2	22.4	2.9	20.4
AR09-1.18	89.2	89.2	22.4	2.9	22.4
AR09-1.19	60.0	86.5	25.5	3.1	2.3
AR09-1.19	64.4	86.5	25.5	3.1	3.4
AR09-1.19	69.0	86.5	25.5	3.1	4.4
AR09-1.19	77.2	86.5	25.5	3.1	9.2
AR09-1.19	78.1	86.5	25.5	3.1	11.3
AR09-1.19	79.2	86.5	25.5	3.1	13.3
AR09-1.19	81.0	86.5	25.5	3.1	15.3
AR09-1.19	82.1	86.5	25.5	3.1	17.3
AR09-1.19	83.6	86.5	25.5	3.1	19.2
AR09-1.19	84.7	86.5	25.5	3.1	21.2
AR09-1.19	85.2	86.5	25.5	3.1	23.5
AR09-1.19	86.5	86.5	25.5	3.1	25.5
Af10-1	18.7	64.2	24.3	6.2	0.1
Af10-1	27.1	64.2	24.3	6.2	0.9
Af10-1	30.0	64.2	24.3	6.2	1.8
Af10-1	33.2	64.2	24.3	6.2	2.7
Af10-1	36.5	64.2	24.3	6.2	3.5
Af10-1	38.2	64.2	24.3	6.2	4.1
Af10-1	39.4	64.2	24.3	6.2	4.6
Af10-1	44.7	64.2	24.3	6.2	7.1
Af10-1	48.6	64.2	24.3	6.2	9.6
Af10-1	51.5	64.2	24.3	6.2	12.0

Af10-1	54.2	64.2	24.3	6.2	14.7
Af10-1	55.4	64.2	24.3	6.2	17.3
Af10-1	56.9	64.2	24.3	6.2	20.1
Af10-2	39.5	66.7	23.4	3.8	0.4
Af10-2	40.4	66.7	23.4	3.8	1.3
Af10-2	43.3	66.7	23.4	3.8	1.8
Af10-2	46.0	66.7	23.4	3.8	2.4
Af10-2	48.3	66.7	23.4	3.8	2.9
Af10-2	48.4	66.7	23.4	3.8	3.5
Af10-2	51.5	66.7	23.4	3.8	5.4
Af10-2	50.1	66.7	23.4	3.8	4.4
Af10-2	53.7	66.7	23.4	3.8	6.6
Af10-2	55.6	66.7	23.4	3.8	8.1
Af10-2	57.5	66.7	23.4	3.8	9.9
Af10-2	61.4	66.7	23.4	3.8	17.3
Af10-2	61.4	66.7	23.4	3.8	19.0
Af10-2	59.3	66.7	23.4	3.8	12.0
Af10-2	59.8	66.7	23.4	3.8	13.4
Af10-2	60.9	66.7	23.4	3.8	15.2
Af10-3	29.0	72.2	21.6	5.8	0.4
Af10-3	33.8	72.2	21.6	5.8	1.4
Af10-3	36.1	72.2	21.6	5.8	2.2
Af10-3	37.3	72.2	21.6	5.8	2.6
Af10-3	39.1	72.2	21.6	5.8	3.1
Af10-3	40.3	72.2	21.6	5.8	3.5
Af10-3	43.3	72.2	21.6	5.8	5.1
Af10-3	42.6	72.2	21.6	5.8	4.2
Af10-3	48.5	72.2	21.6	5.8	7.3
Af10-3	52.8	72.2	21.6	5.8	9.3
Af10-3	58.0	72.2	21.6	5.8	11.2
Af10-3	61.8	72.2	21.6	5.8	13.2
Af10-3	65.3	72.2	21.6	5.8	15.5
Af10-3	67.7	72.2	21.6	5.8	17.7
Af10-4	35.4	75.4	20.7	5.0	0.4
Af10-4	40.4	75.4	20.7	5.0	1.0
Af10-4	41.6	75.4	20.7	5.0	1.5
Af10-4	42.4	75.4	20.7	5.0	2.1
Af10-4	44.9	75.4	20.7	5.0	2.8
Af10-4	46.7	75.4	20.7	5.0	3.4
Af10-4	50.8	75.4	20.7	5.0	5.5
Af10-4	48.8	75.4	20.7	5.0	4.3
Af10-4	54.6	75.4	20.7	5.0	6.9
Af10-4	57.4	75.4	20.7	5.0	8.5

Af10-4	59.6	75.4	20.7	5.0	9.9
Af10-4	66.4	75.4	20.7	5.0	14.8
Af10-4	67.2	75.4	20.7	5.0	16.6
Af10-4	61.3	75.4	20.7	5.0	10.9
Af10-4	63.0	75.4	20.7	5.0	12.1
Af10-4	64.6	75.4	20.7	5.0	13.5
Af10-5	15.2	37.7	20.7	5.9	0.4
Af10-5	16.7	37.7	20.7	5.9	1.2
Af10-5	17.5	37.7	20.7	5.9	1.9
Af10-5	19.5	37.7	20.7	5.9	2.5
Af10-5	21.0	37.7	20.7	5.9	3.3
Af10-5	22.3	37.7	20.7	5.9	4.0
Af10-5	22.6	37.7	20.7	5.9	4.6
Af10-5	23.5	37.7	20.7	5.9	5.2
Af10-5	24.1	37.7	20.7	5.9	6.5
Af10-5	27.0	37.7	20.7	5.9	8.1
Af10-5	28.5	37.7	20.7	5.9	9.9
Af10-5	29.6	37.7	20.7	5.9	11.2
Af10-5	31.0	37.7	20.7	5.9	13.2
Af10-5	32.9	37.7	20.7	5.9	15.2
Af10-5	33.5	37.7	20.7	5.9	16.9
Af10-6	26.3	56.5	20.7	5.8	0.7
Af10-6	27.8	56.5	20.7	5.8	1.3
Af10-6	29.5	56.5	20.7	5.8	2.1
Af10-6	33.5	56.5	20.7	5.8	3.7
Af10-6	34.2	56.5	20.7	5.8	4.4
Af10-6	35.1	56.5	20.7	5.8	4.9
Af10-6	35.8	56.5	20.7	5.8	5.9
Af10-6	36.3	56.5	20.7	5.8	7.1
Af10-6	42.4	56.5	20.7	5.8	9.5
Af10-6	44.3	56.5	20.7	5.8	10.6
Af10-6	45.6	56.5	20.7	5.8	12.3
Af10-6	47.1	56.5	20.7	5.8	13.9
Af10-6	48.7	56.5	20.7	5.8	15.2
Af10-6	48.7	56.5	20.7	5.8	16.0
Af10-7	20.2	65.9	20.7	5.1	0.1
Af10-7	36.1	65.9	20.7	5.1	1.2
Af10-7	37.8	65.9	20.7	5.1	1.9
Af10-7	39.9	65.9	20.7	5.1	2.4
Af10-7	41.2	65.9	20.7	5.1	3.0
Af10-7	41.9	65.9	20.7	5.1	3.4
Af10-7	42.7	65.9	20.7	5.1	4.0
Af10-7	43.2	65.9	20.7	5.1	4.9

Af10-7	44.6	65.9	20.7	5.1	5.5
Af10-7	48.2	65.9	20.7	5.1	7.4
Af10-7	52.8	65.9	20.7	5.1	10.4
Af10-7	55.6	65.9	20.7	5.1	12.3
Af10-7	57.0	65.9	20.7	5.1	14.3
Af10-7	58.8	65.9	20.7	5.1	15.7
Af10-7	45.4	65.9	20.7	5.1	6.3
Af10-7	50.7	65.9	20.7	5.1	8.7

APPENDIX B

Streamwise velocity spectra plotted in pre-multiplied form for selected time series. The dotted line is Kolmogorov -5/3rd indicating that velocity displays the existence of the inertial subrange.

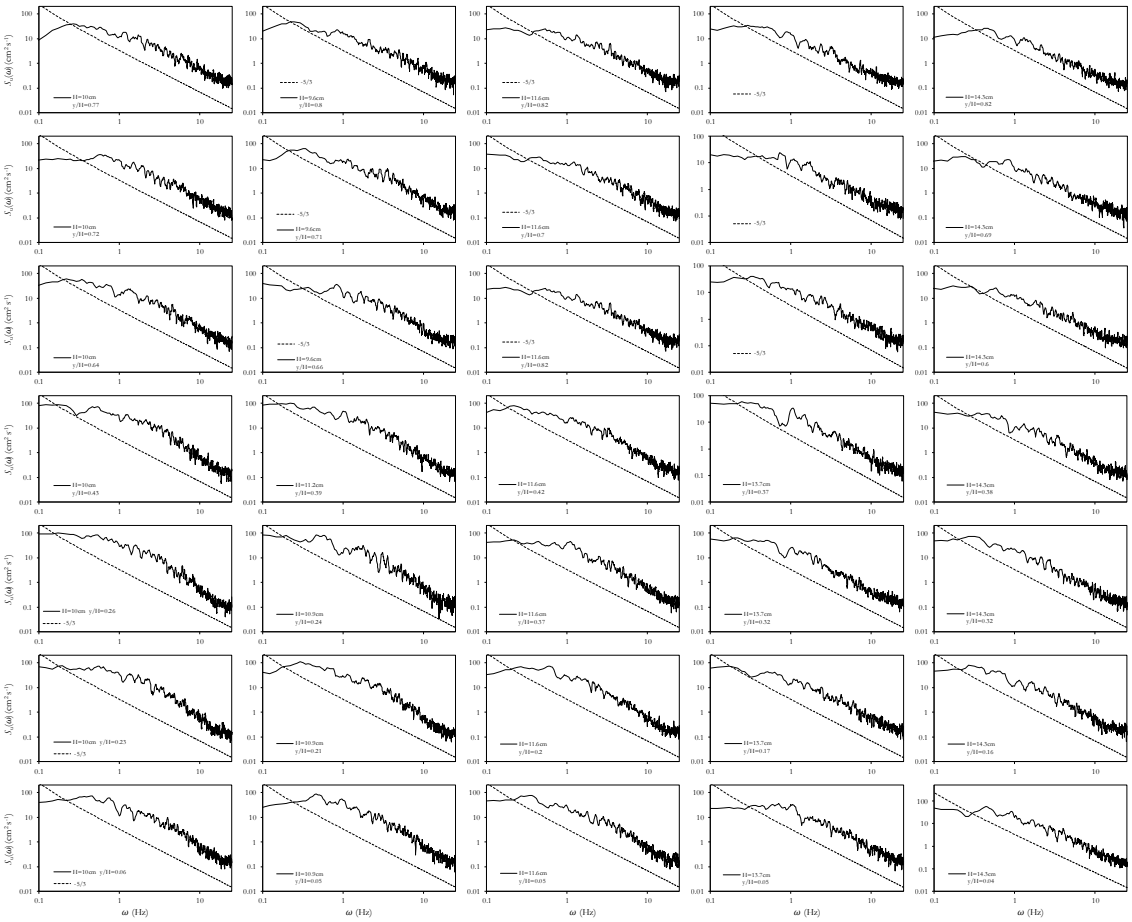

REFERENCES

Adrian, R. J. (2007). Hairpin vortex organization in wall turbulencea). *Physics of Fluids (1994-present)*, *19*(4), 041301.

Adrian, R. J., Meinhart, C. D., and Tomkins, C. D. (2000). "Vortex organization in the outer region of the turbulent boundary layer." Journal of Fluid Mechanics, 422: 1–54.

Adrian, R. J., & Marusic, I. (2012). Coherent structures in flow over hydraulic engineering surfaces. *Journal of Hydraulic Research*, *50*(5), 451-464.

Afzalimehr, H., & Anctil, F. (1999). Velocity distribution and shear velocity behaviour of decelerating flows over a gravel bed. *Canadian Journal of Civil Engineering*, *26*(4), 468-475.

Afzalimehr, H. and Rennie, C.D. (2009). Determination of bed shear stress in gravel-bed rivers using boundarly layer parameters. *Hydrological Sciences*, 54(1): 147-159.

Afzalimehr, H. (2010). Effect of non-uniformity of flow on velocity and turbulence intensities over a cobble-bed. *Hydrological processes*, *24*(3), 331-341.

Afzalimehr, H., Najafabadi, E. F., & Gallichand, J. (2012). Effects of accelerating and decelerating flows in a channel with vegetated banks and gravel bed. *International Journal of Sediment Research*, *27*(2), 188-200.

Ahmed, F., & Rajaratnam, N. (1998). Flow around bridge piers. *Journal of Hydraulic Engineering*, *124*(3), 288-300.

Albayrak, I., & Lemmin, U. (2011). Secondary currents and corresponding surface velocity patterns in a turbulent open-channel flow over a rough bed. *Journal of Hydraulic Engineering*, *137*(11), 1318-1334.

Alben, S., Shelley, M., Zhang, J. 2004. How flexibility induces streamlining in a two dimensional flow. Physics of Fluids, 16(5): 1694-1713.

Alben, S., Shelley, M., Zhang, J. 2002. Drag reduction through self-similar bending of a flexible body. Letters to Nature 420(5): 479-481.

Amir, M. and Castro, I.P. (2011). Turbulence in rough-wall boundary layers: universality issues. *Experiments in Fluids*, 51(2): 313-326.

Babin, M., & Stramski, D. (2004). "Variations in the mass-specific absorption coefficient of mineral particles suspended in water." *Limnology and Oceanography*, 49(3), 756-767.

Baker, E. T., & Lavelle, J. W. (1984). "The effect of particle size on the light attenuation coefficient of natural suspensions." *Journal of Geophysical Research: Oceans*, 89(C5), 8197-8203.

Bathurst, J.C. (1985). "Flow resistance estimation in mountain rivers." *Journal of Hydraulic Engineering*, ASCE, 111(4), 625-643.

Belcher, B. (2009). Vortex model of open channel flows with gravel beds. PhD Thesis, University of Kentucky, Lexington, Kentucky.

Belcher, B., and Fox, J. (2009). Discussion of Rodriguez, J. F., and Garcia, M. H. 2008. Laboratory measurements of 3-D flow patterns and turbulence in straight open channel with rough bed. *Journal of Hydraulic Research*, 46(4), 454-688.

Belcher, B.J. and Fox, J.F. (2011). Outer scaling for open channel flow over a gravel bed. *Journal of Engineering Mechanics*, ASCE, 137(1): 40-46.

Biggs, R. B., Sharp, J. H., Church, T. M., & Tramontano, J. M. (1983). "Optical properties, suspended sediments, and chemistry associated with the turbidity maxima

of the Delaware Estuary." *Canadian Journal of Fisheries and Aquatic Sciences*, 40(S1), 172-179.
Biron, P. M., Robson, C., Lapointe, M. F., & Gaskin, S. J. (2004). Comparing different methods of bed shear stress estimates in simple and complex flow fields. *Earth Surface Processes and Landforms*, *29*(11), 1403-1415.
Blanckaert, K., Duarte, A., & Schleiss, A. J. (2010). Influence of shallowness, bank inclination and bank roughness on the variability of flow patterns and boundary shear stress due to secondary currents in straight open-channels. *Advances in Water Resources*, *33*(9), 1062-1074.
Boppe, R. S., and W. L. Neu, (1995). Quasi-coherent structures in the marine atmospheric surface layer. J.Geophys Res.*,* 100 (C10): 20 635–20 648
Bohren, C. F., & Huffman, D. R. (2008). *Absorption and scattering of light by small particles*. (Wiley, 2008).
Boss, E., Slade, W., & Hill, P. (2009). "Effect of particulate aggregation in aquatic environments on the beam attenuation and its utility as a proxy for particulate mass." *Optics Express*, 17(11), 9408-9420.
Bray, D.I. (1979). "Estimating average velocity in gravel-bed rivers." *J. Hydraul. Div*. ASCE, 105(HY9), Proc. Paper 14810, pp.1103-1122.
Brzek, B., Chao, D., Turan, Ö., & Castillo, L. (2010). Characterizing developing adverse pressure gradient flows subject to surface roughness. *Experiments in fluids*, *48*(4), 663-677.
Bowers, D. G., Braithwaite, K. M., Nimmo-Smith, W. A. M., & Graham, G. W. (2009). "Light scattering by particles suspended in the sea: The role of particle size and density." *Continental Shelf Research*, 29(14), 1748-1755.
Buffin-Bélanger, T., & Roy, A. G. (1998). Effects of a pebble cluster on the turbulent structure of a depth-limited flow in a gravel-bed river. *Geomorphology*, *25*(3), 249-267.
Buffin-Belanger, T., and Roy, A.G. 2005. 1min in the life of a river: selecting the optimal record length for the measurement of turbulence in fluvial boundary layers. Geomorphology 68: 77-94.
Bunt, J. A., Larcombe, P., & Jago, C. F. (1999). "Quantifying the response of optical backscatter devices and transmissometers to variations in suspended particulate matter." *Continental Shelf Research*, 19(9), 1199-1220.
Cao, Z. 1997. Turbulent bursting based sediment entrainment function. *J. Hyd. Engr* 123(3):233-236.
Carollo, F. G., Ferro, V., & Termini, D. (2005). Analyzing turbulence intensity in gravel bed channels. *Journal of Hydraulic Engineering*, *131*(12), 1050-1061.
Castillo, L., & George, W. K. (2001). Similarity analysis for turbulent boundary layer with pressure gradient: outer flow. *AIAA journal*, *39*(1), 41-47.
Castillo, L., Seo, J., Hangan, H., & Johansson, T. G. (2004). Smooth and rough turbulent boundary layers at high Reynolds number. *Experiments in fluids*, *36*(5), 759-774.
Chang, H. H. 1988. *Fluvial processes in river engineering*, Wiley, New York.
Chang, W.Y., Fang, T.H. and Lin, Y.C. (2008) "Physical characteristics of polyimide films for flexible sensors." *Applied Physics A*, 92: 693–701**.**
Chao, X., Jia, Y., Shields Jr, F. D., Wang, S. S., & Cooper, C. M. (2010). Three-dimensional numerical simulation of water quality and sediment-associated processes

with application to a Mississippi Delta lake. *Journal of environmental management*, 91(7), 1456-1466.
Christian, D., & Sheng, Y. P. (2003). Relative influence of various water quality parameters on light attenuation in Indian River Lagoon. *Estuarine, Coastal and Shelf Science*, 57(5), 961-971.
Church, M., Biron, P., & Roy, A. (Eds.). (2012). *Gravel Bed Rivers: Processes, Tools, Environments*. John Wiley & Sons.
Clauser, F. H. (1956). The turbulent boundary layer. *Adv Appl Mech*, 4, 1-51.
Clavano, W.R., Boss, E., & Karp-Boss, L., (2007). Inherent Optical Properties of Non-Spherical Marine-Like Particles- From Theory to Observation. *Oceanography and Marine Biology: An Annual Review*, 45, 1-38
Clifford, N. J., Richards, K. S., Brown, R. A., & Lane, S. N. (1995). Laboratory and field assessment of an infrared turbidity probe and its response to particle size and variation in suspended sediment concentration. *Hydrological Sciences Journal*, 40(6), 771-791.
Cloern, J. E. (1987). Turbidity as a control on phytoplankton biomass and productivity in estuaries. *Continental Shelf Research*, 7(11/12), 1367-1381.
Coles, D. (1956). The law of the wake in the turbulent boundary layer. *Journal of Fluid Mechanics*, *1*(02), 191-226.
Colijn, F. (1982). "Light absorption in the waters of the Ems-Dollard estuary and its consequences for the growth of phytoplankton and microphytobenthos." *Netherlands Journal of Sea Research*, 15(2), 196-216.
Dancey, C. L. 1990. Measurements of second order turbulence statistics in an axial flow compressor via 3-component LDA. AIAA J., 90: 2017.
Davies-Colley, R.J. Vant, W.N. and Smith, D.G. 2003: Colour and clarity of natural waters. Science and management of optical water quality. Blackburn Press, New Jersey. 310p.
Davies-Colley, R. J., & Smith, D. G. (2001). Turbidity, suspended sediment, and water clarity: a review. *JAWRA Journal of the American Water Resources Association*, 37(5), 1085-1101.
Davies-Colley, R.J. and J.W. Nagels 2008. Predicting Light Penetration Into River Waters. *Journal of Geophysical Research-Biogeosciences* 113:G03028, doi: 03010.01029/02008JG000722.
Devlin, M. J., Barry, J., Mills, D. K., Gowen, R. J., Foden, J., Sivyer, D., & Tett, P. (2008). Relationships between suspended particulate material, light attenuation and Secchi depth in UK marine waters. *Estuarine, Coastal and Shelf Science*, 79(3), 429-439.
Devlin, M. J., Barry, J., Mills, D. K., Gowen, R. J., Foden, J., Sivyer, D., Greenwood, N., Pearce, D., & Tett, P. (2009). "Estimating the diffuse attenuation coefficient from optically active constituents in UK marine waters." *Estuarine, Coastal and Shelf Science*, 82(1), 73-83.
Downing, J. P., & Beach, R. A. (1989). Laboratory apparatus for calibrating optical suspended solids sensors. *Marine Geology*, 86, 243-249.
Doxaran, D., Ruddick, K., McKee, D., Gentili, B., Tailliez, D., Chami, M., & Babin, M. (2009). "Spectral variations of light scattering by marine particles in coastal waters, from visible to near infrared." *Limnology and oceanography*, 54(4), 1257-1271.
Droppo, I. G., Nackaerts, K., Walling, D. E., & Williams, N. (2005). "Can flocs and

water stable soil aggregates be differentiated within fluvial systems?." *Catena*, 60(1), 1-18.
Duncan, W.J. (1970). Mechanics of fluids. Elsevier, New York.
Einstein, H. A., & Barbarossa, N. L. (1952). River channel roughness. *Transactions of the American Society of civil Engineers*, *117*(1), 1121-1132.
Einstein, H. A., & Li, H. (1958). Secondary currents of turbulent flow over smoot and rough boundaries. *Transactions of the American Society of Civil Engineers*, *39*(1), 1085-1088.
Emadzadeh, A., Chiew, Y. M., & Afzalimehr, H. (2010). Effect of accelerating and decelerating flows on incipient motion in sand bed streams. *Advances in Water Resources*, *33*(9), 1094-1104.
Ford, W. I., & Fox, J. F. (2014). Model of particulate organic carbon transport in an agriculturally impacted stream. *Hydrological Processes*. 28(3), 662-675, DOI: 10.1002/hyp.9569.
Fox, James F., Charles M. Davis, and Darren K. Martin, 2010. "Sediment Source Assessment in a Lowland Watershed Using Nitrogen Stable Isotopes." Journal of the American Water Resources Association (JAWRA) 46(6):1192-1204. DOI: 10.1111/ j.1752 1688.2010.00485.x.
Fox, J.F. and Belcher, B.J. 2011. Comparison of macroturbulence measured using decomposition of PIV, ADV and LSPIV data. *Journal of Hydr. Res.*, 49(1): 122-126.
Fox, J. F., Papanicolaou, A. N., and Kjos, L. (2005). Eddy taxonomy methodology around a submerged barb obstacle within a fixed rough bed. Journal of Engineering Mechanics, 131: 1082–1101.
Fox, J.F., and Patrick, A. 2008. Large-scale eddies measured with large scale particle image velocimetry. Flow Measurement and Instrumentation 19: 283–291.
Fox, J. F. and Stewart, R. L. (2014) Mixed Scaling for Open Channel Flow Over Gravel and Cobbles, *Journal of Engineering Mechanics* DOI: 10.1061/(ASCE)EM.1943-7889.0000793, 06014010.
Franca, M.J., Ferreira, R.M.L. and Lemmin, U. (2008) "Parameterization of the logarithmic layer of double-averaged streamwise velocity profiles in gravel-bed river flows." *Advances in Water Resources*, 31:915–925.
George, W.K. and Castillo, L. (1997). Zero-pressure-gradient turbulent boundary layer. *Appl Mech Rev*, 50(11), 689-729.
Glasgow, H. B., Burkholder, J. M., Reed, R. E., Lewitus, A. J., & Kleinman, J. E. (2004). Real-time remote monitoring of water quality: a review of current applications, and advancements in sensor, telemetry, and computing technologies. *Journal of Experimental Marine Biology and Ecology*, 300, 409-448.
Gordon, H. R. (1989). Can the Lambert-Beer law be applied to the diffuse attenuation coefficient of ocean water?. *Limnology and Oceanography*, 34(8), 1389-1409.
Gosselin, F., Langre, E., and Machado-Almeida, B.A. 2010. Drag reduction of flexible plates by reconfiguration. Journal of Fluid Mechanics 650: 319-341.
Graf, W. H., & Song, T. (1995). Bed-shear stress in non-uniform and unsteady open-channel flows. *Journal of Hydraulic Research*, *33*(5), 699-704.
Gray, J. R., and J. W. Gartner (2009), Technological advances in suspended-sediment surrogate monitoring, *Water Resources Research*, 45, W00D29, doi:10.1029/2008WR007063.

Guo, J., Julien, P. Y., & Meroney, R. N. (2005). Modified log-wake law for zero-pressure-gradient turbulent boundary layers. *Journal of Hydraulic Research*, *43*(4), 421-430.

Harnett, C. K., Schueler, M. T., Blumenthal, N. R., Hopf, K. L., Fox, J. F., and Pulugurtha, S. (2011). Calibration and field deployment of low-cost fluid flow-rate sensors using a wireless network. IEEE Transactions on Instrumentation and Measurement, 60(2): 633-641.

Hart, J.K., and Martinez, K. 2006. Environmental Sensor Networks: A revolution in the earth system science? Earth-science Reviews 78:177-191.

Harun, Z., Monty, J. P., Mathis, R., & Marusic, I. (2013). Pressure gradient effects on the large-scale structure of turbulent boundary layers. *Journal of Fluid Mechanics*, *715*, 477-498.

Hauer, F. R., & Lamberti, G. A. (2006). *Methods in stream ecology*. Academic Press, Amsterdam.

Hill, P. S., Boss, E., Newgard, J. P., Law, B. A., & Milligan, T. G. (2011). Observations of the sensitivity of beam attenuation to particle size in a coastal bottom boundary layer. *Journal of Geophysical Research: Oceans* 116, (C02023), doi:10.1029/2010JC006539.

Hommema, S. E., and Adrian, R. J. (2002). "Similarity of apparently random structures in the outer region of wall turbulence." *Experiments in Fluids*, 33, 5-12.

Horsburgh, J.S., Jones, A.S., Stevens, D.K., Tarboton, D.G., and Mesner, N.O. 2010. A sensor network for high frequency estimation of water quality constituent fluxes using surrogates. Environmental Modelling & Software. 25:1031-1044.

van de Hulst, H. C., (1981). *Light scattering: by small particles*. Dover, New York.

Hurther, D., Lemmin, U. and Terray, E.A. (2007). Turbulent transport in the outer region of rough-wall open-channel flows: the contribution of large coherent shear stress structures (LC3S). *Journal of Fluid Mechanics*, 574: 465-493.

Hussain, A. K., and Reynolds, W. (1972). The mechanics of an organized wave in turbulent shear flow. Journal of Engineering Mechanics, 54: 241–261.

Hutchins, N., & Marusic, I. (2007). Large-scale influences in near-wall turbulence. *Philosophical Transactions of the Royal Society A: Mathematical, Physical and Engineering Sciences*, *365*(1852), 647-664.

Julian, J. P., Doyle, M. W., Powers, S. M., Stanley, E. H., & Riggsbee, J. A. (2008). Optical water quality in rivers. *Water Resources Research*, 44(10), W10411.

Julian, J. P., M. W. Doyle, and E. H. Stanley (2008b), Empirical modeling of light availability in rivers, *Journal of Geophysical Research*, 113, G03022, doi:10.1029/2007JG000601.

Khelifa, A., & Hill, P. S. (2006). "Models for effective density and settling velocity of flocs." *Journal of Hydraulic Research*, 44(3), 390-401.

Kirk, J. T. O., (1981). A Monte Carlo study of the nature of the underwater light field in, and the relationships between optical properties of, turbid yellow waters. *Australian Journal of Marine and Freshwater Research*, 32(4) 533-9.

Kirk, J. T. O. (1984). Dependence of relationship between inherent and apparent optical properties of water on solar altitude. *Limnology and Oceanography*, 29(2), 350-356

Kirk, J. T. O. (1994). *Light and photosynthesis in aquatic ecosystems*. Cambridge University press New York New York.

Kirkgoz, M.S., 1989, Turbulent velocity profiles for smooth and rough open channel flow. Journal of Hydraulic Engineering, 115(11): 1543-1561.
Kironoto, B. A., & Graf, W. H. (1995). Turbulence characteristics in rough non-uniform open-channel flow. *Proceedings of the ICE-Water Maritime and Energy*, *112*(4), 336-348.
Kline, S. J., Reynolds, W. C., Schraub, F. A., & Runstadler, P. W. (1967). The structure of turbulent boundary layers. *Journal of Fluid Mechanics*, *30*(04), 741-773.
Kohavi, R. (1995). A study of cross-validation and bootstrap for accuracy estimation and model selection. In *Prodeedings of the Fourteenth International Joint Conference on Artificial Intelligence* (Vol. 14, No. 2, pp. 1137-1145).
Kwan, T.F. 1988. A study of abutment scour. Rep. No. 451, Dept. of Civil Engineering, Univ. of Auckland, Auckland, New Zealand.
Lacey, R. W. J., and Roy, A. G. (2007). "A comparative study of the turbulent flow field with and without a pebble cluster in a gravel bed river." *Water Resources Research*, 43(W05502).
Lacey. R.W.J., and Roy, A.G. (2008). Fine-Scale Characterization of the Turbulent Shear Layer of an Instream Pebble Cluster. Journal of Hydraulic Engineering 134(7): 925-936.
Larios, D. F., Barbancho, J., Sevillano, J. L., Molina, F. J., & Leon, C. (2012). Energy efficient wireless sensor network communications based on computational intelligent data fusion for environmental monitoring. Communications, IET, 6(14), 2189-2197, doi: 10.1049/iet-com.2011.0809.
Latimer, P. (1985). "Experimental tests of a theoretical method for predicting light scattering by aggregates." *Applied optics*, 24(19), 3231-3239.
Lawson, S. E., Wiberg, P. L., McGlathery, K. J., & Fugate, D. C. (2007). Wind-driven sediment suspension controls light availability in a shallow coastal lagoon. *Estuaries and Coasts*, 30(1), 102-112.
Lee, J. H., & Sung, H. J. (2008). Effects of an adverse pressure gradient on a turbulent boundary layer. *International Journal of Heat and Fluid Flow*, *29*(3), 568-578.
Lelouvetel, J., F. Bigillon, D. Doppler, I. Vinkovic, and J.-Y. Champagne (2009), Experimental investigation of ejections and sweeps involved in particle suspension, Water Resour. Res., 45, W02416, doi:10.1029/2007WR006520.
Limerinos, J. T. (1970). "Determination of manning coefficient from measured bed roughness in natural channels." United States Geological Survey.
Liu, Wen-Cheng, Ming-Hsi Hsu, Shu-Yi Chen, Chi-Ray Wu, and Albert Y. Kuo, 2005. Water Column Light Attenuation in Danshuei River Estuary, Taiwan. *Journal of the American Water Resources Association* (JAWRA) 41(2):425-435.
Lund-Hansen, L. C., Andersen, T. J., Nielsen, M. H., & Pejrup, M. (2010). Suspended matter, Chl-a, CDOM, grain sizes, and optical properties in the Arctic fjord-type estuary, Kangerlussuaq, West Greenland during summer. *Estuaries and coasts*, 33(6), 1442-1451. DOI 10.1007/s12237-010-9300-7.
Maciel, Y., Rossignol, K. S., & Lemay, J. (2006). Self-similarity in the outer region of adverse-pressure-gradient turbulent boundary layers. *AIAA journal*, *44*(11), 2450-2464.
MacVicar, B. J., & Rennie, C. D. (2012). Flow and turbulence redistribution in a straight artificial pool. *Water Resources Research*, *48*(2).

MacVicar, B. J., and Roy, A. G. (2007). Hydrodynamics of a forced riffle pool in a gravel bed river: 1. Mean velocity and turbulence intensity. *Water Resources Research*, 43(124).

Maier, H.R., Jain, A., Dand, G.C., and Sudheer, K.P., 2010, Methods used for the development of neural networks for the prediction of water resource variables in river systems: Current status and future directions, Environmental Modelling and Software 25: 891-909.

Manhart, M. (1998). "Vortex shedding from a hemisphere in a turbulent boundary layer." *Theoretical and Computational Fluid Dynamics*, 12(1), 1-28.

Marusic, I., McKeon, B. J., Monkewitz, P. A., Nagib, H. M., Smits, A. J., & Sreenivasan, K. R. (2010). Wall-bounded turbulent flows at high Reynolds numbers: Recent advances and key issues. *Physics of Fluids (1994-present)*, *22*(6), 065103.

McCuen, R. H., Leahy, R. B., & Johnson, P. A. (1990). Problems with logarithmic transformations in regression. *Journal of Hydraulic Engineering*, 116(3), 414-428.

McLelland, S., A., (2013). Coherent Secondary flows over water-worked rough bed in a straight channel. *Coherent Flow Structures at Earth's Surface*, 275-288.

Mishra, D. R., Narumalani, S., Rundquist, D., & Lawson, M. (2005). Characterizing the vertical diffuse attenuation coefficient for downwelling irradiance in coastal waters: Implications for water penetration by high resolution satellite data. Journal of Photogrammetry and Remote Sensing (ISPRS), 60(1), 48-64. doi:10.1016/j.isprsjprs.2005.09.003.

Mobley, C. D. (1994). *Light and water: Radiative transfer in natural waters* (Academic press, San Diego).

Montgomery, D.C. (2005). *Design and Analysis of Experiments* (John Wiley & Sons, New Jersey) pg 390-391.

Naiman, R. J., & Bilby, R. E. (Eds). (1998). *River ecology and management: lessons from the Pacific coastal ecoregion*. (Springer, New York).

Neukermans, G., Loisel, H., Mériaux, X., Astoreca, R., & McKee, D. (2012). "In situ variability of mass-specific beam attenuation and backscattering of marine particles with respect to particle size, density, and composition." *Limnology and Oceanography*, 57(1) 124-144.

Nezu, I. (2005). Open-Channel Flow Turbulence and Its Research Prospect in the 21st Century. Journal of Hydraulic Engineering: 229-246.

Nezu, I., Kadota, A., Nakagawa, H. (1994), Turbulent structures in accelerating and decelerating open-channel flows with laser Doppler anemometer. 9th Cong. of APD-IAHR, Singapore, Vol. 1, 413–420.

Nezu, I., and Nakagawa, H. 1993. Turbulence in open channel flows, A. A. Balkema, Rotterdam, The Netherlands.

Nikora, V., Goring, D., McEwan, I. and Griffiths, G. (2001) Spatially averaged open-channel flow over a rough bed. *Journal of Hydraulic Engineering*, ASCE, 127(2): 123-133.

Nikora, V., & Roy, A. G. (2012). Secondary flows in rivers: Theoretical framework, recent advances, and current challenges. *Gravel Bed Rivers: Processes, Tools, Environments*, 3-22.

Onitsuka, K., Akayama, J., and Matsuoka, S. (2009), Prediction of velocity profiles and Reynolds stress distributions in turbulent open-channel flows with adverse pressure

gradient, Journal of Hydraulic Research, 47(1):58-65.
Painting, S. J., Devlin, M. J., Malcolm, S. J., Parker, E. R., Mills, D. K., Mills, C., Tett, P., Wither, A., Bert, J., Jones, R., & Winpenny, K. (2007). Assessing the impact of nutrient enrichment in estuaries: susceptibility to eutrophication. *Marine pollution bulletin*, *55*(1), 74-90. doi:10.1016/j.marpolbul.2006.08.020.
Pandey, G. R., & Nguyen, V. T. V. (1999). A comparative study of regression based methods in regional flood frequency analysis. *Journal of Hydrology*, 225(1), 92-101.
Papanicolaou, A. N., & Hilldale, R. (2002). Turbulence characteristics in gradual channel transition. *Journal of engineering mechanics*, *128*(9), 948-960.
Phlips, E. J., Lynch, T. C., & Badylak, S. (1995a). Chlorophyll a, tripton, color, and light availability in a shallow tropical inner-shelf lagoon, Florida Bay, USA. *Marine ecology progress series*, 127(1), 223-234.
Phlips, E. J., Aldridge, F. J., Schelske, C. L., & Crisman, T. L. (1995b). Relationships between light availability, chlorophyll a, and tripton in a large, shallow subtropical lake. *Limnology and Oceanography*, 40(2), 416-421.
Phlips, E. J., Cichra, M., Aldridge, F. J., Jembeck, J., Hendrickson, J., & Brody, R. (2000). Light availability and variations in phytoplankton standing crops in a nutrient-rich blackwater river. *Limnology and Oceanography*, 45(4), 916-929.
Pollack, J. B., & Cuzzi, J. N. (1980). Scattering by non-spherical particles of size comparable to a wavelength: A new semi-empirical theory and its application to tropospheric aerosols. *Journal of the Atmospheric Sciences*, 37(4), 868-881.
Rehmel, M. 2007. Application of Acoustic Doppler Velocimeters for Streamflow Measurements. Journal of Hydraulic Engineering 133(12) 1433-1438.
Rice, C.E., Kadavy, K.C. and Robinson, K.M. (1998) "Roughness of loose rock riprap on steep slopes." *Journal of Hydraulic Engineering*, ASCE, 124(2):179-185.
Rodriquez, J.F., and Garcia, M.H. (2008). Laboratory measurements of 3-D flow patterns and turbulence in straight open channel with rough bed. Journal of Hydraulic Research 46(4): 454-465.
Rouse, H. (1965). Critical analysis of open-channel resistance. *Journal of the Hydraulics Division*, *91*(4), 1-25.
Roy, A. G., Buffin-Bélanger, T., Lamarre, H., and Kirkbride, A. D. 2004. Size, shape and dynamics of large-scale turbulent flow structures in a gravel-bed river. Journal of Fluid Mechanics, 500: 1–27.
Rundel, P.W., Graham, E.A., Allen, M.F., Fisher, J.C., and Harmon, T.C. 2009. Environmental sensor networks in ecological research. New Phytologist 182(3): 589-607.
Schoppa, W., & Hussain, F. (2002). Coherent structure generation in near-wall turbulence. *Journal of fluid Mechanics*, *453*, 57-108.
Shvidchenko, A. B., and Pender, G. (2001). "Macroturbulent structure of open-channel flow over gravel beds." *Water Resour. Res.*, 37(3), 709–719.
Singh, A., Porté-Agel, F. and Foufoula-Georgiou, E. (2010) On the influence of gravel bed dynamics on velocity power spectra. Water Resources Research, 46, W04509.
Smart, G.M. (1999) "Turbulent velocity profiles and boundary shear in gravel bed rivers." *Journal of Hydraulic Engineering*, ASCE, 125(2):106-116.
Smits, A.J., McKeon, B.J., Marusic, I. (2011). "High-Reynolds number wall turbulence." *Annu. Rev. Fluid Mech*. 43:353-75.

Song, T. (1994). ‘‘Velocity and turbulence distribution in nonuniform and unsteady open-channel flow.’’ Doctoral dissertation, Ecole Polytechnique Federale de Lausanne, Lausanne, Switzerland.
Song, T., and Chiew, Y.M. 2001. Turbulence measurement in nonuniform open-channel flow using acoustic Doppler velocimeter (ADV). Journal of Engineering Mechanics, 127(3): 219-232
Song, T., and Graf, W.H. 1994, Non-uniform open-channel flow over a rough bed. *Journal of Hydroscience and Hydraulic Engineering*, 12(1): 1-25.
Sorensen, C. M. (2001). Light scattering by fractal aggregates: a review. *Aerosol Science & Technology*, 35(2), 648-687.
Squires, M. M., & Lesack, L. F. (2003). “Spatial and temporal patterns of light attenuation among lakes of the Mackenzie Delta.” *Freshwater Biology*, 48(1), 1-20.
Stavn, R. H. (2012). “Mass-specific scattering cross sections of suspended sediments and aggregates: theoretical limits and applications.” *Optics Express*, 20(1), 201-219.
Stewart, J. 2008. Calculus Early Transcendentals-Custom edition for University of Kentucky 6th edition Cengage Learning.
Stewart, R. L., Fox, J. F., & Harnett, C. K. (2014). Estimating Suspended Sediment Concentration in Streams by Diffuse Light Attenuation. *Journal of Hydraulic Engineering,* ##(#), ##-##.
Stone, M. C., & Hotchkiss, R. H. (2007). Turbulence descriptions in two cobble-bed river reaches. *Journal of Hydraulic Engineering*, *133*(12), 1367-1378.
Stramski, D., Babin, M., & Wozniak, S. B. (2007). “Variations in the optical properties of terrigenous mineral-rich particulate matter suspended in seawater.” *Limnology and Oceanography*, 52(6), 2418-2433.
Stumpf, R. P., & Pennock, J. R. (1991). “Remote estimation of the diffuse attenuation coefficient in a moderately turbid estuary.” *Remote Sensing of Environment*, 38(3), 183-191.
Sukhodolov, A. N., Nikora, V. I., & Katolikov, V. M. (2011). Flow dynamics in alluvial channels: the legacy of Kirill V. Grishanin. *Journal of Hydraulic Research*, *49*(3), 285-292.
Sunita, M., Malik, J., & Mor, S. (2012). Comprehensive Study of Applications of Wireless Sensor Network. *International Journal of Advanced Research in Computer Science and Software Engineering,* 2 (11), 56-60.
Tamburrino, A., & Gulliver, J. S. (2007). Free-surface visualization of streamwise vortices in a channel flow. *Water Resources Research*, *43*(11).
Townsend, A.A. (1976). The structure of turbulent shear flow, 2nd ed. Cambridge University Press, Cambridge, UK.
Tritico,H.M. and Hotchkiss, R.H. (2005). Unobstructed and obstructed turbulent flow in gravel bed rivers. *Journal of Hydraulic Engineering*, 131(8): 635-645.
Twardowski, M. S., Boss, E., Macdonald, J. B., Pegau, W. S., Barnard, A. H., & Zaneveld, J. R. V. (2001). A model for estimating bulk refractive index from the optical backscattering ratio and the implications for understanding particle composition in case I and case II waters. *Journal of Geophysical Research: Oceans* (2001), 106(C7), 14,129-14,142.
Van de Hulst, H. C., (1981). *Light scattering: by small particles*. (Dover, New York).
Van Duin, E. H. S., Blom, G., Los, F. J., Maffione, R., Zimmerman, R., Cerco, C. F.,

Dortch, M., & Best, E. P. H. (2001). Modeling underwater light climate in relation to sedimentation, resuspension, water quality and autotrophic growth. *Hydrobiologia*, 444, 25-42.
Vannote, R. L., Minshall, G. W., Cummins, K. W., Sedell, J. R., & Cushing, C. E. (1980). The river continuum concept. *Canadian Journal of Fisheries and Aquatic Sciences*, 37, 130-137.
Vanoni, V. A., & Nomicos, G. N. (1960). Resistance properties of sediment-laden streams. *Transactions of the American Society of Civil Engineers*, *125*(1), 1140-1167.
Venditti, J. G., and S. J. Bennett (2000), Spectral analysis of turbulent flow and suspended sediment transport over dunes, J. Geophys. Res., 105: 22,035– 22,047.
Venditti, J. G., & Bauer, B. O. (2005). Turbulent flow over a dune: Green River, Colorado. *Earth Surface Processes and Landforms*, *30*(3), 289-304.
Venditti, J. G., Hardy, R. J., Church, M., & Best, J. L. (2013). What is a Coherent Flow Structure in Geophysical Flow?. *Coherent Flow Structures at Earth's Surface*, 1-16.
Vivoni, E.R., and Camilli, R. 2003. Real-time streaming of environmental field data. Computers & Geosciences 29: 457-468.
Wahl TL. 2000. Analyzing ADV data using WinADV. *Proceedings Joint Conference on Water Resources Engineering and Water Resources Planning and Management, American Society of Civil Engineers*, Minneapolis, 30 July–2 August. www.usbr.gov/wrrl/twahl/winadv.
Walling, D. E., Collins, A. L., Jones, P. A., Leeks, G. J. L., & Old, G. (2006). Establishing fine-grained sediment budgets for the Pang and Lambourn LOCAR catchments, UK. *Journal of Hydrology*, 330, 126-141.
Wang, N., Zhang, N., and Wang, M. 2006. Wireless sensors in agriculture and food industry-Recent development and future perspective. Computers and Electronics in Agriculture 50:1-14.
Williams, N. D., Walling, D. E., & Leeks, G. J. L. (2008). An analysis of the factors contributing to the settling potential of fine fluvial sediment. *Hydrological Processes*, 22(20), 4153-4162.
Willmarth, W. W., & Lu, S. S. (1972). Structure of the Reynolds stress near the wall. *Journal of Fluid Mechanics*, *55*(01), 65-92.
Wosnik, M., Castillo, L., & George, W. K. (2000). A theory for turbulent pipe and channel flows. *Journal of Fluid Mechanics,* 421, 115-145.
Wozniak, S. B., Stramski, D., Stramska, M., Reynolds, R. A., Wright, V. M., Miksic, E. Y., Cichocka, M., & Cieplak, A. M. (2010). "Optical variability of seawater in relation to particle concentration, composition, and size distribution in the nearshore marine environment at Imperial Beach, California." *Journal of Geophysical Research: Oceans,* 115(C8), C08027.
Wu, Y. and Christensen, K.T. (2007). Outer-layer similarity in the presence of a practical rough-wall topography. *Physics of Fluids*, 19: 085108.
Yang, S. Q., & Chow, A. T. (2008). Turbulence structures in non-uniform flows. *Advances in Water resources*, *31*(10), 1344-1351.
Yang, S. Q. (2009). Mechanism for initiating secondary currents in channel flows. *Canadian Journal of Civil Engineering*, 36(9), 1506-1516.
Yang, S. Q., Xu, W. L., & Yu, G. L. (2006). Velocity distribution in a gradually accelerating free surface flow. *Advances in water resources*, *29*(12), 1969-1980.

Yick, J., Mukherjee, B., and Ghosal, D. 2008. Wireless sensor network survey. Computer Networks 52: 2292-2330.

Zagarola, M. V., and Smits, A. J. (1998). Mean-flow scaling of turbulent pipe flow. *Journal of Fluid Mechanics*, 373, 33-79.

Zhang, Y., Zhang, B., Ma, R., Feng, S., & Le, C. (2007). "Optically active substances and their contributions to the underwater light climate in Lake Taihu, a large shallow lake in China." *Fundamental and Applied Limnology/Archiv für Hydrobiologie*, 170(1), 11-19.

Zhu, H. 2007, Viscous flow past a flexible fibre tethered at its centre point: vortex shedding, Journal of Fluid Mechanics, 587: 217-234

VITA

Robert Lynn Stewart III

Education

University of Kentucky, 2011 Master of Science, (Civil Engineering)
Tennessee Technological University, 2009 Bachelor of Science (Civil Engineering)

Professional Experience

Graduate Research Leader, University of Kentucky, (2010-present)
Graduate Research Assistant, University of Kentucky, (2009-present)
Lecturer, Water Resources Engineering CE461G, University of Kentucky, (Currently)
Graduate Teaching Assistant, University of Kentucky, (2009-2013)

Awards

Tau Beta Pi outstanding graduate student award (2013-2014)
KY NSF EPSCoR bridge funding support award (3048108525) (2013-2014)
University of Kentucky College of Agriculture Research Assistantship (2012-2013)
United States Geological Survey Summer Research Fellowship (2012)
University of Kentucky Student Travel Grant (2011, 2012)
National Science Foundation Research Assistantship (2009-2012)
TTU Dean's Honor List (2006-2009) seven semesters

Publications

Stewart, R. L., Fox, J. F., and Harnett, C. K. (2013) Time-Average Velocity and Turbulence Measurement Using Wireless Bend Sensors in Open Channel with Rough Bed, Journal of Hydraulic Engineering 139(7): 696-706.

Stewart, R. L., Fox, J. F., and Cindy, K. H., (2014) Estimating suspended sediment concentration in streams by diffuse light attenuation. Journal of Hydraulic Engineering, 140(8)

Fox, J. F. and Stewart, R. L., Mixed Scaling for Open Channel Flow Gravel and Cobbles, Journal of Engineering Mechanics DOI: 10.1061/(ASCE)EM.1943-7889.0000793, 06014010.

Stewart, R. L. and Fox, J. F., Dimensionless Scaling of Diffuse Light Attenuation by Suspended Sediment, Ecohydrology Paper in Preparation

Fox, J.F., Stewart, R. L., and others, Outer Region Scaling Using the Freestream Velocity for Nonuniform Open Channel Flow Over Gravel, Journal of Engineering Mechanics, Paper in Preparation

Stewart, R. L. and Fox, J. F., Structure of Turbulence in a Gradually Decelerating Open Channel Flow Over a Gravel Bed, Journal of Hydraulic Research Paper in Preparation